

Crystal and Magnetic Structure of CrAs under Extreme Conditions

Andreas Eich

Schlüsseltechnologien / Key Technologies

Band / Volume 260

ISBN 978-3-95806-655-7

Forschungszentrum Jülich GmbH
Jülich Centre for Neutron Science (JCNS)
Quantenmaterialien und kollektive Phänomene (JCNS-2/PGI-4)

Crystal and Magnetic Structure of CrAs under Extreme Conditions

Andreas Eich

Schriften des Forschungszentrums Jülich
Reihe Schlüsseltechnologien / Key Technologies

Band / Volume 260

ISSN 1866-1807

ISBN 978-3-95806-655-7

Bibliografische Information der Deutschen Nationalbibliothek.
Die Deutsche Nationalbibliothek verzeichnet diese Publikation in der
Deutschen Nationalbibliografie; detaillierte Bibliografische Daten
sind im Internet über <http://dnb.d-nb.de> abrufbar.

Herausgeber
und Vertrieb: Forschungszentrum Jülich GmbH
 Zentralbibliothek, Verlag
 52425 Jülich
 Tel.: +49 2461 61-5368
 Fax: +49 2461 61-6103
 zb-publikation@fz-juelich.de
 www.fz-juelich.de/zb

Umschlaggestaltung: Grafische Medien, Forschungszentrum Jülich GmbH

Druck: Grafische Medien, Forschungszentrum Jülich GmbH

Copyright: Forschungszentrum Jülich 2022

Schriften des Forschungszentrums Jülich
Reihe Schlüsseltechnologien / Key Technologies, Band / Volume 260

D 82 (Diss. RWTH Aachen University, 2022)

ISSN 1866-1807
ISBN 978-3-95806-655-7

Vollständig frei verfügbar über das Publikationsportal des Forschungszentrums Jülich (JuSER)
unter www.fz-juelich.de/zb/openaccess.



This is an Open Access publication distributed under the terms of the [Creative Commons Attribution License 4.0](https://creativecommons.org/licenses/by/4.0/),
which permits unrestricted use, distribution, and reproduction in any medium, provided the original work is properly cited.

Abstract

In the ongoing and wide-ranging efforts to understand superconductivity and its interplay with magnetism, chromium arsenide (CrAs) is considered a model system for the coexistence of superconductivity and helimagnetism. The superconductivity in CrAs is induced by pressure and forms a dome-like phase region with a maximum $T_c = 2.2$ K at about 1 GPa in the vicinity of the magnetic phase region where the magnetic structure of CrAs is described as a double helix. With most of the research into CrAs so far focused on macroscopic properties, the principal aim of this work was the investigation of the crystal and magnetic structure of CrAs at low temperatures and high pressures on the basis of X-ray and neutron diffraction measurements.

The crystal structure of CrAs was investigated at ambient pressure in the temperature range 35...400 K and at room temperature in the pressure range up to 9.46 GPa with synchrotron and laboratory X-ray single-crystal measurements.

For the lattice parameters, our results confirm the previously reported abrupt changes that are coupled to the magnetostructural transition from the paramagnetic to the magnetically ordered phase at $T_N = 267$ K. The associated large change in the unit cell volume and the resulting formation of microcracks is indirectly also seen in supporting measurements of the macroscopic resistance over several cooling/heating cycles. Beyond this previously known effect of the phase transition, our results show a second effect in that the microstructure exhibits severe twinning below the transition temperature, which is attributed to the specific behavior of the lattice parameters. In contrast to the low-temperature behavior, no anomalous behavior is observed in the crystal structure as function of pressure up to 9.46 GPa.

In the detailed study of the interatomic distances in the crystal structure of CrAs, the Cr–Cr distances are of primary interest, since the Cr atoms carry the magnetic moment in the structure. It reveals that in particular one distance shows anomalous behavior in that within the paramagnetic region of CrAs – above the transition temperature and at high pressures – it is remarkably unaffected by either temperature or pressure within the experimental range, i.e. it remains approximately constant.

The magnetic structure of CrAs was investigated in this work for the first time by means of neutron single-crystal diffraction. The result clearly shows that the model of the magnetic structure of CrAs that has been used in the literature so far has to be revised. Based on our single-crystal data, the established double-helical model can definitely be discarded. While our data do not allow an unambiguous determination of the correct model, we identify four candidate models based on the agreement with the data, for which the lower-symmetrical magnetic superspace groups and magnetic

moment restraints are taken into account: $P2_1^{[010]}|_{\text{eq.}+\text{opt.}}$, $Pa|_{\text{eq.}+\text{opt.}}$, $P\bar{1}|_{\text{eq.}+\text{opt.}}$ and $P1|_{\text{eq.}+\text{opt.}}$. None of the characteristic features of the reported double-helical model (Cr spins restrained to a crystallographic plane, Cr magnetic moment value, symmetry dependence of Cr sites, and local antiferromagnetic order) is replicated in any of these models. In addition to the single-crystal measurements, supporting neutron powder diffraction measurements provide the temperature-dependence of the propagation vector of the incommensurate magnetic structure of CrAs.

Aside from the scientific investigation of the crystal and magnetic structure of CrAs, part of this thesis is devoted to the development of high-pressure devices suitable for neutron diffraction experiments under extreme conditions, i.e. simultaneous high pressure, low temperature and high magnetic fields. Several such devices, based on the general design of a *clamp cell*, are specifically designed to fit into the existing experimental setups of selected instruments at the Heinz Maier-Leibnitz Zentrum (MLZ), where they are intended for future use as generally available sample environment. Within this work, various tests on these clamp cells were performed regarding characterization and calibration. This includes pressure/load curves, experimental neutron transmission and measurement of magnetic reflections using neutron radiation. Independent of neutrons, the thermal response in a cryostat and loading calibration curves based on ruby luminescence are measured. This work thus presents a new experimental option available for instruments and users at the MLZ, opening new possibilities for science under extreme conditions.

Kurzzusammenfassung

In den andauernden und weitreichenden Bemühungen, Supraleitung und ihr Zusammenspiel mit Magnetismus zu verstehen, wird Chromarsenid (CrAs) als Modellsystem für die Koexistenz von Supraleitung und Helimagnetismus betrachtet. Die Supraleitung in CrAs wird durch Druck induziert und bildet einen kuppelförmigen Phasenbereich mit einer maximalen Sprungtemperatur von $T_c = 2.2\text{ K}$ bei etwa 1 GPa angrenzend an den magnetischen Phasenbereich, wo die magnetische Struktur von CrAs als Doppelhelix beschrieben wird. Da sich die meisten Studien zu CrAs bisher auf makroskopische Eigenschaften konzentrierten, bestand das Hauptziel dieser Arbeit in der Untersuchung der Kristall- und magnetischen Struktur von CrAs bei tiefen Temperaturen und hohen Drücken auf der Grundlage von Röntgen- und Neutronenbeugungsmessungen.

Die Kristallstruktur von CrAs wurde bei Umgebungsdruck im Temperaturbereich von 35...400 K und bei Raumtemperatur im Druckbereich bis zu 9.46 GPa mit Synchrotron- und Labor-Röntgenmessungen an Einkristallen untersucht.

Für die Gitterparameter bestätigen unsere Ergebnisse die bereits bekannten abrupten Änderungen, die an den magnetostrukturellen Übergang von der paramagnetischen zur magnetisch geordneten Phase bei $T_N = 267\text{ K}$ gekoppelt sind. Die damit verbundene große Änderung des Einheitszellvolumens und die daraus resultierende Bildung von Mikrorissen zeigt sich indirekt auch in unterstützenden Messungen des makroskopischen Widerstands über mehrere Kühl/Heiz-Zyklen. Neben diesem bereits bekannten Effekt des Phasenübergangs zeigen unsere Ergebnisse einen zweiten Effekt auf die Mikrostruktur, der sich durch eine ausgeprägte Zwillingsbildung unterhalb der Übergangstemperatur auszeichnet, die auf das spezifische Verhalten der Gitterparameter zurückgeführt wird. Im Gegensatz zum Verhalten bei niedrigen Temperaturen wird kein anomales Verhalten in der Kristallstruktur als Funktion des Drucks bis zu 9.46 GPa beobachtet.

Bei der detaillierten Untersuchung der interatomaren Abstände in der Kristallstruktur von CrAs sind die Cr–Cr-Abstände von vorrangigem Interesse, da die Cr-Atome die Träger des magnetischen Moments in der Struktur sind. Es zeigt sich, dass insbesondere ein Abstand ein anomales Verhalten aufweist, indem er innerhalb des paramagnetischen Bereiches – oberhalb der Übergangstemperatur und bei hohen Drücken – und in den experimentellen Grenzen nahezu unbeeinflusst von Temperatur und Druck ist, d.h. er bleibt annähernd konstant.

Die magnetische Struktur von CrAs wurde in dieser Arbeit erstmals mit Hilfe von Neutronen-Einkristallbeugung untersucht. Das Ergebnis zeigt deutlich, dass das bisher in der Literatur verwendete Modell der magnetischen Struktur von CrAs revidiert werden muss. Basierend auf unseren Einkristalldaten kann das etablierte

Doppelhelix-Modell definitiv verworfen werden. Während unsere Daten keine eindeutige Bestimmung des korrekten Modells erlauben, ermitteln wir vier Kandidatenmodelle auf der Grundlage der Übereinstimmung mit den Daten, wozu die niedersymmetrischen magnetischen Superraumgruppen und Einschränkungen des magnetischen Momentes berücksichtigt werden: $P2_1^{[010]}|_{\text{eq.}+\text{opt.}}$, $Pa|_{\text{eq.}+\text{opt.}}$, $P\bar{1}|_{\text{eq.}+\text{opt.}}$ und $P1|_{\text{eq.}+\text{opt.}}$. Keins der charakteristischen Merkmale des publizierten Doppelhelix-Modells (Einschränkung des Cr-Spins auf eine kristallographische Ebene, Wert des magnetischen Momentes von Cr, Symmetrieabhängigkeit der Cr-Lagen, und lokale antiferromagnetische Ordnung) wird von einem dieser Modelle wiedergegeben. Zusätzlich zu den Einkristallmessungen liefern unterstützende Neutronenbeugungsmessungen an Pulver die Temperaturabhängigkeit des Propagationsvektors der inkomensurablen magnetischen Struktur von CrAs.

Neben der wissenschaftlichen Untersuchung der Kristall- und magnetischen Struktur von CrAs widmet sich ein Teil dieser Arbeit der Entwicklung von Hochdruckzellen, die für Neutronenbeugungsexperimente unter extremen Bedingungen geeignet sind, d.h. unter simultan hohem Druck, niedriger Temperatur und starken Magnetfeldern. Mehrere solcher Zellen, die auf dem allgemeinen Prinzip der *Klemmzelle* basieren, wurden speziell für die bestehenden Vorrichtungen ausgewählter Instrumente am Heinz Maier-Leibnitz Zentrum (MLZ) entwickelt, wo sie in Zukunft als für die Allgemeinheit verfügbare Probenumgebung eingesetzt werden sollen. Im Rahmen dieser Arbeit wurden verschiedene Tests zur Charakterisierung und Kalibrierung dieser Klemmzellen durchgeführt. Dies umfasst Druck/Belastung-Kurven, experimentelle Neutronentransmission und die Messung von magnetischen Reflexen mit Neutronenstrahlung. Unabhängig von Neutronen werden der thermische Verlauf im Kryostaten und Lade-Kalibrierungskurven auf der Grundlage von Rubinlumineszenz gemessen. Diese Arbeit präsentiert damit eine neue experimentelle Option, die für die Instrumente und Nutzer am MLZ zur Verfügung steht, und neue Möglichkeiten für Wissenschaft unter extremen Bedingungen bietet.

Contents

1	Introduction	1
2	Previous Work on CrAs	3
2.1	Crystal Structure	3
2.2	Magnetic Structure	4
2.3	Magnetic and Structural Phase Transitions	6
2.4	Electronic Structure	9
2.5	Pressure-Induced Superconductivity	12
2.6	CrAs and other Transition-Metal Monopnictides	13
3	Theoretical Background	17
3.1	Relation of the NiAs and MnP Structure Types	17
3.2	Magnetic Structures	19
3.2.1	Magnetic Exchange Interaction	19
3.2.2	Magnetic Order	20
3.2.3	Form Factors	22
3.2.4	Magnetic Structure Determination	23
4	High Pressure Techniques	25
4.1	Clamp Cell	25
4.2	Diamond Anvil Cell	25
4.3	Materials for High Pressure Applications with Neutron Radiation	27
4.3.1	Copper Beryllium	28
4.3.2	“Russian Alloy”	29
4.3.3	Titanium-Zirconium	29
4.3.4	Comparison CuBe/NiCrAl/TiZr	30
4.3.5	Tungsten Carbide	33
4.3.6	Further Components	36
4.4	Ruby Luminescence Method	36
4.5	NaCl Pressure Determination	38
4.6	Pressure-Transmitting Media	39
4.6.1	4:1 Methanol–Ethanol	40
4.6.2	Fluorinert	40
4.7	Temperature Dependence of the Pressure	40
5	Experimental Methods	43
5.1	Sample Preparation	43
5.1.1	Synthesis of Polycrystalline Samples	43
5.1.2	Single Crystal Growth	43

5.2	Physical Properties Measurements	44
5.2.1	Magnetization Measurements	45
5.2.2	Resistance Measurements	46
5.3	Diffraction Experiments on CrAs	47
5.3.1	In-House Diffraction Experiments	47
5.3.1.1	Laue X-ray Diffraction	47
5.3.1.2	Powder X-ray Diffraction	47
5.3.1.3	Single-Crystal X-ray Diffraction	48
5.3.2	Synchrotron Single Crystal Diffraction Experiments	48
5.3.3	Neutron Diffraction Experiments	50
5.3.3.1	Neutron Powder Diffraction: HRPT	50
5.3.3.2	Neutron Single-Crystal Diffraction: D9	51
5.4	Test Measurements on High-Pressure Equipment	52
5.4.1	Test of the Thermal Response of the Clamp Cells on DNS	52
5.4.2	Temperature-Dependent Pressure Calibration of the Clamp Cell on HEiDi	53
5.4.3	Calibration of the Clamp Cell on POLI	53
5.4.4	Tests of the Clamp Cell on MIRA	54
6	Clamp Cell Development	57
6.1	Design	57
6.1.1	General Types of Clamp Cells	57
6.1.1.1	Monobloc Clamp Cells	58
6.1.1.2	Fretted Clamp Cells	60
6.1.2	Specific Requirements of the Cells	62
6.1.3	Specific Cell Designs	63
6.1.3.1	Monobloc Clamp Cell M1	63
6.1.3.2	Modified Monobloc Clamp Cell M1D	67
6.1.3.3	Fretted Clamp Cell F1	70
6.2	Simulations	73
6.2.1	Simulation of Clamp Cell Type M1	73
6.2.2	Simulation of Clamp Cell Type F1	75
6.3	Practical Tests	76
6.3.1	Calibration Curve	77
6.3.2	Neutron Transmission	78
6.3.3	Measurement of Magnetic Reflections	80
6.3.4	Thermal Response	81
6.3.5	Feasibility of the Ruby Luminescence Method in Clamp Cells	83
6.3.5.1	Application of the Ruby Luminescence Method	83
6.3.5.2	Calibration of Pressure as Function of Temperature	87
6.3.5.3	Calibration of Pressure as Function of Load Force	89
6.3.5.4	Transmission Loss Correction for the Clamp Cells	93
7	Data Processing	101
7.1	Integration and Indexing	101
7.1.1	Synchrotron and Laboratory X-ray Single-Crystal Data	101
7.1.2	Neutron Single-Crystal Data	103
7.2	Refinement	103
7.2.1	X-ray Single-Crystal Data	103

7.2.2	Neutron Single-Crystal Data	104
7.2.3	Neutron Powder Data	105
8	Results and Discussion	107
8.1	Macroscopic Properties	107
8.1.1	Magnetization	107
8.1.2	Resistance	110
8.2	Crystal Structure	111
8.2.1	Symmetry Considerations	112
8.2.2	Lattice Parameters as Function of Temperature	112
8.2.3	Lattice Parameters as Function of Pressure	114
8.2.4	Refinements and Twinning	116
8.2.5	Atom Coordinates	118
8.2.6	Interatomic Distances	119
8.2.7	Discussion	124
8.3	Magnetic Structure	127
8.3.1	Temperature Dependence of the Propagation Vector	128
8.3.2	Determination of the Magnetic Structure from Single-Crystal Data	129
8.3.3	Validation of the Magnetic Models with Powder Data	135
8.3.4	Discussion	136
9	Summary and Outlook	145
	References	151
	List of Figures	167
	List of Tables	171
	Acknowledgments	173
A	Manual for the Loading of a Clamp Cell	177
B	Details of Ruby Luminescence Test Measurements	181
C	Measurement and Refinement Details	187
D	Supporting Figures to Chapter “Results and Discussion”	227
E	Calculation of Distance Distortion and Angular Distortion	233

Chapter 1

Introduction

Magnetism and superconductivity are of major importance for modern technological applications and thus subject of significant research activities. To allow a systematic control of target material properties on a macroscopic level that are the basis for practical use, a fundamental understanding of the underlying mechanisms and principles on a microscopic level is necessary. This requires to precisely know the structure of the considered material, which is ultimately responsible for the emergent phenomena. This includes the crystal structure and the magnetic structure of the material. Both are coupled to the underlying electronic structure, which in turn is also responsible for superconductive properties and thus mediates interplay between crystal structure, magnetism and superconductivity. Hence, the knowledge of the precise crystal and magnetic structure plays an important role in the understanding of superconducting properties. Since superconductivity emerges only under extreme conditions regarding temperature and pressure, structural investigations in dependence of those parameters are a prerequisite for any conclusive study of a given material.

Chromium arsenide (CrAs) is one material that is of interest for the investigation of magnetism, superconductivity and particularly their coexistence. CrAs exhibits a low-temperature antiferromagnetic phase that is described by a helimagnetic model in the literature, as well as a superconducting phase induced by pressure. At very low temperatures and moderately high pressures, the two phases coexist in a two-phase region. Combined with the rather special form of magnetism (helimagnetism), this coexistence of magnetic order and superconductivity account for the significant research interest in CrAs. Consequently, numerous investigations of the magnetic and superconducting phases have been published. Those, however, focus for the most part on macroscopic properties to deduce the nature of the superconductivity of CrAs. So far, little attention has been devoted to the precise crystal and magnetic structural behavior of the compound, despite those being of major importance for a comprehensive understanding.

This work thus presents the first dedicated and systematic structural study of CrAs under extreme conditions. Based on X-ray and neutron diffraction, measurements at low temperature and at high pressure are performed to allow a detailed analysis of the crystal and magnetic structure of CrAs.

To provide the necessary background for this work, an overview of the previously published work on CrAs is given in **Chapter 2**. This includes the current state of research with regard to the crystal and magnetic structure, corresponding phase transitions, and the electronic structure proposed based on those observations. Furthermore, the pressure-induced superconductivity crucial for the interest in CrAs is introduced in more detail. Last, CrAs is put into broader context of the group of transition-metal monpnictides.

A more detailed theoretical background of specific importance for this work is given in **Chapter 3**. On the one hand, this concerns structure types relevant for the description of the crystal structure of CrAs. On the other hand, the fundamentals of magnetic structure and its determination are discussed here.

Since part of this work focuses on measurements performed at high pressure – which are less routine than those at low temperatures –, **Chapter 4** introduces some important key concepts related to the general application of high pressures in the context of experimental scientific work. This covers the basic types of employed devices and materials as well as methods of pressure determination.

An overview of the experimental methods involved in this work is given in **Chapter 5**. This comprises the sample preparation methods, the measurements of macroscopic physical properties, and diffraction experiments with X-ray and neutron radiation. Additionally, the experimental setup for tests of the high-pressure equipment is briefly introduced.

Chapter 6 focuses on the development of custom-made high-pressure devices suitable for neutron scattering experiments. As an in-detail expansion of the more general chapter on high-pressure techniques, the general type of the *clamp cell* is introduced and its specific implementation in the context of this work is presented. In addition to the technical design, various simulations and practical tests using these cells are reported here.

In **Chapter 7**, the processing procedures for the treatment of the data obtained from the X-ray and neutron measurements are discussed.

The results based on the measured data are then presented and discussed in **Chapter 8**. The chapter comprises three parts: the macroscopic properties magnetization and resistance of CrAs as function of temperature, the behavior of the crystal structure of CrAs in dependence on temperature and on pressure, and lastly the determination of the magnetic structure of CrAs.

A summary of the key results of this work is given in **Chapter 9** together with an outlook regarding future work based on these results.

Supplementary information to various subjects within this thesis is provided in the **Appendices A–E** at the end.

Chapter 2

Previous Work on CrAs

CrAs has been first mentioned as part of broader investigations into the binary system Cr–As and the quasi-binary systems TiAs–CrAs and VAs–CrAs, where its structure at ambient conditions [1, 2] and its thermomagnetic behavior were studied [3–5]. Although the reported magnetic properties proved to be not reproducible in the end, the observed anomalies instigated further research into the magnetic structure of CrAs [6]. Using neutron powder diffraction, this first study focusing on CrAs revealed an interesting magnetic structure, namely a double-helical antiferromagnetic order at low temperatures. The finding of this unusual magnetic structure led in turn to further investigations of CrAs and its magnetic, structural and electronic properties.

2.1 Crystal Structure

CrAs crystallizes in the MnP-type structure with space group $Pnma$ ¹ and $Z = 4$ formula units per unit cell [2]. This structure is a distorted derivative of the NiAs-type structure with space group $P6_3/mmc$ and $Z = 2$ [7]. The unit cell of CrAs and its relationship to the hexagonal NiAs-type structure are shown in Figure 2.1.

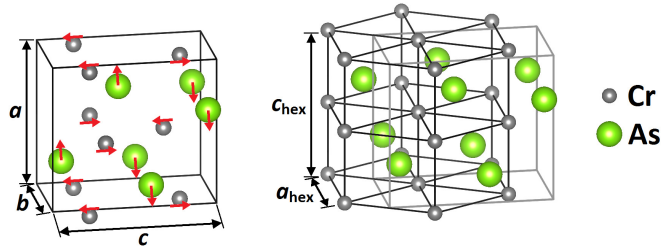


Figure 2.1: Crystal structure of the MnP-type (*left*) and its relationship to the NiAs-type structure (*right*) for CrAs. a , b and c denote the orthorhombic unit cell, a_{hex} and c_{hex} the hexagonal one. Arrows mark the displacements of the atomic positions in the MnP-type structure from the NiAs-type structure. After [8].

¹ $Pnma$ is the setting commonly used today for CrAs, but not necessarily for isostructural compounds.

At ambient conditions, the lattice parameters of CrAs are $a = 5.6490(6) \text{ \AA}$, $b = 3.4609(6) \text{ \AA}$ and $c = 6.2084(7) \text{ \AA}$ [9]. Both the Cr and the As atoms are located at Wyckoff positions $4c$ with coordinates $(x_{\text{Cr}}, 1/4, z_{\text{Cr}})$ and $(x_{\text{As}}, 1/4, z_{\text{As}})$, respectively. The Cr atoms are six-fold coordinated by the As atoms in the shape of distorted octahedra $[\text{CrAs}_6]$, the As atoms are six-fold coordinated by the Cr atoms in the shape of distorted trigonal prisms $[\text{AsCr}_6]$. The $[\text{CrAs}_6]$ octahedra form face-connected columns along the a -axis, which in turn are connected by shared edges. The $[\text{AsCr}_6]$ prisms are edge-connected forming a three-dimensional framework.

The precise dependence of the crystal structure on temperature and on pressure has not been conclusively investigated. The reported structural data are mostly ‘by-products’ of studies concerning the magnetic structure, and no dedicated structural investigation has been performed yet. In addition, presumably for experimental reasons, the reported data cluster at only three different temperatures: around room temperature and around the base temperatures of N_2 and He cryostats. The significant scattering and inconsistency of the available data do not allow a conclusive analysis of the crystal structure of CrAs as a function of temperature and pressure.

2.2 Magnetic Structure

Below the magnetic transition at $T_N \approx 265 \text{ K}$, the Cr atoms carry a magnetic moment of $\sim 1.7 \mu_{\text{B}}$ (at 80 K) with the spins lying in the a, b -plane [9]. For each Cr position within the unit cell, the spins order helically, with the helix propagating along the c -axis with an incommensurate propagation vector $\mathbf{k} = (0, 0, k_c) \approx (0, 0, 0.381) = 0.381 \cdot \mathbf{c}^*$ at 265 K [9], meaning that the helix completes one full turn within $1/0.381 \approx 2.625$ unit cells stacked along the c -axis (Figure 2.2). Due to the fact that these four helices can be separated into two *in-phase* pairs with a fixed angle between them, this structure is commonly described as *double helical* [10].

This complex magnetic structure is assumed to be caused by competing direct and indirect interactions between neighboring Cr atoms [9]. In particular, the spins of Cr^{I} and Cr^{IV} (Cr^{II} and Cr^{III}) are antiparallel, indicating a direct exchange interaction coupling these atoms antiferromagnetically. Between Cr^{I} and Cr^{II} (Cr^{III} and Cr^{IV}), on the other hand, the noncollinear spin arrangement hints at competing indirect exchange interactions, with antiferromagnetic interactions favoring an antiparallel spin order, and Dzyaloshinskii-Moriya interactions (DMI) favoring a noncollinear spin order [12]. The interplay of these competing Cr–Cr interactions is then responsible for the exhibited helimagnetic structure.

With decreasing temperature, the propagation vector decreases from $k_c = 0.381$ at 265 K to $k_c = 0.356$ at 1.5 K [9, 13], which has been linked to a weakening of the DMI between Cr^{I} and Cr^{II} [12]. The magnetic moment increases slightly with decreasing temperature following the few reported data points, with $1.52(4) \mu_{\text{B}}$ at 198 K and $1.67(6) \mu_{\text{B}}$ at 4.2 K [14], though more recent data show no significant change between 80 K and 1.5 K ($1.71(2) \mu_{\text{B}}$ and $1.73(2) \mu_{\text{B}}$, respectively) [13].

While the observed temperature dependence of the propagation vector is rather consistent [9, 11, 13, 15], the influence of pressure on the propagation vector is a question of debate. At effectively the same temperature near liquid helium (1.5...4 K), different studies show either a slight decrease (from $k_c = 0.356$ to $k_c = 0.342$ at 0.69 GPa, measured on a single crystal [11]), a slight increase (from $k_c = 0.356$ to $k_c = 0.363$ at 0.65 GPa, measured on powder [13]) or even a decrease (from

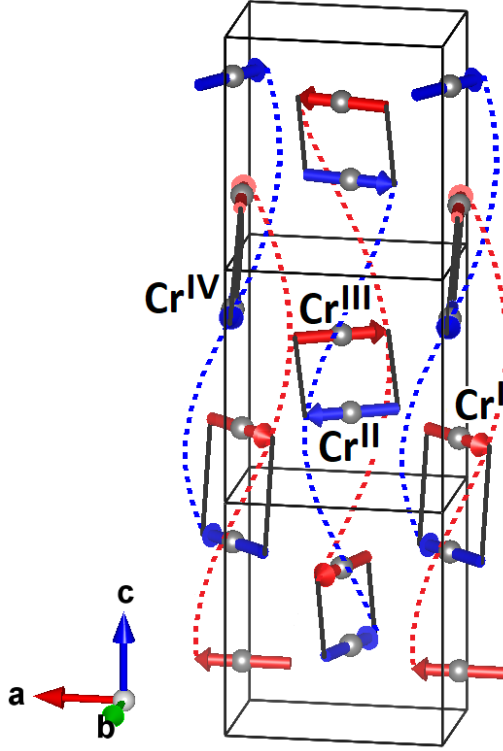


Figure 2.2: The helical magnetic structure of CrAs shown for three unit cells along c , based on the structure reported by Matsuda *et al.* [11]. For clarity, only the Cr atoms are shown. The two *in-phase* pairs of helices are indicated by the red (through Cr^I and Cr^{III}) and blue (through Cr^{II} and Cr^{IV}) dashed lines, and the corresponding spins are marked accordingly. The antiparallel spin alignments of nearest-neighbor Cr^I/Cr^{IV} and Cr^{II}/Cr^{III} pairs are indicated by black lines.

$k_c = 0.356$ to $k_c = 0.175$ at 0.71 GPa, measured on powder [15]). According to the latter reference, the change in \mathbf{k} -vector is accompanied by a spin reorientation. The form of the sample, i.e. single crystal versus powder, has been offered as explanation for the discrepancies concerning the spin reorientation [11], though the precise reasoning for this was not elaborated. However, the differences in the two powder measurements show that this cannot fully explain the differences. This implies, that the behavior of the magnetic structure of CrAs is far from being conclusively understood, and that the system might be affected by external factors in unforeseen ways. The effect of pressure on the magnetic structure extends also to the magnetic moment on the Cr atoms. Generally, it decreases with increasing pressure at the investigated very low temperatures. Depending on the used technique, the ordered magnetic moment decreases strongly (from neutron diffraction) or only moderately (from nuclear magnetic resonance (NMR)) [13]. The difference can partly be ex-

plained by the fact that neutron diffraction yields the ordered moment averaged over the whole sample, while NMR takes into account only the actually magnetic domains. The divergence of the resulting magnetic moment thus indicates that the magnetic volume fraction is reduced by the increasing pressure in favor of the paramagnetic phase, which lowers the average moment obtained by the neutron scattering.

Above T_N , CrAs exhibits Pauli paramagnetism [9, 16], where no localized moments are present and only the spins of unpaired valence electrons near the Fermi level contribute to the magnetic moment. Unlike in the magnetically ordered state, the magnetic susceptibility behaves isotropically and is increasing linearly – a behavior remarkably similar to the one observed in some iron-pnictide superconductors [17–19].

2.3 Magnetic and Structural Phase Transitions

CrAs undergoes two phase transitions in dependence on the temperature: A structural transition at high temperature, and a magnetostructural transition to the previously mentioned helimagnetic phase at lower temperature.

The high-temperature phase transition was first predicted to be an antiferromagnetic-paramagnetic transition based on anomalies in magnetic measurements at ~ 820 K [4, 5], but later asserted to be a purely structural transition from the MnP-type to the NiAs-type structure [6]. A transition at this temperature, however, could later not be experimentally confirmed, and was instead explained by inhomogeneities and/or nonstoichiometricity [9, 14]. A renewed indication for this transition in pure CrAs was seen in the behavior of the measured lattice parameters at $T_t = 1170(20)$ K in a gradual approach of the hexagonal symmetry [20]. Such a second-order transition from the distorted MnP- to the undistorted parent NiAs-type structure seems plausible and has been observed for a number of related compounds. Measurements of the heat capacity support a transition at $T_t = 1180(10)$ K [21].

The existence of the purported transition from a hexagonal to the orthorhombic phase at high temperature is supported by its residual effect seen when CrAs single crystals are grown: in the often-used method of growing CrAs crystals by Sn-flux method, in which temperatures of above 1300 K are reached, the resulting single crystals tend to be multi-domain [22]. This is presumably due to the fact that during the growth process, the initially hexagonal CrAs goes through the structural transition, in which three kinds of deformation are possible, thus forming a multi-domain twinned structure (see Chapter 5.1.2). A lowering of the maximum process temperature to 1150 K yields mono-domain crystals, further supporting the existence of the high-temperature phase transition and the reported transition temperature.

The magnetic transition from the low-temperature helimagnetic phase to the high-temperature paramagnetic phase at $T_N \approx 265$ K is accompanied by a structural transition which leads to large and abrupt changes in the lattice parameters and the unit cell volume. Upon heating and within a temperature range of only ~ 1 K, the lattice parameters change by $\Delta a/a = +0.58\%$, $\Delta b/b = -3.29\%$ and $\Delta c/c = +0.96\%$ (Figure 2.3) [23]. Consequently, the corresponding unit cell volume contracts by

$\Delta V/V = -2.0\%$. The large change as well as the observed hysteresis of about 11 K [9] show the phase transition to have a strong first-order character. Despite the significant change in the lattice parameters, however, the symmetry remains arguably the same with space group $Pnma$ [23], though for clarity it is useful to distinguish between the high-temperature, paramagnetic $Pnma^{(HT)}$ and the low-temperature, helimagnetic $Pnma^{(LT)}$ structures.

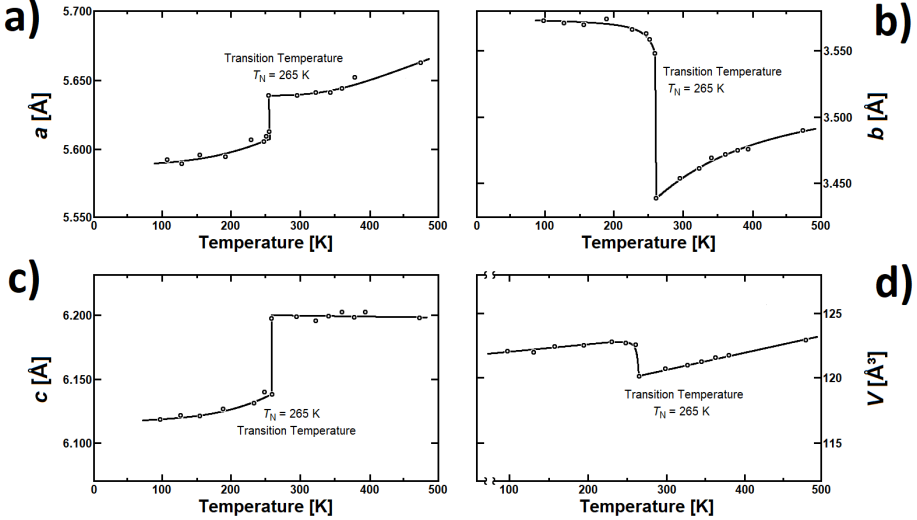


Figure 2.3: Temperature dependence of the lattice parameters a , b and c (a–c) and the unit cell volume (d) of CrAs at low temperatures. Adapted from [23, 24].

This strong anisotropy in the behavior of the lattice parameters on going through the transition is also observed in the temperature dependence of the magnetic and resistive properties. Due to the previously mentioned growth-dependent domain structure, however, not all directions are accessible, with only the behavior parallel to the a -axis and perpendicular to it being distinguishable.

In the magnetic susceptibility, the transition behavior depends on the direction of the applied magnetic field H , with an abrupt drop for $H \parallel a$ and an abrupt jump for $H \perp a$ [17, 25]². The observed anisotropy of the magnetic properties can also explain why no remarkable anomalies were seen in earlier measurements on polycrystalline samples [23]; the random distribution of the crystallites leads to an averaging out of the anisotropic effects [17].

For the electrical resistivity, a further experimental difficulty besides the multi-domain structure is posed by the shape of the CrAs single crystals, which are needle-shaped grown along a [25, 26]. As a consequence, the crystals are sufficiently large to allow the placing of the necessary contacts in practice only along the a -axis, and measurements of the electric resistivity are thus limited to a configuration with

²The measurements reported in [17] show the anisotropy, but are inconsistent in their designation of the axes; the noted dependencies are based on a comparison with [25].

the current flowing along a . The reported results for the behavior of the resistivity across the phase transition are, however, not consistent; both abrupt drops [17, 25, 27] and jumps [26] have been reported. These inconsistencies might be related to another phenomenon that has been concordantly observed in CrAs: The large, abrupt changes in the lattice parameters and the unit cell volume lead to the formation of microcracks in the single-crystalline samples [26, 27]. These cracks in turn lead to an increase of the electric resistivity, so that the measurement depends on the thermal history of the specific sample.

The displayed strong interplay of structural, magnetic and electrical degrees of freedom makes the investigation of the influence of hydrostatic pressure particularly interesting, as it directly affects the unit cell volume without changing the chemical structure. With regard to the change in unit cell volume during the magnetostructural phase transition, the application of pressure should shift the transition temperature T_N towards lower temperatures as the pressure stabilizes the lower-volume, high-temperature phase of CrAs. Indeed, the transition is suppressed rapidly by the application of pressure, with an initial gradient of $dT_N/dp \approx -18 \text{ K/kbar} = -180 \text{ K/GPa}$, which steepens at higher pressures [16], and above $\sim 0.8 \text{ GPa}$, the helimagnetic phase is suppressed completely [28]. At all pressures, the magnetic and the structural transition are coupled [11], and an observed hysteresis indicates that the structural transition remains of first order up to its suppression. Although, according to a model postulated by Matsuda *et al.* [11], the structural and magnetic transition have to be of the same order, the precise nature of the magnetic transition is less clear; nuclear quadrupole resonance measurements show a strong first-order character [29], while the magnetic susceptibility indicates a near second order [11]. Figure 2.4 shows the p - T -diagram of CrAs obtained from resistivity measurements [28] and in particular the suppression of the magnetostructural transition at T_N .

An additional phase transition has been reported if pressure is applied to the paramagnetic high-temperature phase at ambient temperature. Based on measurements of the lattice parameters, a structural phase transition is induced at ~ 0.18 – 0.35 GPa [30]. Another pressure-induced phase transition has been predicted to occur at 33.1 GPa in the ground state based on *ab initio* calculations, with a symmetry change $Pnma \rightarrow P2_13$ [31]. As this pressure region has not been experimentally accessed yet, such a phase transition could not be confirmed.

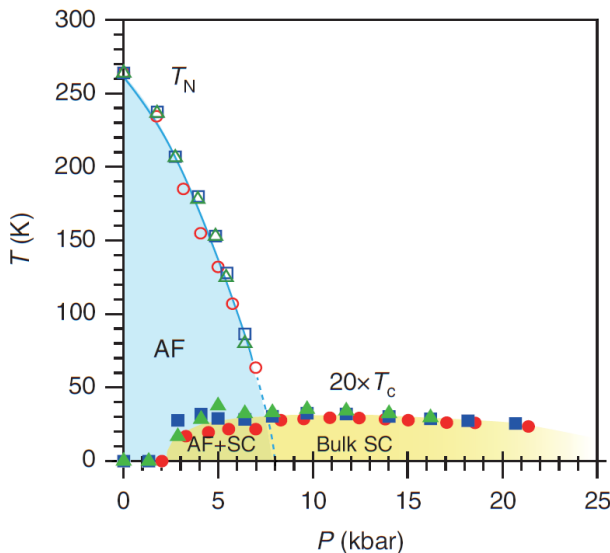


Figure 2.4: Phase diagram of CrAs in dependence on pressure and temperature, showing the helically ordered antiferromagnetic phase (AF), the superconducting phase (SC) as well as the antiferromagnetic (T_N) and the superconducting (T_c) transition temperatures. T_c has been scaled by a factor of 20 for clarity. *Adapted from [28].*

2.4 Electronic Structure

To explain the strong coupling of structural, magnetic and electronic properties observed in the magnetic phase transition of CrAs, Zavadskii and Sibarova proposed a qualitative band scheme [16] based on an earlier model by Boller and Kallel [14].

Such a model has to explain the three following experimental observations:

- In both the high- and the low-temperature phase, the electric conductivity exhibits metallic character.
- In the low-temperature phase the Cr atoms carry a magnetic moment of $\sim 1.7 \mu_B$, and these moments are ordered helically.
- Going through the phase transition, the crystal structure exhibits large, anisotropic changes in the interatomic distances as seen from the behavior of the lattice parameters.

The basic assumption of the proposed model to explain these phenomena is a reconfiguration of the electron structure involving a transition of electrons from a localized state at low temperatures to an itinerant state at high temperatures.

The electron configuration of chromium is $[\text{Ar}] 3d^5 4s^1$, that of arsenic is $[\text{Ar}] 3d^{10} 4s^2 4p^3$. The model assumes that in the CrAs structure, both Cr and As are trivalent and that $3d^2 4s^1$ electrons of Cr form a strong covalent bond with $4p^3$ electrons of As; this assumption of Cr^{3+} with a $3d^3$ configuration was later confirmed by X-ray

absorption spectroscopy [12]. Following the notation used by Boller and Kallel [14] to describe the orbital structure of Cr, where $z \parallel a$, $x \parallel b$ and $y \parallel c$ (Figure 2.5), the d_{z^2} lobes are directed along the a -axis toward the nearest Cr neighbor, the $d_{x^2-y^2}$ lobes along the b -axis toward the equivalent Cr neighbor in the next unit cell, and the d_{xy} lobes toward the next-nearest Cr neighbors in the b, c -plane. The d_{xz} and d_{yz} lobes are directed toward the neighboring As atoms.

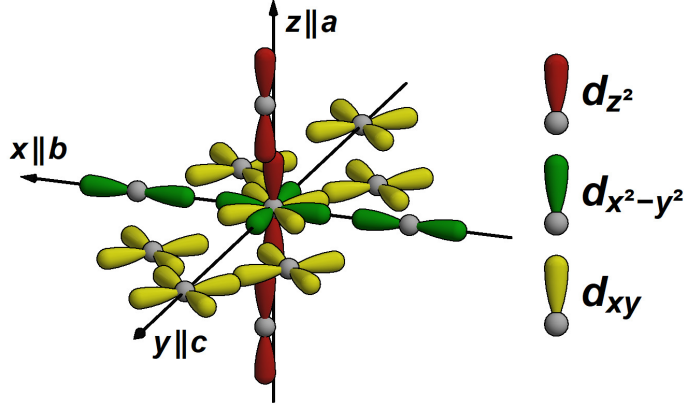


Figure 2.5: Orientation of the d -orbitals in CrAs; only Cr atoms are shown. [14]

Due to the ligand field, the Cr $3d$ energy levels are split. In the idealized NiAs-type structure, Cr is surrounded by six As atoms in shape of an octahedron, leading to an octahedral field splitting of the energy levels. In the used notation, d_{xz} and d_{yz} form the doubly degenerated e_g states, while d_{z^2} , $d_{x^2-y^2}$ and d_{xy} form the triply degenerated t_{2g} states. These energy levels are, however, affected by the orthorhombic distortion of the CrAs crystal structure. The e_g levels are split by this distortion, but since they are not filled they do not play an important role; in the qualitative band scheme (Figure 2.6) they are represented by a single broad band $a_4 + a_5$.

The influence of this distortion on the t_{2g} levels is much larger due to the effect of the Cr neighbors and the variation in their different distances. Crucial for the assessment of these distances is the critical distance R_c for the transition from a localized to an itinerant state of the involved electrons. For Cr–Cr, this distance was estimated as $R_c = 3.18 \text{ \AA}$ [14]. The comparison of the experimental Cr–Cr distances in light of this critical distance is key to the qualitative description of the behavior of CrAs during the magnetostructural phase transition.

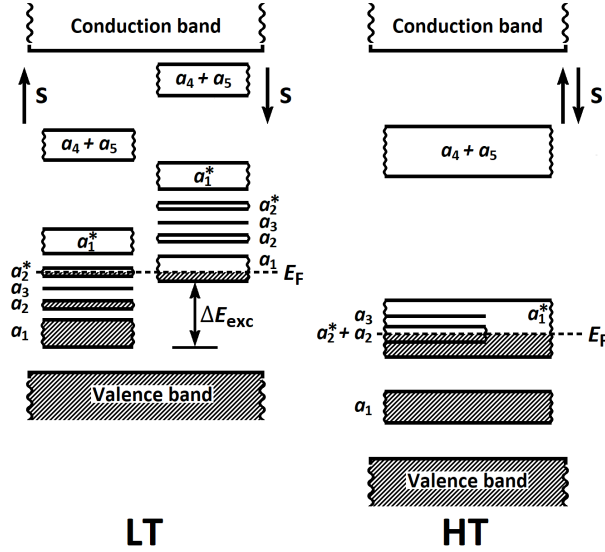


Figure 2.6: Qualitative band scheme of CrAs in the low-temperature helimagnetic phase (*left*) and the high-temperature paramagnetic phase (*right*). Adapted from [16].

Above T_N (Figure 2.6, *right*), the distance between the nearest Cr neighbors (along the a -axis) is 2.889 \AA and thus significantly smaller than R_c . Hence, between these two Cr atoms a strong covalent bond should exist due to overlap of the d_{z^2} orbitals, forming broad bands of itinerant electrons, a binding one a_1 and an antibinding one a_1^* . The distance between next-nearest Cr neighbors (along the b, c -diagonal) is 3.010 \AA and thus also below R_c . Accordingly, there is some overlap of the d_{xy} orbitals, which produces the binding a_2 and antibinding a_2^* bands. The third Cr–Cr distance (along the b -axis) is with 3.445 \AA significantly larger than R_c , and the $d_{x^2-y^2}$ orbitals oriented in this direction do not overlap, creating the band a_3 .

To explain the observed properties of CrAs, Zavadskii and Sibarova postulate the Fermi level E_F as shown in Figure 2.6, *right*, with the electrons distributed to the energy levels in a way motivated by the observed magnetic moment of $1.7 \mu_B$ in the low-temperature phase. The according electronic structure in this high-temperature configuration has two main features: First, the a_3 band is unfilled, and thus the orbitals directed along the b -axis are not occupied; as a consequence, there is no electronic interaction between the Cr-atoms in this direction. Second, the electrons occupying the a_2 bands are itinerant, carrying no localized magnetic moment. In this state, CrAs is a Pauli paramagnet, where only unpaired electrons near the Fermi level contribute to the magnetism. An increase in temperature leads to an increase in the transfer of electrons from a spin-paired configuration to unpaired states above the Fermi level, giving rise to the experimentally observed increase of the magnetic susceptibility in the paramagnetic phase [9].

With decreasing temperature, the distance between the Cr atoms along the b -axis decreases, resulting in a lowering of the a_3 band. At a certain temperature – the transition temperature T_N –, a_3 goes below the Fermi level and electrons can occupy the according $d_{x^2-y^2}$ orbitals. This change in the electronic configuration (Figure 2.6, *left*) has major consequences for the crystal and magnetic structure of CrAs: Since the Cr–Cr distance along the b -axis is too large for an attractive interaction, the only possible interaction of the electronic occupation of the $d_{x^2-y^2}$ orbitals is an electrostatic repulsion, which leads to the large and abrupt increase in the b -axis to 3.573 Å. The Cr–Cr distance along the b , c -diagonal, which is coupled to the Cr–Cr distance along the b -axis by symmetry, increases accordingly to 3.143 Å, close to R_c . Following that, the overlap of the d_{xy} orbitals gets weaker and the a_2 bands get narrower. In these bands, the high state density and the high correlation energy lead to a spontaneous band magnetism that is responsible for the observed magnetic moment of the Cr atoms [32]. The presence of this magnetic moment leads to the lift of the minority-spin (\downarrow) levels by the intraatomic exchange energy ΔE_{exc} shown in Figure 2.6. The less than half-filled $a_{2\uparrow}^*$, responsible for the magnetic moment, should couple the Cr atoms along this direction antiferromagnetically as it has been observed in the magnetic structure.

The half-filled energy bands in both the low-temperature and the high-temperature phase explain the metallic conductivity in both phases as observed in the experiments.

2.5 Pressure-Induced Superconductivity

Aside from the suppression of magnetic order mentioned before, a second effect of hydrostatic pressure on CrAs is the induction of superconductivity. CrAs is the first Cr-based compound in which superconductivity was discovered [26]. Above a pressure of ~ 0.3 GPa, CrAs exhibits a dome-like shaped superconducting phase region (Figure 2.4) with a maximum critical temperature of $T_c = 2.2$ K at ~ 1.0 GPa [26]. At higher pressures, the critical temperature decreases again, until the superconducting phase is suppressed at ~ 4.4 GPa [11]. Between the onset of superconductivity at 0.3 GPa and the suppression of magnetic order at 0.8 GPa, a two-phase region with competing magnetic and superconducting properties is observed [13, 33].

The reported phase diagram of CrAs, with a superconducting dome adjacent to a magnetically ordered state, resembles those of other known superconductors, including heavy-fermion [34], cuprate [35] and iron-pnictide [36] systems. The superconductivity in these systems is of unconventional nature, meaning that the Cooper pairs responsible for the superconducting properties are not mediated by phonons as described by the conventional Bardeen-Cooper-Schrieffer (BCS) theory [37], but instead by other mechanisms, e.g. magnetic fluctuations [38]. While this, in agreement with the observed similarities in the high-temperature paramagnetic behavior, hints at a similar unconventional nature of the superconductivity in CrAs, the pairing mechanism in CrAs has not yet been conclusively elucidated, and both conventional and unconventional superconductivity are supported by experimental findings.

The main evidence for the conventional nature of the superconductivity comes from a muon spin rotation study [33], where the observed correlation of the pressure-dependent critical temperature and the zero-temperature magnetic penetration

depth follows the BCS theory. The unconventional nature of the superconductivity on the other hand is supported by a number of studies that either reject the conventional nature or support the unconventional one: the absence of a Hebel-Slichter peak³ in zero-field NMR measurements has been considered a strong indication that the superconductivity does not fit the BCS model [29]. A detailed study of the electrical resistivity showing an extremely low electron-phonon coupling also contradicts the conventional pairing mechanism and favors the presence of an unconventional one [41]. The sensitivity of the superconductivity to the sample quality has been taken as further evidence for this [22, 28]. As alternative to the conventional phonon-mediated coupling, a coupling *via* magnetic fluctuations has been proposed. Short-range magnetic fluctuations near the superconducting phase in absence of long-range magnetic order have been observed in zero-field NMR and neutron scattering studies and interpreted as responsible for the unconventional coupling [11, 29]. Such a magnetic-mediated coupling has also been supported by further studies of the magnetic structure [13, 15] and the angle-dependent resistivity [42].

Based on the observation that the magnetic transition can be completely suppressed by an external parameter (in this case hydrostatic pressure), the existence of a *quantum critical point* (QCP) has been proposed for CrAs [28]. QCP exist at zero temperature, where thermal fluctuations cease to exist and the transition is driven by quantum fluctuations associated with Heisenberg’s uncertainty principle [43] instead. Although the QCP itself exists only at absolute zero, it can have significant influences well into the non-zero temperature range [44]. If a QCP exists in CrAs, it must be hidden beneath the dome-shaped superconducting region as observed in various systems [45]. In those cases, the superconductivity can be mediated by critical fluctuations originating from the QCP, e.g. from antiferromagnetic spin fluctuations in the vicinity of an antiferromagnetically ordered phase [35]. However, it is not clear whether the observed superconductivity in CrAs is actually associated with critical fluctuations near the potential QCP which would support the pairing *via* antiferromagnetic spin fluctuations. If the superconductivity is indeed coupled to the QCP, the position of the superconducting dome should be tied to the suppression of the magnetic order. The observation that in Al-doped CrAs the superconducting dome is detached from the suppression of magnetic order suggests that the superconductivity is not primarily – if at all – mediated by critical magnetic fluctuations [45].

2.6 CrAs and other Transition-Metal Monopnictides

CrAs is a member of the generalized group of $3d$ transition-metal monopnictides TPn , where $T = \text{Ti-Ni}$ and $Pn = \text{P-Bi}$. The special interest in these compounds originates from the large variety of magnetic properties they exhibit [46]. The majority of these compounds crystallizes in either the MnP or the NiAs structure type [23]. Phase transitions, both between the two structure types and isosymmetrical

³The *Hebel-Slichter coherence peak* describes the phenomenon that in a conventional superconductor the spin relaxation rate exhibits a sharp increase just below T_C , originating from the increase of the electron state density near the superconducting energy gap and the constructive scattering coherence factor of the involved Cooper pairs [39, 40].

ones⁴ are commonly observed. Of particular interest for CrAs are the isostructural compounds which crystallize in the MnP-type, as this might give insight into the role of the structure for the observed magnetic and superconductive properties. For the compounds that exhibit the MnP-type structure, an overview is given in Table 2.1, including the observed phase transitions and the available structural data.

Like CrAs, the compounds CoAs [47] and MnAs [48] exhibit a transition between the MnP- and the NiAs-type structure, though as proposed for CrP [49], a theoretical NiAs→MnP transition at high temperatures might be a more general phenomenon in these compounds. Isosymmetrical phase transitions are reported both between two NiAs-type structures (CrSb [50], MnSb [51] and MnBi [51]) and between two MnP-type structures (MnP [52, 53], FeP [54, 55] and FeAs [56, 57]). In the latter compounds, as in CrAs, the isosymmetrical $\text{MnP}^{(h)} \rightarrow \text{MnP}^{(l)}$ transition from a higher-temperature (h) to a lower-temperature (l) phase is coupled to the onset of magnetic order. The magnetic structure at low temperatures is consistently a helimagnetically ordered phase with the helix propagating along the c -axis, with only MnP showing in addition an intermediate ferromagnetic phase. While the $\text{MnP}^{(h)} \rightarrow \text{MnP}^{(l)}$ transitions in FeP and FeAs and the high-temperature one in MnP (from a para- to the ferromagnetic state) are described to be of second order – although theoretical consideration show that any isosymmetrical phase transition is necessarily of first order [58] –, the low-temperature transition in MnP (from the ferro- to the helimagnetic state) and the transition in CrAs are of first order and accompanied by abrupt changes in the lattice parameters, though the precise changes in MnP are controversial [59, 60]. MnP and CrAs show a further similarity as for both compounds, pressure-induced superconductivity has been confirmed [10]. Although the current lack of systematic structural data for MnP prohibits a conclusive analysis, the observed similarities might indicate a more general connection between the structural and the superconducting properties of the transition-metal monopnictides.

⁴These transitions are commonly denoted as *isostructural*; however, the term *isosymmetrical* should be preferred as the symmetry of the involved phases is identical, while there can be significant changes in the structure.

Table 2.1: Overview of the structural transitions of transition-metal monopnictides (TP_n) compounds exhibiting the MnP-type structure. FM indicates ferromagnetic order; $\parallel c$ indicates ferromagnetically ordered spins along the c -axis; HM indicates helimagnetic order; $\uparrow c$ indicates a helimagnetic propagation vector along the c -axis; FS indicates full structural data; LP indicates lattice parameters; TE indicates thermal expansion data.

TP_n	Magnetic Order no ^[49]	Transition					Superconductivity
		Order	Structure (T_\downarrow)	Temperature	Hysteresis	Pressure	
CrP	no ^[49]	second ^[49]	(NiAs \rightarrow MnP) ^[49]	> 1350(50) K ^[49]	–	ambient	FS: 1.2 K, 4.2 K, 293 K ^[49] 17 K, 81 K, 293 K ^[61] 293 K ^[1, 2, 62, 63] LP: 4...1200 K ^[20]
MnP	FM ($\parallel c$) ^[64]	second ^[59]	MnP \rightarrow MnP ^[52]	291.5(2) K ^[65]	–	ambient (suppressed by p)	FS: 10 K, 60 K, 293 K ^[52] 293 K ^[53, 62, 66] 0...40 GPa ^[67] LP: 300...1300 K ^[70] TE: 4...80 K ^[60, 59]
HM ($\uparrow c$) ^[64] (complex magnetic p - T - H -diagram)	first ^[59]		MnP \rightarrow MnP* ^[52] *no crossing of $c/b = \sqrt{3}$	47 K ^[69]	0.24 K ^[59]	ambient (suppressed at p $\simeq 1.4$ GPa)	yes (p -induced) $p_c \simeq 7.8$ GPa, $T_c \leq 1$ K ^[68]
FeP	HM ($\uparrow c$) ^[72]	(second) ^[55]	MnP \rightarrow MnP ^[55]	125(1) K ^[72]	–	ambient	FS: 293 K ^[62, 72, 73] 30...300 K ^[55] LP: 30...1300 K ^[70] 0...16 GPa ^[74] TE: 100...293 K ^[54]
CoP	no ^[46, 70]						FS: 293 K ^[62] LP: 300...1300 K ^[20]
VAs	no ^[73]						FS: 293 K ^[75, 76] LP: 4...1200 K ^[20]

Table 2.1 (continued): Overview of the structural transitions of transition-metal monopnictides (TPn) compounds exhibiting the MnP-type structure. FM indicates ferromagnetic order; $\parallel c$ indicates ferromagnetically ordered spins along the c -axis; HM indicates helimagnetic order; $\uparrow c$ indicates a helimagnetic propagation vector along the c -axis; FS indicates full structural data; LP indicates lattice parameters; TE indicates thermal expansion data.

TPn	Magnetic Order	Transition					Superconductivity
		Order	Structure ($T\downarrow$)	Temperature	Hysteresis	Pressure	
CrAs	HM ($\uparrow c$) ^[6]	second ^[20]	NiAs \rightarrow MnP ^[20]	1170(20) K ^[20]	–	ambient	FS: 90 K, 285 K ^[14]
							80 K, 285 K ^[9]
							90 K, 295 K ^[25]
							1.5 K, 80 K, 300 K ^[13] (1.5...290 K) @ 0...0.94 GPa ^[15]
MnAs	FM ^[79] (complex magnetic (p - T - H -diagram))	first ^[14]	MnP \rightarrow MnP ^[77]	267 K ^[17]	7 K ^[17]	ambient (suppressed at p $\simeq 0.8$ GPa)	LP: 90...320 K ^[77]
							90...300 K ^[78]
							100...1300 K ^[20]
							FS: 293 K ^[80, 81] 328 K ^[48]
FeAs	HM ($\uparrow c$) ^[56]	(second) ^[56]	MnP \rightarrow MnP ^[56]	77(1) K ^[56]	–	ambient (suppressed by p)	284 K, 317 K ^[82]
							4.2 K, 298 K ^[83]
							(1.5 K, 295 K) @ 3.8 GPa ^[84]
							LP: 100...500 K ^[85]
CoAs	no ^[88]	second ^[20]	NiAs \rightarrow MnP ^[47]	1225 K ^[47]	–	ambient	FS: 12...293 K ^[56] 293 K ^[86]
							0...8.3 GPa ^[87]
							LP: 12...1325 K ^[56]
							FS: 293 K ^[88] 0...4.9 GPa ^[87] LP: 4...1200 K ^[20]

Chapter 3

Theoretical Background

3.1 Relation of the NiAs and MnP Structure Types

The hexagonal NiAs structure type is one of the most common for binary transition-metal compounds, which crystallize either in this structure type or in a derived lower symmetrical phase [89]. The orthorhombic MnP structure type is one of the derivative structures, and commonly found in the transition-metal monpnictides [46]. Within this group, a structural phase transition between the NiAs and the MnP structure type is found in several compounds, e.g. in CrAs, and it is instrumental to discuss the relation between these two structure types in more detail. The following condensed explanation is based on the work of Tremel, Hoffmann and Silvestre [89], and leaves out most of the underlying details regarding the electronic structures. It is applied specifically to CrAs, but is generally valid for the other transition-metal monpnictides.

The high symmetry parent structure NiAs is described by space group $P6_3/mmc$ with $Z = 2$ formula units per unit cell; Figure 3.1 (*top*) depicts the structure in two projections. The structure can be considered as consisting of two sublattices: the As atoms form a hexagonal closed-packed sublattice, which is interpenetrated by a primitive hexagonal sublattice of Cr atoms. The Cr atoms are thus coordinated by 6 As atoms in form of a regular octahedron, while the As atoms are coordinated by 6 Cr atoms in form of a regular trigonal prism; more details regarding the coordination polyhedra are given in Appendix E.

The lower symmetry MnP structure is commonly described as a distorted version of the NiAs structure, where the hexagonal symmetry is broken. Its space group is usually given as $Pnma$ ($Z = 4$), but for this derivation it is helpful to use the non-standard setting $Pmcn$ instead, and unless otherwise specified, orthorhombic axes will in the following refer to the latter setting. $Pmcn$ is a subgroup of $P6_3/mmc$, but not a maximal one. Following group-subgroup relations [90], $Pmcn$ can be reached through the intermediate $Cmcm$ structure, with $Pmcn$ being a maximal subgroup of $Cmcm$, which is in turn a maximal subgroup of $P6_3/mmc$. The structural relationships at the transitions $P6_3/mmc \rightarrow Cmcm \rightarrow Pmcn$ are shown in detail in Figure 3.1.

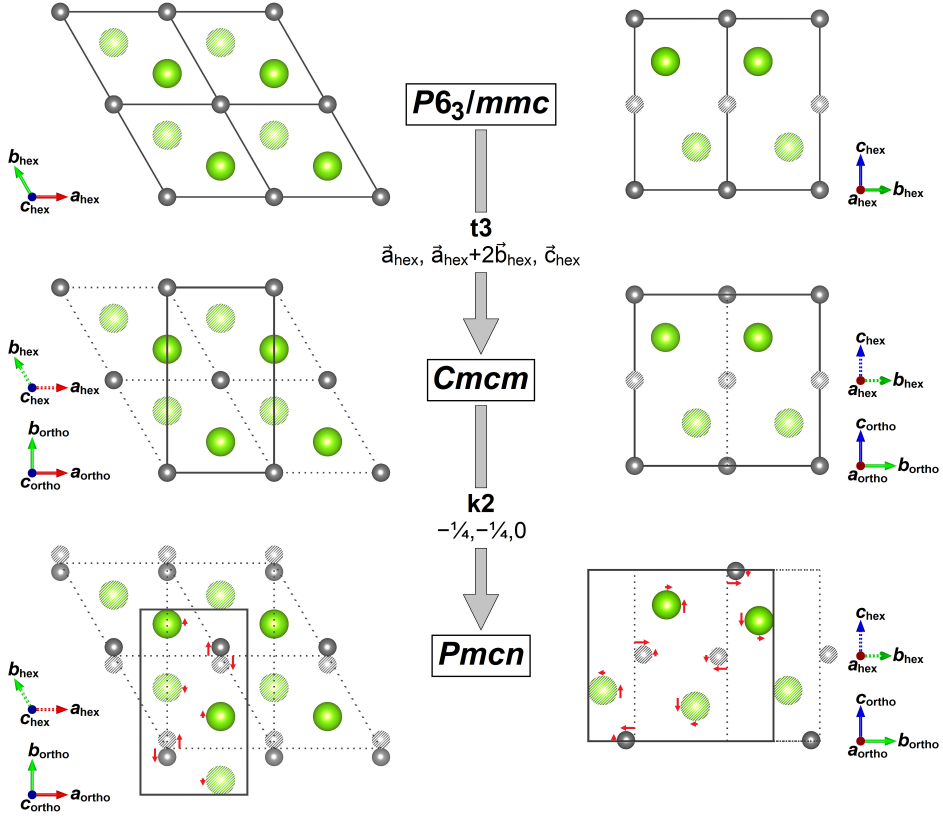


Figure 3.1: The crystal structures with space groups $P6_3/mmc$, $Cmcm$ and $Pmcn$ and their group-subgroup relations. Cr atoms are shown in gray, As atoms in green. Shading distinguishes atoms of the same type at different heights in the unit cell. Red arrows indicate the displacement of the atoms. Adapted from [89].

In the first step, the hexagonal $P6_3/mmc$ structure is transformed into the orthorhombic description $Cmcm$. The sixfold axis is lost in the process, but the translational symmetry is conserved; hence, $Cmcm$ is a *translationengleiche* subgroup of $P6_3/mmc$ with index $t = 3$ ¹.

The size of the unit cell is doubled, with $\vec{a}_{\text{ortho}} = \vec{a}_{\text{hex}}$, $\vec{b}_{\text{ortho}} = \vec{a}_{\text{hex}} + 2\vec{b}_{\text{hex}}$ and $\vec{c}_{\text{ortho}} = \vec{c}_{\text{hex}}$ ($a_{\text{ortho}} = a_{\text{hex}}$, $b_{\text{ortho}} = \sqrt{3} \cdot a_{\text{hex}}$, $c_{\text{ortho}} = c_{\text{hex}}$), yet it includes a C -centering. The unit cell thus contains $Z = 4$ formula units per unit cell.

In the second step, the structure is distorted by the displacement of the atoms from their ideal positions, indicated by red arrows in Figure 3.1. As a result, the C -centering is lost and the space group symmetry is reduced to $Pmcn$. $Pmcn$ is a *klassengleiche* subgroup of index $k = 2$ of $Cmcm$ as the point group (mmm) remains

¹ t is given by $t = P(P6_3/mmc)/P(Cmcm)$ with P the point group orders of the space groups. Here, $Z(P6_3/mmc) = Z(Cmcm) = 2$, $P(P6_3/mmc) = 24$ and $P(Cmcm) = 8$ hence $t = 3$ [90].

the same².

The transition is accompanied by an origin shift of $(-1/4, -1/4, 0)$. The commonly used setting of space group $Pnma$ employed for the description of the MnP structure type can be achieved by cyclical permutation of the axes: $\vec{a}_{Pnma} = \vec{c}_{Pmcn}$, $\vec{b}_{Pnma} = \vec{a}_{Pmcn}$ and $\vec{c}_{Pnma} = \vec{b}_{Pmcn}$.

The distortion of the $Cmcm$ towards the $Pmcn$ structure is explained by considering the effect of Cr–Cr interactions [89]. In the $Cmcm$ structure, each Cr atom has four equidistant neighbors lying in the a, b -plane as shown in Figure 3.2 (*left*). A pseudo Jahn-Teller effect³ leads to the breaking of this symmetry in favor of two shortened Cr–Cr bonds, shown in Figure 3.2 (*right*), which form zig-zag chains along the a -axis. The formation of these bonds is essential for the observed properties of CrAs, where they are considered to be closely related to the magnetic properties.

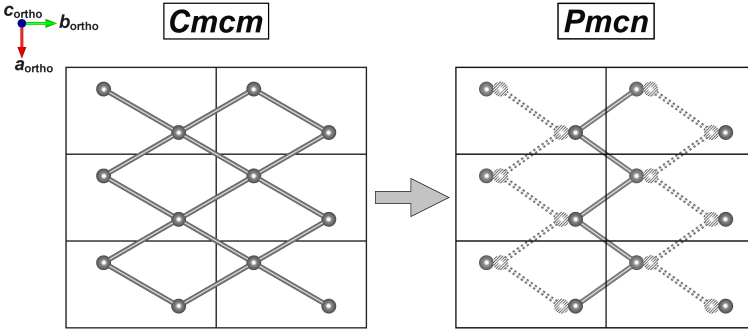


Figure 3.2: Comparison of the Cr–Cr interactions in the a, b -plane in the $Cmcm$ and $Pmcn$ structures. Shading distinguishes atoms of the same type at different heights in the unit cell. Adapted from [89].

3.2 Magnetic Structures

The magnetic structure of a material describes the arrangement of magnetic spins, and is an emergent phenomenon based on the interactions between individual magnetic moments. Various kinds of magnetic order can exist in dependence on the specifics of these interactions.

3.2.1 Magnetic Exchange Interaction

The interaction of the spins of neighboring atoms is based on the exchange interaction between the involved electrons. This exchange interaction is a quantum mechanical effect based on the Pauli exclusion principle and the Coulomb repulsion, and governs the relative orientation of neighboring spins. In a simplified way, the

² k is given by $k = V(P6_3/mmc)/V(Pmcn) \cdot CO(Pmcn)/CO(Cmcn) = 2$, where V is the volume of the unit cells and CO the number of centering operations of the space groups [90].

³Also referred to as *second-order Jahn-Teller effect* in the literature.

Pauli exclusion principle favors the antiparallel alignment of the spins, so that they are allowed in the same quantum state, while the Coulomb repulsion favors their parallel alignment to keep them apart.

For two isolated electron spins \vec{s}_a and \vec{s}_b , and in the absence of an external magnetic field, the exchange interaction can be expressed by the *Heisenberg exchange Hamiltonian*:

$$\hat{H} = -2J_{ab} \langle \vec{s}_a \cdot \vec{s}_b \rangle,$$

with the exchange constant J_{ab} . For $J_{ab} > 0$, the spins are in parallel alignment, for $J_{ab} < 0$ the alignment is antiparallel. The magnitude of J_{ab} indicates the strength of the particular interaction.

In the generalization of the two-electron description for a many-electron system, the spin orientations are determined by the sum of the contributions from all neighboring atoms. Hence, the Heisenberg exchange Hamiltonian becomes

$$\hat{H} = \frac{1}{2} \cdot \left(-2 \sum_{i,j} J_{ij} \langle \vec{s}_i \cdot \vec{s}_j \rangle \right) = - \sum_{i,j} J_{ij} \langle \vec{s}_i \cdot \vec{s}_j \rangle,$$

considering all pairs of spins \vec{s}_i and \vec{s}_j with their respective exchange constant J_{ij} ; the factor $1/2$ removes the double consideration of each pair. The interplay of the individual spin alignments of all spin pairs results in the emergent spin arrangement which determines the magnetic structure of the system.

3.2.2 Magnetic Order

The magnetic structure of a system fully describes the arrangement of the spins with respect to the crystal lattice following from the individual interactions of the spins. These magnetic structures can be classified based on their macroscopic magnetic order, which is often sufficient for practical purposes.

Magnetic order is, however, only assumed by the system if it is energetically favorable. The exchange interaction responsible for the spin interaction is associated with a certain interaction energy. In particular if the thermal energy in the system is too large, i.e. the temperature too high, this interaction energy is not sufficient to establish the magnetic order. In this *paramagnetic* state, the spins are not ordered, but randomly oriented with a net magnetization of zero in the absence of an external magnetic field (Figure 3.3, *left*). A paramagnetic state as absence of magnetic order can also be caused by parameters other than temperature which affect the interplay of the spins, e.g. by pressure.

Figure 3.3 (*right*) shows representations of basic types of magnetic order that can be distinguished. For the sake of simplicity, the orientation of the spins is confined to the plane.

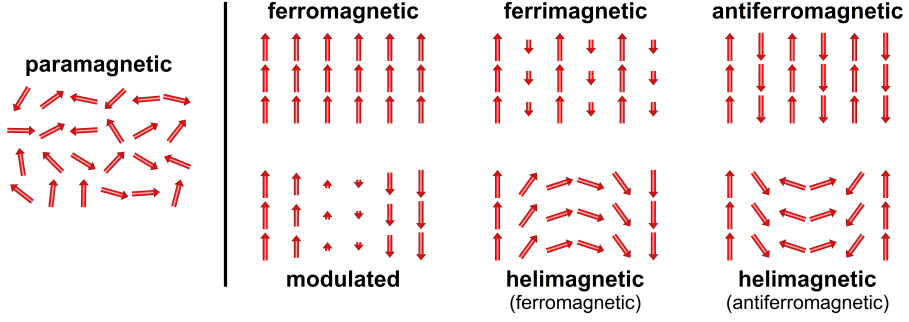


Figure 3.3: Schematic representations of magnetic disorder (*left*) and basic types of magnetic order (*right*). The orientation of the spins is confined to the plane.

As previously mentioned, the exchange interaction between neighboring spins favors either a parallel or an antiparallel spin orientation. Hence, the simplest magnetic orders can be taken as systems in which the spins are arranged either fully parallel (*ferromagnetic*) or fully antiparallel (*antiferromagnetic*). A ferromagnetic arrangement results in a non-zero net magnetic moment and exhibits spontaneous magnetization, i.e. there is a net magnetization in the absence of an external magnetic field. Ferromagnetic order is practically characterized by the temperature where it vanishes, the *Curie temperature* T_C . In the antiferromagnetic systems, there is no net magnetic moment and no spontaneous magnetization, and the temperature below which the antiferromagnetic order is stable is called the *Néel temperature* T_N .

Regarding the other types of magnetic order, it is helpful to consider the orientation of neighboring spins as comprised of two separate components: a turning angle φ to describe how far the neighboring spin is turned, and a modulus r to describe its relative length. In this description, the ferromagnetic state is characterized by $\varphi = 0^\circ$ (spins parallel) and $r = 1$ (spins of constant length), while for the antiferromagnetic state it is $r = 1$ with $\varphi = 180^\circ$ (spins antiparallel). By keeping $\varphi = 180^\circ$, but setting $r \neq 1$ – a more precise description would be $r = a^{\exp[i(\varphi_{\text{tot}} - 180^\circ)]}$, with $a < 1$ and φ_{tot} the total turning angle from the starting atom –, one realizes the *ferrimagnetic* order: neighboring spins are antiparallel, but not of equal length. Hence, the spins pointing in the opposite directions do not cancel each other fully out, and some net magnetic moment remains.

If r follows a more complicated behavior, e.g. a sine function, while $\varphi = 0^\circ$, the magnetic order is *modulated*. The existence of a net magnetic moment then depends on the specific function. This modulation function is periodic, yet the periodicities of the crystal and magnetic structure can be independent. If the combination of crystal and magnetic structure can be described by one periodicity, the modulation is *commensurate*, otherwise it is *incommensurate*.

In the general case of $r = 1$ and $\varphi < 180^\circ$, the magnetic order is *helimagnetic*. For $\varphi < 90^\circ$, the spins of neighboring atoms have a parallel component and the interaction is thus considered to be predominantly ferromagnetic, resulting in a *helical ferromagnetic* order, while for $90^\circ < \varphi < 180^\circ$ it analogously results in a *helical antiferromagnetic* order. Regardless of the turning angle, however, the theoretical

net magnetic moment of any helimagnetic structure (with the spins confined to one plane) is zero.

The extension to three-dimensional ordering of the spins naturally vastly increases the possible magnetic order, and just by suitable superposition of the discussed magnetic orders, arbitrarily complicated magnetic structures can be created. Hence, to determine the precise magnetic structure of a system, a suitable experimental method is needed. The most prominent method for this is neutron scattering, the fundamentals of which are explained in the following.

3.2.3 Form Factors

The determination of the structure of a given material is based on the interaction of a probe with the sample. The two most common probes in the context of crystallography are X-ray and neutron radiation. The precise information that can be obtained from such experiments depends on the respective interaction of the probe with the sample. One crucial parameter here is the *form factor* f , which describes the dependence of the diffracted intensity on the scattering angle θ . The form factor for different probes is shown in Figure 3.4 for the example of the Cr^{3+} ion.

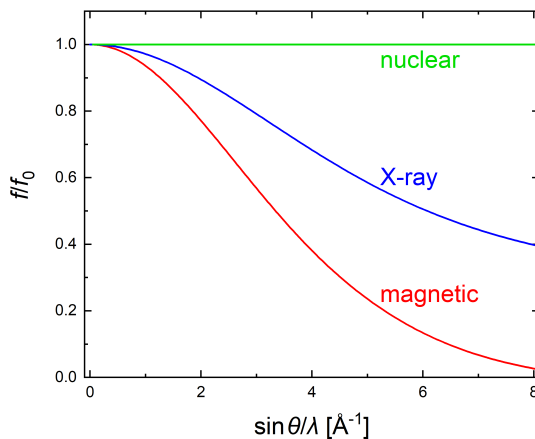


Figure 3.4: Qualitative comparison of the normalized form factors f of Cr^{3+} for X-ray scattering as well as nuclear and magnetic neutron scattering as function of the scattering angle θ ; λ is the probing wavelength. The calculations are based on [91] (X-ray) and [92] (magnetic).

In the case of X-ray radiation, interaction takes place between the electromagnetic wave of the probe and the electron cloud of the atoms of the sample. This spatial distribution of the electron density around the atom leads to the decline of

the form factor with increasing scattering angle⁴. As consequence, X-rays are sensitive to the oxidation state of an atom, but less sensitive to light elements with few electrons and to differences between neighboring elements with similar numbers of electrons.

In contrast to X-ray radiation, the uncharged neutrons comprising neutron radiation interact with the nucleus of the atom instead. Since the nucleus of an atom is about five orders of magnitude smaller than its electron cloud, it can in good approximation assumed to be point-like. Hence, the form factor does not decline with increasing scattering angle and stays basically constant. In addition, the interaction depends on the exact composition of the nucleus, meaning that neutron scattering is isotope-sensitive. Furthermore, neutrons are highly sensitive to light elements and, as the form factor is independent of the atomic number, they can in many cases distinguish neighboring elements in the periodic table.

As mentioned in the previous paragraph, the uncharged neutrons do not interact directly with the charges of the electron cloud – however, they do carry a spin and thus a magnetic moment. The presence of unpaired spins in the electron cloud of an atom results also in a magnetic moment, with which the neutron’s magnetic moment interacts. This *magnetic* scattering is the basis for the determination of magnetic structures. Since unpaired electrons appear only in the outer electron orbitals of an atom, the electron density distribution relevant for the magnetic scattering is different from the one relevant for X-ray scattering. The negligence of the inner electron shells leads to a form factor curve which shows an even faster decline as function of the scattering angle when compared to the X-ray form factor. As a consequence, magnetic reflections can only be experimentally accessed in the low-angle region.

3.2.4 Magnetic Structure Determination

To practically determine the magnetic structure for any given sample compound, two things are of fundamental importance:

First and rather trivially, experimental data, e.g. from neutron powder or single-crystal diffraction measurements, are required on whose basis the subsequent structure determination is carried out. From a practical point of view and considering neutron diffraction experiments as performed in the context of this work, there is no significant difference in experiments aiming to elucidate the nuclear or the magnetic structure of a sample. Hence, strictly speaking no *a priori* knowledge⁵ or consideration of the magnetic structure has to be present in this step.

⁴Mathematically speaking, the form factor is the Fourier transform of the electron density distribution. More graphically, the form factor describes how the spatial distribution of the electron density leads to reduced constructive interference due to the interfering waves not originating from the same point. The larger the scattering angle, the larger is the path difference between the waves and the more incomplete the constructive interference.

⁵While in a single-crystal experiment some knowledge of the magnetic structure, e.g. the propagation vector, might be applied, this only serves to restrict the measurement to relevant detector positions in order to not waste time, and is in theory not actually required.

Second, for the analysis of those experimental data, a theoretical framework to describe magnetic structures is needed.

For the description of an incommensurate magnetic structure like the one in CrAs, the most fundamental characteristic is the *propagation vector* \mathbf{k} of the corresponding modulation, which describes the periodicity of the modulation based on the underlying crystal structure [93]. As such, it is defined as $\mathbf{k} = \alpha\mathbf{a}^* + \beta\mathbf{b}^* + \gamma\mathbf{c}^*$, with the reciprocal lattice vectors \mathbf{a}^* , \mathbf{b}^* , \mathbf{c}^* . If α , β and γ are all rational, the modulation is *commensurate* and the magnetic structure is a superstructure of the crystal structure, which can be described in three-dimensional space. In the case of at least one parameter (α , β , γ) being irrational, the modulation is *incommensurate*. While for commensurate magnetic structures the possible magnetic symmetries can be deduced on the basis of the irreducible representations of the nuclear structure in combination with the observed \mathbf{k} -vector, incommensurate structures require a different approach.

By definition, in commensurate structures the periodicity of the underlying nuclear structure and the propagation vector can be described by a common periodicity. This approach does not work for structures with incommensurate modulation, as there is no common periodicity between the nuclear structure and the incommensurate propagation vector. In order to describe such a structure, two formalisms have been developed: *superspace groups* and *representation analysis*. Both formalisms are general frameworks that allow the description of any commensurate or incommensurate modulated structure, with modulations of any kind (e.g. magnetic, displacive, substitutional). Here, only a very brief introduction to the underlying concept is given, for details, the reader is referred to the dedicated literature.

In the *superspace group* approach, the structure, which exhibits incommensurate modulation in three-dimensional (3-dim) space, is described by expanding the description into $(3+d)$ -dim space, where d is the number of independent incommensurate modulation functions. This $(3+d)$ -dim structure is periodic and thus crystallographic concepts and algorithms can be applied. The symmetry of the $(3+d)$ -dim structure is described by a *superspace group* analogous to the regular space group in 3-dim space, and an analysis of data within this $(3+d)$ -dim framework is possible. Details regarding the superspace group formalism can be found in [94], [95] and references therein.

In the *representation analysis* approach, the symmetry properties of the modulated structure in 3-dim space are described by a set of irreducible representations (irrep). An irrep represents how the properties of the modulated structure transform under the operation of the regular (3-dim) space groups. By considering the active irreps in a structure, restrictions for the modulation (e.g. the components of a magnetic moment on a certain atom) are obtained, allowing the deduction of the magnetic configuration. Details regarding the representation analysis formalism can be found in [96].

Although the two presented formalisms for the analysis of incommensurate modulated structures follow fundamentally differently approaches and were seen as competing concepts, it has been shown that a combination of both yields the best results for the determination of magnetic structures [97]. For the analysis performed within this work, the superspace group formalism as implemented in the program *Jana2006* [97] was used.

Chapter 4

High Pressure Techniques

Unlike temperature-dependent experiments, for which usually only a cryostat is required, the application of high pressure to a sample for diffraction experiments relies on the availability of more specialized equipment. In particular and in the context of this work, this includes pressure cells suitable for neutron and X-ray radiation, as well as methods to determine the pressure in the experimental setup.

4.1 Clamp Cell

The most commonly used device for high-pressure experiments with neutron radiation is the *clamp cell*. Since part of this thesis focuses on the development of such a device, the principle of clamp cells and their design is explained in detail in Chapter 6. In addition, a detailed description of the procedure for the preparation of a clamp cell experiment is given in Appendix A.

4.2 Diamond Anvil Cell

Diamond anvil cells (DAC) are the prevalent tool used to reach high pressures in combination with X-ray radiation, though they can also be adapted for the use with neutron radiation [98–107]. While DACs may differ in their specific design, the basic principle is the same for all types. Since the generated pressure p is determined by the applied force F and the considered area A by $p = F/A$, high pressure can be achieved by making the area very small. This is done by employing the tips of two cut-off diamonds as opposing anvils between which the sample is placed. The basic working principle of a DAC is shown in Figure 4.1.

The central and most important part of a DAC are the two diamond anvils, which are separated by a thin metal disk, the gasket. A hole drilled into the gasket serves as sample chamber in which the sample, a ruby for pressure determination, and the pressure-transmitting medium are placed. The latter serves for converting the uniaxial to hydrostatic pressure conditions. The diamond face directed towards the sample – the *culet* – is smaller than the face directed outwards – the *table*. Applying a force to the table of the diamond through the diamond support plates thus leads to a significantly increased pressure at the culet. A smaller culet size allows higher pressures, at the cost of a reduced sample size. In order to access the sample chamber with X-ray radiation, the diamond support plates feature openings,

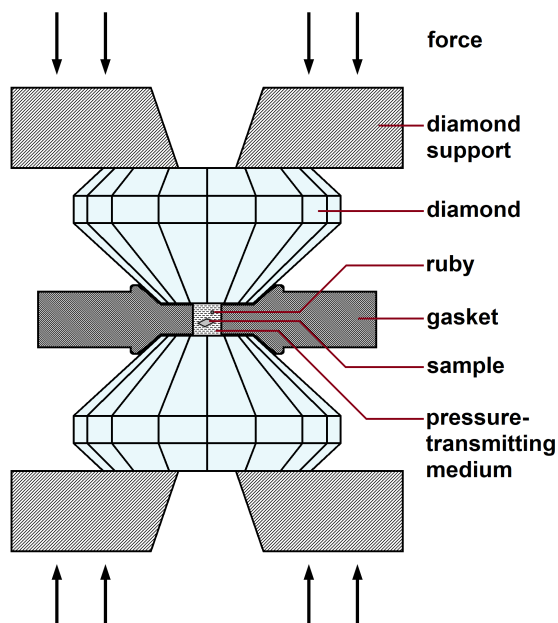


Figure 4.1: Basic principle of the DAC. Adapted from [108].

whose size and shape determine the optical opening angle of the DAC. This basic principle of pressing opposing diamonds together to apply high pressure on a sample chamber is the same for all types of DAC. The differences in types of DAC mainly concern the realization of the surrounding mechanism to generate the force on the diamonds. Two main types can be distinguished: mechanically driven screw types [109] and gas-membrane driven types [110]. In screw-driven cells, the pressure has to be set *ex situ*, but they can be used independently in a wide range of applications. Membrane-driven cells allow the *in situ* change of pressure, but have to be connected to the gas supply.

The choice of diamonds as material for the anvils is based on two crucial properties: their mechanical strength and their transparency.

Mechanically, the anvils should ideally only transmit the applied force from the table to the culet, without being themselves affected by the force, e.g. by deforming. While it is common knowledge that diamond is the hardest (natural) substance, that property is not of direct relevance in the case of the DACs, as *hardness* describes a material's resistance against a local plastic deformation. Instead, its *stiffness* – the resistance against elastic deformation under stress – is of importance. Although separate concepts, these properties are not independent, and diamond also exhibits a very high stiffness [111–113], which makes it an excellent choice to use as force-transmitting material.

While the mechanical strength of diamond is enough to simply apply the high pressure, the transparency is just as important to actually make the pressure chamber experimentally accessible. Diamonds are transparent to photons in both the

low-energy infrared to near-ultraviolet range ($\leq 5\text{ eV}$) and the high-energy range for hard X-rays ($\geq 10\text{ keV}$) [114]. In particular, this allows the application of diamonds with laboratory and synchrotron X-ray diffraction experiments. For neutron radiation, diamonds are nearly fully transparent, with the absorption loss being practically negligible [115]. For both X-ray and neutron radiation, however, the single-crystalline nature of the diamonds can lead to intensity loss by diffraction of the respective beam, for which corrections have to be applied [115].

In the present work, three different types of DAC are used in the experiments on the synchrotron (see Chapter 5.3.2): the *Ahsbahs* type [116], the *Boehler-Almax* type [117] and the *YaoDAC* type [118] (Figure 4.2).



Figure 4.2: The three types of DAC used for experiments in the present work: (from left to right) Ahsbahs, Boehler-Almax and YaoDAC.

The Ahsbahs type is a “standard” DAC where the pressure onto the diamonds is applied by pulling the two backing plates parallel together [116]. Its full conical opening angle is 90° . The Boehler-Almax type also uses screws to increase the pressure, but here the tightening of the screws effects a bending of the backing plates towards each other, which leads to the applied pressure. The opening angle of this cell is 85° [117]. The YaoDAC is a standard screw-tightened DAC specifically developed with a large opening angle of 120° to enable both synchrotron X-ray and neutron experiments on the same sample [118]. While in principle all three types of DAC could be made in a way that is simultaneously compatible with X-ray and neutron radiation, the YaoDAC is the only type for which this is done in the standard version. The reason for this is the fact that the materials used in standard DACs intended only for X-ray radiation are not suitable for use with neutron radiation.

4.3 Materials for High Pressure Applications with Neutron Radiation

Materials that are used for pressure cells have to fulfill certain criteria that are posed by the target sample environment (e.g. low temperature, magnetic field) and the probing method (e.g. synchrotron X-ray radiation, neutron radiation). In the context of this work, a pressure cell intended for use at low temperatures and high magnetic fields in combination with neutron radiation is designed. Considering this

specific application, a material used in the design of such a pressure cell has to meet the following criteria:

- (1) The cell material has high mechanical strength.
- (2) The cell material is non-magnetic.
- (3) The cell material is compatible for use with neutron radiation.

Criterion (1) is rather trivial as it correlates with the basic idea of the high pressure cell. Criterion (2) is needed to allow the measurement of magnetic properties of the sample. An intrinsic magnetic signal from the cell would drown out the signal from the much smaller sample or at least significantly interfere with it. Criterion (3) does not precisely define the required properties but has to be taken into account in the choice of materials. The “compatibility” with neutron radiation concerns on the one hand the characteristic transmission and background properties which are relevant for the geometry; on the other hand and not directly related to the experimental use of the cell but to its practical handling, the material should not be activated too severely by neutron radiation. If the cell takes too long to reach safe levels of radiation, the time between uses of the cell might make it impractical for repeated use during subsequent measurement sessions.

Based on the aforementioned criteria, certain materials are commonly used due to their specific properties in clamp cell designs.

The criterion of non-magnetism basically excludes the large field of ferrous alloys, in particular steels, which have otherwise excellent mechanical properties. Therefore, the materials used are generally highly specialized non-ferrous alloys. In particular, three materials are commonly used for pressure cells suitable for neutron radiation: Copper Beryllium, “Russian Alloy” and Titanium-Zirconium; these will be first briefly introduced and then compared. Materials used for other parts of the cell will be discussed afterwards.

4.3.1 Copper Beryllium

Copper beryllium (CuBe) – also called beryllium copper or beryllium bronze – is one of the most commonly used materials in clamp cells. The CuBe typically used for high-pressure applications contains 2 mass-% beryllium, which is responsible for its excellent mechanical properties, with traces of cobalt, nickel and iron being present (combined below about 0.6 mass-%). It can be hardened by cold working and annealing, allowing the yield strength to be adjusted up to about 1.2 GPa [119]. With decreasing temperature, the yield strength of CuBe increases, reaching about 1.5 GPa at 20 K. This, in addition to the fact that it does not embrittle at low temperatures, makes it very well suited also for low temperature applications. The second reason for the use of CuBe besides its mechanical properties is its very small paramagnetic susceptibility, which makes it compatible with magnetic measurements [120]. Pure CuBe would indeed be diamagnetic and thus ideal for magnetic applications, but the addition of trace amounts of nickel or cobalt are necessary to keep the beryl-

lithium content below the safety limit of 2.2 mass-%¹ [114, 120, 121]. This leads to a small magnetic moment, but eliminates the risk associated with the handling of pure CuBe.

CuBe is commercially available in the hardened state, but care has to be taken in the machining process; since beryllium is toxic and carcinogenic, CuBe dust that is produced during machining has to be safely removed and consequently a workshop has to be equipped accordingly to handle the manufacture of CuBe parts.

4.3.2 “Russian Alloy”

“Russian alloy”² is a nickel-based alloy with the nominal composition Ni₅₇Cr₄₀Al₃ (57.0 mass-% Ni, 40.0 mass-% Cr and 3.0 mass-% Al), or NiCrAl for short [124]. Its mechanical properties are excellent and can be adjusted by the thermal treatment, with a possible yield strength of up to about 2 GPa [120]. In practice, however, NiCrAl with lower strength is used, as fully-hardened NiCrAl is too brittle and too hard to machine, so that a yield strength of about 1.5 GPa is reached [120, 124]. Like CuBe, its mechanical properties do not diminish with decreasing temperatures [122] and it is non-magnetic even at liquid helium temperature [123, 124], making it very well suited for the use in high-pressure cells for magnetic measurements at low temperatures. While it thus can be regarded as mechanically superior to CuBe, the use of NiCrAl is hindered by the general problem related to its procurement; it was not commercially available for a long time, and had to be custom cast and heat treated as was done for this work [124]. Recently, however, raw NiCrAl material became available from at least one commercial provider³, and it is planned for use in commercially available pressure cells [125].

4.3.3 Titanium-Zirconium

In the system titanium-zirconium (Ti-Zr), one particular composition is of great importance for neutron applications in general. With coherent scattering lengths of -3.44 fm for Ti and $+7.16$ fm for Zr, an alloy with a molar Ti/Zr ratio of $7.16/3.44 = 2.08$ has a combined coherent scattering length of zero. This ratio corresponds to a molar composition of 67.5% Ti and 32.5% Zr or – with molar weights of 47.88 g mol⁻¹ for Ti and 91.22 g mol⁻¹ for Zr – a mass composition of 52.2% Ti and 47.8% Zr. The alloy with this specific composition is called *null-scattering*, and the lack of coherent scattering leads to a high neutron transmission and the absence of Bragg reflections in the measurement background. However, the null-scattering TiZr still shows incoherent scattering which produces background in the measurement.

The alloy’s neutron transparency is the reason for its use with neutron radiation in general, but high-pressure application is only possible due to its mechanical properties. The yield strength at room temperature is about 0.6 GPa, with a significant increase at lower temperatures to about 1.3 GPa [119]. While this is significantly

¹At higher beryllium levels, toxic beryllium oxide (BeO) is formed at the surface of the CuBe part, which can cause contamination and subsequent berylliosis by handling it. Below 2.2 mass-%, BeO is not formed and the handling is safe.

²The name refers to the alloy’s origin in the Soviet Union, where it was used by experimentalists. Outside of the Soviet Union it was unavailable and its exact process of production a secret, so that it became known under this name [122, 123].

³Pascalloy™, Tevonic LLC, Lisle, Illinois, USA

lower than CuBe or NiCrAl, in particular at room temperature, it is useful in applications where a lower pressure limit is acceptable to achieve a better neutron transmission. Like NiCrAl, it is non-magnetic and has been used for the study of magnetic signals [126].

While other TiZr alloys are used in various fields, the null-scattering TiZr alloy is used only for neutron applications. Since this is a rather small field, null-scattering TiZr is not commercially available and has to be custom produced. TiZr is not toxic and it can be machined by standard means, but it poses a certain fire hazard during processing. In finely divided form, it may be ignited in air at temperatures above 200 °C and will be hard to extinguish.

4.3.4 Comparison CuBe/NiCrAl/TiZr

For the design of the clamp cells and the according choice of material, the introduced materials – CuBe, NiCrAl and TiZr – can and must be compared with respect to their mechanical properties on the one hand, and their neutron compatibility on the other hand.

From a purely mechanical point of view, NiCrAl is the most suitable, followed by CuBe and TiZr ($\sigma_Y^{\text{NiCrAl}} > \sigma_Y^{\text{CuBe}} > \sigma_Y^{\text{TiZr}}$). At low temperatures, the mechanical strength of all three materials increases.

The mechanical properties have to be balanced against the characteristic neutron transmission. Based on the tabulated scattering cross sections, the theoretical neutron transmission τ can be calculated and compared [127–129]. For the calculated neutron attenuation, the contributions from neutron absorption as well as incoherent and coherent scattering are relevant. Figure 4.3 shows the theoretical values of the neutron transmission for the three materials. For each material, the transmission is calculated once with the coherent scattering taken into account, and once without it. As coherent scattering depends on the specific experimental conditions, it is not necessarily present in a given measurement, but it cannot be generally eliminated either. The comparison shows that without the coherent scattering being considered, CuBe exhibits the highest neutron transmission and NiCrAl the lowest, with TiZr being in between. However, since the big advantage of TiZr is specifically its zero coherent scattering, the consideration of coherent scattering leads to TiZr exhibiting the highest neutron transmission. The transmission of CuBe and NiCrAl decreases significantly, with NiCrAl still being the lowest.

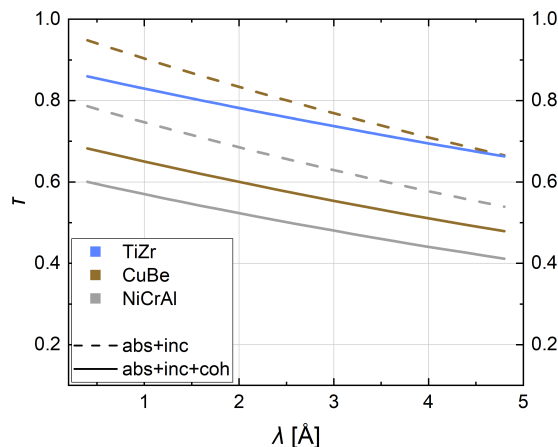


Figure 4.3: Calculated neutron transmission as a function of the neutron wavelength for samples of TiZr, CuBe and NiCrAl, taking into account the contributions to the beam attenuation from neutron absorption (abs), incoherent scattering (inc) and coherent scattering (coh), but not from resonant and inelastic scattering. The calculations are performed for a sample thickness of 0.5 cm. *Calculated with help of [129].*

While these calculations can be helpful to support the choice of material, it is not possible to actually simulate the real transmission behavior; the coherent scattering contribution depends on the specific setup, and attenuation from resonant and inelastic scattering are not taken into account at all. As such, the neutron transmission is measured experimentally for exemplary samples to give a more accurate and realistic assessment. Figure 4.4 shows the experimental neutron transmission for TiZr, CuBe and NiCrAl [130]. There are two obvious observations: First, the real transmission curves are naturally more complicated than the calculated ones, with various dip-like features, especially looking at CuBe and NiCrAl. However, these features might not be actually related to the tested materials. Although the materials are different, the transmission features are very similar, pointing towards an origin that is not material-specific; no explanation for the features are given by the authors [130]. Second, the experiment confirms the basic result from the calculations in that TiZr has the highest transmission, followed by CuBe and then NiCrAl.

Although these experimental values might be close to the transmission that is actually observed for a given clamp cell, in the end only transmission measurements with the real clamp cells can show the precise characteristics. Practical transmission tests were performed for the M1-CuBe clamp cell, see Chapter 6.3.2 for details.

⁴The source states a width of 0.5 mm for the sample disks. However, it stands to reason that this is a mistake and the actual width is instead 0.5 cm, as a width of 0.5 mm should yield a significantly higher transmission.

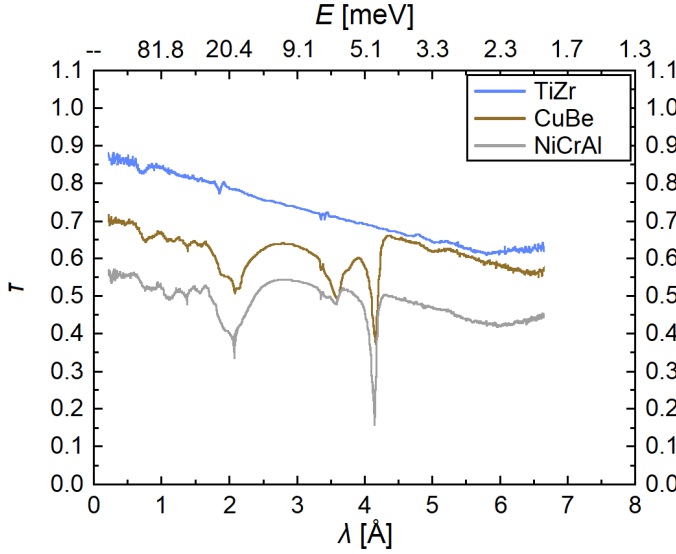


Figure 4.4: Experimentally determined neutron transmission as a function of the neutron wavelength for samples of TiZr, CuBe and NiCrAl, measured for a sample thickness⁴ of 0.5 mm [sic]. *Adapted from [130].*

Following these properties, materials can be selected for application in the different clamp cell designs. TiZr is not used in monobloc designs due to its comparatively low mechanical strength, but it can be used as outer cylinder material in a fretted cell. CuBe and NiCrAl can both be used in a monobloc cell and in fretted cells. Different material variants of a particular cell design allow to choose the cell best suited for a particular application, i.e. a choice between higher maximum pressure and high transmission.

Aside from the neutron transmission, the potential activation of the cell material during the exposure to neutron radiation has to be considered. The calculated activity A as function of time is given in Figure 4.5 for NiCrAl, CuBe and TiZr. Although this does not correspond directly to the effective radiation dose that would be measured for the cell, it can give an indication of the relative activation of the materials and the decay over time.

It is evident that the activities are quite different, with CuBe exhibiting an activity about two orders of magnitude higher than NiCrAl, whose activity is again about two orders of magnitude higher than TiZr. All three materials show a pronounced decrease in the first hour after removal from the beam. Following this, a cooling period of one hour (or even less for CuBe and NiCrAl) should already reduce the expected radiation significantly. For the practical use of the cell, this means that if one hour has not reduced the activation enough for handling, it will take much more time and make multiple measurements with the same cell difficult.

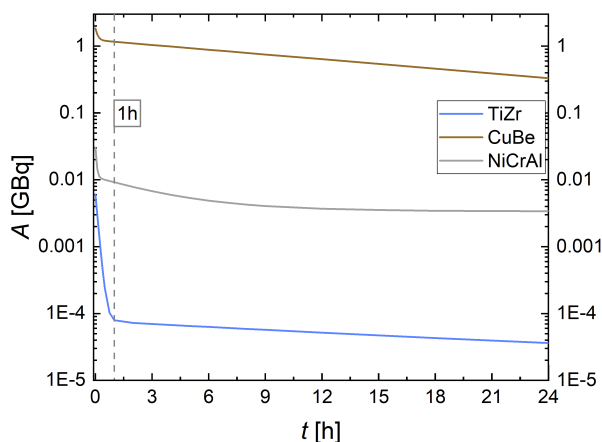


Figure 4.5: The activation after removal from the beam as function of time, calculated for TiZr, CuBe and NiCrAl on the exemplary basis of an exposure time of 10 h, a sample mass of 1 kg and a thermal neutron flux of 10^8 n/cm²/s. Calculated with [129].

As experience shows that neither of the three materials reaches critical levels of activation, it does in practice not play a role in the choice of material for a cell; the activation and necessary cooling period for safe handling are just accepted for a given cell.

4.3.5 Tungsten Carbide

Tungsten carbide (WC) in its raw form is a very hard and high-melting ceramic material. For application, e.g. in tools, it is not used in pure form, but is sintered with a metal acting as binder. As is typical for ceramic and sintered materials, WC is hard, with a very low compressibility and a high compression strength compared to alloys like CuBe or NiCrAl, but it is susceptible to breaking by shear forces. This makes it unsuitable for the use in cylinders of clamp cells, where it would be subject to both compressive and tensile stresses. Its very high resistance to compression, however, makes it very well suited for use in parts that are subjected exclusively to compressive forces. In a clamp cell, this applies to the pistons, which ideally should only transmit the external load to the sample chamber. The combination of low compressibility and high compression strength means that a piston made from WC deforms elastically less than the cylinder and plastically only after other parts of the cell have started deforming already. Hence, the changes in the shape of the piston upon load are practically negligible.

While the choice of binder used in the WC for a clamp cell is not important for the mechanical properties (as in practice it only has to have a higher compressive strength than NiCrAl), this plays a role in the magnetic properties of WC, and like

the main cell materials, the pistons have to be non-magnetic.

For the design of the clamp cells within the context of this work, three WC variants were available, and their magnetic properties were tested to determine their suitability: WC with the standard cobalt binder (Co-WC), WC with nickel binder (Ni-WC) and binderless WC (WC). For the respective samples, the magnetization was measured in dependence on temperature (2...300 K at 1 kOe) and on applied magnetic field ($-90...90$ kOe at 2 K and at 300 K). Figure 4.6 shows an overview of the measured magnetic mass susceptibilities χ_g as function of temperature. Co-WC has the largest susceptibility, which stays almost constant over the whole temperature range. The susceptibilities of Ni-WC and WC at room temperature are similar and almost four orders of magnitude lower than that of Co-WC. For Ni-WC, χ_g increases significantly with decreasing temperature, but it stays below the level of Co-WC. The susceptibility of binderless WC also increases at lower temperatures, but considerably less than Ni-WC.

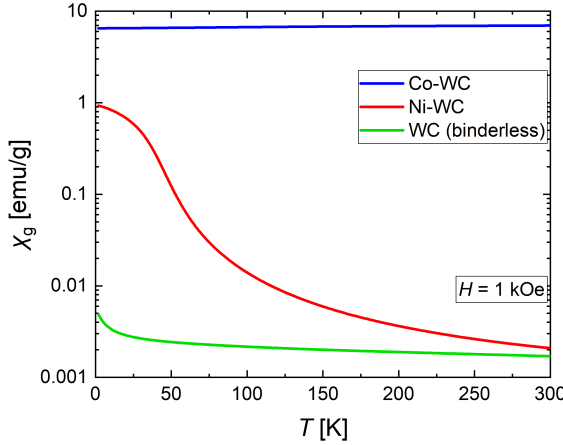


Figure 4.6: The temperature dependence of the magnetic mass susceptibility of the three WC variants Co-WC, Ni-WC and binderless WC.

For the measurements of magnetic properties, however, the important characteristic of a material's magnetization is its coercivity H_c , which determines the necessary field that has to be applied to demagnetize the material and is obtained from the field-dependent measurements of the susceptibility (Figure 4.7). A non-zero coercive field, which would mean that the material exhibits a non-degenerated hysteresis loop, would lead to significant problems in magnetic measurements and make the results unreliable. In a paramagnetic material, the applied magnetic field and the induced magnetization are unambiguously coupled, so that for a given magnetic field strength the contribution from the material is independent of previously applied magnetic fields and can thus be simply subtracted.

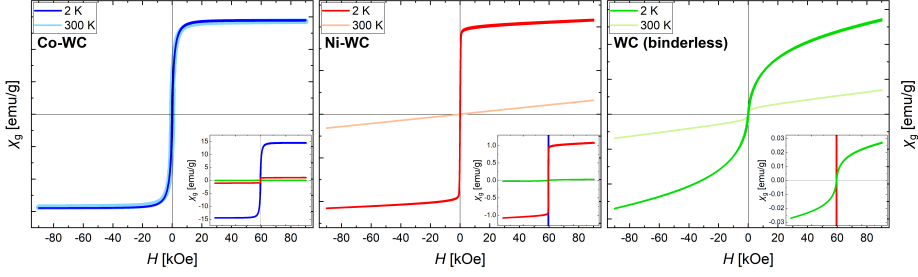


Figure 4.7: The magnetic mass susceptibility of three WC variants as function of applied magnetic field: Co-WC (*left*), Ni-WC (*center*) and binderless WC (*right*) at 300 K and 2 K. The insets show the respective curves in comparison with the other variants.

The coercive fields of the three WC variants are shown and indicated in Figure 4.8. The lowest coercive fields are found in Ni-WC, with values that are lower by a factor of about 2 at 300 K and by a factor of about 10 at 2 K than those of Co-WC and binderless WC ⁵.

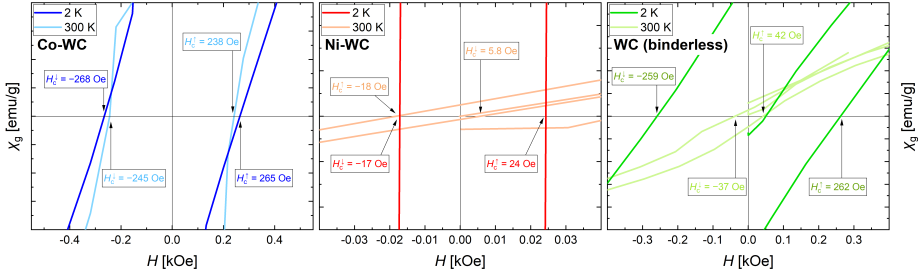


Figure 4.8: The coercive fields at 2 K and 300 K with increasing (\uparrow) and decreasing (\downarrow) applied magnetic field for (*left*) Co-WC, (*center*) Ni-WC and (*right*) binderless WC.

Albeit not precisely zero, the coercivity of Ni-WC is sufficiently small for the material to be generally referred to as paramagnetic, making it the preferred choice for the use of WC in high-pressure neutron applications [119]; binderless WC and Co-WC are not chosen for this due to their higher experimental coercivities compared to Ni-WC. Co-WC would have, in addition to its less desirable magnetic properties, the disadvantage of a strong activation during neutron measurements as the radioactive ^{60}Co isotope is formed by neutron capture.

However, unlike in the cases of the cylinder materials CuBe, NiCrAl and TiZr, the neutron transmission of Ni-WC is not important. Cell parts that are made from

⁵Considering that pure WC should exhibit no coercive field based on its constituent atoms, the measured coercivity indicates magnetic impurities in the material or a contamination during the sample preparation.

Ni-WC should generally not be within the beam if the cell is positioned correctly, and would thus not affect the neutrons interacting with the sample.

4.3.6 Further Components

So far, only the actual clamp cell and its requirements were discussed. The materials discussed until now concern the major load-bearing parts of a cell. For the practical use of a cell in an experiment, in particular with regard to clamp cells, additional equipment is needed, namely the sample capsules whose purpose is to contain the sample and the pressure-transmitting medium. The employed materials do not have to withstand the large stresses; they are deformed during the measurement and discarded afterwards. This gives more freedom for the choice of material with regard to the mechanical properties and also makes the potential activation less relevant. Since the capsule is naturally positioned within the neutron beam path through the sample, its neutron transmission is of importance, though.

Polytetrafluoroethylene

Polytetrafluoroethylene (PTFE)⁶ is probably the material most commonly used for sample capsules [126, 131–136]. It is soft, chemically inert and amorphous. The first two points concern the general suitability for use in a pressure cell, where the capsule itself should not have a significant mechanical resistance to the pressure application, and not react with the sample in any way. The latter part is specifically of interest for scattering experiments, where the capsule should ideally not lead to additional reflections in the measurement. In particular for experiments with neutron radiation, PTFE is suitable as it has a very high neutron transmission.

Aluminium-Magnesium

Aluminium finds general use in the application of neutron radiation as a commonly available construction material with a very high neutron transmission. It can be alloyed with small amounts of magnesium for better machining and mechanical properties, while retaining its transmissive properties. Specifically, an aluminium-magnesium alloy with 5 mass-% Mg (AlMg5, EN AW-5019) is used for the sample capsules based on experience with it for other applications. AlMg5 is harder than PTFE, meaning that it will deform less for a given pressure.

Lead

Similar to PTFE, lead is used sometimes for sample capsules due its high neutron transmission and softness [137, 138]. One disadvantage of lead compared to PTFE is the potential coherent scattering due to its crystalline nature.

4.4 Ruby Luminescence Method

The pressure inside a diamond anvil cell is commonly determined using the *ruby luminescence method* [139, 140]. One or more small pieces of ruby are placed next

⁶The material is commonly known and referred to as Teflon™, a brand name owned by *Chemours*; the use of “Teflon” is so widespread that a distinction between general PTFE and actual Teflon™ is practically impossible.

to the sample in the sample chamber of the cell. Hence, it can be assumed that they are subject to the same pressure as the actual sample. With this ruby, the pressure can be determined as follows:

Ruby is the red variety of the mineral corundum, crystalline aluminium oxide Al_2O_3 (ideal space group $R\bar{3}c$, $Z = 6$ [141], real space group $R3$ due to slight distortions [142–145]), with the red color originating from incorporated traces of Cr. This Cr – in the form of Cr^{3+} ions on Al positions – is responsible for the emission of the characteristic red light; the same fundamental principle is used in ruby lasers [146]. Within the crystal structure of corundum, the Cr^{3+} ion has energy levels as shown in Figure 4.9. Excitation by green or blue light leads to the emission of red light in the characteristic red ruby lines R_1 and R_2 .

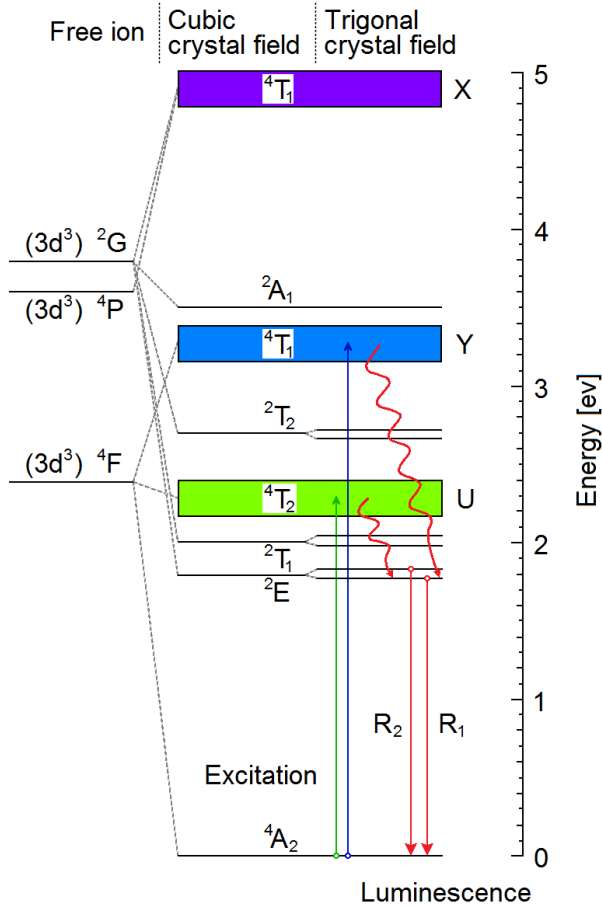


Figure 4.9: The energy levels of the Cr^{3+} in the crystal structure of ruby. The excitation and emission of the R_1/R_2 lines is indicated by arrows. Adapted from [147].

The energy levels from which these lines are emitted have two properties that are important for the use of ruby luminescence for pressure determination. First, they

are very narrow, and the emitted lines are thus very sharp. This allows to determine the energy/wavelength of these lines with a good precision, which is essential for any quantitative use. Second, the precise energy level is affected by the applied pressure as the neighboring ions within the crystal structure are pushed closer together, altering the crystal field potential at the Cr^{3+} site [148]. The wavelength of the ruby lines – in practice, the R_1 is used due to its strength and sharpness [148] – can then be calibrated as function of the applied pressure with the help of standards (e.g. NaCl [149, 150]), resulting in the ruby luminescence pressure scale [151]. Hence, by measuring the change in the R_1 wavelength in a given experimental setup, the pressure can be determined by the use of those calibrations.

Since the energy levels of Cr^{3+} are affected not only by pressure, but also by temperature, this has to be taken into account when using the ruby luminescence method. Temperature-corrections exist for the low temperature [152] and high temperature [153] region.

The ruby luminescence method is, as mentioned, the prevalent method for pressure determination in diamond anvil cells and used to measure pressures up to more than 100 GPa [151]. While tests performed within this work show that ruby luminescence can also be used in clamp cells (see Chapter 6.3.5), it is not ideal for this application: since the pressure in a clamp cell is limited to very low pressures (in the order of 2 GPa) compared to diamond anvil cells, the shift in the ruby luminescence is correspondingly quite small and thus the experimental uncertainty in the determined wavelength is more significant. This problem, however, concerns only the real “ruby” luminescence, where actual ruby is used as luminescent sample. Other substances employing the principle of pressure-dependent luminescence have been found to be better suited for application with clamp cells, e.g. samarium-doped strontium tetraborate $\text{SrB}_4\text{O}_7:\text{Sm}^{2+}$ [154–156], which has better properties regarding the luminescence (no peak doublet, sharper luminescence line), but has approximately the same pressure coefficient (the shift in luminescence with pressure) as standard ruby. In order to improve the pressure sensitivity in the range of interest for clamp cells, a larger pressure coefficient would be desirable. One candidate is the so-called “molecular ruby”, a chromium(III) complex containing⁷ $[\text{Cr}(\text{ddpd})_2]^{3+}$ [157–159], which exhibits a pressure coefficient that is approximately 20 times higher than that for ruby in the pressure range up to about 3 GPa. Coupled with a high luminescence quantum yield and simple preparation, it would be excellent for the purpose of pressure determination in clamp cells, but it has one considerable disadvantage: the crystals are very soft and are thus completely crushed by the application of even smallest pressures, although the effect of this crushing on the luminescence properties has not yet been investigated. If this “molecular ruby” could be successfully used for pressure determination, the pressure sensitivity would be increased significantly.

4.5 NaCl Pressure Determination

Of similar importance to the ruby luminescence method for diamond anvil cells is the pressure determination with NaCl for clamp cells. The pressure within the sample

⁷ddpd = *N, N'*-dimethyl-*N, N'*-dipyridine-2-yl-pyridine-2,6-diamine

chamber is here measured with help of a calibration sample that is inserted into the sample space and thus under the same pressure conditions as a real sample. To determine the pressure, neutron diffraction is used to measure the lattice parameters of the calibration sample; these are calibrated against pressure so that the applied pressure can be calculated [149]. NaCl is the common choice as sample material as it has a number of advantageous properties: Most fundamentally, it has a high symmetry (cubic, $Fm\bar{3}m$ [160]⁸), which means that the effect of pressure is isotropic and that only a small number of reflections is observed. Furthermore, it is relatively soft, ensuring a sufficiently high sensitivity at low pressures. In addition – important for practical use – it is easily available in form of large single crystals that can be oriented thanks to its high anisotropic cleavability.

4.6 Pressure-Transmitting Media

Measurements at high pressures are most commonly performed or aimed to be performed under hydrostatic conditions [161], i.e. the pressure to which the sample is subjected is isotropic. The theoretical reason is that hydrostatic pressure is a thermodynamic parameter, meaning that it allows the measurement of intrinsic material properties. Practically, it has the advantage of being the most well-defined and thus reproducible pressure state⁹. To realize hydrostatic conditions in practice, a *pressure-transmitting medium* is used, which transforms the applied (usually uniaxial) pressure into hydrostatic pressure. To do this, the medium ideally should have a negligible viscosity to not support any shear stress. As a consequence, the most common pressure-transmitting media are fluids [119] (liquid), although also soft rigid (solid) media are sometimes used [119, 162]. However, the fluidity of each pressure-transmitting medium is restricted to a certain specific range depending on temperature and pressure. Going to low temperatures, the fluids freeze out, undergoing phase transitions to solid phases in which the shear stresses are no longer negligible. The same happens on going to high pressures, where the solidification is induced by the applied pressure. With the appearance of shear stresses, the conditions are not hydrostatic anymore, and although this might be tolerated if the effects are small enough (“quasihydrostatic”), it eventually leads to ill-defined experimental conditions.

As this is related only to the pressure application itself, the aforementioned issue concerns any probing method (e.g. X-ray or neutron radiation) likewise. However, especially the use of a pressure-transmitting medium with neutron radiation poses additional requirements in order to avoid experimental problems arising from the interaction of neutrons with the medium.

Hence, for any given high-pressure application, a suitable pressure-transmitting medium has to be chosen. In the following, the media involved in the context of this work are briefly introduced.

⁸Although the crystal structure of NaCl is described as ‘simple cubic’ in the reference, it is clear from context that in today’s terms the face-centered cubic system is described.

⁹“Non-hydrostatic” pressure conditions are, as the name implies, defined solely by the fact that they are not hydrostatic and thus comprise a large variety of vastly different pressure conditions, which result in correspondingly different effects.

4.6.1 4:1 Methanol–Ethanol

A 4:1 volume mixture of methanol and ethanol is the most commonly used pressure-transmitting medium [161]. At room temperature, it has a pressure-induced glass transition at around 10 GPa [161, 163], which is reduced to about 0.35 GPa at 125 K [164]. Regular 4:1 methanol–ethanol is used for X-ray radiation experiments, but it is not suited for use with neutron radiation. The hydrogen¹⁰ contained in the two alcohols produces a strong background signal due to its large incoherent neutron cross section. For application in neutron experiments, the use of deuterated methanol and ethanol is required, where the regular hydrogen is replaced by deuterium atoms. Deuterium has a significantly smaller neutron cross section and does thus not lead to the strong background.

4.6.2 Fluorinert

“Fluorinert” refers to a series of liquids trademarked by 3M, comprising a variety of perfluoro-carbon liquids with the general chemical composition $(C_8F_{18})_n(C_8F_{16}O)_m$. Due to the lack of contained hydrogen, Fluorinert varieties have been widely used for applications with neutron radiation for a long time [161], either in pure form or in mixtures. The pressure limit depends on the exact Fluorinert, but it is generally inadequate for pressures beyond 2 GPa. Unlike in the case of 4:1 methanol–ethanol, experiments show that this pressure limit can be retained even at low pressures if the cooling rate is sufficiently small (< 1 K/min) [165]. Although the pressure limit for Fluorinert is comparably low, it is well suited for the application with clamp cells, where the pressure is limited to low pressures already by the cell design and the low-temperature properties are of great importance.

4.7 Temperature Dependence of the Pressure

Temperature has a direct influence onto the pressure that is obtained at the sample position in a high-pressure cell. Going to low temperatures, the thermal contraction of the pressure cell and the pressure-transmitting medium as well as the sample itself change the compression state and thus the effective pressure. The contraction of the cell materials reduces the inner volume and would thus on its own lead to an increase in pressure. However, the simultaneous contraction of the pressure-transmitting medium is generally larger due to the liquid or soft-solid nature of the medium. As a consequence, the medium would contract even further than based on the reduced volume, so that the relaxation to fill out the full volume effects a decrease in pressure. Aside from the cell and the pressure-transmitting medium, also the sample itself could affect the pressure by its volume change. In practice, however, this effect is negligible, in particular if the sample volume is considerably smaller than the sample space. The same principle in reverse is valid on going to high temperatures, where the thermal expansion leads to an increase in pressure.

At low temperatures, the change in pressure is mainly of importance for the actual pressures that can be obtained in a pressure cell. Since the pressure decreases, and the mechanical properties of the cell materials stay constant or become even

¹⁰Here, “hydrogen” means specifically the hydrogen isotope protium ^1H , which is commonly referred to simply as hydrogen.

better, there is no danger in cell failure due to the low temperature. At high temperatures, however, the pressure within the cell increases, while the cell materials also become weaker, meaning that a pressure cell could be destroyed if too high a temperature is applied. In part as a consequence of this, if experiments are performed at simultaneously high pressures and high temperatures, setups are used where only the actual sample is heated, e.g. by laser-heating, to avoid collateral thermal effects from the cell and the pressure-transmitting medium as far as possible.

To determine the pressure in dependence of the temperature, the materials used as pressure marker, e.g. NaCl for clamp cells, are calibrated as function of temperature [149, 150]. Figure 4.10 shows exemplarily the significant change in pressure with temperature as measured from the change in lattice parameters of an NaCl sample crystal using the clamp cell developed in the context of this work (M1-CuBe, see Chapter 6).

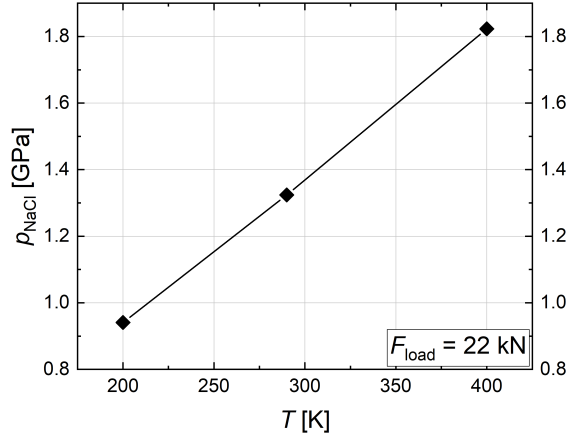


Figure 4.10: The pressure inside of the clamp cell calculated from the change in lattice parameters of an NaCl single crystal as function of temperature with an applied force load of 22 kN using an M1-CuBe clamp cell. The connecting lines are guides for the eye.

Chapter 5

Experimental Methods

This chapter provides details regarding the various experimental methods that were employed to first synthesize and then investigate the compound CrAs.

5.1 Sample Preparation

The preparation of suitable samples is naturally the first step necessary for any experimental investigation of a sample. This work on CrAs relied on the availability of bulk samples in both polycrystalline and single-crystalline form. Here, the synthesis procedures for both kinds of sample are briefly presented.

5.1.1 Synthesis of Polycrystalline Samples

Polycrystalline samples of CrAs were prepared by solid-state reaction from high-purity elements chromium (99.9%, Chempur) and arsenic (99.9999%, Chempur). The elemental precursors (chromium powder and arsenic pieces) were weighed in according to the stoichiometry with a slight excess of chromium to avoid elemental arsenic remaining¹. The precursors were filled into a standard quartz glass ampoule in a glove box under argon atmosphere. The ampoule was then evacuated and sealed. It was subsequently placed in a furnace and heated up to 680 °C for about 48 h. The reaction product was removed from the ampoule under argon atmosphere in a glove box and finely ground. The product was confirmed to be CrAs by X-ray powder diffractometry, which also revealed the presence of slight amounts of non-reacted elemental chromium, as expected from the slight initial, safety-related excess.

This synthesis process was done in two batches, each aiming for about 10 g of product, one to obtain polycrystalline sample itself and one as precursor step for the subsequent growth of single crystals.

5.1.2 Single Crystal Growth

Single crystals of CrAs were grown using the tin-flux method following the general process reported in the literature [17]. Powdered polycrystalline sample of CrAs prepared by the aforementioned procedure (about 5 g) and pieces of elemental tin (99.999%, Chempur) were put in a quartz glass ampoule with a molar ratio of

¹The presence of elemental arsenic should be avoided, as non-reacted arsenic could lead to a contamination of the used equipment, which would render it unusable.

CrAs:Sn \approx 1:10 under argon atmosphere and then sealed. The ampoule was placed in the furnace and heated to about 880 °C². The temperature was kept below 900 °C (corresponding to the phase transition temperature of CrAs from the NiAs to the MnP structure type) as otherwise the crystal will form a multi-domain twin structure during cooling [22]. After the heating, the ampoule was slowly cooled to 700 °C. At this temperature, the ampoule was decanted to separate the tin flux from the grown crystals. The remaining tin was removed by repeated etching with a 30% HNO₃ solution. The crystal growth process resulted in one large and several smaller single crystals of CrAs of irregular shape as well as several platelets of polycrystalline CrAs.

In addition to the newly synthesized crystals, single crystals of CrAs that were grown previously at the Karlsruhe Institute of Technology by Dr. Thomas Wolf were used for the single crystal experiments. In principle, the procedure was the same as described above. However, as the temperature during the growth process reached 900 °C, the resulting single crystals were severely twinned from crossing the transition temperature from the hexagonal to the orthorhombic structure. These crystals were elongated along the *a*-axis with an approximately hexagonal habit and a size of up to 3×3×8 mm³. Despite their twinning, these crystals were used in the experiments, as their shape was more regular and dense than the one of the newly grown crystal. Exemplary crystals are shown in Figure 5.1.

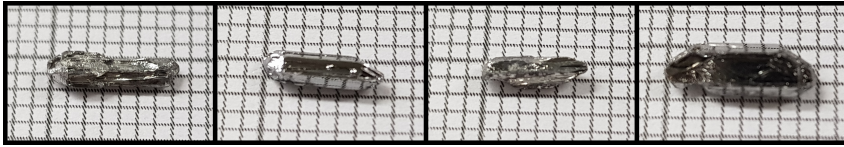


Figure 5.1: As-grown CrAs single crystals obtained by the tin-flux method; displayed on millimeter paper for reference.

5.2 Physical Properties Measurements

In addition to the scattering investigations on CrAs, magnetization and resistivity measurements were performed in-house. Most of these investigations replicate already reported experiments, yet were still conducted to provide a full characterization of the CrAs samples and to confirm the earlier literature results.

For these investigations, two Physical Property Measurement System (PPMS) instruments were used: the *Quantum Design PPMS* [166] and the *Quantum Design PPMS DynaCool* [167] (both Quantum Design, Inc., San Diego, CA, USA). They offer similar options for electrical transport (AC and DC resistance), magnetometry (vibrating sample magnetometry (VSM), AC susceptibility) and thermal (heat capacity, thermal transport) measurements in the temperature range of about 2...400 K at magnetic fields up to 9 T. The main difference between the two instruments is the low temperature control – while the Quantum Design PPMS has to be

²The nominal temperature of the furnace was set to 930 °C, the actual temperature at the sample position was lower as it was placed on a cooling finger; the actual process temperature was measured at the cooling finger.

externally supplied with liquid helium, the Quantum Design PPMS DynaCool uses a closed pulse tube cryocooler system without the need for liquid cryogen. Regarding the available sample environments, the Quantum Design DynaCool is additionally equipped with the option of a VSM oven for magnetometric measurements up to 1000 K.

5.2.1 Magnetization Measurements

Magnetometric measurements on single crystals were performed to determine the magnetization in dependence on the sample orientation using the VSM option. This method works on the principle of electromagnetic induction, and thus requires that either the applied field, the coil position or the sample position changes with time [168]. The VSM option – where the sample is moved – is based on an earlier *vibrating-coil* technique [168, 169]. The working principle of a VSM instrument is depicted in Figure 5.2.

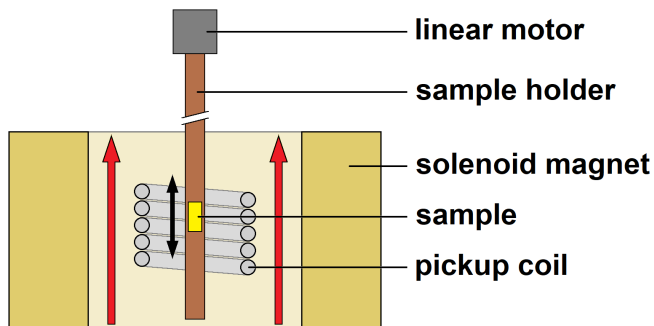


Figure 5.2: Working principle of the VSM option. The black arrow indicates the movement of the sample, the red ones the direction of the applied magnetic field. *Based on [168].*

The sample is mounted onto a sample holder which is connected to a linear motor, which oscillates in the vertical direction. The position of the sample is adjusted to be fully inside the pickup coils. In these, a current is induced by the moving magnetic field of the sample. The current is proportional to the magnetization of the sample. In order to manipulate the magnetization of the sample, the pickup coil is placed within a solenoid magnet in which a uniform magnetic field with orientation parallel to the vertical axis can be generated³. The whole measurement setup can be placed within a cryostat to enable temperature-dependent magnetometric measurements. For high-temperature measurements, a wire-connected holder is employed, which regulates the sample temperature by resistive heating.

In our low-temperature measurements, the sample is glued onto a polyimide sample holder with GE varnish. In the case of a single-crystalline sample, it is glued

³This arrangement concerns specifically the used PPMS instruments; in other VSM instruments (e.g. the original design), the magnetic field is generated by two magnetic poles and thus perpendicular to the axis of movement.

with a certain orientation (as determined by Laue diffraction) with respect to the magnetic field direction. For further fixation, the mounted sample can be wrapped in tape, e.g. Teflon™ or Kapton™ (a polyimide film); however, the use of tape can lead to a magnetic signal from oxygen adsorbed to the large surface of the tape interfering with the sample signal [170]. In the high-temperature measurements, a ceramic holder with inlaid wires was used, where the sample is fixed by a cement and wrapped with a thin sheet of copper.

For CrAs, single crystals were measured in both isothermal (magnetization as function of magnetic field) and isofield (magnetization as function of temperature) conditions for two cases: with the a -axis parallel to the applied magnetic field, and with it perpendicular to the applied magnetic field – other directions were not distinguishable due to the twinning of the CrAs single crystals. The isofield measurements were conducted in the temperature range 5...1000 K at magnetic fields between 0.1 kOe and 90 kOe. Isothermal measurements to obtain hysteresis loops were conducted in the field range $-90...+90$ kOe at temperatures between 2 K and 300 K. The samples were cut from an as-grown crystal whose orientation had been determined by Laue diffraction; the sample used in the measurements with the field parallel (perpendicular) to the a -axis was of size $3\times2\times2$ mm³ ($2\times2\times2$ mm³) and mass 30.0 mg (24.4 mg).

In addition, low-temperature isothermal and isofield measurements in the same temperature/field range were performed on polycrystalline samples of several types of tungsten carbide in order to characterize their magnetic properties and thus their suitability for use as material for clamp cells operating in magnetic fields.

5.2.2 Resistance Measurements

The resistance was measured in the classic four-terminal geometry (4-wire configuration) with the four sample contacts equidistant in a line. The wires connect the sample contacts to the puck contacts in a standardized manner, with two current leads and two voltage leads [171]. For the determination of the resistance, a certain current I is applied to the current leads and the resulting potential difference V is measured. The resistance then follows from Ohm's law as $R = V/I$.

For the measurement, the sample is fixed to the puck with grease or varnish and then connected to the puck with platinum wires. On the puck, the wire ends are fixed with silver paint, the wire connection to the sample can be made with silver paint, solder, wire bonding – either direct or through a contact metal, e.g. indium –, or silver epoxy, depending on the sample properties.

The measurements on CrAs were performed using an as-grown CrAs single crystal. Due to its needle-shape, the resistance could only be measured along the growth axis (a -axis). The sample contacts were made with silver epoxy⁴, for which the two-component epoxy was cured at 100 °C for about 30 min. The resistance was measured in the ac mode (50 Hz square-wave excitation) with an excitation amplitude of 5000 μ A in the temperature range 5...300 K.

⁴Previous tests with the other mentioned methods did not yield sufficiently stable contacts.

5.3 Diffraction Experiments on CrAs

The majority of the experiments performed for this work are single-crystal or powder diffraction measurements using either X-ray or neutron radiation. Experiments were carried out in-house on laboratory instruments, as well as at synchrotron and neutron sources. The corresponding setups are explained here.

5.3.1 In-House Diffraction Experiments

5.3.1.1 Laue X-ray Diffraction

Laue diffractometry is an essential method to determine the quality of a single crystal and its orientation using ‘white’ X-ray radiation with a continuous range of wavelengths rather than a discrete wavelength [172]. By fulfilling Bragg’s condition for any given wavelength, a pattern of reflections is created on the detector, which is directly related to the symmetry of the crystal. If the crystal structure of the sample is known, this allows the determination of the sample orientation. For unknown samples, turning the crystal gives information about the Laue symmetry of the sample. By this method, also the presence of twinning can be deduced from the pattern as a superposition of single-crystal patterns.

For the in-house Laue measurements, an *MWL120 Real-Time Back-Reflection Laue Camera System* (Multiwire Laboratories, Ltd., Ithaca, NY, USA, [173]) was used, featuring a tungsten X-ray tube and a multiwire detector. The tungsten X-ray source allows the generation of wavelengths down to about 0.5 Å (25 keV). The detector has a size of 30×30 cm² and is placed between the sample and the X-ray source, i.e. in back-reflection geometry. It allows real-time observation of the Laue diffraction on the connected computer. The auxiliary equipment also includes a camera, which in combination with a mirror enables the centering and alignment of the crystal on the holder with respect to the X-ray beam. Three axes are available to manipulate the orientation of the sample with continuous feedback from the detector.

The Laue camera was used to elucidate whether the as-grown CrAs crystals were single crystals or twinned and to determine their respective orientation.

5.3.1.2 Powder X-ray Diffraction

Powder X-ray diffractometry measurements were performed on a *HUBER Imaging Plate Guinier Camera G670* (HUBER Difraktionstechnik GmbH & Co. KG, Rimsting, Germany, [174]) operating in transmission geometry and using monochromatized Cu K_α radiation with $\lambda = 1.5418$ Å. The curved imaging plate detector covers an angular range of 4°...100° 2θ with a resolution of 0.005°. The sample holder can be oscillated horizontally with a frequency of about 1 Hz to reduce the effect of sample inhomogeneities by increasing the statistics.

For the measurements, a few milligrams of sample were ground to a fine powder and distributed on a thin cellophane foil on top of the sample holder. To improve the homogeneity of the sample dispersion, a drop of solvent (e.g. acetone or isopropanol) is given to the powder to promote the spread. To fixate the powder, a second cellophane foil is placed on top of the powder and secured by a metal ring pressing

onto the sample holder. The surface of the foils is stretched by the application of the ring and thus avoids the formation of creases. This minimizes the contribution of the foils to the measured X-ray diffractogram, where the non-crystalline material results in a small background signal at low angles.

The powder X-ray diffractometry was used to confirm the phase purity of the grown polycrystalline and ground single-crystalline CrAs samples as well as to determine the nature of additional growth products.

5.3.1.3 Single-Crystal X-ray Diffraction

In-house single-crystal diffraction experiments were performed using a *SuperNova* single-crystal diffractometer (Agilent Technologies XRD Products, Ltd., Yarnton, UK, [175], now Rigaku Oxford Diffraction, Tokyo, Japan). The instrument is a four-circle diffractometer in Kappa geometry, equipped with a dual source – switchable between Mo K_α ($\lambda = 0.7093 \text{ \AA}$) and Cu K_α ($\lambda = 1.5418 \text{ \AA}$) – and a CCD area detector ($\varnothing 135 \text{ mm}$, sample distance 40...150 mm). For temperature-dependent measurements, a nitrogen flow gas jet cryostat/heater (Oxford Instruments PLC, Abingdon, UK) is available, with a temperature range of about 100...400 K.

To measure a sample, it was glued with commercial two-component glue to the tip of a borosilicate glass fiber, whose diameter approximately matched the size of the sample. The glass fiber was fixed in a brass pin and mounted in the goniometer head. The runlist for the measurement was generated automatically for a complete coverage of the reciprocal space with a high redundancy assuming symmetry $P1$ for the sample regardless of the actual (known) symmetry.

The in-house single-crystal diffractometry was used for two purposes. Quick test measurements were done to determine the quality of candidate single crystals and to thus select suitable ones for subsequent measurements with synchrotron X-ray radiation. Full measurements in the temperature range 240...400 K were performed to complement the temperature-dependent synchrotron measurements. Details of these measurements can be found in Appendix C.

5.3.2 Synchrotron Single Crystal Diffraction Experiments

The main part of the X-ray diffraction experiments were carried out using synchrotron X-ray radiation at beamline P24 at the synchrotron X-ray source PETRA III at DESY in Hamburg, Germany [176]. The beamline is dedicated to chemical crystallography for studies in various fields, e.g. physics, chemistry, biology, earth and material sciences. It provides the means to perform single-crystal diffraction measurements for crystal structure determination in a variety of sample environments, like temperature, pressure, and magnetic fields. An overview of the beamline layout is given in Figure 5.3.

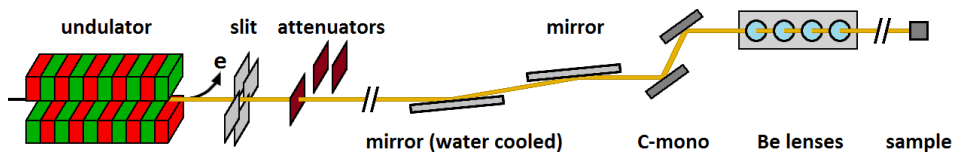


Figure 5.3: Schematic layout of beamline P24, PETRA III, DESY. [176]

The X-ray radiation is generated in an undulator, which produces a narrow radiation cone of high brilliance (see [177] for details). After being narrowed by a slit system, at least one attenuator and two mirrors in the beam path act as band pass filter to reduce the thermal load on the subsequent components. To define the energy (wavelength) of the radiation, a monochromator is employed. At P24, it consists of a pair of either Si(111) or Si(311) crystals, which allow energies between 2.4 keV ($\lambda = 5.17 \text{ \AA}$) and 44 keV ($\lambda = 0.28 \text{ \AA}$). To focus the beam after monochromatization, a series of beryllium compound refractive lenses (Be CRL) can be inserted. Afterwards, a collimator is placed to limit the beam divergence.

P24 is equipped with two four-circle diffractometers in two experimental hutches, EH1 and EH2. In EH1, a diffractometer with Kappa geometry is used, in EH2 one with Euler geometry. Our experiment took place at EH1 using a beam energy of 27.5 keV ($\lambda = 0.45085 \text{ \AA}$) and a Pilatus CdTe 1M area detector. We performed measurements to determine the full crystal structure in separate dependence on temperature and on pressure.

Low temperatures between 35 K and 275 K were achieved with a Cryocool G2b-LT helium gas jet cryostat. The measured CrAs single crystal had a size of about $70 \times 50 \times 50 \mu\text{m}^3$ and fixed on a glass fiber with standard commercial two-component glue. At each of the selected temperature points, 2 φ - and 6 ω -scans were measured, the full scan list can be found in the Appendix, Table C.1.

The high-pressure measurements were carried out using several diamond anvil cells (one of the *Ahsbabs* type, two of the *YaoDAC* type, and three of the *Boehler-Almax* type, see Chapter 4.2 for details), each one pre-loaded with a CrAs single crystal of about $50 \times 50 \times 50 \mu\text{m}^3$ and a ruby chip in a 4:1 methanol-ethanol mixture used as pressure-transmitting medium. The pressure during all high-pressure measurements was determined by means of an offline ruby luminescence system. As in the low-temperature measurements, each data point comprises 2 φ - and 6 ω -scans. The precise run parameters were chosen in accordance with the used diamond anvil cells (opening angle) and are given in the Appendix, Tables C.2–C.4. After the initial measurement of the pre-set pressure cells, the pressure was increased and the newly set pressure cells were measured again; the cells were given approximately two days for pressure equilibration.

5.3.3 Neutron Diffraction Experiments

5.3.3.1 Neutron Powder Diffraction: HRPT

The neutron powder diffractometer HRPT⁵ is located at the neutron spallation source SINQ at PSI in Villigen, Switzerland [178, 179]. At wavelengths between 0.84 Å and 2.96 Å, two modes (high intensity and high resolution) are available for studies of chemical and magnetic order. The layout of the instrument is shown in Figure 5.4.

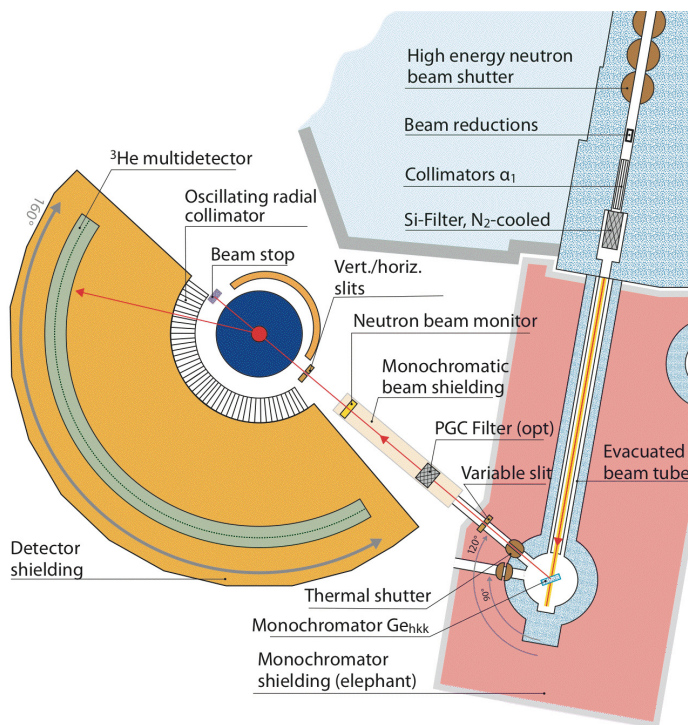


Figure 5.4: Schematic layout of the HRPT instrument at SINQ, PSI. [179]

The neutrons generated at the target station of the spallation source are moderated to thermal energies by a water reservoir. The collimated neutron beam is monochromatized using a focusing $\text{Ge}(hkk)$ monochromator and guided to the sample position. The neutron beam monitor counts the incoming neutrons. The scattered neutron beam is detected by a position-sensitive ^3He detector that allows the simultaneous measurement of an angular range of 160° with a step size of 0.1° .

On HRPT, the magnetic structure of CrAs was measured as function of temperature at ambient pressure between 1.5 K and 300 K. For the measurement, about 6 g of CrAs powder were filled into an $\varnothing 8$ mm sample container made from vanadium. The sample container was continually rotated to minimize the effect of inhomogene-

⁵“High-Resolution Powder Diffractometer for Thermal Neutrons”

ity and preferred orientation. At selected temperatures (see details in Appendix C), powder diffractograms were obtained using a wavelength of 2.45 \AA in the high intensity mode. In addition, measurements using a wavelength of 1.49 \AA were performed at a few temperatures to serve as reference for the crystal structure. In all measurements, instead of a set time per measurement point, a certain neutron monitor value is chosen for each measurement, with the measurement continuing until that specific number of neutrons has reached the sample. This accounts for the interruptions in the neutron beam caused by the operation of more than one target station at the spallation source.

5.3.3.2 Neutron Single-Crystal Diffraction: D9

D9 is a hot neutron four-circle diffractometer for single-crystal studies at the ILL, a part of the EPN science campus in Grenoble, France. Figure 5.5 shows the layout of the instrument.

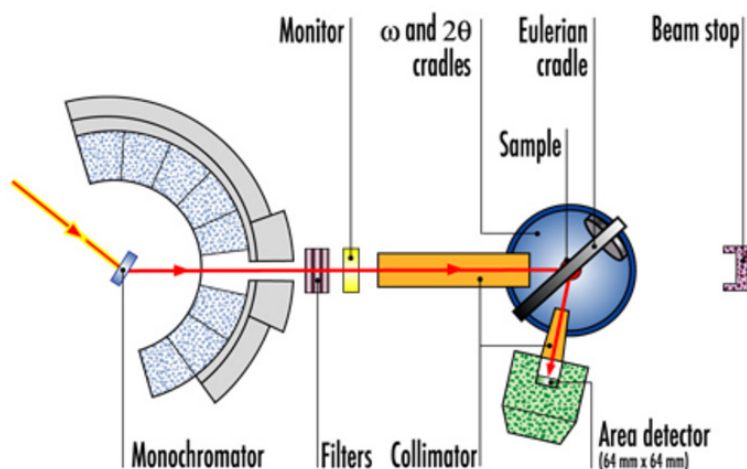


Figure 5.5: Schematic layout of the D9 instrument at ILL, EPN. *Adapted from [180].*

The wavelength can be chosen in the range of 0.35 \AA to 0.85 \AA by means of a Cu(220) monochromator. D9 employs an area detector with 32×32 pixels of $2 \times 2 \text{ mm}^2$ size each, which allows to gain a quick overview of the reciprocal space and is particularly useful for the detection of satellites and twinning.

At D9, measurements on CrAs were performed at simultaneously low temperature and high pressure using an ILL standard TiZr clamp cell supplied by their high-pressure laboratory. In this cell, the cell body is made from the “null-scattering” Ti–Zr alloy, the bottom locking nut (also functioning as bottom piston) is made from copper beryllium, the top locking nut from aluminium and the top piston from tungsten carbide. The sample was an as-grown CrAs single crystal that was cut to length of 3 mm along its growth axis (a -axis) for a size of $2 \times 2 \times 3 \text{ mm}^3$. It was oriented on a neutron Laue camera (OrientExpress, ILL [181]) and glued onto a small cylinder

made from aluminium to preserve the orientation when inserted into the sample capsule and to position the sample at the correct height for the neutron beam. The CrAs sample was oriented with the a -axis parallel to the cell axis (vertical when mounted in the cryostat) and the b, c -plane perpendicular (in the horizontal); the precise orientation of b and c could not be determined due to twinning of the crystal. The used sample capsule was $\varnothing 4$ mm and made from aluminium, filled with Fluorinert FC770 as pressure-transmitting medium. The capsule was closed with copper seals. Pressure was applied using a stationary, wheel-driven hydraulic press with digital load display. With the load applied, the cell was left for about an hour to stabilize. The loaded cell was inserted into an orange-type cryostat mounted on D9, with a temperature sensor placed on the outside of the cell. The difference in temperature between the sensor and the cell interior was considered to be negligible.

With this setup, two full data sets including nuclear and magnetic reflections were measured: the first at 0.17 GPa and 2 K, the second at 1.2 Gbar and 2 K. The pressure refers in both cases to the nominal pressure applied at room temperature based on the calibration of the press; the expected drop in pressure due to the temperature decrease was not considered. The measurements consisted of a series of ω -scans in both cases. Measuring of reflection outside of the horizontal reflection plane was possible due to the lifting counter range of the detector of $-12.5...25^\circ$. The same set of reflections was measured at both pressures for comparability⁶. Monitor values⁷ of $4 \cdot 10^4$ ($5 \cdot 10^4$) were used for the nuclear reflections at 0.17 GPa (1.2 GPa), and $2 \cdot 10^5$ ($4 \cdot 10^5$) for the magnetic reflections; the monitor values are increased for magnetic reflections due to their relative weakness, and for the measurement at higher pressure due to the pressure-induced peak broadening. In addition to the two full data sets, the temperature dependence of one magnetic peak was followed at 1.2 GPa in increasingly larger steps⁸ up to 180 K.

5.4 Test Measurements on High-Pressure Equipment

5.4.1 Test of the Thermal Response of the Clamp Cells on DNS

DNS⁹ is a diffuse scattering neutron time-of-flight spectrometer at the research reactor FRM II at MLZ in Garching near Munich, Germany [182], operating with cold neutrons at wavelengths between 1.5 Å and 6 Å, with the option of polarization analysis.

DNS is equipped with various cryostats for temperatures down to 20 mK and a cryomagnet for fields up to 5 T. The orange-type cryostat (temperatures down to about 4 K) was used for tests of the thermal response of the clamp cells M1-CuBe and M1-NiCrAl (see Chapter 6.3.4). Actual measurements with neutron radiation on CrAs using the clamp cells developed within this work were planned and scheduled

⁶A few reflections could eventually not be measured at high pressure due to time constraints.

⁷A measurement runs until the selected neutron monitor value is reached, i.e. until that many neutrons have been counted by the detector. This is used instead of a set time per measurement to account for changes in the neutron flux – however, a higher monitor value is effectively the same as a longer measurement time.

⁸5 K steps up to 20 K, 10 K steps up to 60 K, and 20 K steps up to 180 K.

⁹“Diffuse Neutron Scattering”

on DNS, but could not take place due to the prolonged reactor shutdown.

5.4.2 Temperature-Dependent Pressure Calibration of the Clamp Cell on HEiDi

The single-crystal diffractometer HEiDi¹⁰, also located at the FRM II, is designed for investigations with short wavelengths between 0.55 Å and 1.2 Å using hot neutrons for the determination of the crystal and magnetic structure of single crystals [183].

In the standard setup, HEiDi is a four-circle diffractometer; the use of the instrument's cryostat (down to 2 K) or furnaces (up to 1500 K) restricts the available position parameters. In order to perform high-pressure experiments on HEiDi using diamond anvil cells [103], the instrument is equipped with an offline ruby luminescence system. This system allows the measurement of ruby luminescence with the pressure cell inside of the instrument cryostat, and thus *in situ* pressure determination. It was used for temperature-dependent calibration measurements of the ruby luminescence option in the M1D clamp cells (see Chapter 6.3.5.1 for details).

5.4.3 Calibration of the Clamp Cell on POLI

POLI is a two axes single crystal diffractometer at the FRM II dedicated to the use of polarized hot neutrons for the investigation of magnetic structures [184]. In particular, the instrument's cryostat and magnet allow measurements of exotic magnetic states under low temperature/high magnetic field conditions. A schematic overview of the instrument is given in Figure 5.6.

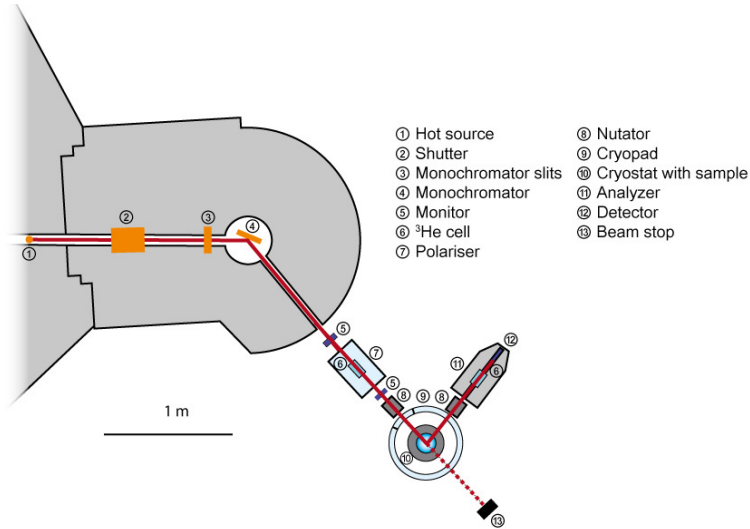


Figure 5.6: Schematic layout of the POLI instrument at FRM II, MLZ. [184]

¹⁰“Heiðes Einkristalldiffraktometer”

Like at HEiDi, the neutrons pass through the hot source to reach the target neutron energy and through a slit system to limit the beam divergence. From the monochromator, where the specific neutron wavelength is selected, the neutrons go through the polarizer (a ^3He cell) to set the neutron spin polarization. The diffracted signal is measured by the point detector – a $2''$ ^3He single detector tube – after passing through the analyzer, (another ^3He cell). The detector can be moved out of plane (out-of-plane lifting counter) to extend the accessible reciprocal space in the vertical direction.

POLI was used for the pressure calibration measurements using the M1-CuBe prototype clamp cell. The pressure cell loaded with a NaCl single crystal ($2.8 \times 2.8 \times 2.8 \text{ mm}^3$) and filled with a 1:1 mixture of Fluorinert FC770 and FC70 as pressure-transmitting medium was placed within the instrument's 8T magnet. The pressure was applied *ex situ* with a standard hydraulic laboratory press. The magnet has a vertical opening of 30° ($-5^\circ/+25^\circ$). The combination of a short wavelength used in the measurements ($\lambda = 1.15 \text{ \AA}$ and $\lambda = 0.90 \text{ \AA}$) and the out-of-plane lifting counter detector thus allowed the collection of data from several scattering planes. In total, 21 reflections from the NaCl were measured above the 3σ limit with 10 s per counting point and used for the determination of the orientation matrix and the NaCl lattice parameters, from which the pressure inside of the pressure cell was determined (see Chapter 6.3.1).

5.4.4 Tests of the Clamp Cell on MIRA

MIRA is a multipurpose cold neutron instrument at the FRM II. In its standard configuration, it is a three-axis spectrometer used for inelastic scattering experiments with excellent resolution in Q , with wavelengths between 3.5 \AA and 6 \AA . Additional equipment allows the use of the instrument for diffraction measurements with optional polarization or for high-resolution spin-echo measurements. Furthermore, elliptic guides for focusing can be used to improve the signal-to-background ratio, e.g. for experiments on small samples or with pressure cells. Figure 5.7 shows the layout of the standard setup of MIRA as three-axis spectrometer.

The purpose of the three-axis spectrometry is the measurement of the momentum and energy transfer during the scattering process. The three axes are used to define the incoming wave vector (axis 1, the monochromator) and the scattering angle (axis 2, the sample), and to select the outgoing wave vector to be detected (axis 3, the analyzer). For the present work, however, the instrument was used for elastic scattering experiments only, where axes 1 and 3 are fixed and only the scattering angle is changed.

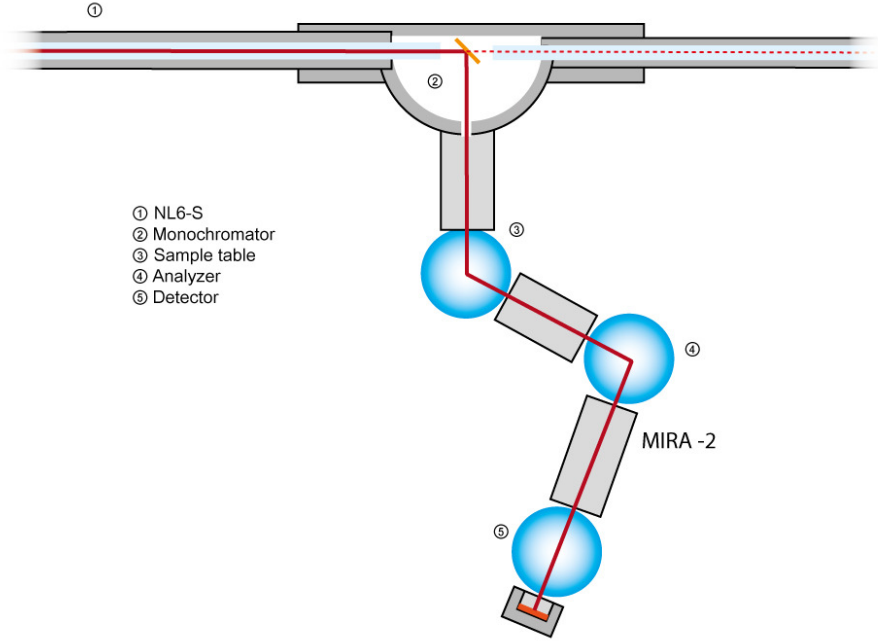


Figure 5.7: Schematic layout of the MIRA instrument at FRM II, MLZ. [185]

In the context of this work, MIRA was used to perform test measurements with the M1-CuBe prototype clamp cell. The cell was loaded with a MnSi single crystal sample ($1.8 \times 2.0 \times 8.0 \text{ mm}^3$) that was glued on top of a NaCl crystal ($2.8 \times 2.8 \times 2.8 \text{ mm}^3$), with a 1:1 mixture of Fluorinert FC770 and FC70 as pressure-transmitting medium. However, no actual pressure was applied. Using a wavelength of 4.05 \AA , measurements were performed to determine the neutron transmission of the M1-CuBe clamp cell and to show the feasibility of measuring magnetic reflections in the pressure cell.

Chapter 6

Clamp Cell Development

Pressure is one of the most basic and important parameters that can be used to tune the properties of a sample in a controlled manner, and can induce various changes, e.g. in the crystal, magnetic and electronic structures [120]. To experimentally access the high pressure region (pressure above 0.1 GPa = 1 kbar), the availability of suitable pressure devices is the fundamental requirement. These devices have to be tailored to the specific demands posed by the employed methods and instruments, the corresponding samples, the targeted pressure range, and any intended additional sample environment.

The combination of high pressure with neutron radiation is of particular importance for the investigation of properties involving magnetic order and light elements [119]. The design of a suitable pressure device is dictated by the inherent characteristics of the neutron radiation. The samples generally have to be rather large (in the order of 1 mm³) due to the generally low neutron flux at the neutron source [119]. The large sample volume in turn leads to the requirement of large forces to achieve high pressures, and, to safely maintain these large forces, comparatively massive designs of the cells are necessary. This is only possible due to the large penetration depth of the neutrons.

6.1 Design

Different types of *large volume devices* have been developed for neutron applications, like the *McWhan cell* [186], the *Paris-Edinburgh press* [187] and the so-called *clamp cell*. While the first two devices can generate higher pressures, they come with the significant disadvantage of being quite large. In addition to general problems (e.g. mobility and/or placement of the device on the instrument), this hinders or even prohibits the use of additional sample environments like cryostats and magnets for the measurements. Hence, to enable the combination of high pressure with low temperatures and magnetic fields, the *clamp cell* is the most common type of device [119].

6.1.1 General Types of Clamp Cells

The basic idea of any high pressure device is the compression of a sample space by an applied force. For most cases, the generated pressure should be hydrostatic (isotropic), which requires the sample to be surrounded by a pressure-transmitting

medium and thus the sample space to be closed. In a clamp cell, this sample space is located within the bore of a cylinder, closed by pistons. These pistons are then locked (“clamped”) by nuts, this way fixing the pressure. On the one hand, this means that the pressure has to be applied *ex situ* which implies the disadvantage that it has to be taken out of the sample environment for every pressure change. On the other hand, the significant advantage of this clamped design is its versatile use – after it has been loaded, it can be used in various setups, even with the same load.

It is worth mentioning that the term “clamp cell” for this type of device specifically refers to a clamped piston-cylinder cell [119], although the concept of fixing the pressure by clamping is not restricted to this cell design. Other cell types can also be clamped (e.g. diamond anvil cells), and piston-cylinder cells can also be used in non-clamped ways (e.g. with a membrane).

In a clamp cell, the central and most crucial part is the cylinder, whose properties determine the practical limitations for the whole cell. Based on the design of the cylinder, different kinds of clamp cells can be distinguished.

6.1.1.1 Monobloc Clamp Cells

Monobloc clamp cells feature a cylinder that is made from one single piece. There are two variants of the monobloc cell:

In an *open-end cylinder* cell, the cylinder simply consists of a massive cylinder with a full-length bore (Figure 6.1, *right*). The pressure is applied by two pistons pressing into the bore from both sides. In practice, one piston is commonly fully inserted from the beginning to fix its position, so that only one piston is actively moving. The fixed piston allows a more stable positioning of the sample within the cell.

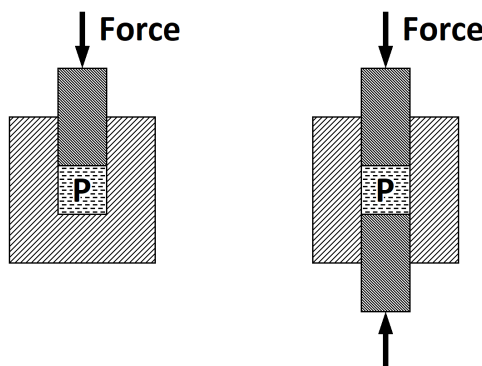


Figure 6.1: Schematic designs of a monobloc clamp cell: closed-end cylinder (*left*) and open-end cylinder design (*right*). Adapted from [120].

In a *closed-end cylinder* cell, the bore does not go fully through the cylinder. Hence, the cell is closed by the cylinder itself on one end, essentially taking the position of a fixed piston. As the piston and clamping nut can thus be omitted for one side, the total length of the cell is reduced. However, the lack of access from the

closed end makes it significantly more difficult to remove a sample; while an open-end cylinder cell can be opened and the sample can be pushed out, a closed-end cell does not offer this option. Due to these practical problems, most existing clamp cells are open-end cylinder cells.

The cylindrical shape has the general advantage, that it poses one of the few problems for which an analytical solution for the stress state and the deformations resulting from a load is possible. In this case, the analysis is based on the theory of *thick-walled cylinders*¹ [119, 120]. This means that the behavior of the cylinder under load can be calculated based on its geometrical and material properties, allowing a design approach that is based on theory and supported by simulations instead of a purely empirical one. Details can be found in the dedicated literature [119, 120, 188], but a brief introduction will be given here.

The cylinder is fully described by its inner and outer radius, r_i and r_o , respectively; the length is sufficiently large to ignore any influence of the ends but otherwise unspecified. If only an internal pressure p_i is applied and the cylinder is assumed to be longitudinally restrained² (which are effectively the conditions under which thick-wall monobloc cylinders are used), the relevant stress distributions follow from the Lamé equations [189]:

$$\sigma_\theta = p_i \cdot \frac{1 + r_o^2/r^2}{K^2 - 1} \quad (6.1)$$

$$\sigma_r = p_i \cdot \frac{1 - r_o^2/r^2}{K^2 - 1} \quad (6.2)$$

$$\sigma_z = p_i \cdot \frac{1}{K^2 - 1} \quad (6.3)$$

with the *wall ratio* $K = r_o/r_i$ and considering $r_i \leq r \leq r_o$. σ_θ is the tangential stress or *hoop stress*, σ_r is the radial stress, and σ_z is the axial stress.

Several observations follow from these equations:

1. σ_θ and σ_z are always positive, corresponding to tensile stresses within the tangential and the axial direction. In contrast, σ_r is always negative, indicating compression in the radial direction.
2. σ_θ is always larger in magnitude than σ_r and σ_z .
3. Both σ_θ and σ_r are maximal at $r = r_i$, the bore of the cylinder, with respective values of $\sigma_\theta(r_i) = p_i \cdot (K^2 + 1)/(K^2 - 1)$ and $\sigma_r(r_i) = -p_i$.

Figure 6.2 shows the resulting stress distribution in tangential and radial direction. It is evident that the stresses decrease rapidly with increasing r as $\sim 1/r^2$.

¹Cylinders are considered ‘thick-walled’ if the wall strength is more than $1/10$ of the inside diameter. In cylinders with thinner walls the tangential stress can be assumed to be constant [188].

²In the longitudinally restrained case, the strain ε_z in the axial direction is considered to be zero. Although this assumption is not strictly valid, the stress contribution from ε_z is negligible compared to the effect of the wall strength for $K > 2$ and is thus ignored [188].

The maximum stresses occurring at the bore determine the achievable maximum pressure within the cell since the cylinder material has to withstand these stresses. For reversible use of the cell, they have to stay within the material's *elastic regime*, where the initial shape of the cell is fully recovered after the stresses are removed. The limit of this regime is the *yield strength* σ_Y . If the stresses in the cylinder exceed this limit, the cylinder starts to deform plastically, meaning that the initial shape is not recovered. While this cannot be equated with the cell being necessarily broken, adjustments would have to be made to use the cell again, so that plastic deformation is generally to be avoided.

For the relation of the occurring stresses and the yield strength of the material, different approaches exist [119, 188]. Based on these theoretical considerations, the pressure limit of the cell can be estimated from the wall ratio K . Generally, an increase in K will improve the pressure limit – however, for $K > 3$, the gain in strength will only be marginal, and not be justified by the increase in external diameter and weight [119]. Hence, most existing clamp cells are designed with $K = 3$.

This treatment of the cylinder shows that the strength of a monobloc clamp cell is basically determined by only two parameters, one geometrical (K) and one material dependent (σ_Y). For a given form set by K , the pressure limit thus only depends on the selected material. As even high-strength materials like CuBe or NiCrAl (see Chapter 4.3) have yield strengths below 2 GPa, the monobloc design is not suited to reach pressures higher than that.

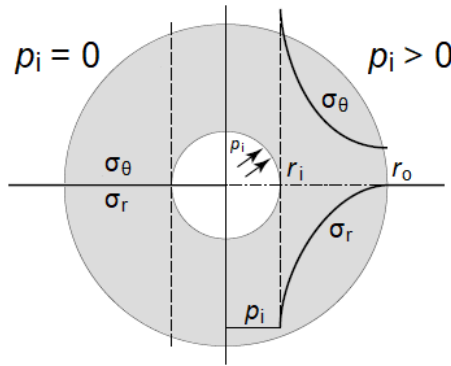


Figure 6.2: The stress distribution in a monobloc cylinder following from the theory of thick-walled cylinders. *Left*: without applied internal pressure ($p_i = 0$), *right*: with applied internal pressure ($p_i > 0$). *Adapted from [119]*.

6.1.1.2 Fretted Clamp Cells

As seen in the previous section, the pressure limit of a cell is determined by the maximum occurring stresses. In a monobloc design, the only way to improve this limit is to increase the strength of the material to withstand higher stresses, which leads to the aforementioned limitations. An alternative way to increase the pressure limit, however, is to instead reduce the occurring stresses. This is possible by in-

roducing residual stresses in the cell which counteract the stresses induced by the pressure load.

To achieve this, a compound cylinder construction is used, consisting of two assembled monobloc cylinders (Figure 6.3, *left*), an inner and an outer one. In the initial, pre-assembled state, the inner diameter of the outer cylinder is slightly smaller than the outer diameter of the inner cylinder. The difference in these diameters is called the *interference*. In assembling the two cylinders (interference fit), both parts are necessarily plastically deformed to fit each other and thus residual stresses are introduced at the contact surfaces – the cylinders are “fretted”. The stress distribution of such a fretted cell in the unloaded state is shown in Figure 6.3, *left* ($p_i = 0$). In the radial direction (σ_r), both parts experience compression, with a maximum at the contact surface. In tangential direction (σ_θ), the outer cylinder is under tensile stress at the surface ($\sigma_\theta > 0$), while the inner cylinder is under compression ($\sigma_\theta < 0$). If a load is applied ($p_i > 0$, Figure 6.3, *right*), the residual stresses and the load-induced stresses (see Figure 6.2) are superimposed. Effectively, this leads to a reduction of the maximal tensile stress occurring at the bore. As a consequence, higher loads can be applied without exceeding the yield strength of the cell material.

In principle, the introduction of residual stresses originates solely from the interference of the inner and outer cylinder, and does not directly depend on their material properties. As such, it is possible to either use the same material or different materials for the two cylinders. Fretting of two cylinders made from the same material is functionally equivalent to *autofretting*, where residual stresses are introduced in a monobloc cell by overloading it. As it is easier to manufacture a monobloc cell, a fretted cell with cylinders from the same material offers no advantages. Hence, two different materials are usually used for the cylinders in fretted cells. Since the highest stresses occur near the bore, the inner cylinder is in that case made from a harder material than the outer cylinder, which does not have to withstand such high stresses [120].

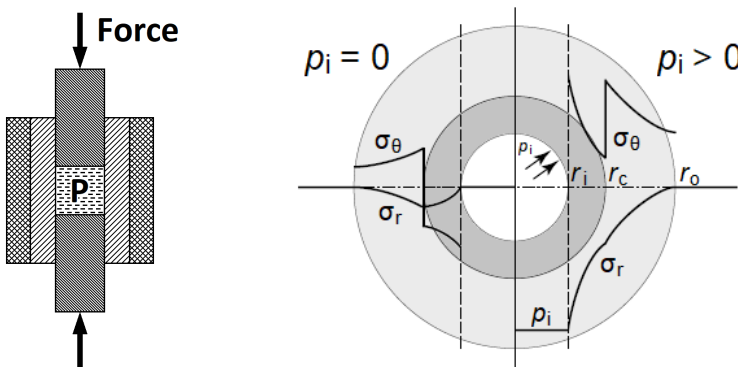


Figure 6.3: *Left*: Schematic designs of a fretted clamp cell; *right*: the stress distribution in a fretted cylinder without applied internal pressure ($p_i = 0$; *left*) and with applied internal pressure ($p_i > 0$; *right*). Adapted from [119].

The assembly of the two cylinders is done either by shrink fitting or press fitting

(or a combination of both).

For a shrink fit, the outer cylinder is heated to thermally expand the inner diameter sufficiently to allow the inner cylinder to fit into the bore. When cooling down to ambient temperature, the outer cylinder will contract and thus put the inner cylinder under radial compression.

Press fitting is done by simply pushing the inner cylinder into the bore of the outer cylinder; to facilitate this, the contact surfaces (inner surface of the outer cylinder and outer surface of the inner cylinder) are slightly conical with a half-angle of about 1–2°.

In both cases, the cylinders are held together in the fretted state by friction forces, preventing them from disassembling. The necessary interference depends on the cell geometry (outer radius of the outer cylinder r_o , inner radius of the inner cylinder r_i , and targeted contact radius r_c , see Figure 6.3, *right*) and the used materials [119]. Theoretical considerations show that for a given wall ratio of $K = r_o/r_i$ an optimal r_c exists with

$$r_c = \sqrt{r_o \cdot r_i} . \quad (6.4)$$

The design of a fretted cell cylinder can thus be simplified to the independent choices of overall inner and outer radius, and used cylinder materials.

For the use of a compound cylinder made from different materials, it should, however, be kept in mind that the considered properties of the interference fit are specifically valid only for ambient conditions. At other temperatures, the different thermal expansion coefficients of the involved materials will lead to changes that affect the interference fit of the cylinders and thus the induced stresses.

6.1.2 Specific Requirements of the Cells

The development of a clamp cell naturally has to take into account the restrictions imposed by its intended purpose. Within the present work, clamp cells were developed for use in neutron scattering experiments on selected instruments and under various experimental conditions. Three instruments, located at the Heinz Maier-Leibnitz Zentrum (MLZ) are directly involved in the development of the cells (see also Chapters 5.3 and 5.4 for more details):

- DNS: a diffuse scattering cold neutron time-of-flight spectrometer
- POLI: a polarized hot neutron single-crystal diffractometer
- MIRA: a cold neutron three axes spectrometer

While the cells have been developed with regard to the specifications of these instruments, and the experimental tests of the cells were performed there, the use of the produced cells is not restricted to these instruments. On the contrary, they are eventually intended as a standard sample environment available at the MLZ for all suitable instruments and the whole user community.

The experimental conditions under which the clamp cells are intended to be used include low temperatures and high magnetic fields – hence, the cells have to fit within the available cryostats and magnets. In order to ensure the usability of the cells at the mentioned instruments, this imposes the following specific geometrical requirements for the clamp cells:

- (1) The maximal outer diameter of the cell is less than 33 mm.
- (2) The maximal total length of the cell is less than 100 mm.
- (3) The distance between the cold flange of the cryostat and the sample position is not larger than 75 mm.
- (4) The sample space diameter within the cell is as large as possible.
- (5) The cell diameter at the sample position is as small as necessary.

Requirements (1) and (2) are simply due to the available space within the instrument cryostats, and (3) ensures that the sample can be correctly positioned within the neutron beam. (4) and (5) are not directly imposed by the specific instrument but by the use of neutron radiation: On the one hand, as neutron scattering experiments require large samples, particularly with inelastic neutron scattering, the sample space within the clamp cell should be as large as possible to accommodate the needed sample size. On the other hand, an increase in diameter means an increase in cell material that is in the beam path. Since this causes both attenuation of the neutron beam and background signals in the measurement, the amount of material in the beam path should be kept low. The combination of (4) and (5) thus requires the choice of some intermediate diameter as compromise.

Aside from these specific geometrical requirements, a clamp cell that is intended for the previously mentioned tasks has to fulfill the criteria given in Chapter 4.3 with regard to the used materials, namely high mechanical strength, non-magnetism, and compatibility with neutron radiation.

6.1.3 Specific Cell Designs

Taking into account previously established requirements, several types of clamp cell have been designed in the context of this work, two monobloc cells and one fretted cell.

6.1.3.1 Monobloc Clamp Cell M1

The monobloc clamp cell *M1* is an adapted version of existing clamp cell designs, modified slightly to meet the specific requirements of the instruments at MLZ. While in principle all existing clamp cells can be seen as more or less similar, the M1 is in particular based on a clamp cell developed by Sadykov *et al.* [137].

Figure 6.4 shows an overview of this clamp cell type M1. The central part of the cell, the *body*, has a cylindrical shape with threads at both ends and a more narrow part in between. The *top piston* and the *bottom piston* are inserted from the two sides into the cylinder bore. The length of the pistons is chosen in such a way that the sample – mounted inside of a *capsule* closed by a *plug* – is located in the center of the narrow part of the cylinder. For this, the bottom piston is fully inserted during the preparation of the cell, fixing the position of the bottom end of the capsule. Between the pistons and the capsule, *anti-extrusion rings* are inserted to seal the capsule and prevent leakage. The pistons are fixated by the *top nut* and the *bottom nut*, which are screwed on to the cylinder threads. For a measurement,

the cell position is adjusted so that the beam axis goes through the narrow part of the cylinder with the minimal amount of cell material within the beam path.

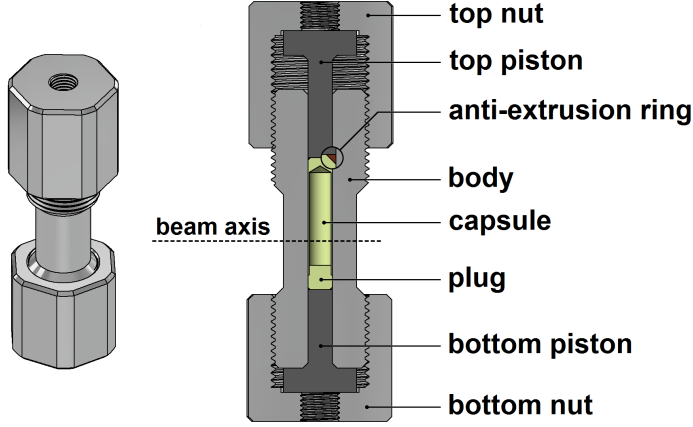


Figure 6.4: Overview of the monobloc clamp cell type M1.

The dimensions of the M1 type in the uncompressed state are given in Figure 6.5. The narrow part of the cell body adheres to the wall ratio of $K = 3$ with an inner diameter of 5 mm and an outer diameter of 15 mm. The maximum length of the M1 cell is 86 mm (taking into account an inserted sample capsule) and the maximum diameter is 30 mm to satisfy the geometrical requirements. The distance between the bottom piston and the top end of the cell is with 59 mm significantly below the necessary 75 mm, which enables the optimal positioning of the sample within the beam by changing the height of the sample rod.

The distance of 7 mm between the top end of the cell body and the bottom side of the top piston's head defines the maximum length compression of the inserted sample capsule and thus the maximum pressure that theoretically can be applied.

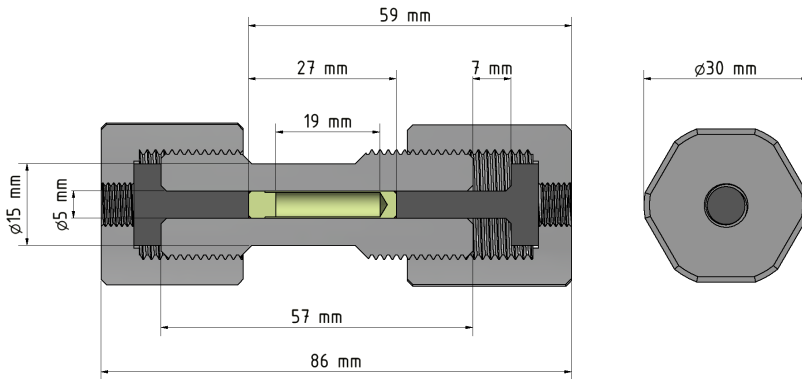


Figure 6.5: Important dimensions of the clamp cell type M1 in the uncompressed state. *Left*: side view; *right*: top view.

The sample space available within the cell is determined by the used capsule. Three different sizes of capsules – long, standard and short – are available, differing in their length to accommodate samples of various sizes (Figure 6.6). To keep the total length of the cell constant, corresponding variants of the top piston exist to match the capsule length. In diameter, the wall strength of the capsules necessarily reduces the sample space diameter from the inner bore diameter of 5 mm to about 4.0...4.5 mm; the precise wall strength depends on the used material. In all three sizes, capsules are manufactured in variants made from PTFE, AlMg5 and lead. The harder AlMg5 allows machining of wall strengths of 0.25 mm, while for the softer PTFE and lead the walls have to be thicker, up to 0.5 mm. For all capsules, the anti-extrusion rings are made from soft (unhardened) CuBe.

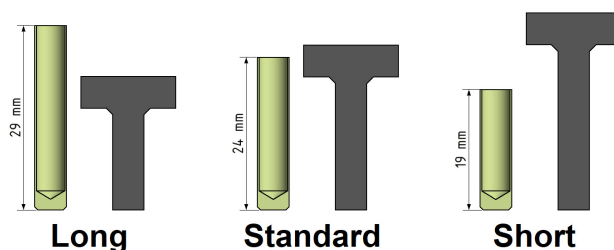


Figure 6.6: Variants of the capsules used in the M1 clamp cell. For each capsule variant, a corresponding variant of the top piston is available to keep the total length constant.

For the application of external pressure, both nuts feature a central bore. Through these bores, the *thrust pistons* can be inserted from both sides (Figure 6.7), which transmit the pressure to the top and bottom piston and thus to the sample chamber. The external pressure can be applied by means of a standard hydraulic laboratory press. The bores in the nuts are threaded to allow mounting of the clamp cell on the sample rod of an instrument with a simple screw adapter.

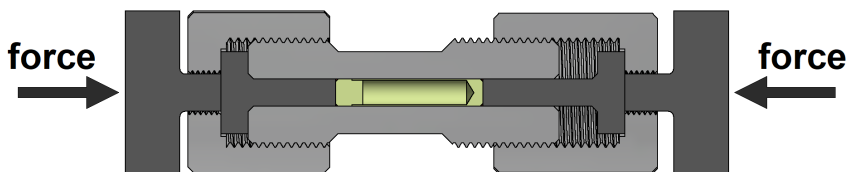


Figure 6.7: Schematic representation of the application of pressure onto the M1 clamp cell.

The application of pressure by a press does not allow direct control of the pressure within the cell. Hence, for a target loading, a calibration curve – the pressure within the cell as function of the press load – has to be measured (see Section 6.3). To determine the pressure within the cell to which the sample is subjected, a calibration crystal has to be inserted into the sample chamber (Figure 6.8). This can be done either previously with only the calibration crystal to establish a calibration curve

which is then used for the actual loading, or with the calibration crystal mounted next to the sample in the capsule for a simultaneous determination of the pressure during the experiment. By means of neutron radiation, the lattice parameters of the calibration crystal are measured *in situ*; as the lattice parameters are pressure dependent, the pressure can be determined *via* calibration tables from the literature. A calibration crystal should be of high symmetry (e.g. cubic) to feature as few reflections as possible, soft in order to be sensitive to the pressure, and available as sufficiently large single crystals for use with neutron radiation. The most commonly used calibration crystal is standard NaCl (symmetry $Fm\bar{3}m$) [149, 150, 190].

Since the calibration crystal is located within the sample chamber under the same conditions as the sample, it provides the most accurate measurement of the actual pressure value. However, this method has the significant disadvantage that it relies on the availability of neutron radiation.

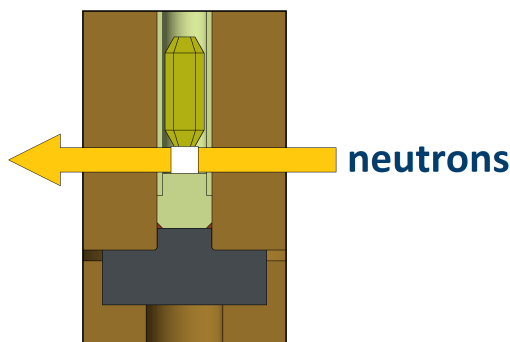


Figure 6.8: Principle of the pressure determination *via* neutrons in the M1 clamp cell. The calibration crystal is shown in white, the sample in dark yellow.

The M1 clamp cell design has been produced in two variants³: The M1-CuBe (Figure 6.9, *left*) and the M1-NiCrAl (Figure 6.9, *right*). In case of the M1-CuBe, the cell body, top nut and bottom nut are made from CuBe, while the pistons are made from NiCrAl (originally) or Ni-WC (later). In the M1-NiCrAl, the cell body and nuts are made from NiCrAl, while the pistons are made from Ni-WC. For each variant, a number of cells has been produced. To facilitate the independent use of the cells, each cell has its own set of pistons, comprising one bottom piston, one short top piston, one standard top piston and one long top piston.

³Parts for the clamp cells were machined by the following companies: HAKU GmbH, Alsdorf, Germany: CuBe and NiCrAl clamp cell parts; JCNS workshop, Forschungszentrum Jülich GmbH, Jülich, Germany: NiCrAl clamp cell parts and various other equipment; Hawedia GmbH, Marklkofen, Germany: WC parts.

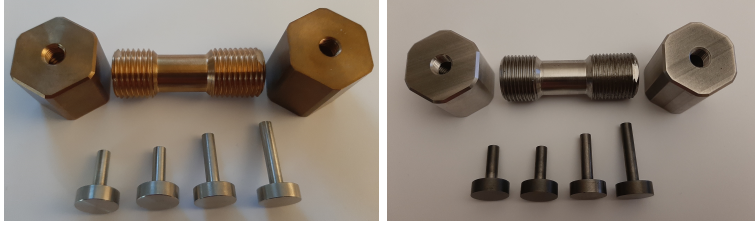


Figure 6.9: Produced variants of the M1 clamp cell design. *Left*: M1-CuBe, with body and nuts made from CuBe, and NiCrAl pistons; *right*: M1-NiCrAl, with body and nuts made from NiCrAl, and Ni-WC pistons.

6.1.3.2 Modified Monobloc Clamp Cell M1D

To enable the determination of the pressure within the cell independently from neutron radiation, a modified version of the M1 was designed, the clamp cell type *M1D* (Figure 6.10). The difference between the cell types M1 and M1D concerns the bottom part of the cell. The M1D design features an optical path to the capsule space through a narrow hole in the bottom piston. The optical access hole in the bottom piston is sealed by a diamond. In order to keep the bottom piston and thus the narrow part of the optical path short, the bottom nut is adapted from an externally screwed nut to an internally screwed one. This allows shortening the piston length while retaining the thread length necessary to safely fix the nut.

The top part of the M1D is in principle the same as in the M1; however, a cutout fitting the head of the top piston is added to reduce the total length of the cell.

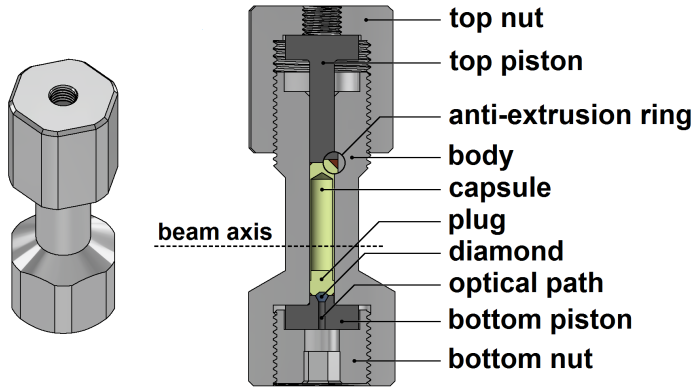


Figure 6.10: Overview of the monobloc clamp cell type M1D.

As seen in Figure 6.11, the maximum length of the M1D is thus 77.5 mm compared to 86 mm for the M1. The maximum diameter is with 30 mm unchanged. The M1D is designed for use of the same capsules and top pistons as the M1 (Figure 6.6) to avoid the need for dedicated parts for every cell type.

The central cylindrical part of the M1D is identical to that of the M1 with $K = 3$, meaning that the same pressure behavior is expected for the two cell types.

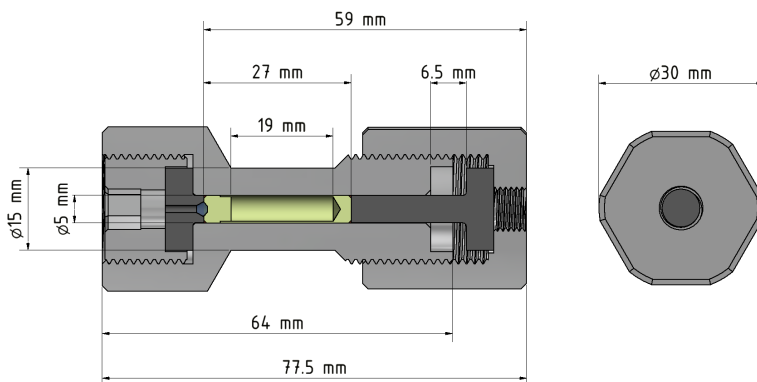


Figure 6.11: Important dimensions of the clamp cell type M1D in the un-compressed state. *Left*: side view; *right*: top view.

The fundamental difference between the M1 and the M1D – the optical access to the inner of the cell – allows the use of other methods to determine the pressure. In particular, it is intended for use with the *ruby luminescence* method (Figure 6.12), in which the pressure is determined by the shift of the ruby luminescence wavelength [151, 191, 192]. To enable this, a small ruby chip is placed on top of the diamond sealing the optical hole in the bottom piston. By shining a laser through the optical path onto this ruby, the characteristic ruby luminescence is excited. Unlike in the usual application of the ruby luminescence in diamond anvil cells, where the luminescence is employed in transmission, in the clamp cell the luminescence is measured from the reflection. The ruby is pressed between the diamond and the capsule plug. To transmit the pressure within the capsule to the ruby as hydrostatically as possible, the plug itself must be made out of a soft material, e.g. PTFE. While the conditions at the sample position and the ruby are thus only approximately the same, this method has the advantage that it does not depend on neutrons and should in addition allow for a faster determination of the pressure. For a more accurate determination of the pressure at the sample position from the ruby luminescence measurements, a cross-calibration of ruby luminescence and neutron (NaCl) calibrations is necessary.

A further advantage is that with the options of ruby luminescence and neutron radiation, the pressure within the cell can be determined by two independent methods. Assuming that the conditions (pressure and temperature) at the sample and the ruby position are the same (or at least very similar), this allows the experimental determination of both pressure and temperature. If, like in the M1 design, only one method can be used, the temperature of the sample and the calibration crystal has to be taken as the temperature in the cryostat, which is a valid approximation only after sufficient time has passed to reach thermal equilibrium.

The optical path in principle also allows other methods of pressure determination based on the measurement of resistivity [193] and superconducting transition temperature [194], but this has not been realized so far in the available cells.

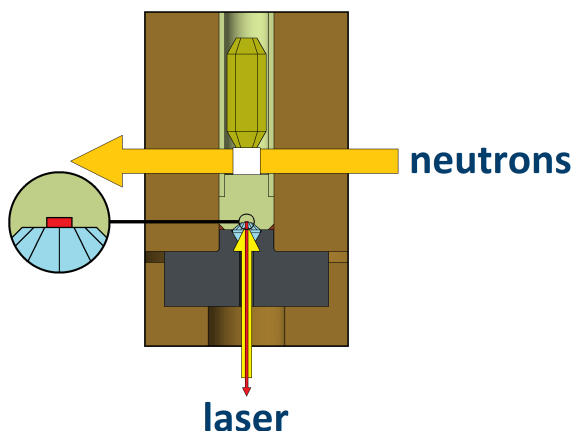


Figure 6.12: Principle of the pressure determination *via* neutrons and *via* ruby luminescence in the M1D clamp cell. The calibration crystal is shown in white, the ruby chip in red, and the sample in dark yellow.

Like the M1, the M1D has been produced in two variants, the M1D-CuBe with body and nuts made from CuBe and pistons made from NiCrAl, and the M1D-NiCrAl with body and nuts made from NiCrAl and pistons made from Ni-WC (Figure 6.13). For every cell, a separate set of pistons is available, including a bottom piston with a mounted diamond.

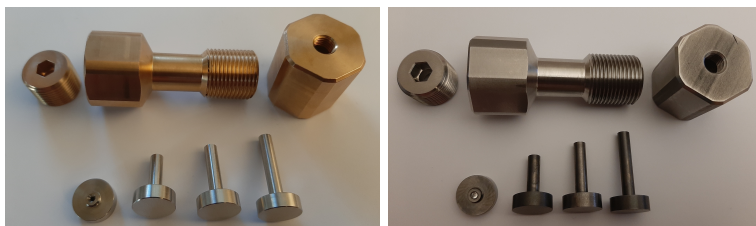


Figure 6.13: Produced variants of the M1D clamp cell design. *Left*: M1D-CuBe, with body and nuts made from CuBe, and NiCrAl pistons; *right*: M1D-NiCrAl, with body and nuts made from NiCrAl, and Ni-WC pistons.

The specific diamond used in the M1D design are of the *Boehler-Almax* type Ia [195] with an optical aperture of 30° (Figure 6.14). The diameter of the culet is 1.0 mm or 0.9 mm; to ensure that it can safely withstand the pressure in the cell, it cannot be larger. The diamond is mounted with glue that is filled into the free space between diamond and piston at the rim of the seat. Since during the pressure application the diamond is subject only to pressing forces, the glue does not have to withstand high forces, and it can happen that it comes loose during the opening of the cell. In that case, it can simply be cleaned and remounted.



Figure 6.14: Bottom pistons made from Ni-WC (*left*) and NiCrAl (*center*) with mounted diamond, and schematic view of the bottom piston (*right*).

6.1.3.3 Fretted Clamp Cell F1

The fretted clamp cell design *F1* is in principle the same as the M1D, as it has a conceptually equivalent design, in particular featuring the optical path into the inner of the cell (Figure 6.15). The key difference is that the F1 is a fretted cell and is thus able to reach higher pressures.

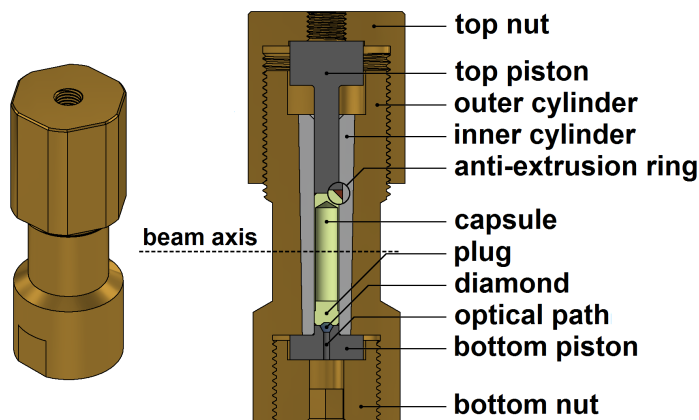


Figure 6.15: Overview of the fretted clamp cell type F1.

Following the nature of the fretted cell design, the dimensions of the F1 are adjusted compared to the ones from the M1D cell (Figure 6.16). To accommodate the same capsules as the M1 and M1D, the inner diameter of the cell is kept at 5 mm. The outer diameter is chosen as 22 mm. This value represents a compromise between high strength (larger diameter) and high transmission (smaller diameter). Following the previously mentioned ideal relation, this results in a contact diameter of $\sqrt{22 \text{ mm} \cdot 5 \text{ mm}} \approx 10.5 \text{ mm}$. The contact surface between inner and outer cylinder is designed for assembly by press fitting, with a conical angle of 1° . Due to this, the ideal contact diameter can only be approximately estimated at one point; the F1 is designed so that the according point is located in the center of the narrow part of the cell.

Due to the increase in diameter of the cylinder part, the maximum diameter of the cell is 32 mm – slightly larger than in the case of M1 and M1D, but still matching the geometrical requirements to fit into the instruments DNS, POLI and MIRA. The dimensions of other parts, e.g. the bottom nut, are also adjusted to fit the increased diameter compared to the M1D. One particular change is the increase of the top piston head length. This is done to increase the possible compression while at the same time offering enough overlap with the thread of the body to safely secure the top nut.

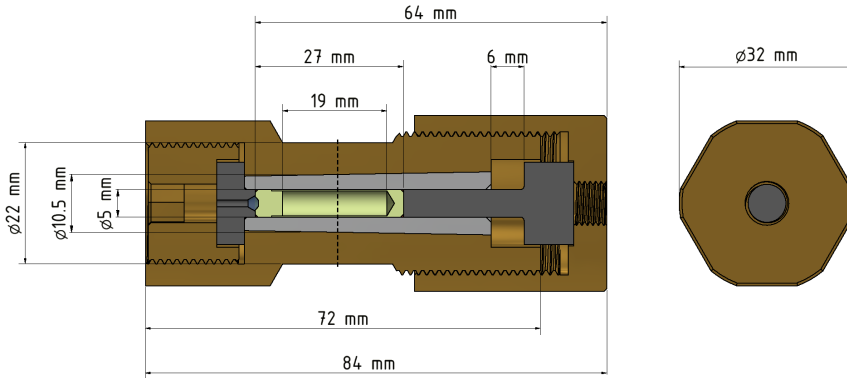


Figure 6.16: Important dimensions of the clamp cell type F1 in the uncompressed state. *Left*: side view; *right*: top view. The dashed line marks the center of the narrow part, where the ideal diameter ratio is assumed.

While the F1 is designed for use with the same capsules as the M1/M1D, the difference in length of the inner bore requires a separate set of top pistons that are comparatively longer (Figure 6.17) than the ones for the other cells. Since an elongation of the piston shaft makes the piston more prone to breaking, only the standard and long capsules are used in the F1; the short capsule would require too long a piston. The bottom piston of the F1 is identical to the one of the M1D, enabling the use of ruby luminescence to determine the pressure as previously shown (Figure 6.12).

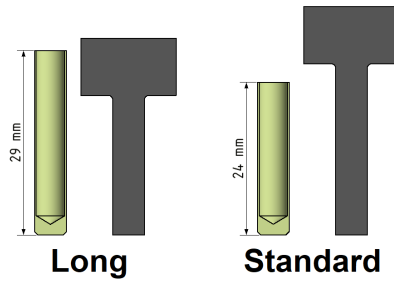


Figure 6.17: Variants of the capsules used in the F1 clamp cell. For each capsule variant, a corresponding variant of the top piston is available to keep the total length constant.

The F1 is again produced in two variants, which differ in the material of the outer cylinder (Figure 6.18). In both cases, the inner cylinder is made from NiCrAl to achieve the best mechanical strength at the bore. The outer cylinder is made from either CuBe (F1-CuBe) or TiZr (F1-TiZr).

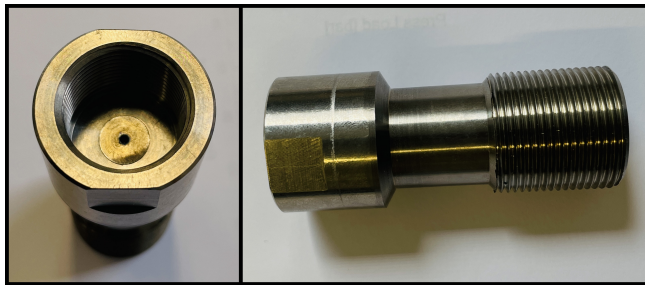


Figure 6.18: The F1-TiZr prototype clamp cell before final manufacturing with the NiCrAl inner cylinder pressed into the TiZr outer cylinder. The interference value is 0.10 mm. *Left*: view from the bottom of the cell; *right*: side view.

The F1-CuBe is able to withstand higher pressures, while the F1-TiZr has a possibly better neutron transmission without the coherent scattering contribution from the outer cylinder (Figure 6.19). Hence, depending on the requirements of a given experiment, the more suitable option can be chosen.

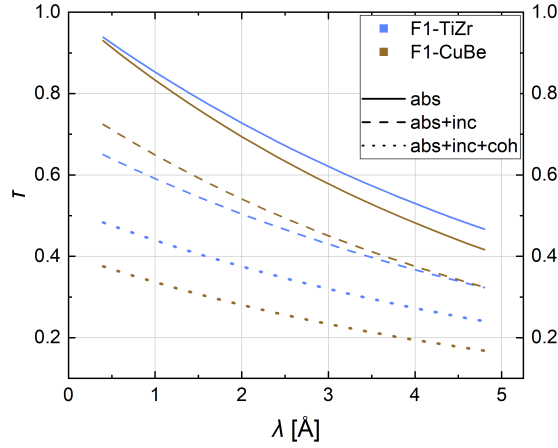


Figure 6.19: Calculated neutron transmission as a function of the neutron wavelength for the F1-CuBe and F1-TiZr clamp cells, taking into account the contributions to the beam attenuation from neutron absorption (abs), incoherent scattering (inc) and coherent scattering (coh), but not from resonant and inelastic scattering. *Calculated with help of [129].*

6.2 Simulations

As part of the development of the different types of clamp cells, simulations using Finite Element Analysis have been performed. All simulations were done in collaborative work by Muni Kishore Babu Poli (Institute of Crystallography, RWTH Aachen University), and the principal results are shown here in context of the general development of the clamp cells.

6.2.1 Simulation of Clamp Cell Type M1

For the clamp cell type M1, the simulations were performed in order to validate the theoretical expectations of the monobloc design. Since the mechanical limit for the cell is determined by its weakest point, only the cell body was simulated. The hydrostatic pressure inside of the capsule is represented by a corresponding force acting perpendicular to the surface of the inner bore. The relevant material properties are taken from the literature. An exemplary result of the simulation is shown in Figure 6.20 for the M1-CuBe. The *safety factor* s is calculated as ratio of the yield strength and the strain, so a safety factor of 1 indicates that the material starts to deform plastically while for safety factors larger than 1 the cell material remains in the elastic regime.

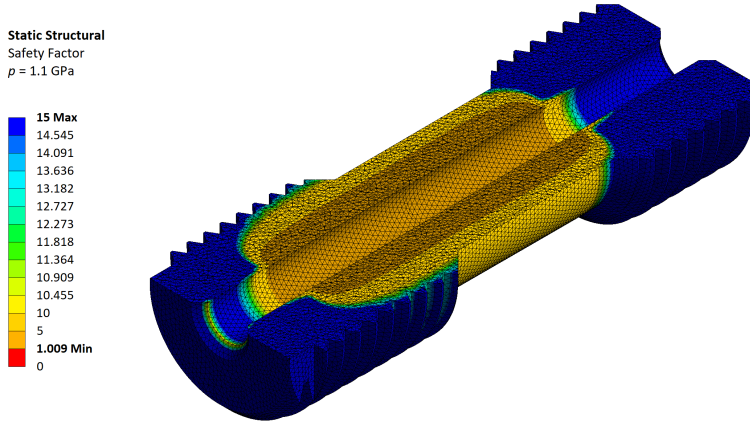


Figure 6.20: The safety factor for the M1-CuBe based on the simulation for a simulated pressure load of 1.1 GPa.

As expected, the largest strains occur at the bore where the pressure is applied and the capsule would be located, and decrease towards the outer surfaces of the cell. For an applied pressure of 1.1 GPa, the safety factor reaches a minimum value of just above 1, in good agreement with the provided yield strength of CuBe.

Figure 6.21 shows the minimal safety factor s_{\min} for the M1-CuBe and M1-NiCrAl as function of applied pressure. For NiCrAl, the critical value of 1 is reached for 1.5 GPa, again in good agreement with the assumed yield strength.

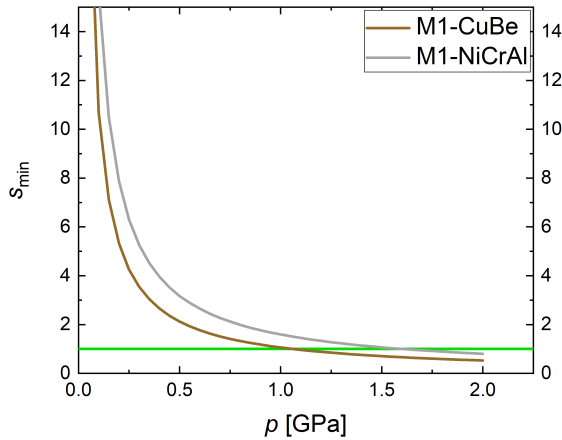


Figure 6.21: The minimal safety factor for the clamp cell type M1 based on the simulations as function of applied pressure. The green line indicates the critical safety factor of 1.

For the M1, the results of the simulations show that no unexpected stress concentrations are present in the design, and the pressure limit is solely determined by the used material in accordance with the prediction from theory.

The fact that the threaded end parts of the M1 clamp cell are virtually unaffected by the applied pressure (Figure 6.20) indicates that the same pressure limits can be assumed for the M1D-type, since the differences between M1 and M1D concern only those end parts.

6.2.2 Simulation of Clamp Cell Type F1

Unlike the monobloc designs M1 and M1D, the fretted design of the F1 is not fully determined by the used material. In particular, a suitable fit of the inner and outer cylinder has to be determined, which concerns two factors: the contact radius and the interference.

The contact radius r_c is, for a set inner radius r_i , defined by the outer radius r_o of the cell, and has to be a compromise between higher strength (larger r_o) and higher transmission (smaller r_o). The choice for the eventual value of r_o was supported by simulations of the pressure limit for various values of r_o .

The interference is the crucial factor for the working principle of fretted cells, leading to the introduction of the residual stresses that allow exceeding of the mechanical properties of the individual materials. A larger interference results in a higher deformation and thus in larger residual stresses, but also makes the assembly of the two cylinders for the cell more difficult. In order to select a suitable interference, simulations were performed for various interference values. In these simulations, the effect of the interference was represented by the contact pressure on the surface of the inner cylinder, with a high contact pressure indicating a good transmission of force from the inner to the outer cylinder and thus a good interference fit. The limit for the transmitted force is given by the material of the outer cylinder (CuBe or TiZr). The theoretical value for the interference was determined by trial simulations, for which a contact pressure of 0.7 GPa was taken as target following reference [120]. These simulations showed that interference values of 0.175 mm and above yield this targeted value, with larger interferences resulting in higher contact pressures. To test the practicality of the simulated interference values, press tests with substitute parts of the relevant geometry were performed, where an inner cylinder made from steel was pressed into an outer cylinder made from aluminium; this keeps the approximate difference in material strength between the two parts while avoiding the use of expensive NiCrAl, TiZr or CuBe. The use of substitute parts was possible as the interference fit poses primarily a geometrical problem in that the material in the interference zone has to be displaced somewhere, which can be assumed to be independent of the material. Load from the press was applied until the inner cylinder was fully inserted into the outer cylinder, reaching an effective maximum load of about 200 kN. The substitute press tests show that an assembly is in principle possible with interference values of up to 0.35 mm considering material flow. However, a first press test using a NiCrAl inner cylinder and a TiZr outer cylinder with an interference value of 0.175 mm revealed that due to specific properties of the NiCrAl, already this value was too large for assembly. As a consequence, the interference value was decreased to 0.10 mm, following from the length the inner

cylinder was pressed in successfully. According to the simulations, this value should still result in a sufficiently high contact pressure.

Based on the chosen geometry and interference of the F1, the pressure limit for this cell was again determined from the safety factor for both material combinations (NiCrAl inner cylinder with outer CuBe and TiZr cylinder, respectively). As shown in Figure 6.22, the critical value for the F1-CuBe is reached for a pressure of 2.6 GPa, for the F1-TiZr, the simulations give a pressure limit of 2.0 GPa. The intermediate increase in the safety factor is caused by strain hardening of the material at the contact surface between inner and outer cylinder. The maxima of these increases are remarkably close to the yield strengths of the respective material of the outer cylinder (0.7 GPa for TiZr, 1.2 GPa for CuBe), but the underlying reasons in the simulations are not further investigated in the context of this work.

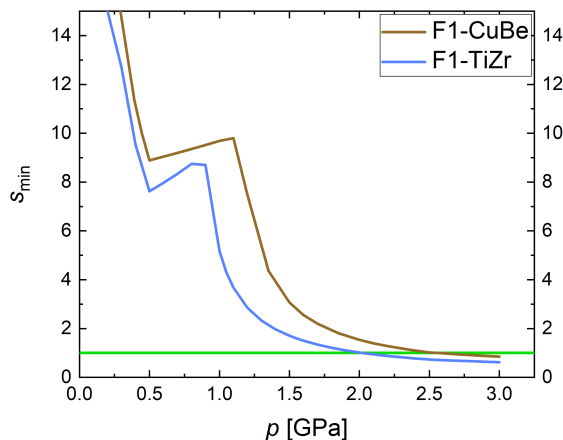


Figure 6.22: The minimal safety factor for the clamp cell type F1 based on the simulations as function of applied pressure. The green line indicates the critical safety factor of 1.

6.3 Practical Tests

To fully characterize the different clamp cell designs, several practical tests had to be performed. These included tests of the mechanical strength in form of the calibration curve, tests of the neutron transmission at different instruments and wavelengths, tests of the suitability for measurements of magnetic properties, and tests of the thermal response in a cryostat. In addition, the feasibility of the ruby luminescence method employed in the M1D and F1 design had to be shown. Due to problems⁴ beyond our control, however, not all planned tests with the clamp cells

⁴The operation of the MLZ was suspended as a consequence of the SARS-CoV-2 pandemic as well as due to technical problems with the neutron generation.

and in particular for the cross-calibration between the pressure scales from ruby luminescence and NaCl could be performed.

Parts of the results presented here have already been published [196].

6.3.1 Calibration Curve

The calibration curve of a clamp cell – the pressure at the sample position within the cell as a function of the press load applied in the loading step – has two important purposes: First, it serves as reference curve for subsequent uses of the cell. Since the pressure within the cell cannot be measured *in situ* during the loading, it allows the (approximate) adjustment of the target pressure by applying the appropriate press load. Second, a full calibration curve indicates the pressure limit up to which the respective cell can safely be used. As mentioned before, the cell is supposed to work only in the linear-elastic regime given by the used cell materials, and the onset of deviation from the linear-elastic behavior indicates the onset of plastic deformation and thus the operational pressure limit. The linear-elastic behavior as well as the possible deviation from it are directly obtainable from the calibration curve.

We have determined the calibration curve for the M1-CuBe at POLI, where measurements were performed at a wavelength of $\lambda = 0.90 \text{ \AA}$ and $\lambda = 1.15 \text{ \AA}$ using an NaCl single crystal. The resulting curve is shown in Figure 6.23.

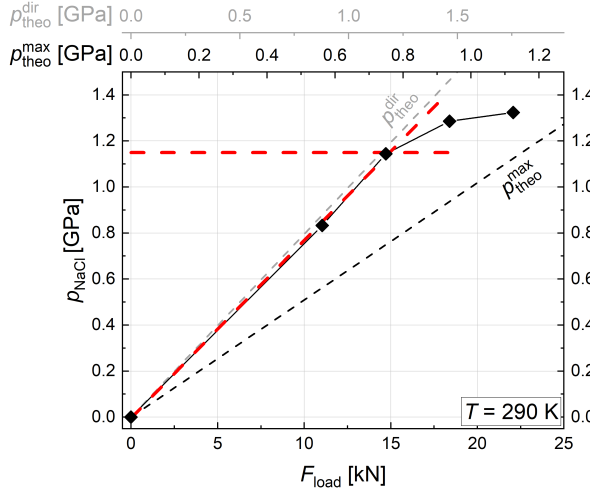


Figure 6.23: The pressure calculated from the change in lattice parameters of an NaCl single crystal as function of applied force load in the M1-CuBe. The red dashed lines mark the linear-elastic regime and the pressure at which the curve starts to deviate from it, indicating the onset of plastic deformation of the cell material. The black and gray dashed lines mark the equivalence of p_{NaCl} and p_{theo} , with p_{theo} calculated with regard to the maximum contact area A_{max} and to the direct contact area A_{dir} , respectively. The connecting lines are guides for the eye.

Red dashed lines mark the linear-elastic behavior and the pressure at which the

curve starts to deviate from it. From this, the pressure limit and maximum operational pressure of the M1-CuBe is deduced to be 1.15 GPa. Since during the experiment a maximum pressure of about 1.3 GPa was reached, the cell was unfortunately deformed plastically and can thus not be safely used in further experiments at high pressures. This overloading of the cell – while giving valuable information – was in part caused by a discrepancy of the actually measured and the theoretically expected pressure. The latter was calculated based on the force load from the press and the maximum cross section area $A_{\max} = \pi \cdot (2.49 \text{ mm})^2$ of the piston through which the force is transmitted to the capsule. The measurement of respectively higher pressures from the NaCl sample, however, indicate that this assumption was not valid. A better agreement between measured and calculated pressures is obtained if only the actual direct contact area A_{dir} between the piston and the capsule is considered for the calculation of the theoretical pressure, i.e. the cross section area of the piston is reduced by the area of the anti-extrusion ring. The underlying reason for the discrepancy in pressure and a possible relation to the considered contact area cannot be deduced from the present experiment, though. The theoretical pressure calculation is discussed in more detail in Chapter 6.3.5.3.

As the pressure limit should only depend on the cell material and the central, cylindrical part of the cell, the determined calibration curve and pressure limit are assumed to be valid for all M1-CuBe and M1D-CuBe cells.

Analogous calibration measurements for the M1-NiCrAl were planned, but could not be performed.

6.3.2 Neutron Transmission

While it is possible to estimate the expected neutron transmission based on the used material composition and thickness of the walls, it has to be measured experimentally to get the actual value. In particular, the decrease in transmission based on coherent scattering is impossible to calculate beforehand as it depends on the specific structure of a cell.

For the experimental transmission measurements, the same M1-CuBe cell as for the determination of the calibration curve was used; while due to the plastic deformation this cell cannot be used for measurements at high pressures, this has no influence on the neutron transmission of this type of cell. The measurements were conducted only at ambient pressure conditions. The first test was performed at MIRA with a wavelength $\lambda = 4.05 \text{ \AA}$. As test sample, a manganese silicide (MnSi) single crystal with defined orientation (with the (110) and (111) reflections in the scattering plane) was used (Figure 6.24, *left*). To determine the transmission, the (110) nuclear Bragg reflection of MnSi was measured two times, once within the clamp cell and once without it (Figure 6.24, *right*). The ratio of the maximum peak intensity of the two measurements (I_{in} and I_{out} , respectively) was taken as the experimental transmission T_{exp} of the M1-CuBe clamp cell.

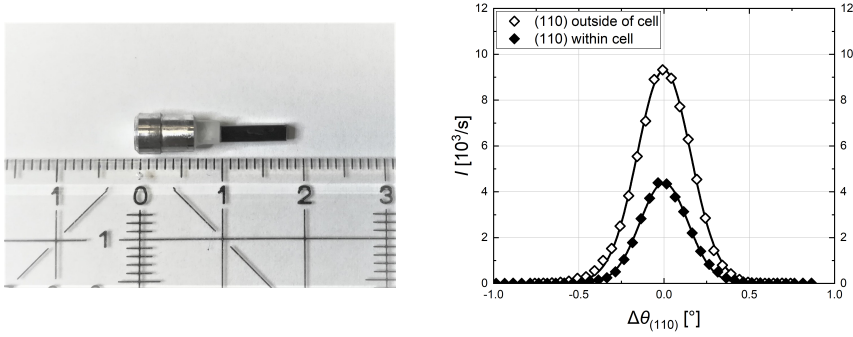


Figure 6.24: *Left*: the MnSi single crystal sample (black) used for the transmission measurements; *right*: the (110) nuclear Bragg reflection of MnSi in air and in the M1-CuBe clamp cell. Reflections were centered to their respective peak position. The connecting lines represent the Gaussian fits of the peaks.

For the M1-CuBe cell and with the intensities I_{in} and I_{out} determined from the Gaussian fit of the peaks, this ratio results in $T_{\text{exp}} = I_{\text{in}}/I_{\text{out}} = 47.2(10)\%$. This value is in fairly good agreement with the theoretical transmission calculated for a thickness of 1 cm (corresponding to twice the wall strength of the cell; Figure 6.25), which is about $T_{\text{theo}} = 49.94\%$ in the case of no coherent scattering.

While this particular result agrees with the theoretical calculations of the transmission, further measurements with the same method have to be performed to expand on this, and for each combination of wavelength and cell material, the transmission should ideally be determined individually.

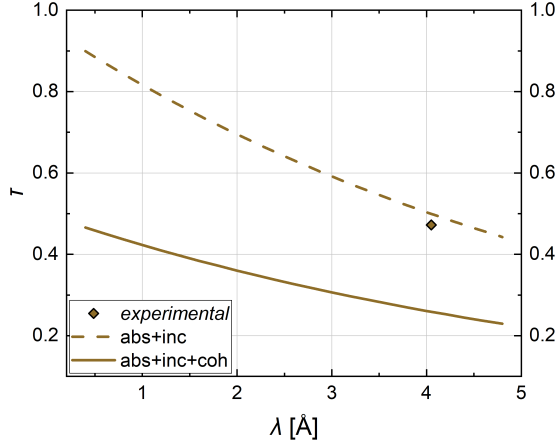


Figure 6.25: The experimentally determined transmission for CuBe compared with the calculated neutron transmission for a thickness of 1 cm as a function of the neutron wavelength for CuBe, taking into account the contributions to the beam attenuation from neutron absorption (abs), incoherent scattering (inc) and coherent scattering (coh), but not from resonant and inelastic scattering. *Calculated with help of [129].*

6.3.3 Measurement of Magnetic Reflections

To confirm the suitability of the clamp cells for measurements of magnetic properties with neutrons, a magnetic signal from a sample within the cell was measured. These measurements were performed for the M1-CuBe on an MnSi sample.

MnSi has a magnetic phase transition at $T_C = 29.5$ K from a paramagnetic high-temperature to a helimagnetic low-temperature phase [197]. The pressure dependence of this magnetic phase, which includes for example the formation of skyrmions [198], makes it an interesting compound to study in the parameter range offered by the clamp cells. The helimagnetic phase is characterized by a small magnetic moment of $0.4 \mu_B$ and a large helical pitch length of about 180 \AA [199]. Consequently, the magnetic reflections of MnSi are relatively weak, which makes the compound suitable for benchmarking the suitability of the clamp cell. Since for these tests only the fundamental feasibility of the measurement of a magnetic signal was of importance, temperature-dependent measurements at ambient pressure were sufficient.

Figure 6.26 shows the (110) Bragg reflection of MnSi at 40 K (above T_C) and at 15 K (below T_C). In the paramagnetic phase at 40 K, only the nuclear reflection is observed as expected. In the helimagnetic phase at 15 K, magnetic satellite reflections $(110)^\pm$ at about $\pm 1.3^\circ$ from the (110) peak position are clearly visible, albeit with an intensity roughly 50 times smaller than the nuclear reflection.

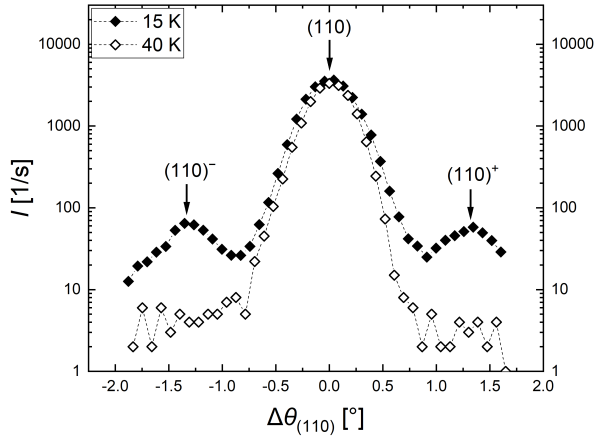


Figure 6.26: The (110) Bragg reflection of MnSi measured at 40 K and 15 K in the M1-CuBe clamp cell; at 15 K magnetic satellite reflections $(110)^\pm$ are visible. The dashed lines are guides for the eye.

This observation evidences that for the M1-CuBe clamp cell, the cell background is sufficiently low to allow the detection of even weak magnetic signals.

6.3.4 Thermal Response

In order to use the developed clamp cells at very low temperatures as intended, the thermal response of the cells within the instrument cryostat has to be determined. This includes two important properties: the time needed for cooling down and heating up, and the lowest temperature that can be reached.

Cooling down the clamp cell in the cryostat is naturally inevitable to conduct experiments at low temperature, as is the heating up after measuring. Hence, these times have to be taken into account when planning an experiment at the instrument. They are of particular importance for clamp cells, since the pressure can only be changed *ex situ*, meaning that for any pressure change, the cell has to be removed and reinserted into the cryostat. Due to the nature of the cryostat, the time needed to cool down is not only dependent on the inserted material, but also on the state of the cryostat, i.e. a pre-cooled cryostat needs significantly less time to cool down than a warm one.

For the M1-CuBe and the M1-NiCrAl, the thermal response was measured in the cryostat of the DNS instrument. As a placement of the temperature sensors within the closed cell is not possible, the temperature was taken at the bottom of the cell furthest away from the thermal conduct between cell and cryostat. The cooling rate of the cryostat is affected by its thermal state – if it is already pre-cooled, i.e. after a previous low-temperature measurement with the cryostat components still being at lower temperatures, it cools down faster than if it is at room temperature in the

warm state. Hence, only the initial measurement (with the M1-NiCrAl inserted) gives the thermal response for the warm state, while all subsequent measurements are in the pre-cooled state. As reference for the cooling-down with inserted clamp cells, the empty cryostat was measured.

The temperature as function of time is shown in Figure 6.27 for the different setups. For cooling down (Figure 6.27, *left*), the temperature was measured going directly from room temperature to base temperature. There is no significant difference in the time needed to cool down between the M1-CuBe and M1-NiCrAl, with both needing between 2.5 and 3 hours in the pre-cooled state. If the cryostat is not pre-cooled, reaching the lowest temperature takes about half an hour longer. On the other side, cooling down the empty cryostat in the pre-cooled state is about half an hour faster than with inserted cells. Unlike in the cooling-down process, the heating-up was done in steps, which was done to see how fast the temperature settles with an inserted cell. As such, the temperature behavior (Figure 6.27, *right*) does not show the time needed for a simple heating, but gives an indication of the time needed to stabilize at a given temperature upon heating. While the specific times depend on the temperature and temperature step, it is evident that the two cells again affect the temperature in a similar way.

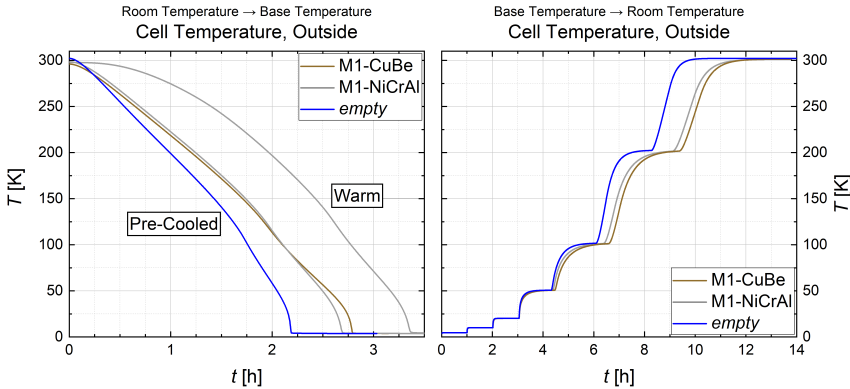


Figure 6.27: The thermal response of the M1-CuBe and M1-NiCrAl cell in the cryostat of DNS. *Left*: the temperature as function of time going from room temperature to base temperature; *right*: the temperature as function of time going in steps from base temperature to room temperature.

Besides the time necessary to reach the lowest temperature in the cryostat with the clamp cell inserted, the absolute value of the lowest temperature itself is of interest. While in theory the presence of the clamp cell should not affect the minimum temperature in the cryostat, it will in practice take a long time to reach this temperature. Therefore, it is more important to determine the temperature that can be reached within a reasonable time span.

Figure 6.28 shows the temperature as function of time in the vicinity of the lowest reached temperature. Without inserted cell, the cryostat reaches a base temperature of 3.77 K after about 3 hours. With inserted cells the lowest temperature is with

3.81 K slightly higher for both cells. For the M1-CuBe, the time needed to reach the base temperature is just a bit longer than for the empty cryostat, while the M1-NiCrAl needs about half an hour longer. The change in temperature within this last half hour, however, is only about 0.02 K, making it practically negligible.

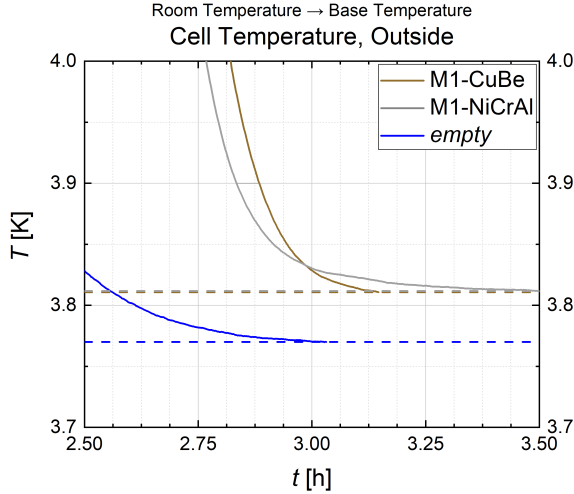


Figure 6.28: The thermal response of the M1-CuBe and M1-NiCrAl cell in the cryostat of DNS. The temperature as function of time is shown in detail in the vicinity of the base temperature.

It should be emphasized that, since the temperature is measured on the outside of the cell and conduction the heat from the inside of the cell towards the surface takes some time, the actual temperature within the cell will be higher than shown here. Hence, the necessary time to cool-down will accordingly be longer, and the lowest reached temperature accordingly higher. However, the presented lowest temperature does show that the cryostat can reach this temperature with the heavy cell load inserted.

6.3.5 Feasibility of the Ruby Luminescence Method in Clamp Cells

As mentioned previously, the ruby luminescence method is a standard method of pressure determination commonly used in diamond anvil cells [200]. While the basic principle remains the same, its practical application for the purpose of use in the clamp cells has to be modified. In the clamp cells, the ruby luminescence method offers a second pressure scale complementary to the pressure obtained from neutron diffraction from a single-crystal standard, e.g. NaCl, within the cell.

6.3.5.1 Application of the Ruby Luminescence Method

In the usual application of the ruby luminescence method in a diamond anvil cell, the ruby is employed in a transmission geometry. In a clamp cell, this is not possible,

as the ruby is covered by the sample container, so that the ruby is instead used in reflection geometry. While this difference does not matter for the principle of the ruby luminescence, the change in geometry does have implications for its practical application. The simple reason is that in order to use the ruby with the laser, its position has to be known. In the transmission geometry, light from the back shining through the diamonds can be used to locate the ruby. In the clamp cell, this option does not exist, which makes locating the ruby more difficult. As the surrounding sample container made from PTFE is in itself not noteworthy reflective, light that is shone in does not suffice for visual ruby location. To solve this problem, a reflective layer is inserted between the diamond and the sample container. This layer should affect the pressure transmission through the PTFE to the ruby as little as possible and thus should be made from a soft material.

One possibility employed here is the deposition of a thin Al-layer on the top face of the sample container plug. For this, a regular PTFE plug used for measurements not involving the ruby luminescence method (Figure 6.29, *left*) is sputtered with 50 μm of Al (Figure 6.29, *center*). This forms a layer that is tightly bonded, allowing a normal handling of the plug in the sample assembly, although the layer is very susceptible to scratch damage. During the measurement, the diamond is pressed into the layer, leaving an indentation after removal of the plug from the cell (Figure 6.29, *right*).



Figure 6.29: The PTFE plugs of the sample containers used for the clamp cells. *Left*: the regular PTFE plugs; (*center*): the PTFE plugs with the Al-layer on the top face; *right*: the PTFE plugs with the Al-layer after usage.

To test the general feasibility of this concept, the clamp cell, containing the ruby-equipped diamond covered by the plug, is placed in the sample chamber of an offline ruby system (Figure 6.30). By means of an objective and either the eye or a camera, the system can be focused. The illuminating light and the exciting laser are directed to the ruby with the help of beam splitters. The light emitted from the ruby is likewise led towards a spectrometer, where the precise spectrum and in particular the wavelength of the R_1 line are measured.

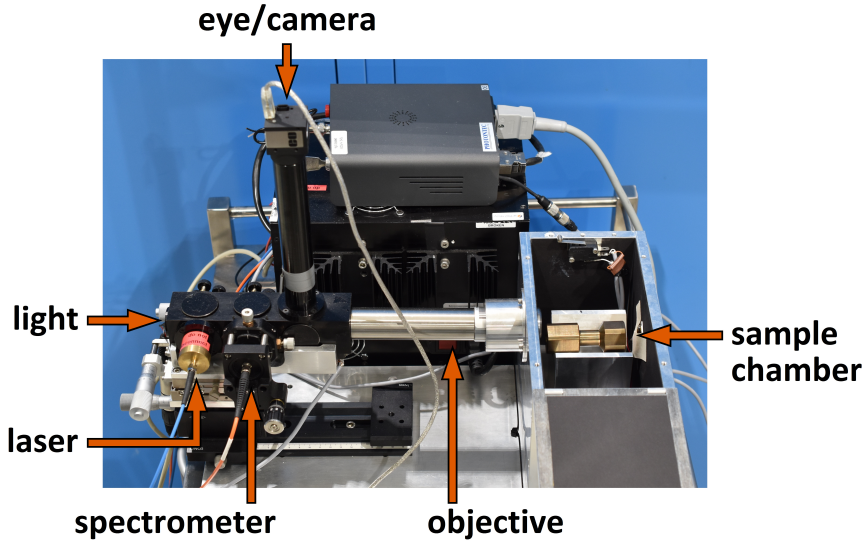


Figure 6.30: View of the offline ruby system used to test the general feasibility of the reflective ruby luminescence geometry.

Figure 6.31 illustrates the procedure: In the first step, the ruby chip is mounted with glue on the culet of the diamond (Figure 6.31, *left*). The ruby should ideally be sufficiently large, single-crystalline, homogeneous, and compact in order to get the best result. Figure 6.31, *center*, shows the light emitted from the ruby in response to the exciting green laser light; this is a visual confirmation of the quality of the ruby and its suitability for ruby luminescence. After the diamond with the ruby has been inserted into the cell, the ruby is pressed to the contact surface between the diamond and the aluminium-layered plug. As shown in Figure 6.31, *right*, this contact surface is clearly visible under the microscope. From this, it is also evident that the aluminium layer forms cracks when the diamond is pressed in, but as the layer is fixed in position, it still completely fulfills its purpose. Since the ruby is not pressed flat against the diamond, it is not directly visible in this state. However, the print of the glue with which it is mounted can clearly be distinguished by its lack of reflected light, allowing the indirect locating of the ruby.

For the quantitative verification of the feasibility of this setup, the ruby luminescence spectrum was measured in two arrangements for comparison: In the first setup, serving as reference independent from the clamp cell, the ruby is mounted on the diamond but oriented directly towards the laser. This way, the diamond does not affect the ruby luminescence. The second setup corresponds to the actual setup in which the ruby is used in an experiment, with the ruby pressed between diamond and aluminium layer. Here, the diamond does affect the ruby luminescence as both the laser and the emitted light have to pass through it.

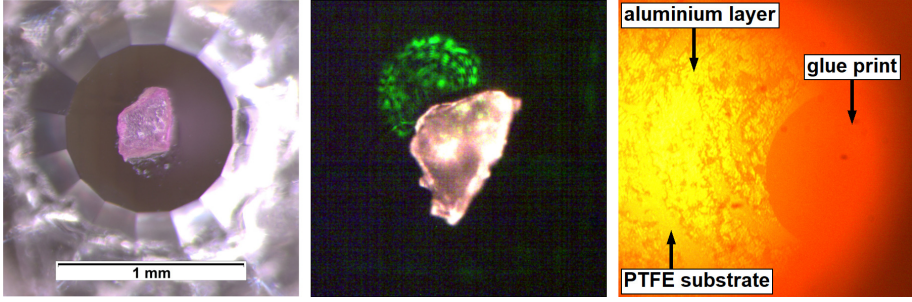


Figure 6.31: *Left*: the ruby placed on the culet of the diamond; *center*: the ruby with clearly visible light emission from the excitation by the green laser; *right*: view through the microscope on the interface of diamond and plug.

The result of this test is presented in Figure 6.32. It shows that the setup with the ruby in reflection geometry works and can be used for the ruby luminescence method. Although the passing of the laser and the emitted light through the diamond inevitably leads to absorption and a significant reduction of the measured intensity, the R_1 and R_2 lines are still clearly visible with a well-defined peak position. As for the ruby luminescence method only the wavelength given by this peak position of the R_1 line is of importance, the loss of intensity is in practice irrelevant.

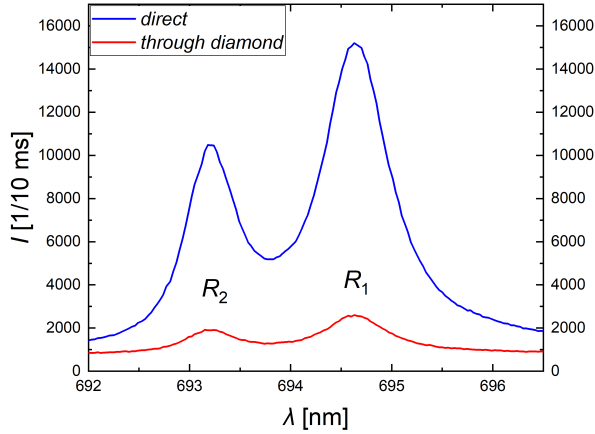


Figure 6.32: Comparison of the ruby lines R_1 and R_2 measured for the ruby luminescence in direct orientation and through the diamond. The counting time for both spectra is 10 ms.

6.3.5.2 Calibration of Pressure as Function of Temperature

To determine how the pressure inside of the cell changes with the temperature, a M1D-CuBe was loaded to some arbitrary pressure – about 0.47 GPa based on the applied force load and the assumption of the full piston/capsule contact area – and placed in the cryostat. The ruby luminescence signal was then measured as function of the set temperature using the offline ruby luminescence system. Since the pressure is calculated not from the absolute value of the luminescence wavelength but from its shift relative to the position at ambient pressure, a reference curve is measured. For this, a ruby was placed in the M1D-CuBe and the measurement repeated without applied pressure. Figure 6.33 shows the recorded ruby luminescence spectra in the relevant wavelength range around the R_1 peak at selected temperatures.

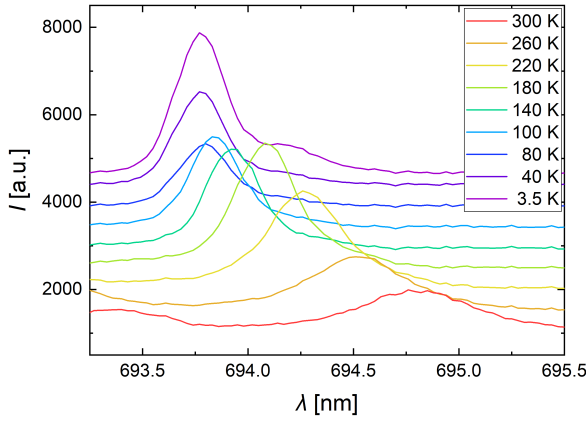


Figure 6.33: Ruby luminescence spectra measured at selected temperatures for the temperature-dependent calibration measurements. The spectra are shifted against the 300 K spectrum for better visibility.

The shift in the R_1 peak to lower wavelengths with decreasing temperature is clearly visible. While the observed behavior of the peak intensity is not intrinsic as it is dominated by the influence of the manual adjustments for the measurements, the change in the peak shape with a narrowing at low temperatures follows the reported behavior [201]. The wavelengths of the peak position extracted from the spectra for the two measurement runs are shown in Figure 6.34.

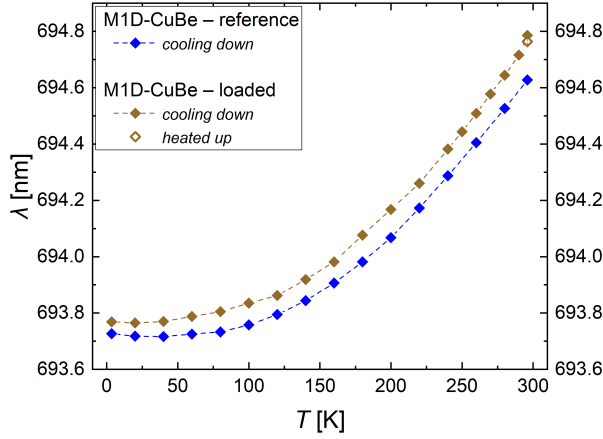


Figure 6.34: The measured ruby luminescence wavelength as function of temperature using an M1D-CuBe clamp cell for runs with applied pressure (loaded) and without applied pressure (reference).

The curves show a similar behavior with a smooth decrease with temperature, levelling out at temperatures below about 50 K. Based on the difference $\Delta\lambda$ between these two curves at each given temperature, the pressure p is calculated using the published ruby luminescence pressure scale [151] with

$$p \text{ [GPa]} = 1.87(\pm 0.01) \cdot 10^3 \left(\frac{\Delta\lambda}{\lambda_0} \right) \cdot \left[1 + 5.63(\pm 0.03) \left(\frac{\Delta\lambda}{\lambda_0} \right) \right],$$

where λ_0 is the respective reference wavelength at that temperature. The resulting pressure values are given in Figure 6.35. The indicated standard deviation is not directly from the measurements, but taken as representative from later measurements of the ruby pressure.

The pressure measured at room temperature is with 0.44 GPa remarkably close to the theoretically expected value. With decreasing temperature, the pressure decreases as expected. The thermal contraction of the liquid pressure medium outweighs that of the solid cell material, resulting in the net reduction of pressure. The pressure drop is quite significant with about 75%, although it has to be kept in mind that this only reflects the pressure at the ruby position, and does not necessarily reflect the pressure at the sample position; to determine the latter, a cross-calibration using neutron radiation is needed. The same holds for the relative pressure behavior with temperature at the two positions, and without a temperature-dependent cross-calibration, it cannot be assumed that the relative pressure drop is the same. The loss of pressure is partially reversible and reaches 84% of the initial value after heating up back to room temperature.

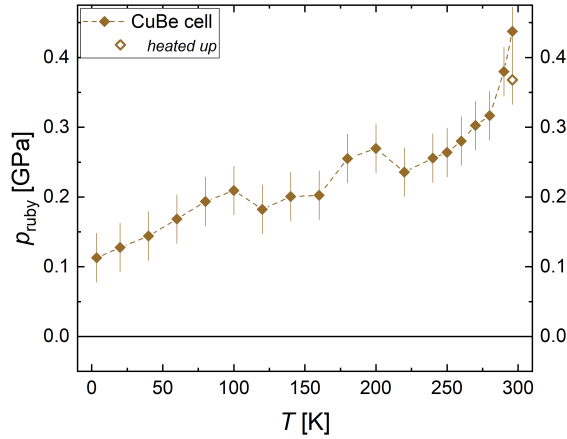


Figure 6.35: The pressure calculated from the shift in ruby luminescence as function of temperature for the measurement with applied pressure in an M1D-CuBe clamp cell.

The presented measurement of the temperature-dependent ruby luminescence (Figure 6.34) also reveals directly a practical issue of this method in that at temperatures below about 50...100 K, the pressure determination gets less precise. Since this is an inherent property of the employed material (ruby), only the use of alternative materials with better temperature-dependent luminescence properties can improve upon this. While such materials are actively researched (see Chapter 4.4), there are currently none for which a low-temperature calibration is available. Unlike the ruby luminescence method, the pressure determination based on NaCl *via* neutron radiation goes reliably down to lowest temperatures, and thus allows a precise pressure determination using clamp cells.

6.3.5.3 Calibration of Pressure as Function of Load Force

For the practical use of the clamp cells, the dependence of the effective pressure inside of the cell on the applied force load has to be known. This is necessary to adjust the pressure to the value targeted for the experiment. Using the ruby luminescence option for the pressure determination, calibration tests with the various clamp cells were performed. For both cell variants (M1D-CuBe and M1D-NiCrAl), tests with all three capsule materials (AlMg5, Pb, PTFE) were performed.

Since the temperature-dependence was not investigated, the measurements could be performed in-house without a cryostat.

The tests were conducted using sample capsules filled only with a 1:1 FC-70:FC-770 Fluorinert mixture as pressure-transmitting medium. The load force F_{load} was applied using a hydraulic laboratory press, and the theoretical pressure applied to the capsule calculated as

$$p_{\text{theo}} = \frac{F_{\text{load}}}{A},$$

with A the contact area between piston and capsule. With regard to the earlier mentioned discrepancy between measured and calculated pressure in the calibration measurements with NaCl (Chapter 6.3.1), the contact area was calculated in two ways: the maximum contact area $A_{\text{max}} = \pi r_i^2$ based on the full inner radius r_i (2.5 mm), and the direct contact area $A_{\text{dir}} = A_{\text{max}} - A_{\text{ring}} = \pi(r_i - w_{\text{ring}})^2$ taking into account the width w_{ring} (0.5 mm) of the anti-extrusion ring between piston and capsule. The force limits were calculated assuming a yield strength of 1.1 GPa and 1.5 GPa for CuBe and NiCrAl, respectively⁵. After each force step, the pressure p_{ruby} acting on the ruby was determined using the same pressure calibration as mentioned before, with the reference wavelength λ_0 being determined independently for every measurement run.

Figure 6.36 shows an overview of all test runs, details are given in Appendix B. The capsules made from lead proved to be too easily deformed – the maximum compression given by the cell geometry was reached before a load force of 2 kN was applied – and are thus not considered here. The AlMg5 capsules were used with turned-off plugs and PTFE disks inserted between the plug and the bottom piston to transmit the pressure to the ruby mounted on the diamond.

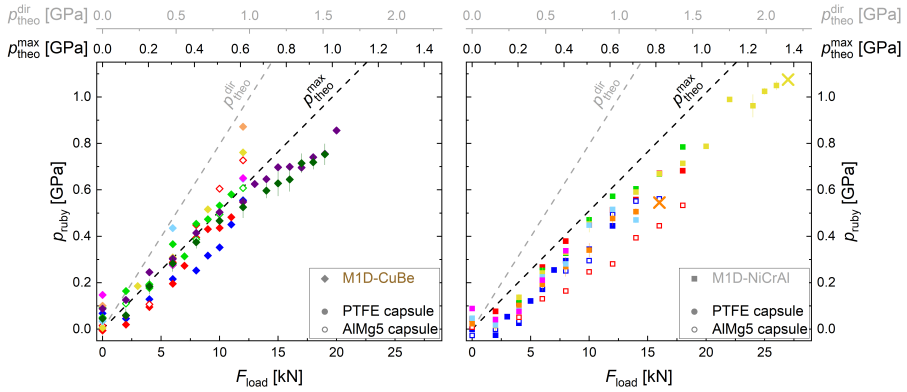


Figure 6.36: The pressure calculated from the shift of the ruby luminescence as function of applied force load for the calibration tests with the M1D-CuBe (*left*) and the M1D-NiCrAl (*right*). The colors represent different runs (see Appendix B for details), the crosses indicate that the used clamp cell broke. The black (gray) dashed lines mark the equivalence of p_{ruby} and $p_{\text{theo}}^{\text{max}}$ ($p_{\text{theo}}^{\text{dir}}$), see discussion below.

The comparison of the various test runs among each other shows that, in general, the pressure as function of the load force follows a linear trend. However, the pressure spread for a given load force can be considerable. While distinct features are observed in individual runs, the overview shows that all combinations of cell

⁵In practice, the force limit corresponded to the highest ‘safe’ pressure-scale unit on the press.

material and capsule material exhibit approximately the same trend, with no clear indication of any particular material effect.

Comparing the measured pressures p_{ruby} to the expected pressures p_{theo} shows that the pressure calculated assuming the maximum contact area, $p_{\text{theo}}(A_{\text{max}}) = p_{\text{theo}}^{\text{max}}$, fits significantly better (Figure 6.36, black line), and poses a rather good upper limit for the ruby pressure. While some outliers lie above that line, the pressure calculated assuming only the direct contact area, $p_{\text{theo}}(A_{\text{dir}}) = p_{\text{theo}}^{\text{dir}}$, poses a general upper limit⁶ (Figure 6.36, gray line). This indicates that, in general, the maximum contact area is a valid assumption, but that in individual cases load-specific factors can cause the reduction of the effective contact area. Such a factor might be the canting of an anti-extrusion ring, but this cannot be experimentally assessed in the scope of this work.

Of further particular interest is the fact that while for the calibration measurements using ruby luminescence $p_{\text{theo}}(A_{\text{max}})$ is a good fit, the calibration measurements using NaCl are in significantly better agreement with $p_{\text{theo}}(A_{\text{dir}})$. This difference in measured pressure is caused by the different positions at which the pressure probes are located – the ruby between plug and diamond, and the NaCl within the pressure-transmitting medium at the actual sample position. Hence, to correlate the pressures determined from the ruby luminescence option during loading with the target pressures at the sample position, a cross-calibration for the two methods is needed. For this, the availability of sufficient neutron beam time is a basic requirement, and it was thus not possible in the present work.

Aside from providing a first approximate calibration, the calibration measurements using the ruby luminescence option give valuable insights into practical issues related to the operation of the clamp cells:

- First, the significant scattering of the pressure values is at least partially not inherent to the system but caused by the operator. The loading of the capsule into the cell, the application of force and in particular the tightening of the clamping nuts are affected by various factors, some of which are hard or even virtually impossible to control. To improve the consistency of the test measurement and eventually the clamp cell operation as a whole, it is thus recommended that only a single operator is responsible for the use of the cells. This, in combination with following some strict procedure should reduce the inconsistencies between measurement and result in a better calibration of the M1D.
- Second, the reference wavelength of the ruby luminescence at ambient conditions has to be determined separately for each run, and the pressure cannot be assumed as homogeneous across the ruby. To estimate the uncertainty of the pressure determination, the luminescence wavelength has to be measured at different points on the ruby. Although not done systematically in the present work, the error shown in Figure 6.36 for one run (full diamond symbol in dark green) determined from five points is taken as representative.

⁶Some of the measured pressures at a force load of 0 kN exceed this line, but without any applied force this is attributed to other operational issues.

- Third, from a purely practical point of view, the capsules made from PTFE are significantly better to use than the ones made from AlMg5. Due to their deformability, they are easier to fit into the cells in the first place. The use of a PTFE capsule also eliminates the need for the combination of a turned-off AlMg5 plug with a PTFE disk. Removing the capsule from the cell after use is also markedly simpler, as the AlMg5 capsules are typically stuck due to the material's plastic deformation. After high loads, a removal of the capsule by pressing can prove to be impossible, and the capsule has to be drilled out instead. Both the pressing out and the drilling of a tightly stuck capsule can potentially damage the cell, and should thus be avoided. In addition, drilling out the capsule would inevitably destroy a contained sample, which might be a problem for actual experiments. Aside from these disadvantages of AlMg5 as capsule material, PTFE has the advantage that for the given wall strength, it is actually semitransparent, which allows to see whether the capsule is filled completely with pressure-transmitting medium or whether any bubbles are present.
- Fourth, in addition to the determination of load/pressure calibration curves, the tests were performed to determine the experimental limits for the applied force, i.e. whether the cells can withstand the theoretical force limits and if not, at which force loads they break. In order to validate the load limits, tests were not only performed with the M1D cells, but also with M1 cells; while those do not allow ruby luminescence measurements, it can still be assessed at which force load the cell breaks.

In case of the CuBe clamp cells, both the M1D-CuBe and the M1-CuBe reached the theoretical load limit of 20 kN, corresponding to a theoretical pressure of about $p_{\text{theo}}^{\text{max}} = 1.02 \text{ GPa}$ ($p_{\text{theo}}^{\text{dir}} = 1.59 \text{ GPa}$) without any indication of failure or plastic deformation, thus confirming the assumed yield strength.

For the NiCrAl clamp cells, four different cells were available: the two types M1D-NiCrAl and M1-NiCrAl, manufactured by two different workshops each, but using material from the exact same batch. In contrast to the CuBe cells, all four tested NiCrAl cells broke before reaching the theoretically safe limit. The two M1D-NiCrAl broke at 27 kN ($p_{\text{theo}}^{\text{max}} = 1.38 \text{ GPa}$, $p_{\text{theo}}^{\text{dir}} = 2.15 \text{ GPa}$) and at 16 kN ($p_{\text{theo}}^{\text{max}} = 0.81 \text{ GPa}$, $p_{\text{theo}}^{\text{dir}} = 1.27 \text{ GPa}$), respectively. One M1-NiCrAl started to show cracks at 18 kN, though it was still able to reach 22 kN before breaking completely, while the second M1-NiCrAl showed first cracks at 14 kN and was unable to hold pressure at 15 kN.

The investigation of the broken NiCrAl cells shows that the cell broke due to changes in the material originating from the machining process of the cells. In particular, the drilling of the central bore evidently causes brittleness due to work hardening, and could in addition lead to geometrical weak points due to non-ideal alignment of the bores⁷. The fact that the cells broke at vastly different force loads indicates that the influence of the machining – or, in general, the reason for breaking – is rather individual for the cells. This is supported by the observation that the process of breaking is not the same for

⁷The central bore is machined by drilling from both sides of the cell since the bore is too long for one drilling

all cells, ranging from a very sudden break to a slow increase in visible cracks while still being able to go to higher loads.

Hence, based on the present tests, the actual maximum pressures that can be reached in the NiCrAl cells cannot be assessed. For this, a measurement of the sample pressure *via* NaCl calibration and optimized machining of the cells is necessary. With regard to the machining, it would be advantageous to machine the bore by spark erosion instead of drilling, both avoiding the work hardening of the material surface and the alignment problem of the drilling.

Furthermore and in general, it should be kept in mind that the present measurements only characterize the pressure as determined from the ruby. The actual pressure inside of the capsule to which the sample is subjected has to be calibrated against this ruby pressure in another step to allow a loading of the cell to the real target pressure. However, this second calibration would require test measurements with neutron radiation and is out of scope of this work.

Ultimately, while the ruby luminescence option has not yet yielded a reliable calibration method for the clamp cell operation and further improvements and developments are clearly necessary, even the present calibration is still a significant advancement. In the common clamp cells without the ruby luminescence, the experimental pressure has to be set purely based on experience and/or calculations. The ruby luminescence option offers the possibility to verify that at least a certain pressure has been applied within the cell.

6.3.5.4 Transmission Loss Correction for the Clamp Cells

As discussed in Chapter 4.3.4, the neutron transmission is an important property that has to be taken into account for the choice of the clamp cell material. While a high transmission is targeted for the cell, even the best suited materials will lead to some transmission losses; for a solid material with the necessary mechanical properties, this is inevitable.

When using a clamp cell in an experiment, the transmission losses affect signals depending on the length of their beam path through the material, leading to a systematic error in the detected intensities. Hence, for the analysis of the obtained data, a correction is necessary. A first, analytical correction that is based on a simple geometrical model is presented here. While more sophisticated correction models are possible, e.g. numerically based on Monte Carlo simulations, these are out of the scope of this work.

For the simple geometric model, three assumptions are made: first, the interaction of the neutron beam with the sample takes place in one point (the center of the sample) to avoid complicating the calculations. Second, all beam paths pass solely through the cylindrical center part of the clamp cell, outside of which the cell geometry gets significantly more complicated. This assumption can be assured simply by defining suitable limits for the applicability of the model. Third, the cell is kept upright, with the incoming beam perpendicular to the cell axis. This again is done to keep the calculations simple, but also reflects the typical setup of the clamp

cell in a cryostat, where the cell position remains fixed in the vertical axis⁸.

Figure 6.37 shows the relevant part of a clamp cell, using the M1 design as example. The *incoming beam* passes through the wall of the cell, where the path length is at its minimum. In the *primary beam* direction, the beam passes again through the wall with a minimal beam path. The path of a *scattered beam*, however, is changed by an angle α in relation to the primary beam.

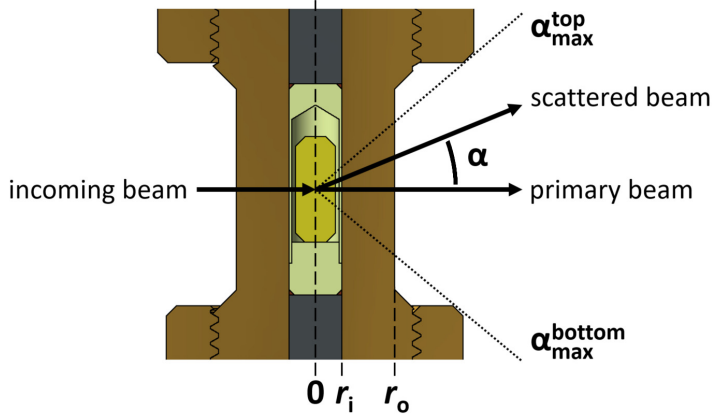


Figure 6.37: Illustration of the geometrical model for the absorption correction in a monobloc clamp cell.

To justify the second assumption that only the cylindrical part of the cell is taken into account, the angular limits of the present model are determined from the cell geometry: Considering a fully closed cell, there are the limiting angles $\alpha_{\max}^{\text{bottom}}$ and $\alpha_{\max}^{\text{top}}$, outside of which the scattered beam would pass not only through the cylindrical part of the cell, but also through the nuts. For the shown M1 cell, both limits are at about 40° .

Figure 6.38 shows a detailed view of the beam paths relevant for the calculation of the absorption correction.

⁸Turning the cell around its axis – coinciding with the instrument φ -axis – is neglected as the cell has cylindrical symmetry in the considered part.

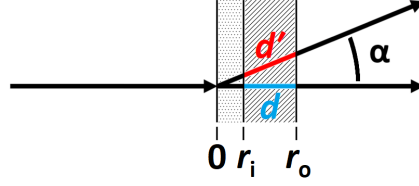


Figure 6.38: The beam paths of the neutron beam through the wall of a monobloc clamp cell.

The path length of the primary beam within the wall d is shown in blue, the path length of the scattered beam within the wall d' in red. Based on the cell dimensions, it is

$$d = r_o - r_i \quad \text{and} \quad d' = (r_o - r_i) \cdot \frac{1}{\cos \alpha},$$

with inner and outer radius of the clamp cell r_i and r_o , respectively. The transmission τ is defined as

$$\tau = \exp \left(-\frac{l}{p(\lambda)} \right),$$

where l is the length within the considered material and $p(\lambda)$ the penetration depth. $p(\lambda)$ is dependent on the material and a function of the neutron wavelength λ for which the transmission loss is calculated; it is defined as the length after which the beam intensity has been reduced to $e^{-1} \approx 36.8\%$. In the present model, transmission losses from absorption of the neutron beam as well as from incoherent scattering are considered. The transmission loss from coherent scattering is not considered, as it depends on the cell-specific orientation of the material, which cannot be generalized. While transmission loss occurs for the incoming beam as well as for the primary and scattered beam, the absolute transmission loss is not relevant for the correction. Hence, the incoming beam can be ignored as it is the same for all beam paths. Furthermore, on the outgoing side, only the change in transmission loss due to the increased path length within the wall has to be considered. Since the primary beam is the path with the minimal transmission loss, the angle-dependent transmission loss is normalized to that value for the correction. Following this, one can define the transmission loss correction factor f_τ :

$$f_\tau = \frac{\tau(d')}{\tau(d)} = \frac{\exp \left(-\frac{d'}{p} \right)}{\exp \left(-\frac{d}{p} \right)} = \exp \left(\frac{d - d'}{p} \right) = \exp \left[\frac{r_o - r_i}{p} \cdot \left(1 - \frac{1}{\cos \alpha} \right) \right].$$

This correction factor is dependent on the cell geometry *via* r_o and r_i , on the cell material and neutron wavelength *via* $p = p(\lambda)$, and on the angle α . To apply the correction factor, the measured intensities are simply divided by the according factor for each reflection:

$$I_{\text{corr}}(\alpha) = \frac{I_{\text{exp}}}{f_{\tau}(\alpha)},$$

where I_{exp} is the experimentally measured intensity and I_{corr} the corrected one. Figure 6.39 gives the calculated values for f_{τ} within the angular range limited by the cell geometry to 40° for the three materials used in the monobloc clamp cells involved in this work⁹. To show the effect of the neutron wavelength, f_{τ} is calculated for $\lambda = 0.9 \text{ \AA}$ (hot neutrons, e.g. at POLI) and $\lambda = 4.05 \text{ \AA}$ (cold neutrons, e.g. at MIRA).

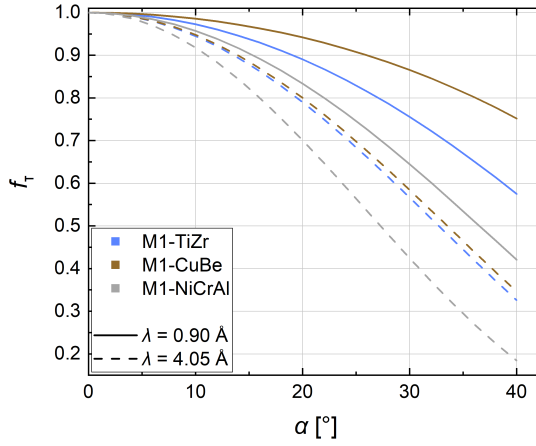


Figure 6.39: Transmission loss correction factor f_{τ} as function of angle α for M1/M1D versions made from the three principal materials (TiZr, CuBe, NiCrAl), calculated for two different wavelengths.¹⁰

In general, the transmission losses are lowest for the CuBe and highest for the NiCrAl, with the TiZr lying in between, and are higher for the longer wavelength¹¹. While the losses at small angles might be negligible (at most 3% up to 5°), for larger angles the transmission losses become significant, reaching values of up to 80% (corresponding to $f_{\tau} = 0.2$) in the case of NiCrAl at $\lambda = 4.05 \text{ \AA}$. In practice, however, the angular range is usually limited by the instrument to values below the 40° considered here based on the cell geometry, e.g. to a maximum of 30° on POLI as the upper limit of the lifting single counter detector. Nonetheless, even within the instrument limits the transmission loss can be substantial and lead to significant errors in the measured intensities. Since the correction is easy to apply

⁹CuBe and NiCrAl were used for the monobloc clamp cells designed for this work, and a TiZr monobloc clamp cell was used in neutron diffraction experiments at ILL (see Chapter 5.3.3.2).

¹⁰The seemingly parabolic shape of the curves, in particular considering $\lambda = 0.90 \text{ \AA}$, is a result of the angular limitation of the figure; all curves have an inflection point and asymptotically approach the x -axis as it follows from the corresponding formula.

¹¹If coherent scattering is taken into account, the transmission losses for CuBe and NiCrAl will increase, while TiZr will be unaffected and exhibit the lowest losses.

and the considered angle α is usually accessible in the measured data in a convenient form for all reflections, it is recommended to generally apply the transmission loss correction to improve the data quality when a clamp cell is used.

So far, the transmission loss correction was based on a monobloc clamp cell, but the principle can be adapted easily to be valid for fretted ones. As shown in Figure 6.40, the scattered beam passes through both layers of the wall, each with a material-dependent penetration depth $p(\lambda)$.

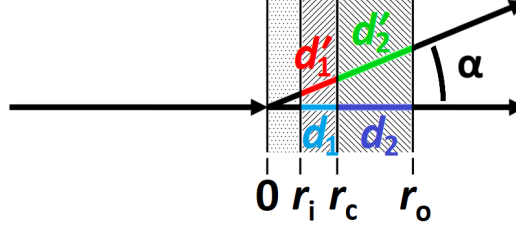


Figure 6.40: The beam paths of the neutron beam through the wall layers of a fretted cell.

The transmission loss is then calculated by treating each layer of the fretted cell like an independent monobloc clamp cell and multiplying the individual contributions for the overall transmission loss:

$$\begin{aligned}
 f_{\tau} &= \frac{\tau(d'_1)}{\tau(d_1)} \cdot \frac{\tau(d'_2)}{\tau(d_2)} = \frac{\exp\left(-\frac{d'_1}{p_1}\right)}{\exp\left(-\frac{d_1}{p_1}\right)} \cdot \frac{\exp\left(-\frac{d'_2}{p_2}\right)}{\exp\left(-\frac{d_2}{p_2}\right)} = \exp\left(\frac{d_1 - d'_1}{p_1}\right) \cdot \exp\left(\frac{d_2 - d'_2}{p_2}\right) \\
 &= \exp\left[\left(\frac{r_c - r_i}{p_1} + \frac{r_o - r_c}{p_2}\right) \cdot \left(1 - \frac{1}{\cos \alpha}\right)\right].
 \end{aligned}$$

For the clamp cell type F1, the different material combinations result in transmission losses shown in Figure 6.41. The losses are larger due to the contribution of the more strongly neutron-attenuating NiCrAl in both variants, but also due to the larger diameter compared to the monobloc cells (22 mm and 15 mm, respectively). As a consequence, a general transmission loss correction is even more important for the fretted cells than for the monobloc cells.

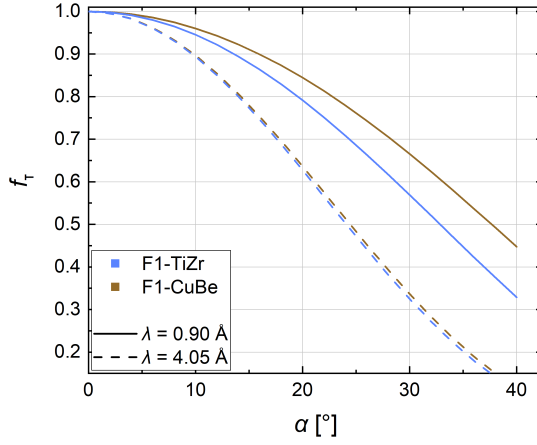


Figure 6.41: Transmission loss correction factor f_τ as function of angle α for the two material combinations used in the clamp cell body of the fretted F1 cell design, calculated for two different wavelengths.

Following the adaption of the transmission loss calculation to the fretted cell design, a generalization of this concept for any cylindrical clamp cell with n layers yields accordingly

$$f_\tau = \prod_{i=1}^n \frac{\tau(d'_i)}{\tau(d_i)} = \exp \left[\left(1 - \frac{1}{\cos \alpha} \right) \cdot \sum_{i=1}^n \frac{r_i - r_{i-1}}{p_i} \right],$$

where r_{i-1} and r_i are the inner and outer radius of the i th layer, respectively, and p_i its penetration depth. This formula is not restricted to the clamp cell itself; the pressure-transmitting medium and the capsule could be treated just as easily as additional layers to account for their neutron attenuation.

One factor that is not considered in the description of the fretted cell so far is the potential conical angle φ of the contact surface, which will be present if the cell is manufactured by press fitting. In order to keep this geometrical model simple, it is assumed that the point of interaction between the neutron beam and the sample is at the height where the ideal wall ratio with $r_c = \sqrt{r_i \cdot r_o}$ is assumed; this is justified as the fretted cell is designed precisely in that way. Figure 6.42 shows the corresponding schematic view of the fretted cell with the respective primary and scattered path lengths d and d' , respectively.

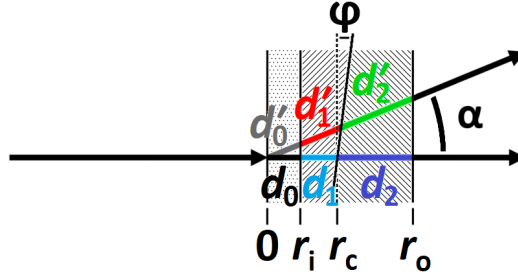


Figure 6.42: The beam paths of the neutron beam through the wall layers of a fretted cell with a conical angle φ on the contact surface.

For the calculation of the transmission loss, the same principle as in the previous cases is applied, with the only difference being the calculation of the scattered path lengths. The scattered path lengths can be calculated iteratively starting from the center of the cell:

$$d'_0 = d_0 \cdot \frac{1}{\cos \alpha},$$

with $d_0 = r_i$. The calculation of d'_1 is based on the triangle with arms $(d_0 + d_1)$ and $(d'_0 + d'_1)$ enclosing angle α , in which the law of sines is applied. This yields

$$d'_1 = (d_0 + d_1) \cdot \frac{\cos \varphi}{\cos(\alpha + \varphi)} - d'_0.$$

For a vanishing conical angle $\varphi = 0$, this formula leads indeed to the previously established formula for the simple cylindrical fretted cell. In the same manner, based on the extended triangle with arms $(d_0 + d_1 + d_2)$ and $(d'_0 + d'_1 + d'_2)$, d'_2 is calculated as

$$d'_2 = (d_0 + d_1 + d_2) \cdot \frac{1}{\cos \alpha} - (d'_0 + d'_1).$$

With these scattered path lengths, the transmission loss factor is calculated exactly as before as

$$f_\tau = \frac{\tau(d'_1)}{\tau(d_1)} \cdot \frac{\tau(d'_2)}{\tau(d_2)} = \frac{\exp\left(-\frac{d'_1}{p_1}\right)}{\exp\left(-\frac{d_1}{p_1}\right)} \cdot \frac{\exp\left(-\frac{d'_2}{p_2}\right)}{\exp\left(-\frac{d_2}{p_2}\right)} = \exp\left(\frac{d_1 - d'_1}{p_1}\right) \cdot \exp\left(\frac{d_2 - d'_2}{p_2}\right).$$

Since the derivation of the scattered path lengths does not assume the conical angle to be positive, the derived terms are valid also for negative conical angles – this corresponds to a conical inner cylinder that is pressed in from the opposite end of the

cell. A negative conical angle can also be used to calculate the effect for scattering angles that go below the scattering plane, with $f_\tau(\varphi, -\alpha) = f_\tau(-\varphi, \alpha)$. The effect of the conical angle φ on the transmission loss factor is shown in Figure 6.43 as ratio $f_\tau(\varphi)/f_\tau$ as function of scattering angle α , with $f_\tau = f_\tau(\varphi = 0^\circ)$. The calculation is based on an F1-CuBe fretted clamp cell (NiCrAl inner cylinder and CuBe outer cylinder) at a neutron wavelength of $\lambda = 4.05 \text{ \AA}$, since the influence of φ is largest for this combination.

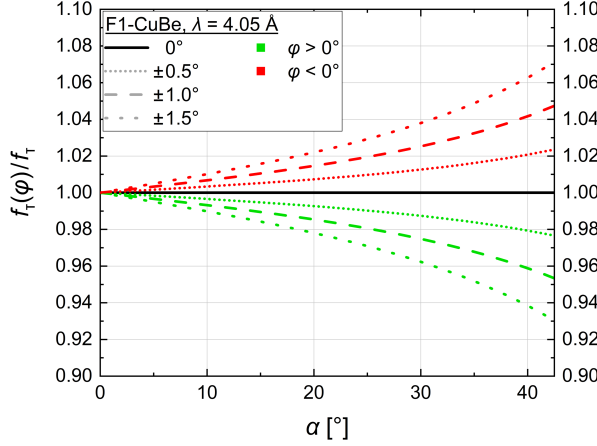


Figure 6.43: Effect of the conical angle φ on the transmission loss factor f_τ as function of scattering angle α for an F1-CuBe clamp cell at a neutron wavelength of $\lambda = 4.05 \text{ \AA}$.

The general trend of increasing f_τ for $\varphi < 0^\circ$ reflects the fact that in case of the F1-CuBe the material of the outer cylinder has a higher neutron transmission than the one of the inner cylinder, and *vice versa* for $\varphi > 0^\circ$. For the actual F1 cell design, the conical angle is 1° , for which – regardless of pressing direction – the change in the transmission loss factor reaches about 4% at the maximum scattering angle of 40° . The influence of the conical angle is for values this small approximately linear, with losses of about 2% and 6% at 40° for $\varphi = 0.5^\circ$ and $\varphi = 1.5^\circ$, respectively. Although the effect of the conical angle is quite small, in particular in the experimentally relevant range of scattering angles, and might in practice be even negligible in many cases, it can be applied easily and should thus also be taken into account.

For the sake of completeness, in the hypothetical case of a fretted cell with n layers, where the i th layer has an outer conical angle φ_i (between the i th and the $(i + 1)$ st layer), the scattered path length is iteratively described by

$$d'_m = \left(\sum_{i=0}^m d_i \right) \cdot \frac{\cos \varphi_m}{\cos(\alpha + \varphi_m)} - \sum_{i=0}^{m-1} d'_i, \quad m \leq n.$$

Chapter 7

Data Processing

7.1 Integration and Indexing

7.1.1 Synchrotron and Laboratory X-ray Single-Crystal Data

To prepare the single-crystal data obtained with synchrotron X-ray radiation for analysis, the frames were converted into the Esperanto format for further treatment using the *CrysAlisPRO* software (v171.40.53; Rigaku Oxford Diffraction, 2019). For this, instrument parameters, i.e. detector distance and position of the primary beam, obtained from calibration measurements performed beforehand were applied. Subsequently, using the same program, the data were indexed and the orientation matrix was determined; this included the refinement of goniometer and detector parameters. In the process of indexing, twinning was taken into account with one additional twin individual above the phase transition, and two additional twin individuals below (see Chapter 8.2.4). The twin components are related to each other by a three-fold rotation around the a -axis. For the following integration of the frames on the basis of the indexing and considering the twinning, parts of the frames were masked to account for the shadow of equipment (beam stop, sample holder, cryostat nozzle) and the reduced background intensity in these regions. An example for a raw frame and the respective masking used in the integration is shown in Figure 7.1.

The integration of the frames was carried out in suitable batches determined by the angular positions of the detector and the scan angle, i.e. φ -scans with the detector at 0° and 45° and ω -scans where integrated separately.

The single-crystal data obtained with laboratory X-ray radiation were treated in the same way, with the exception that the initial conversion was not necessary.

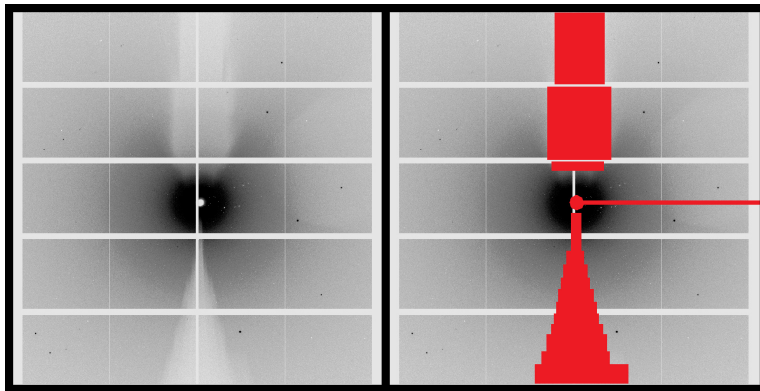


Figure 7.1: Example frame of the synchrotron X-ray single-crystal diffraction measurement at 275 K in the raw state (*left*) and with the mask applied during the integration routine (*right*). The horizontal and vertical lines stem from the used detector.

In the processing of the high-pressure single-crystal data, two additional effects had to be taken into account: the opening angle of the pressure cell and the presence of diamond reflections, shown for an exemplary frame in Figure 7.2. The opening angle of the respectively used pressure cell was considered in the integration process by dynamic masking, rejecting individually parts on each frame which were shadowed by the cell. Diamond reflections were not rejected during the integration procedure, but were identified and removed at a later stage in the refinement process using the manual culling options implemented in *Jana2006* [202].

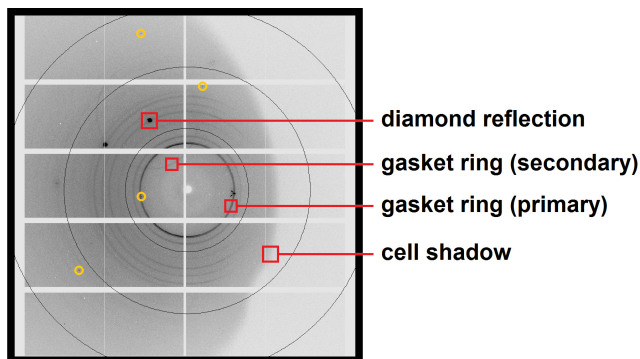


Figure 7.2: Example frame of the synchrotron X-ray single-crystal diffraction measurement in a diamond anvil cell. The yellow circles mark sample reflection for comparison. The horizontal and vertical lines stem from the used detector.

7.1.2 Neutron Single-Crystal Data

In case of the neutron single-crystal diffraction experiments conducted at D9 (ILL), the integration of the data was done directly at the beamline. The performed ω -scans consist of 31 single frames centered around the set value for ω ; Figure 7.3, *left*, shows an exemplary frame with the neutron count for each of the 32×32 detector pixels. The integrated intensity of each such frame is then taken as function of ω , yielding an intensity curve as shown in Figure 7.3, *right*.

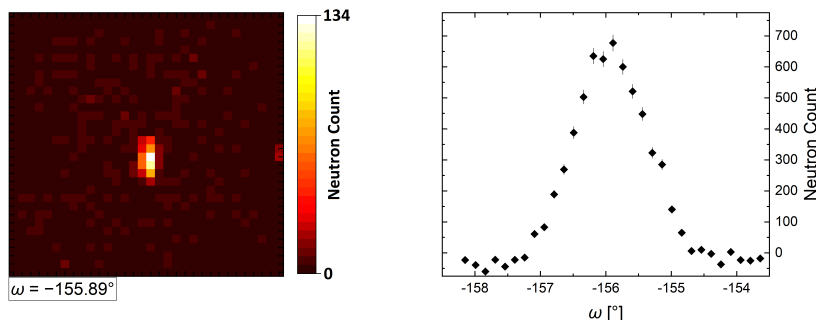


Figure 7.3: Example single frame of the neutron single-crystal diffraction measurement at 2 K and nominally 0.17 GPa (*left*) and the according full ω -scan of the peak (*right*).

The so obtained ω -scans were then integrated using the method described by Wilkinson *et al.* [203], resulting in the integrated intensity for that particular reflection. The indexation of the reflections is based on the (refined) orientation matrix used to determine the measurement positions in the first place.

The magnetic reflections were measured on the basis of a magnetic propagation vector of $\mathbf{k} = (0, 0, 0.35)$ in approximation of $\mathbf{k} = (0, 0, 0.353(2))$ established in previous, unpublished experiments [204]; since magnetic reflections were immediately found based on the assumption of this value for the propagation vector, it was not further refined. The so measured magnetic reflections were integrated in the same way as the nuclear ones.

7.2 Refinement

7.2.1 X-ray Single-Crystal Data

The integrated data obtained from *CrysAlisPRO* were subsequently refined using the program *Jana2006* [205]. Based on the observed extinction rules, the refinements were carried out in space group *Pnma* (see also Chapter 8.2.4). The structural model for the refinement was determined using the *Superflip* software [206] incorporated in *Jana2006*. In the refinements, the free atom coordinates, the anisotropic atomic displacement parameters (ADP), an isotropic extinction coefficient G_{iso} , and the twin volume fractions *twvol2* and *twvol3* were refined corresponding to the twin

individuals defined by the matrices given in Chapter 8.2.4. Details of the refinements are given in Appendix C.

7.2.2 Neutron Single-Crystal Data

In a first step, the list of integrated intensities of the nuclear reflections was subjected to the intensity correction for the transmission loss due to the used clamp cell following the procedure described in Chapter 6.3.5.4. The so corrected intensities were then used as basis for the refinement of the nuclear structure with *Jana2006*. The refinement was carried out in space group *Pnma* in accordance with the literature and our previous findings. Refined parameters were the free atom coordinates, the anisotropic ADP, an isotropic extinction coefficient G_{iso} , and the twin volume fractions *twvol2* and *twvol3* described by the twin matrices given in Chapter 8.2.4. Details of the refinements are given in Appendix C.

The intensity of the magnetic reflections was corrected for the transmission losses in the same way as the nuclear reflections. On the basis of the refined nuclear structure and the propagation vector $\mathbf{k} = (0, 0, 0.35)$, the magnetic models corresponding to different magnetic superspace groups were derived using the built-in algorithms of *Jana2006* [97]. To determine the magnetic structure, the data were refined in all magnetic superspace groups allowed by the nuclear space groups *Pnma*, as well as all the *translationengleiche* subgroups of *Pnma* down to *P1* (see Figure 7.4). For the refinement of the magnetic structure, the nuclear structure was fixed to the values obtained from the nuclear refinement, and the symmetry restrictions posed by *Pnma* were applied also in the cases with formally lower symmetry. In all the tested magnetic superspace groups, the atoms were treated anisotropically. The twin volume fractions (*twvol2* and *twvol3*) and the magnetic modulation amplitudes not restricted by the symmetry were refined (see Table 8.2 in the following chapter). In cases where the lower symmetry leads to a splitting of the atom positions, the harmonic ADP were restricted to follow the higher symmetry with the help of local symmetry operations. For those structures where multiple Cr positions are present, the magnetic modulation amplitudes were in general not restricted, the only exception being the model which corresponds to the double-helical structure reported in the literature. Details of the refinements are given in Appendix C.

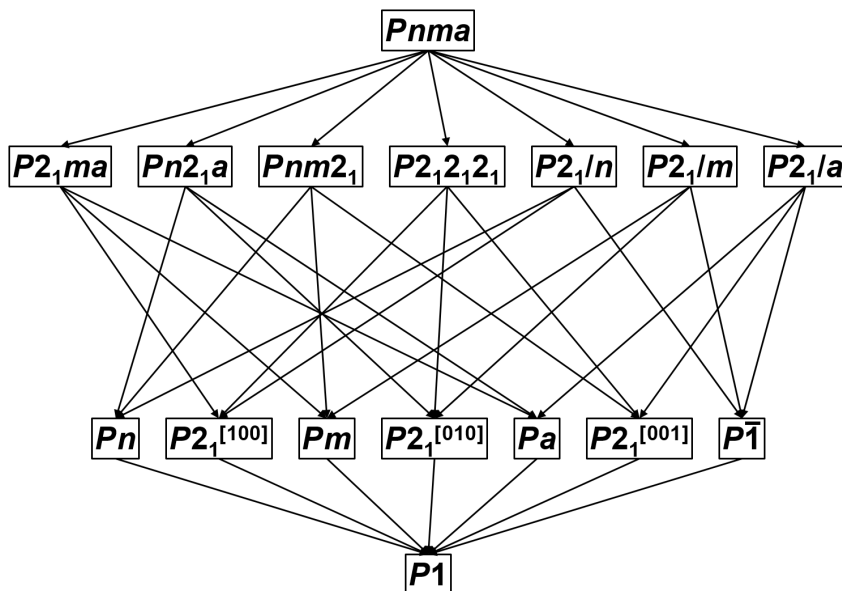


Figure 7.4: Derivation of maximal subgroups from space group $Pnma$. The superscripts $[100]$, $[010]$ and $[001]$ do not belong to the formal space group symbol, but indicate the direction in which the two-fold screw axis of the respective space group $P2_1$ is oriented in order to allow differentiation.

7.2.3 Neutron Powder Data

The neutron powder data obtained from the experiments at HRPT were refined using *Jana2006* in three steps.

In the first step, a Le Bail fit [207] of the powder pattern was made in which the positions of the magnetic reflections were described only by an incommensurate propagation vector of the form $(0, 0, k_c)$. In this Le Bail fit, the lattice parameters a , b , and c , the γ -component of the propagation vector \mathbf{k} , the peak-shape parameters GW and LY , the shift parameter *shift* and the strain tensor parameters $St1022$ and $St0022$ were refined [208, 209]. The background was refined with about 30 manually set points and 5 refined Legendre polynomial terms. As the data showed elemental chromium (space group $Im\bar{3}m$) to be present (see Chapter 5.1.1), this was taken into account as a second phase, with the lattice parameter a_{Cr} being refined. For the Le Bail fit and all subsequent refinements, the correction according to Bérar [210] was applied to the calculated estimated standard uncertainties.

In the second step, the nuclear structure was determined by the Rietveld method [211], for which the magnetic reflections were masked where possible. The lattice parameters a , b and c , the free atom coordinates, the isotropic ADP, the peak-shape parameters GW and LY , and the zero *shift* were refined. The background was described by refining 5 Legendre polynomial background parameters in addition to about 30 manually set points. The refinement was carried out in space group $Pnma$ in accordance with our single crystal data. Chromium was again taken into account

as a second phase, and in addition to the lattice parameter a_{Cr} the phase volume fraction *phvol2* was refined. At higher temperatures, the data showed additionally the presence of CrAs in the paramagnetic high-temperature phase, which was taken into account by refining its lattice parameters $a_{\text{CrAs}}^{\text{HT}}$, $b_{\text{CrAs}}^{\text{HT}}$ and $c_{\text{CrAs}}^{\text{HT}}$, and a corresponding phase volume fraction *phvol3*.

In the third step, the refined nuclear structure, in combination with the deduced propagation vector, was taken as basis for the subsequent derivation of the magnetic superspace groups¹ using the built-in algorithms from *Jana2006* [97]. Refinements of the magnetic structure were carried out in all derived superspace groups. As the fit of the magnetic reflections using the magnetic superspace models derived from the *Pnma* of the nuclear structure did not lead to a satisfactory agreement, it was necessary to test also lower symmetries. For this, the space group in which the nuclear refinement was carried out was artificially reduced to lower-symmetrical space groups. However, in all the lower-symmetrical descriptions, the higher *Pnma* symmetry was retained by fixing the respective atomic coordinates using local symmetry operations. For the refinements of the magnetic structures in all considered magnetic superspace groups, all parameters corresponding to the nuclear structure were fixed and not refined. The refined parameters were in all cases the magnetic modulation amplitudes and 5 background parameters. For those structures where multiple Cr positions are present, the magnetic modulation amplitudes were in general not restricted, the only exception being the model corresponding to the double-helical structure reported in the literature.

Details of the refinements are given in Appendix C.

¹The magnetic structure of CrAs has to be described by a magnetic superspace group since the propagation vector is incommensurate.

Chapter 8

Results and Discussion

8.1 Macroscopic Properties

To characterize the CrAs samples and regarding their macroscopic properties, measurements of the magnetization and the resistance were performed. As corresponding results have been published before, the agreement of the properties and behavior of our samples with the literature can thus be assessed.

8.1.1 Magnetization

The magnetization of CrAs was measured in two setups, one with the magnetic field parallel to the a -axis of CrAs ($H\parallel a$) and one with the field perpendicular to a ($H\perp a$)¹. Above the phase transition temperature, the susceptibility χ is independent of the applied field direction (Figure 8.1); differences in the experimental values ascribed to the fact that different samples were used for the two measurements and that the sample mass could not be determined precisely enough. The phase transition at T_N is clearly visible as abrupt change in the susceptibility curves. These changes display a strong anisotropy, in that an abrupt increase is seen for $H\perp a$ and an abrupt decrease for $H\parallel a$.

The observed hysteresis of $\Delta T = 4.8$ K confirms the reported first-order nature of the phase transition. The phase transition temperature and the size of the hysteresis are not significantly affected by the strength of the applied magnetic field (Figure 8.1, *right*). The field-independent transition temperatures are $T_N^c = 266.7$ K and $T_N^h = 271.5$ K upon cooling and heating, respectively.

¹Following the relation of the CrAs MnP-type structure and the parent NiAs-type structure, these directions correspond to $H\parallel c_{\text{hex}}$ and $H\perp c_{\text{hex}}$, respectively. The latter direction lies in the hexagonal a, b -plane, and due to the previously mentioned twinning the orthorhombic directions b and c cannot be distinguished in an experiment.

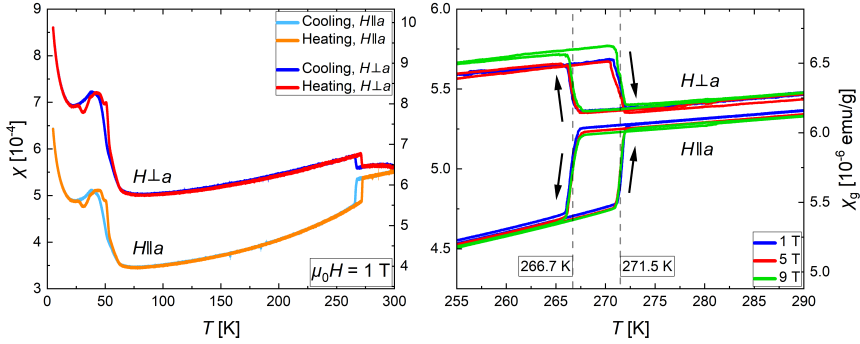


Figure 8.1: *Left*: The magnetic susceptibility of CrAs as function of temperature for $H\parallel a$ and $H\perp a$ with an applied magnetic field of $\mu_0 H = 1$ T; *right*: the susceptibility around the phase transition in dependence on the applied magnetic field. χ is the unitless magnetic susceptibility, χ_g is the often-used, non-SI mass susceptibility.

Below the phase transition, the susceptibility curves run parallel for both applied field directions, and decrease down to a temperature of about 70 K. At this temperature, the signal from the CrAs sample is drowned out by the magnetic signal from adsorbed oxygen² [170] (see Figure D.1 for comparison).

The susceptibility was also measured in the high-temperature region up to 1000 K. Figure 8.2 shows the high-temperature data joined³ to the measurement of the low temperature data shown previously. The susceptibility increases with temperature, but reaches a saturation at about 1000 K. Higher temperatures could not be accessed with the available experimental setup, and from the present data it cannot be stated what happens up to or above the assumed high-temperature phase transition at 1170 K.

²The adsorption of oxygen takes place predominantly on the PTFE tape used for fixing the sample. Measurements without tape were not attempted as the single-crystalline samples were prone to cracking during the phase transition and this could have lead to sample material breaking off during the measurement.

³The high-temperature data are corrected for an absolute offset in the susceptibility caused by the different experimental setup.

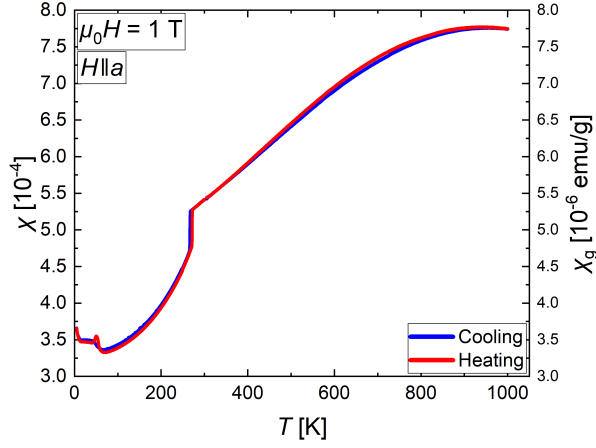


Figure 8.2: The magnetic susceptibility of CrAs as function of temperature in the range 2...1000 K for $H \parallel a$ with an applied magnetic field of $\mu_0 H = 1$ T. χ is the unitless magnetic susceptibility, χ_g is the often-used, non-SI mass susceptibility.

The measurement of the magnetization as function of applied magnetic field (Figure 8.3) confirms that CrAs is paramagnetic at room temperature above T_N , and supports the reported antiferromagnetism of CrAs below T_N at $T = 5, 30, 100$ K, where the $M(H)$ curve is linear, but dependent on the direction of the applied magnetic field. At none of these temperatures a saturation magnetization is reached by the applied maximum field of 9 T.

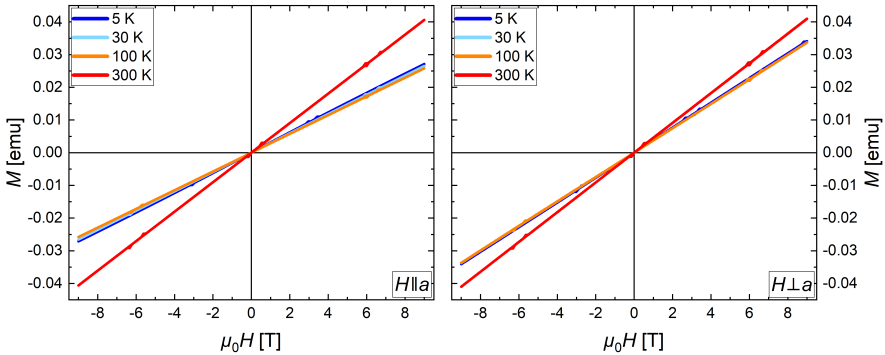


Figure 8.3: The magnetization of CrAs as function of applied magnetic field for $H \parallel a$ (left) and $H \perp a$ (right).

The obtained results on the macroscopic magnetic properties of CrAs are in good agreement with the literature, confirming on the one hand the published results and on the other hand that the considered sample is indeed showing the behavior expected for CrAs from the literature.

The abrupt in- and decreases in susceptibility at T_N in dependence on the direction of the magnetic field can be explained as a consequence of the structural phase transition following the general idea⁴ of Wu *et al.* [17]: The increase in the b axis and the decrease in a and c lead to changes in the spin exchange constants J along these directions; J_b decreases, while J_a and J_c increase. For a magnetic field applied parallel to a , the increase in the spin exchange along that direction results in a stronger antiferromagnetic coupling of the spins, which resists the spin alignment in the applied magnetic field and thus leads to a decrease in the magnetization. In case of the magnetic field applied perpendicular to a , the decrease in J_b outweighs the increase in J_c (due to the significantly larger change in length of the crystallographic axis). The weaker spin coupling facilitates the alignment of the spins with the applied magnetic field and leads to the observed increase in the magnetization.

The behavior of the magnetization at high temperatures is qualitatively in good agreement with the data reported by Selte *et al.* [9]. The specific behavior of the susceptibility – increasing above the transition to the paramagnetic state and seemingly reaching saturation – indicates the Pauli-paramagnetic nature of CrAs, where the number of unpaired electrons increases with temperature due to transfer of electrons from a spin-paired configuration to unpaired states.

8.1.2 Resistance

The resistance measurements on CrAs exhibit clear indications of the phase transition and the general behavior below T_N alludes to significant changes in the sample with repeated measurements. Figure 8.4 shows the resistance as function of temperature from three subsequent measurement runs using the same sample.

The phase transition is observed as abrupt jumps upon cooling and sharp maxima upon heating⁵. The transition temperatures are consistent, with $T_N^c = 265.5$ K and $T_N^h = 271.4$ K, which are in good agreement with the temperatures obtained from the magnetization measurements.

Above the phase transition, the measurement shows various anomalies – however, based on several test runs (not shown), they are evidently not inherent to the CrAs sample and are instead likely caused by issues with the contacts or instrumental artifacts. They are thus not considered further.

Below the phase transition, the resistance decreases smoothly with temperature, and no differences between the cooling and heating curve are observed. Between consecutive runs, however, the resistance increases significantly.

⁴Regardless of the validity of the underlying idea, the explanation proposed by Wu *et al.* cannot be adopted without adjustment. Comparison with further literature on CrAs makes it clear that the axis designation within the paper is not consistent, and thus the conclusions have to be considered very carefully.

⁵During the first heating run, the data acquisition stopped before reaching the phase transition due to unknown technical reasons.

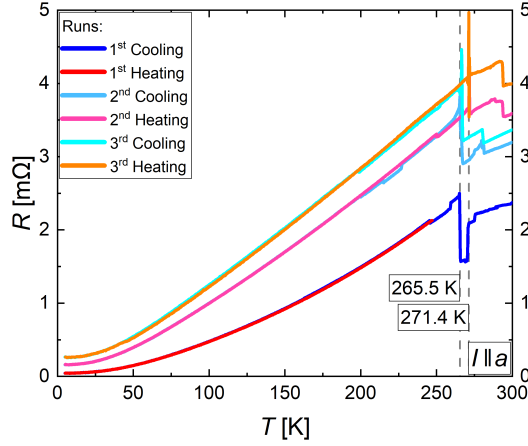


Figure 8.4: The resistance of CrAs as function of temperature measured in consecutive runs with the current I applied along a .

The behavior of the resistance during the phase transition and between the consecutive runs can be explained by the macroscopic effect of the measurement on the microstructure of the used CrAs sample. Going through the phase transition upon cooling, the volume of the unit cell expands abruptly by about +2.25%. This leads to the formation of cracks, which in turn lead to the observed abrupt increase in resistance. While the volume expansion is reversible, the formation of cracks and the related increase in resistance are not. Hence, in subsequent runs with the same sample, the resistance increases due to the cumulative formation of microcracks. Existent cracks can be expected to somewhat mitigate the formation of new cracks, which is reflected in the fact that the difference between the first and second run is significantly larger than between the second and third run.

The influence of the sample's individual behavior, mainly with regard to the formation of cracks, effectively complicates the drawing of conclusions regarding the inherent resistive properties of CrAs. It is most likely also the reason for the inconsistencies in the temperature-dependent resistance reported for CrAs [17, 26–28].

8.2 Crystal Structure

The crystal structure of CrAs (Figure 8.5) is known since 1971 [9, 14, 23], when it was reported independently by three groups, and has been confirmed several times since then [13, 15, 25]. However, as mentioned in Chapter 2 and shown further below in Figure 8.11, these data are from studies at basically only three temperatures – room temperature, liquid nitrogen and liquid helium – and show in addition limited coherence.

Hence, it is worthwhile to elucidate the precise behavior of the CrAs crystal

structure with temperature and with pressure. The data and results shown here form the basis of a publication published in 2021 [212].

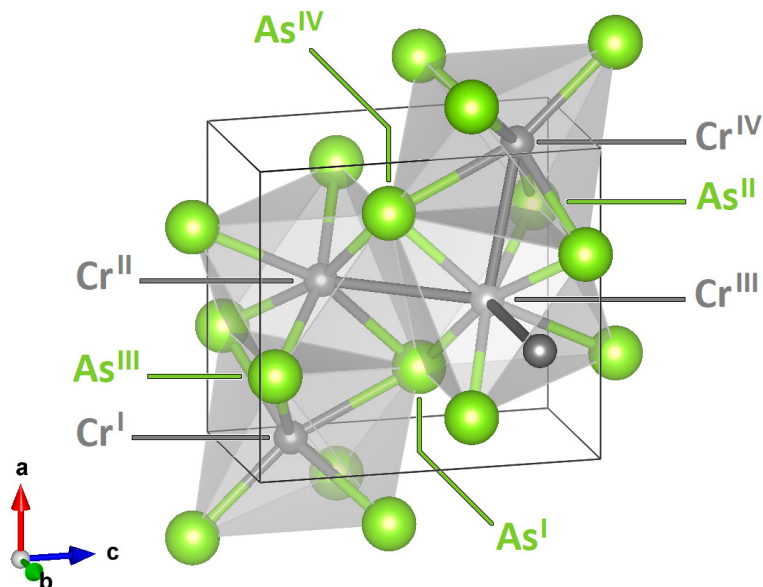


Figure 8.5: The crystal structure of CrAs. The Cr and As atoms are drawn in dark gray and green, respectively. The $[\text{CrAs}_6]$ octahedra are drawn in light gray.

8.2.1 Symmetry Considerations

The reported crystal structure of CrAs is consistently described in space group $Pnma$ with the MnP-type structure. In all performed measurement (synchrotron and laboratory X-ray), the observed extinction rules are in accordance with this space group $Pnma$ as well as its acentric counterpart $Pn2_1a$. Although the intensity statistics hint towards the acentric $Pn2_1a$ structure, a comparison of the overall quality of the fit of refinements in both space groups (including an inversion twin model in space group $Pn2_1a$) showed no significant difference. In addition, the refinement of the parameters y_{Cr} and y_{As} – which are fixed to $1/4$ in space group $Pnma$, but free in space group $Pn2_1a$ – show that within errors they do not deviate from the centrosymmetric value $1/4$ in the whole temperature range. This observation is similar to findings regarding the crystal structure of the isostructural compound FeAs [57]. Based on this observation and thus in accordance with the literature, the space group $Pnma$ was assumed to be the correct choice for CrAs at all conditions.

8.2.2 Lattice Parameters as Function of Temperature

The behavior of the lattice parameters with temperatures has been investigated earlier, and particularly their large and abrupt change coupled to the first-order phase

transition at T_N has been noted [23]. Figure 8.6 shows the lattice parameters as a function of temperature – normalized to the respective values at room temperature – based on our synchrotron and laboratory X-ray measurements. Above room temperature, the observed behavior of the lattice parameters agrees quite well with the reported high-temperature data [20], and shows in particular the same tendencies (see Figure D.2). At T_N , the structural phase transition is clearly visible from the large abrupt changes in all lattice parameters. The exact transition temperature is not resolved with the temperature step of 5 K, but lies between 275 K and 270 K. This slight deviation from the transition temperature obtained from the measurements of magnetization ($T_N = 266.7$ K) and resistance ($T_N = 265.5$ K) – which are in good agreement with each other and the literature – is explained by temperature fluctuations in the open-flow cryostat. The relative changes on cooling from 275 K to 270 K are $\Delta a/a \simeq -0.40\%$, $\Delta b/b \simeq +3.51\%$, $\Delta c/c \simeq -0.83\%$ and $\Delta V/V \simeq +2.25\%$ and confirm the previous observations from the literature. Below the transition, the lattice parameters change smoothly; a and c decrease in a comparable way, b first increases and eventually stays nearly constant below about 200 K. The behavior of the volume V is, in particular below 200 K, dominated by the behavior of a and c , and exhibits a general decrease with temperature.

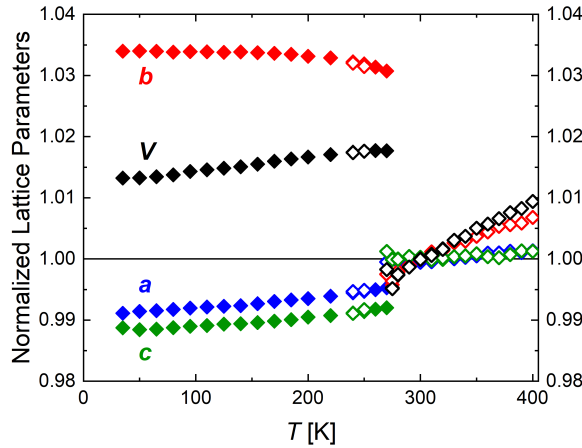


Figure 8.6: Lattice parameters and unit cell volume of CrAs normalized to their respective values at room temperature as a function of temperature. Data from synchrotron and laboratory X-ray measurements are indicated by filled and open symbols respectively.

These drastically different behaviors of b and c result in an important change in the c/b ratio as shown in Figure 8.7 (*left*). This c/b ratio of the orthorhombic setting is related to the $a_{\text{hex}}/b_{\text{hex}}$ ratio of the hexagonal parent structure, and in the ideal orthohexagonal setting it is $c/b = \sqrt{3}$ (see Chapter 3.1). Undergoing the phase transition, CrAs abruptly changes from $c/b > \sqrt{3}$ to $c/b < \sqrt{3}$. While this change in the ratio has been noted before for CrAs [9] and the ratio was used in a general sense to distinguish two subclasses of the MnP-type structure [213], no

further significance was attributed to it. However, we believe that the fact that the c/b ratio crosses the ideal value of $\sqrt{3}$ is crucial for a change in the twin domain structure observed during the transition, which will be discussed in detail below.

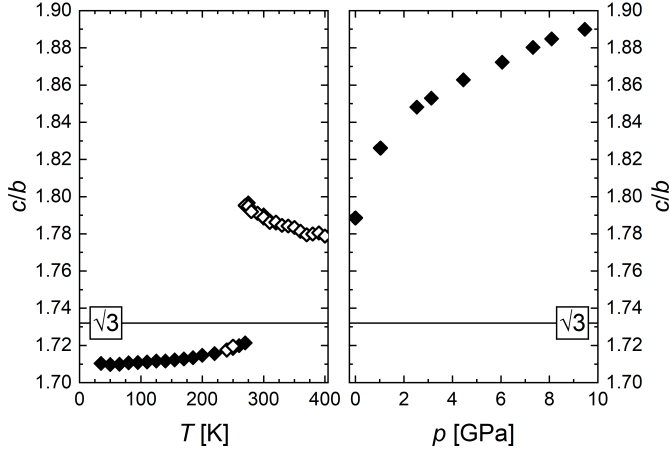


Figure 8.7: The c/b ratio of the CrAs unit cell as a function of temperature (*left*) and pressure (*right*). Data from synchrotron and laboratory X-ray measurements are indicated by filled and open symbols respectively.

8.2.3 Lattice Parameters as Function of Pressure

In contrast to the behavior at low temperatures, the application of pressure does not lead to a first-order phase transition like the one at T_N (Figure 8.8). This is easily understood, as the low-temperature phase transition is coupled to an increase in volume and thus cannot be induced by increasing pressure. All lattice parameters decrease with increasing pressure, with the b axis exhibiting a significantly higher compressibility than the a and c axes, which show approximately the same compressibility. The c/b ratio increases with pressure (Figure 8.7, *right*), moving away from the ideal value of $\sqrt{3}$ corresponding to the orthohexagonal setting. The same pressure-dependent behavior is also observed in other transition-metal monopnictides with the MnP-type structure, e.g. FeAs [214], MnP [67] and FeP [74].

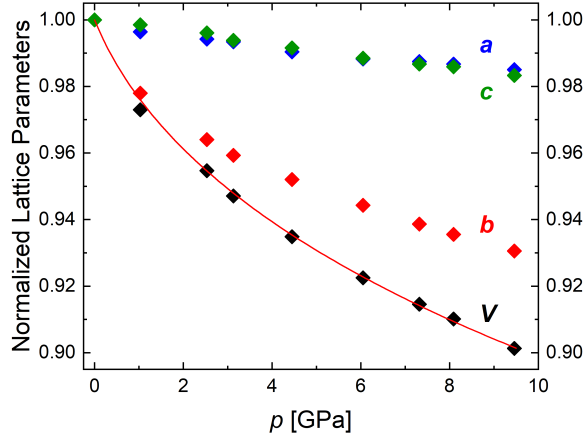


Figure 8.8: Lattice parameters and unit cell volume of CrAs normalized to their respective values at room temperature as a function of pressure. The red line represents the fit of the third-order Birch–Murnaghan equation of state to the data.

The pressure step used in this work does not allow a detailed study of the anomalies in the pressure dependence of the lattice parameters and unit cell volume below 1 GPa as observed by Yu *et al.* [30] in their powder diffraction data. Nevertheless, based on our single-crystal data we confirm that there is no change in symmetry in CrAs upon compression up to 9.5 GPa at room temperature. The pressure-dependent unit cell volumes can be fitted with a third-order Birch–Murnaghan equation of state [215, 216]

$$P(V) = \frac{3B_0}{2} \cdot \left[\left(\frac{V_0}{V} \right)^{\frac{7}{3}} - \left(\frac{V_0}{V} \right)^{\frac{5}{3}} \right] \cdot \left\{ 1 + \frac{3}{4} (B'_0 - 4) \left[\left(\frac{V_0}{V} \right)^{\frac{2}{3}} - 1 \right] \right\},$$

with the unit cell volume at ambient conditions V_0 , the bulk modulus (at ambient conditions) B_0 and the first derivative of the bulk modulus with respect to pressure B'_0 . The experimental value for the unit cell volume at ambient pressure and room temperature is $V = 121.4(1) \text{ \AA}^3$, the fitted unit cell volume at zero pressure is $V_0 = 121.3(2) \text{ \AA}^3$ and thus in excellent agreement. The fitted values for the bulk modulus and its first derivative are $B_0 = 28(4) \text{ GPa}$ and $B'_0 = 36(5)$, respectively.

Compared to other MnP-type compounds (see Table 8.1) the bulk modulus of CrAs is very low and its first derivative very high.

Table 8.1: Values for the bulk modulus B_0 and its first derivative B'_0 of compounds with the MnP-type structure compiled from the literature.

Compound	B_0 [GPa]	B'_0	Reference
CrAs	28(4)	36(5)	this work
FeAs	113.5	5.7	[214]
MnP	116(12)	4.2(8)	[67]
CoAs	123(6)	8.8(33)	[87]
FeP	205(7)	4	[74]

The low bulk modulus reflects the significantly stronger compressibility of CrAs compared to the other compounds (Figure 8.9, *left*). The bulk moduli are negatively correlated with the unit cell volume (Figure 8.9, *right*), with CrAs having the largest unit cell and the lowest bulk modulus.

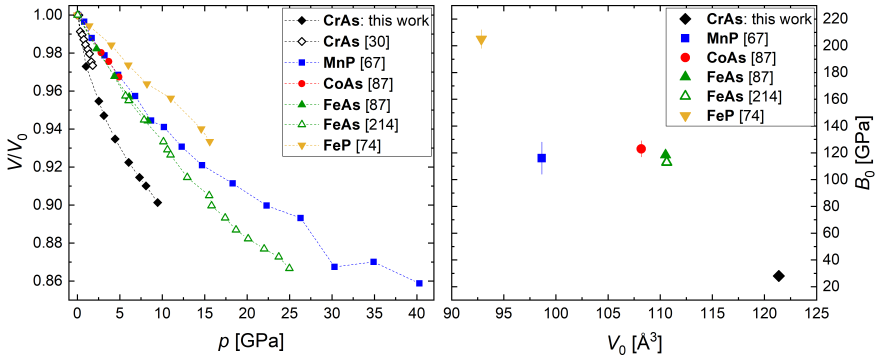


Figure 8.9: Comparison of various compounds with the MnP-type structure compiled from the literature: (*left*) the unit cell volume normalized to the value at ambient pressure as function of pressure; (*right*) the bulk modulus of the compounds as function of the unit cell volume at ambient pressure. The dashed lines are guides for the eye.

8.2.4 Refinements and Twinning

As mentioned before, CrAs undergoes a phase transition from the parent NiAs-type structure to the MnP-type structure at high temperatures, which is coupled to the formation of twin domains with the threefold rotational axis along the orthorhombic a -axis being the twinning element. The passing of this transition temperature in the growth process of CrAs explains the frequent occurrence of twin domains in these crystals. The single crystals used for the present experiments were selected to be largely composed of one single domain, but the presence of additional low-volume

twin domains can be seen in the reciprocal space reconstruction of the measurements above the transition temperature as a splitting of a part of the reflections and of additional reflections that are not indexed by the primary twin (Figure 8.10, *left*); 97.5% of the reflections can be indexed by the primary twin, the second twin component indexes an additional 2.2% of the reflections. The twin matrix for this twinning operation – a rotation by $\varphi_{\text{II}} = 120^\circ$ around the a -axis – is given by

$$M_{\text{II}} = \begin{pmatrix} 1 & 0 & 0 \\ 0 & \cos \varphi_{\text{II}} & \frac{b}{c} \cdot \sin \varphi_{\text{II}} \\ 0 & -\frac{c}{b} \cdot \sin \varphi_{\text{II}} & \cos \varphi_{\text{II}} \end{pmatrix}.$$

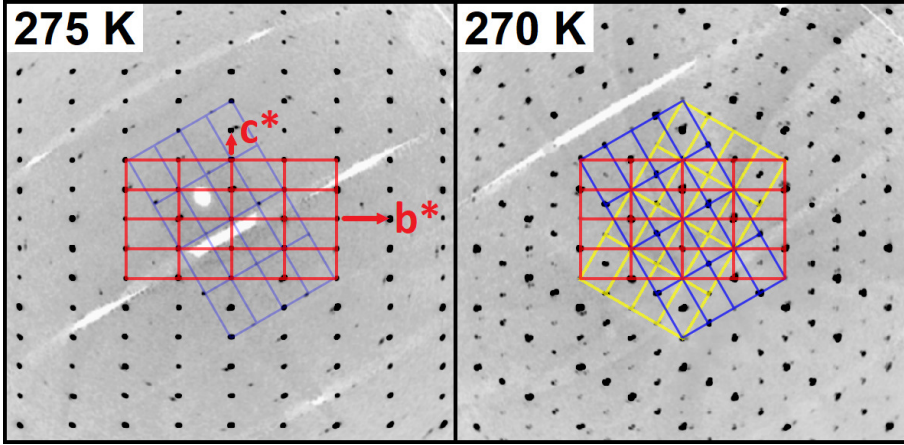


Figure 8.10: Reconstructions of the reciprocal space at 275 K (*left*) and 270 K (*right*) based on the synchrotron X-ray measurements. The lattice of the main twins used for the respective indexing are indicated.

Below the transition temperature T_N , the reciprocal space reconstruction shows a significant change in the domain structure of the CrAs crystal (Figure 8.10, *right*). The primary twin now indexes only 75.8% of the reflections, and the second and third twin individuals index additionally 12.2% and 11.1%, respectively. The twinning matrix M_{III} for the third twin individual is given analogous to M_{II} with $\varphi_{\text{III}} = 240^\circ$. With a further decrease in temperature, the domain structure does not substantially change any more. For the refinements, only the integrated data based on the reflections that can be indexed by the prime twin component (which shows some overlap with the other two twin components) were used in all cases.

In the high-temperature phase transition, the twinning is coupled to the lowering of the symmetry from $P6_3/mmc$ to $Pnma$, with the lost threefold rotational axis along the orthorhombic a axis acting as the twinning element. The same twinning element is observed in the twinning below T_N , although the transition is isosymmetrical and this threefold rotational axis does not play a direct role in the transition. We believe that the reason for this twinning is related to the change in the c/b ratio mentioned before (Figure 8.7). During the change from $c/b > \sqrt{3}$ to $c/b < \sqrt{3}$, the

structure has to briefly assume $c/b = \sqrt{3}$, in which the lattice parameters correspond to the ideal ones from the orthohexagonal setting. In this ‘pseudo-hexagonal’ setting, a pseudo-threefold axis is present in the structure, which could trigger the observed change in the twin domain structure.

This formation of twin domains during the phase transition is furthermore coupled to increased displacement parameters of the atoms (Figure D.3). In addition to the standard refinements with harmonic atomic displacement parameters (ADPs), refinements with anharmonic ADPs were carried out, as this was suggested by a visual inspection of the F_{obs} density maps. The resulting parameters show consistently that around the transition temperature, the displacement parameters of the atoms show a significant anharmonicity, indicating that around and during the phase transition, the atoms show increased and anharmonic movement around their mean positions or that there is an increased degree of static disorder of the atoms which are slightly moved away from their highly symmetric special positions.

The modification of the twin domain structure during the phase transition at T_N does naturally imply a significant change in the microstructure of the CrAs single crystals. This change seems to depend on the temperature rate with which the phase transition is crossed, as the change in the twin domain structure was observed in the (faster) synchrotron measurements, but not in the (slower) laboratory measurements. This also implies that the temperature rate with which the phase transition is crossed might affect the emergence of superconductivity in CrAs, which should be very sensitive to the microstructure and thus to local disorder and strains [11].

In contrast to the temperature-dependent behavior, the application of pressure does not induce such a change in the microstructure, as the behavior of the lattice parameters at high pressures is different: the ideal c/b ratio of the pseudo-hexagonal setting is not assumed and no twinning is observed.

The observed change in the twin domain structure has not been reported for any of the other compounds exhibiting an isosymmetrical phase transition between MnP-type structures. As the $c/b = \sqrt{3}$ setting is not crossed during those transitions, a twinning phenomenon analogous to the one described for CrAs is also not expected. Hence, the twin domain change observed in CrAs seems to originate from a coincidence based on the specific lattice parameters, and is thus not characteristic for the group of MnP-type structure transition-metal monpnictides as a whole.

8.2.5 Atom Coordinates

The free atom coordinates are convenient for a direct comparison of the consistency of the present work and the previously reported data for the full crystal structure of CrAs (Figure 8.11).

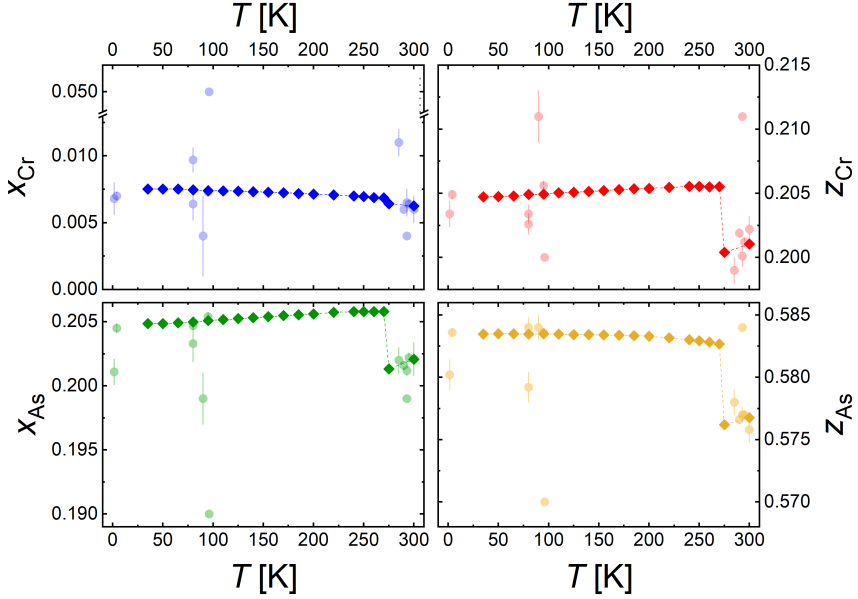


Figure 8.11: The free atomic coordinates of the CrAs crystal structure refined based on the present measurements (dark symbols) compared to the values reported in the literature (light symbols). The dashed lines are guides for the eye. Data compiled from [9, 13–15, 23, 25].

The large spread of the literature values compared to the maximum change over the whole temperature range is a bit surprising, but is likely a consequence of the fact that the results are based on various isolated measurement, which makes a direct comparison difficult.

8.2.6 Interatomic Distances

The majority of the interatomic distances in the CrAs crystal structure show the following general behavior: Above the phase transition, they decrease with decreasing temperature (Figure 8.12). At the transition temperature T_N , they show an abrupt increase, and below the transition they decrease again with lowering the temperature. In all three regimes, however, striking exceptions are observed for specific distances.

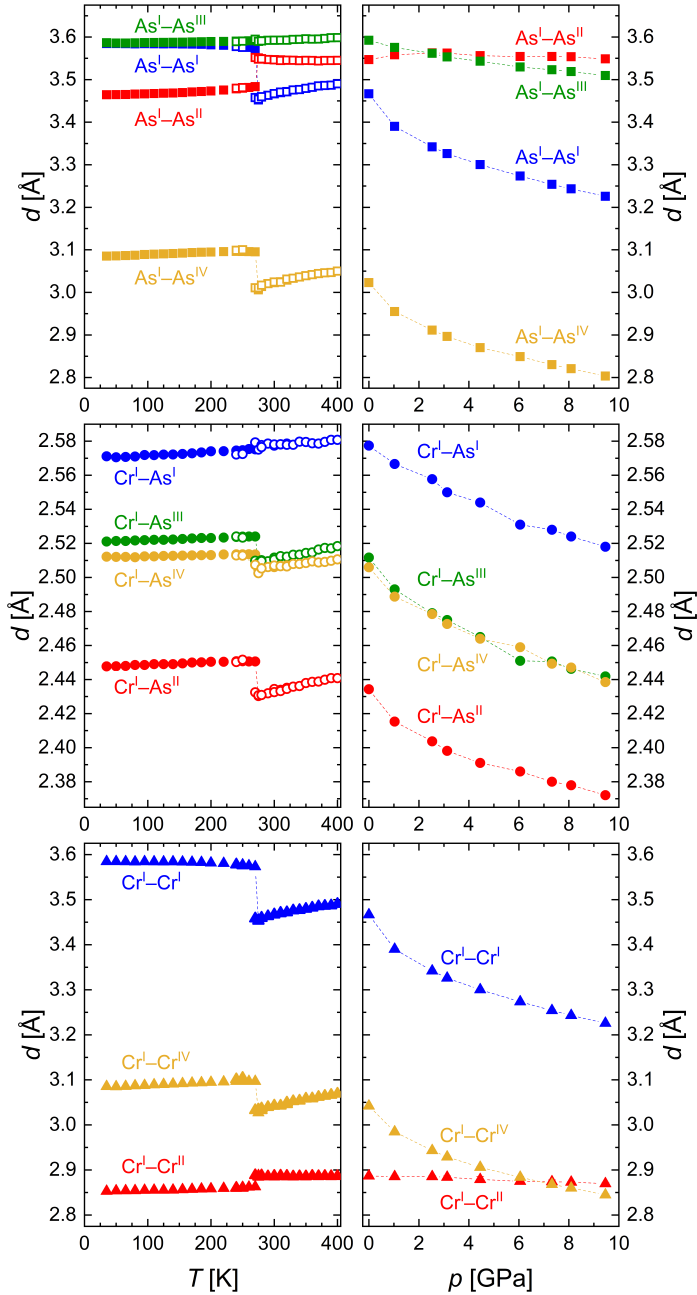


Figure 8.12: Interatomic As-As (*top*), Cr-As (*middle*) and Cr-Cr (*bottom*) distances in the crystal structure of CrAs as a function of temperature (*left*) and of pressure (*right*). Data from synchrotron and laboratory X-ray measurements are indicated by filled and open symbols, respectively. The dashed lines are guides for the eye.

The most interesting distances in the CrAs structure are the Cr–Cr distances (Figure 8.13), as the Cr atoms carry the magnetic moment and they and their interactions are of particular importance for the magnetic and eventually superconducting properties.

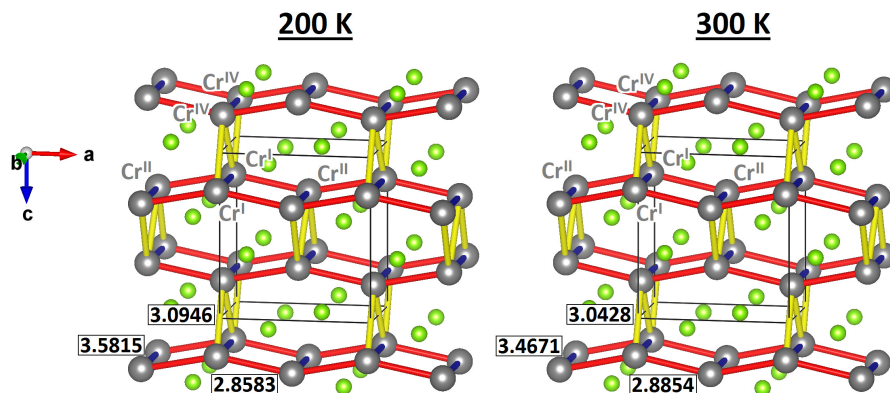


Figure 8.13: Overview of the Cr–Cr distances in the crystal structure of CrAs below the phase transition (200 K, *left*) and above the phase transition (300 K, *right*). The Cr and As atoms are shown in dark gray and green, respectively. The distance values are given in [Å].

Above the phase transition, the distances $\text{Cr}^{\text{I}}\text{--}\text{Cr}^{\text{I}}$ and $\text{Cr}^{\text{I}}\text{--}\text{Cr}^{\text{IV}}$ follow the general trend and decrease with decreasing temperature. However $\text{Cr}^{\text{I}}\text{--}\text{Cr}^{\text{II}}$, the strongest covalent Cr–Cr bond and strongest homoatomic interaction, is remarkable in that it stays constant above T_{N} . At the phase transition, the same distinction between the three homoatomic Cr–Cr distances is seen. Here, $\text{Cr}^{\text{I}}\text{--}\text{Cr}^{\text{I}}$ and $\text{Cr}^{\text{I}}\text{--}\text{Cr}^{\text{IV}}$ increase drastically (upon cooling) at the phase transition, while $\text{Cr}^{\text{I}}\text{--}\text{Cr}^{\text{II}}$ – the shortest Cr–Cr distance – decreases even further⁶. $\text{Cr}^{\text{I}}\text{--}\text{Cr}^{\text{I}}$ directly determines the length of the b -axis of the unit cell, so that its increase is equivalent to the observed discontinuity in the temperature dependence of the b lattice parameter. $\text{Cr}^{\text{I}}\text{--}\text{Cr}^{\text{IV}}$, lying almost in the b, c -plane, increases as well. The decrease in $\text{Cr}^{\text{I}}\text{--}\text{Cr}^{\text{II}}$, which is oriented approximately along the a -axis, leads to the abrupt shortening of this axis. Besides this decrease, the angle $\angle\text{Cr}^{\text{I}}\text{--}\text{Cr}^{\text{II}}\text{--}\text{Cr}^{\text{I}}$ is significantly increased at the transition (Figure 8.14, *left*) and gets closer to the ideal value of 180° that is assumed in the NiAs-type parent structure (see Chapter 3.1). Below the phase transition, $\text{Cr}^{\text{I}}\text{--}\text{Cr}^{\text{I}}$ slightly increases, while $\text{Cr}^{\text{I}}\text{--}\text{Cr}^{\text{II}}$ and $\text{Cr}^{\text{I}}\text{--}\text{Cr}^{\text{IV}}$ decrease only slightly.

⁶Below the transition, $\text{Cr}^{\text{I}}\text{--}\text{Cr}^{\text{II}}$ and $\text{Cr}^{\text{I}}\text{--}\text{Cr}^{\text{IV}}$ decrease with temperature, while $\text{Cr}^{\text{I}}\text{--}\text{Cr}^{\text{I}}$ increases and is eventually constant below about 200 K.

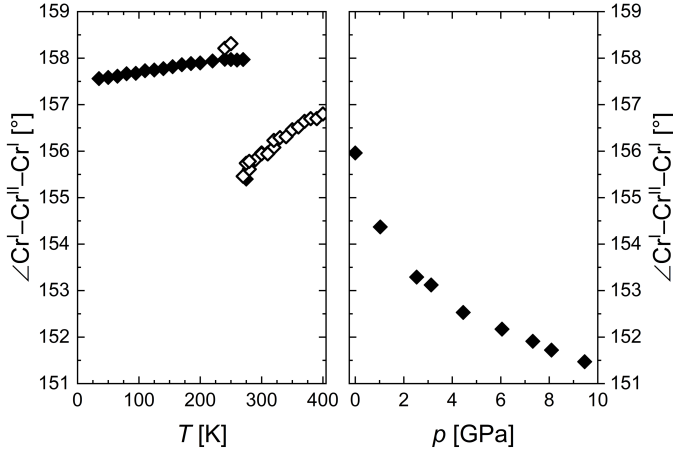


Figure 8.14: The angle $\angle \text{Cr}^{\text{I}}\text{-Cr}^{\text{II}}\text{-Cr}^{\text{I}}$ in the crystal structure of CrAs as a function of temperature (*left*) and of pressure (*right*). Data from synchrotron and laboratory X-ray measurements are indicated by filled and open symbols, respectively.

The Cr-As distances, which determine the size and shape of the coordination polyhedra, all decrease down to T_{N} following the general trend. However, at the phase transition and in contrast to the other Cr-As distances, the longest Cr-As distance, $\text{Cr}^{\text{I}}\text{-As}^{\text{I}}$, decreases. Hence, since the different Cr-As distances approach each other and thus the state of equidistance in the ideal polyhedra, it can be inferred that both the $[\text{CrAs}_6]$ octahedra and the $[\text{AsCr}_6]$ trigonal prisms become more regular in the low-temperature phase. This is also seen in the distance distortion δ_{D} and the angular distortion δ_{A} – calculated as the deviation of the experimental values for the distances and angles, respectively, from the restrictions imposed by the reference shapes (see Appendix E) – which decrease during the phase transition (Figure 8.15, *left*). Below the transition and with further lowering the temperature, the Cr-As distances again all slightly decrease and the distortion of the polyhedra slightly increases again.

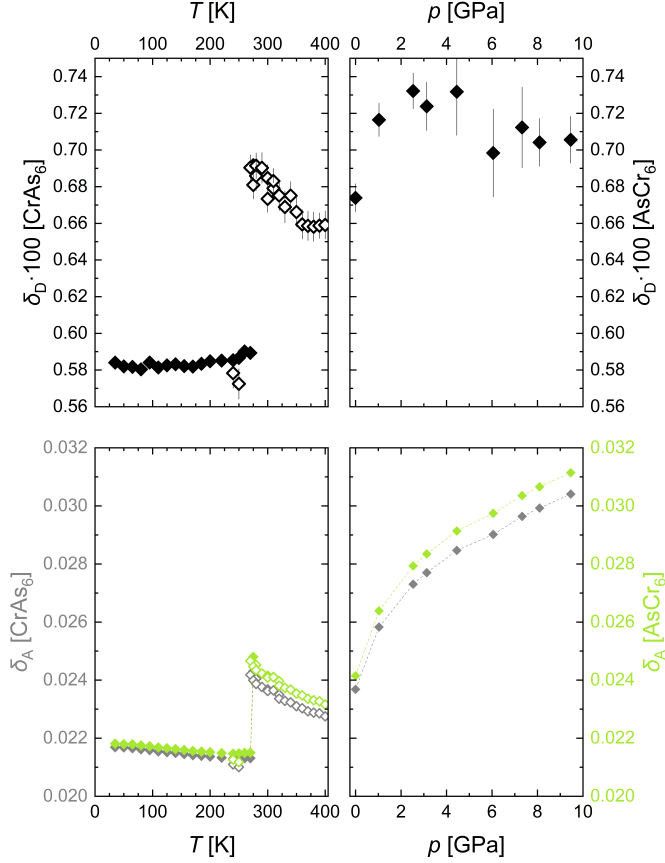


Figure 8.15: Distance distortion δ_D (*top*) and angular distortion δ_A (*bottom*) of the [CrAs₆] octahedra and the [AsCr₆] trigonal prisms in the crystal structure of CrAs as a function of temperature (*left*) and of pressure (*right*); δ_D is identical for the two coordination polyhedra. The dashed lines are guides for the eye.

The calculated As–As distances also show anomalous behavior in the different regimes. Above the transition temperature, As^I–As^I and As^I–As^{IV} follow the general trend of decrease with decreasing temperature; As^I–As^{III} also decreases, but only slightly so. In contrast, As^I–As^{II}, stays approximately constant. At the phase transition, As^I–As^I and As^I–As^{IV} show abrupt increases, with As^I–As^I being directly determined by the length of the b -axis, and As^I–As^{IV} lying almost in the a, b -plane. The decrease in As^I–As^{II}, lying in the a, c -plane, is coupled to the decrease of the a and c lattice parameter. As^I–As^{III} is not visibly affected by the phase transition. Below the phase transition, As^I–As^{III} remains constant, while As^I–As^{II} and As^I–As^{IV} decrease slightly. As^I–As^I shows with a slight increase the same behavior as Cr^I–Cr^I due to its coupling to the b -axis.

In CrAs on compression, all distances decrease with the exception of $\text{Cr}^{\text{I}}\text{--Cr}^{\text{II}}$ and $\text{As}^{\text{I}}\text{--As}^{\text{II}}$ (Figure 8.12), which are almost constant up to 9.5 GPa. Furthermore, $\text{As}^{\text{I}}\text{--As}^{\text{III}}$ decreases with increasing pressure less than the other decreasing distances. The different compressibilities, in particular the approximately constant $\text{Cr}^{\text{I}}\text{--Cr}^{\text{II}}$, lead to an increasing distortion of the $[\text{CrAs}_6]$ octahedra and $[\text{AsCr}_6]$ prisms as well as the $[\text{CrAs}_6]$ columns, seen in the pressure dependence of the $\angle\text{Cr}^{\text{I}}\text{--Cr}^{\text{II}}\text{--Cr}^{\text{I}}$ angle (Figure 8.14, *right*) and the distortions (Figure 8.15, *right*).

8.2.7 Discussion

The measured Cr–Cr distances are in very good agreement with the data reported by Shen *et al.* [15] (Figure D.4) and also in good agreement with those reported by Selte *et al.* [9], although both are much more limited in their investigated temperature and pressure range. Furthermore, the data measured by Shen *et al.* show that above the phase transition the pressure behavior of $\text{Cr}^{\text{I}}\text{--Cr}^{\text{II}}$ and $\text{Cr}^{\text{I}}\text{--Cr}^{\text{IV}}$ does not depend significantly on the temperature based on temperature-dependent measurements at different pressures. In particular, the results confirm that the $\text{Cr}^{\text{I}}\text{--Cr}^{\text{II}}$ distance remains nearly constant in the paramagnetic phase, both as a function of temperature and of pressure, and probably even when temperature and pressure are varied simultaneously following the results of Shen *et al.* [15]. A comparison of the pressure-dependent behavior of CrAs with related transition-metal monpnictides (*TPn*) of the MnP-type structure shows that at least the behavior of the relevant interatomic $T\text{--}T$ distances on compression is similar (Figure 8.16): $T^{\text{I}}\text{--}T^{\text{II}}$ is least affected by the pressure and changes relatively little, while $T^{\text{I}}\text{--}T^{\text{I}}$ and $T^{\text{I}}\text{--}T^{\text{IV}}$ are affected much more and in similar ways. This tendency is observed in CrAs, MnP [67], CoAs [87] and FeAs [87], though the contrast in behavior between $T^{\text{I}}\text{--}T^{\text{II}}$ and $T^{\text{I}}\text{--}T^{\text{I}}/T^{\text{I}}\text{--}T^{\text{IV}}$ is most pronounced in CrAs. The lack of temperature-dependent data for the *TPn* compounds, however, currently prevents a comparison of the $T\text{--}T$ behavior with temperature, and in particular a more comprehensive study of the $T^{\text{I}}\text{--}T^{\text{II}}$ distance and its relation to other properties. Nevertheless, the structural similarities observed so far indicate that the present results for CrAs might also be of importance for the other *TPn* compounds.

In CrAs, above T_{N} the $\text{Cr}^{\text{I}}\text{--Cr}^{\text{I}}$, $\text{Cr}^{\text{I}}\text{--Cr}^{\text{IV}}$ and Cr–As distances increase with increasing temperature and follow the expected thermal expansion. The $\text{Cr}^{\text{I}}\text{--Cr}^{\text{II}}$ distance, however, shows in general a significantly different behavior above T_{N} in the paramagnetic state. It stays constant with increasing temperature up to 400 K and also remains remarkably constant at pressures up to 9.5 GPa.

At T_{N} , the observed changes in the structure during the phase transition agree with observations in the literature and can be explained using the electronic model proposed by Zavadakii & Sibarova [16]. This model can also be taken to explain the behavior of the Cr–Cr distances at lower temperatures and will be briefly outlined in the following (see also Chapter 2.4). In this model, the behavior of CrAs is assumed to be driven by the Cr atoms and their interactions, and homoatomic As–As interactions are not taken into consideration.

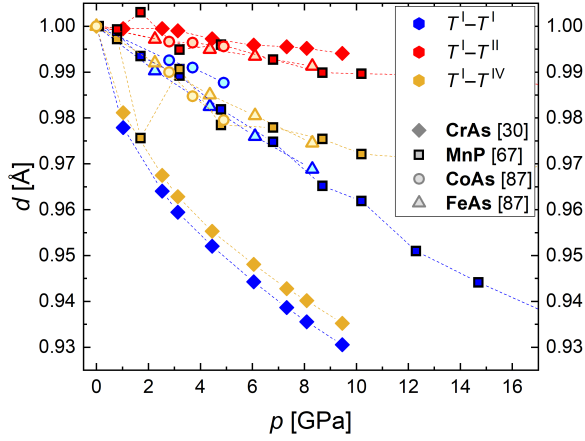


Figure 8.16: The behavior of the interatomic T - T distances in transition-metal monopnictides as function of pressure. The distance designation follows the one used CrAs in the present work. The dashed lines are guides for the eye.

The $\text{Cr}^{\text{I}}\text{-Cr}^{\text{I}}$ distance is oriented along the b -axis, yet too long for an attractive interaction. During the phase transition, the $d_{x^2-y^2}$ orbital⁷ in this direction is partially filled, which leads to the electrostatic repulsion responsible for the abrupt increase in this distance. Below T_{N} , the distance increases further and stays constant below approximately 200 K. With decreasing temperature, the energy of the $3d$ band is lowered further and the orbitals show increased occupation by electrons. This in turn leads presumably to an increased electrostatic repulsion and the observed increase in distance. The more the temperature decreases below the transition temperature, the less the electron occupation of the orbital changes, and eventually a constant distance is reached. Furthermore, the change in $\text{Cr}^{\text{I}}\text{-Cr}^{\text{I}}$ at the transition can be considered as the main reason for the accompanying change in the distance $\text{Cr}^{\text{I}}\text{-Cr}^{\text{IV}}$. This distance lies approximately in the b, c -plane and is directly coupled to the length of the b lattice parameter; the increase in the $\text{Cr}^{\text{I}}\text{-Cr}^{\text{I}}$ distance and the associated increase in the b lattice parameter might force the increase in the $\text{Cr}^{\text{I}}\text{-Cr}^{\text{IV}}$ distance as a side effect⁸. As noted by Boller & Kallel [14], this increase of the $\text{Cr}^{\text{I}}\text{-Cr}^{\text{IV}}$ distance brings it close to the Cr-Cr Mott critical distance of 3.18 Å. Following this, the itinerant electrons can localize and the localized magnetic moment can form at low temperatures. According to this hypothesis, the magnetic transition follows the electronic and structural transition, but no indication of a separation of the two transitions has been observed so far [11].

Above T_{N} , these two distances increase following the expected thermal expansion. The application of pressure at room temperature in the paramagnetic state above the phase transition leads to a decrease in these two distances with increasing pressure

⁷ $x||b$ and $y||c$, following the notation used by Boller & Kallel [14].

⁸While in principle it could also be *vice versa*, the elongation in b and thus in the $\text{Cr}^{\text{I}}\text{-Cr}^{\text{I}}$ distance is considered the driving force within the model.

as the respective atoms are pushed closer, with no hints towards obvious changes in the electronic interactions along the directions of $\text{Cr}^{\text{I}}\text{--Cr}^{\text{I}}$ and $\text{Cr}^{\text{I}}\text{--Cr}^{\text{IV}}$. The decrease of $\text{Cr}^{\text{I}}\text{--Cr}^{\text{IV}}$ moves it away from the Mott critical distance, preventing the formation of the localized magnetic moment. This also explains why the magnetic ordering is suppressed with increasing pressure. $\text{Cr}^{\text{I}}\text{--Cr}^{\text{I}}$ is above the Mott critical distance and approaches it at high pressures, but the corresponding orbital in that direction is – within the considered model – not occupied by electrons above T_{N} .

In contrast, $\text{Cr}^{\text{I}}\text{--Cr}^{\text{II}}$ shows a completely different behavior. As shortest Cr–Cr distance within the structure it is expected to have the strongest Cr–Cr interactions with a strong covalent bond [16], which should result in mostly itinerant electrons that do not significantly contribute to the ordered magnetic moment. The behavior of $\text{Cr}^{\text{I}}\text{--Cr}^{\text{II}}$ during the phase transition can again be explained within the Zavadskii & Sibarova model. Below the phase transition, electrons occupy the $d_{x^2-y^2}$ orbital along the b direction and are responsible for the electrostatic repulsion. At T_{N} , thermal transfer from this orbital to an antibinding $3d$ orbital oriented along $\text{Cr}^{\text{I}}\text{--Cr}^{\text{II}}$ is possible as the energy gap is sufficiently reduced. The increased occupancy of this antibinding orbital weakens the interatomic bond, resulting in an increase of this distance.

While the differences in behavior going through the phase transition can thus be explained within this model, it does not explain the differences in behavior in the paramagnetic state mentioned earlier, where $\text{Cr}^{\text{I}}\text{--Cr}^{\text{II}}$ is distinguished by being nearly unaffected by temperature and pressure. The possible significance of this particular nearest-neighbor Cr distance has been noted by Shen *et al.* [15], whose measurements in the antiferromagnetic phase near the superconducting phase region indicate that the spins of these Cr atoms rotate towards an almost antiparallel order. This might suggest that the superconductivity in CrAs is mediated by antiferromagnetic fluctuations involving these two Cr atoms, where the long-range helical magnetic order is suppressed by pressure and short-range antiferromagnetic fluctuations along the a -axis might be responsible for a superconducting electron coupling. The competition of the mutually exclusive long-range order responsible for the magnetism and the short-range fluctuations responsible for the superconductivity is evident in the evolution of the magnetic/superconducting volume fractions with pressure [13, 15, 33]. Hence, as the nearest-neighbor $\text{Cr}^{\text{I}}\text{--Cr}^{\text{II}}$ distance is assumed to govern the interaction between the spins, it might play an important role in the emergence of the superconductivity.

However, at the experimental conditions where the notable $\text{Cr}^{\text{I}}\text{--Cr}^{\text{I}}$ behavior is observed here – high temperature ($T > T_{\text{N}}$) at ambient pressure and high pressure at room temperature – the importance of this distance for superconductivity at low temperatures and high pressures cannot be considered of immediate relevance. Based solely on the presented observations, it is only evident that in the paramagnetic state the crystal structure of CrAs changes in a way that preserves the $\text{Cr}^{\text{I}}\text{--Cr}^{\text{I}}$ distance. Since the emergence of magnetic order drastically changes the behavior of this distance, it seems likely that the constant length of $\text{Cr}^{\text{I}}\text{--Cr}^{\text{I}}$ is also a consequence of the electronic structure, in particular considering those electrons responsible for the localized magnetic moment below T_{N} . The precise interaction mechanism that governs this particular distance can, however, not be determined on the basis of the present data.

8.3 Magnetic Structure

The magnetic structure of CrAs was first proposed by Watanabe *et al.* in 1969 [6] to be a double-helical structure. It should, however, be noted that this magnetic structure was not determined in a rigorous way. Instead, the helical model that was used by Watanabe *et al.* was selected due to the similarity of the crystal structures of CrAs and MnP, both members of the group of transition-metal monpnictides crystallizing in the MnP-type $Pnma$ structure. Since the helical model proposed for MnP allowed the indexing of the satellite reflections observed for CrAs, it was henceforth taken to describe the magnetic structure of CrAs, too. A rigorous determination of the magnetic structure of CrAs, including a comparison of all symmetry-allowed models for its magnetic structure, was not performed by Watanabe *et al.*, nor to our knowledge in any of the subsequent publications on this subject. Thus, there are two basic issues that should be considered: the validity of the assumption that the magnetic structure of CrAs is analogous to that of MnP based on their similar crystal structure, and the validity of the magnetic structure of MnP itself.

The similarity of the crystal structures of CrAs and MnP has been confirmed and is not in doubt, but the magnetic structures are not simply defined by the crystal structure alone. Since the emergent magnetic structure depends directly on the specific magnetic properties of the magnetic atoms and their interactions, and indirectly also on the underlying electronic configurations, the similarity of the magnetic structures of CrAs and MnP cannot be assumed *a priori*. Hence, while a similar magnetic structure is certainly plausible, alternative magnetic structures which are in agreement with symmetry considerations cannot be outright dismissed. This will be discussed in more detail below.

Even more fundamental, the validity of the helimagnetic structure proposed for MnP has to be considered. The idea of the helical model was first proposed by Goodenough in 1964 [217] on the basis of theoretical considerations regarding the electronic and spin configuration in MnP. This model was subsequently applied by Felcher, 1966 [218], and by Forsyth *et al.*, 1966 [219], to explain the observed experimental data. However, instead of the now-common formalisms used in magnetic structure determination (see Chapter 3.2.4) this was done basically on the basis of a trial-and-error approach and involved certain assumptions to simplify calculations, while concepts like the group-theoretical relation between crystal and magnetic structure were not being fully taken into account. Considering these shortcomings even in the determination of the magnetic structure of MnP, the established model for the magnetic structure of CrAs has to be regarded with caution.

Following these considerations, the magnetic structure of CrAs is determined in the present work on the basis of the obtained experimental data and after a careful comparison of the refinement results for the different possible magnetic models which are in accordance with group theoretical considerations. While the reported helical model is taken into account for comparison, it is not assumed to be the correct model for the magnetic structure of CrAs from the beginning.

8.3.1 Temperature Dependence of the Propagation Vector

Although the model of the precise magnetic structure of CrAs as described in the literature has to be questioned, there is no doubt about the fact that an incommensurate propagation is necessary for the indexing of the satellite reflections in the neutron powder diffraction pattern as shown in Figure 8.17.

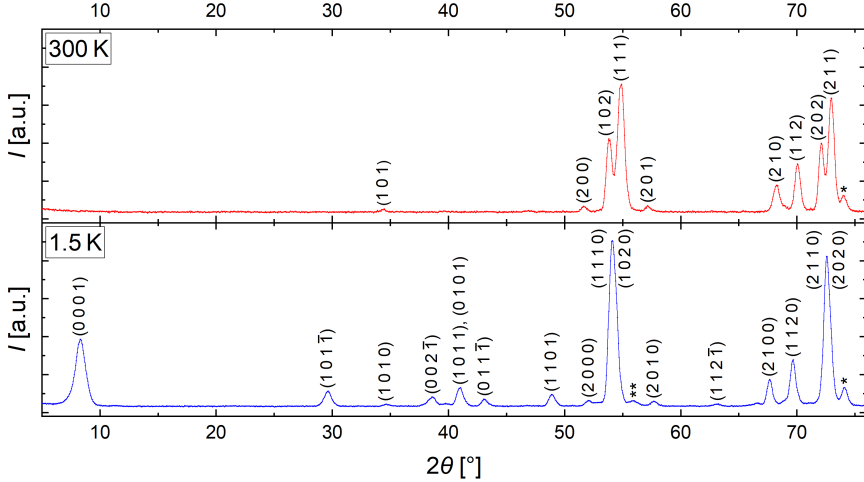


Figure 8.17: Neutron powder diffraction patterns measured for CrAs at 300 K (*top*) and at 1.5 K (*bottom*). The indexing of the most prominent peaks is shown; at 1.5 K the reflections are indexed in (3+1)-dimensional superspace with a \mathbf{k} -vector of $(0, 0, k_c)$. * marks a reflection belonging to the Cr impurity phase, ** marks a reflection belonging to the still-present high-temperature CrAs phase (see Appendix D.5 for details).

The propagation vector defines the direction and period length of the underlying modulation function. In the diffraction pattern, the propagation vector is determined solely by the position of the magnetic satellite reflections. In accordance with the literature, a propagation vector of $\mathbf{k} = (0, 0, k_c)$ is found for CrAs, i.e. the structure is modulated along the c -axis. The precise value of k_c as function of temperature is shown in Figure 8.18, given in reciprocal units of c^* . It can be seen that the propagation vector is constant at low temperatures ($T < 50$ K) with $k_c = 0.3531(6)$, and then linearly increases at higher temperatures, reaching $k_c = 0.3807(7)$ at 260 K.

This observation for the temperature dependence of k_c is in rather good agreement with the one made by Shen *et al.*, 2016 [15], especially taking into account a potential absolute offset. However, it should be emphasized that the fact that the present propagation vector confirms the literature is of no real relevance for the question of the validity of the reported helical magnetic structure of CrAs – as mentioned, the propagation vector can be determined without any knowledge of the actual magnetic structure.

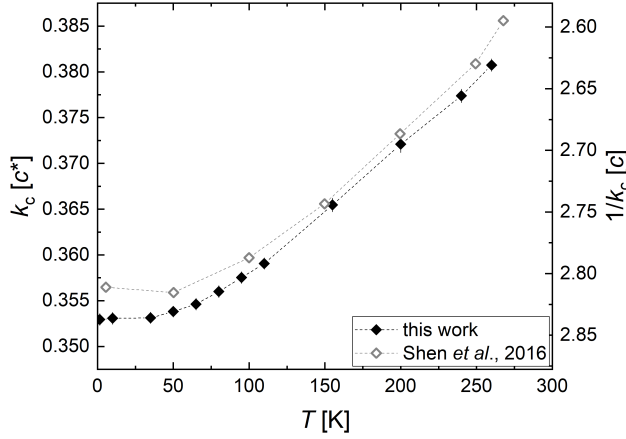


Figure 8.18: The component k_c of the propagation vector of the magnetic structure of CrAs as function of temperature determined from our neutron powder diffraction experiments at HRPT, PSI, compared to the literature values reported by Shen *et al.* [15].

8.3.2 Determination of the Magnetic Structure from Single-Crystal Data

Without the *a priori* assumption of the helical structure, the magnetic structure of CrAs is determined from a comparison of the refinement results from all the possible models allowed by the combination of crystal structure symmetry and propagation vector on the basis of the neutron single-crystal data measured at two different pressures. As mentioned in Chapter 7.2.2, to try additional models the symmetry of the nuclear structure was artificially lowered to allow further magnetic superspace groups, yet in all these the symmetry of the nuclear structure was retained by corresponding restrictions. The restrictions of the directional components of the magnetic moments of the Cr atoms posed by the superspace group symmetries are listed in Table 8.2.

Table 8.3 shows the obtained agreement factors for the refinement of all tested magnetic models based on the data point at $p_{\text{nom}} = 0.17$ GPa, including also the model corresponding to the double-helical structure purported in the literature. Since mainly the fit of the satellite reflections is of direct interest here, the refinement values for only the nuclear reflections are not included in this table. The full table with all refinement values is given in the Appendix (Table C.15).

Table 8.2: The components of the magnetic moment allowed in the magnetic super-space groups derived from space group $Pnma$. “M” indicates that a non-zero value is allowed for the given component. The superscripts [100], [010] and [001] do not belong to the formal space group symbol, but indicate the direction in which the two-fold screw axis of the respective space group $P2_1$ is oriented in order to allow differentiation. A space group symbol in parentheses indicates an artificially lowered symmetry where the $Pnma$ symmetry is retained by suitable restrictions.

Nuclear space group	Magnetic superspace group	M_x		M_y		M_z		Cr positions
		sin	cos	sin	cos	sin	cos	
$Pnma$	$Pnma.1'(00g)000s$	0	0	M	M	0	0	1
	$Pnma.1'(00g)ss0s$	M	M	0	0	M	M	1
	$Pnma.1'(00g)0s0s$	M	M	0	0	M	M	1
	$Pnma.1'(00g)s00s$	0	0	M	M	0	0	1
$(P2_1ma)$	$P2_1ma.1'(00g)000s$	0	0	M	M	0	0	2
	$P2_1ma.1'(00g)0s0s$	M	M	0	0	M	M	2
$(Pn2_1a)$	$Pn2_1a.1'(00g)000s$	M	M	M	M	M	M	1
	$Pn2_1a.1'(00g)s00s$	M	M	M	M	M	M	1
$(Pnm2_1)$	$Pnm2_1.1'(00g)000s$	0	0	M	M	0	0	2
	$Pnm2_1.1'(00g)ss0s$	M	M	0	0	M	M	2
	$Pnm2_1.1'(00g)0sss$	0	0	M	M	0	0	2
	$Pnm2_1.1'(00g)s0ss$	M	M	0	0	M	M	2
$(P2_12_12_1)$	$P2_12_12_1.1'(00g)000s$	M	M	M	M	M	M	1
	$P2_12_12_1.1'(00g)00ss$	M	M	M	M	M	M	1
$(P2_1/n)$	$P2_1/n.1'(0bg)00s$	M	M	M	M	M	M	1
	$P2_1/n.1'(0bg)00ss$	M	M	M	M	M	M	1
$(P2_1/m)$	$P2_1/m.1'(a0g)00s$	0	0	M	M	0	0	2
	$P2_1/m.1'(a0g)s0s$	M	M	0	0	M	M	2
$(P2_1/a)$	$P2_1/a.1'(00g)00s$	M	M	M	M	M	M	1
	$P2_1/a.1'(00g)s0s$	M	M	M	M	M	M	1
(Pn)	$Pn.1'(0bg)0s$	M	M	M	M	M	M	2
	$Pn.1'(0bg)ss$	M	M	M	M	M	M	2
$(P2_1^{[100]})$	$P2_1.1'(0bg)0s$	M	M	M	M	M	M	2
(Pm)	$Pm.1'(a0g)0s$	0	0	M	M	0	0	4
	$Pm.1'(a0g)ss$	M	M	0	0	M	M	4
$(P2_1^{[010]})$	$P2_1.1'(0bg)0s$	M	M	M	M	M	M	2
(Pa)	$Pa.1'(00g)0s$	M	M	M	M	M	M	2
$(P2_1^{[001]})$	$P2_1.1'(00g)0s$	M	M	M	M	M	M	2
	$P2_1.1'(00g)ss$	M	M	M	M	M	M	2
$(P\bar{1})$	$P\bar{1}.1'(abg)0s$	M	M	M	M	M	M	2
$(P1)$	$P1.1'(abg)0s$	M	M	M	M	M	M	4

The present investigation of the magnetic structure of CrAs is based only on the single-crystal data measured at $p_{\text{nom}} = 0.17$ GPa. The refinement values for the data measured at $p_{\text{nom}} = 1.2$ GPa are given in Table C.16 in the Appendix – however, likely due to the increased pressure, the quality of the data is notably worse, which is reflected in the poor agreement factors of the nuclear structure. A well-fitting model of the nuclear structure is, however, a requirement for the subsequent determination of the magnetic structure. The results of refining the nuclear structure in lower-symmetrical subgroups of space group $Pnma$ are better, but still not satisfactory (Table C.17 in the Appendix). As a consequence of the poor data quality, the data at $p_{\text{nom}} = 1.2$ GPa are not further analyzed here in the context of magnetic structure determination.

In general, it should be mentioned that the obtained agreement factors for the different magnetic models even in the best cases are not overwhelmingly good, since they are based on measurements at high pressure. The presence of the inevitable scattering on the components of the high-pressure cell means that agreement factors will not be as good as it can be expected in measurements without such a cell.

It can be seen that the four magnetic superspace groups allowed by the full nuclear symmetry $Pnma$ do not lead to a good agreement with the data, motivating the previously mentioned change to the lower symmetries. For the magnetic models corresponding to the non-centrosymmetric orthorhombic subgroups ($P2_1ma$, $Pn2_1a$, $Pnm2_1$, $P2_12_12_1$) the agreement factors are generally better than for the centrosymmetric supergroup, but still not in a satisfactory range. The centrosymmetric monoclinic subgroups ($P2_1/n$, $P2_1/m$, $P2_1/a$) show overall again better results, but only the superspace group $P2_1/n.1'(0bg)0ss$ yields acceptable agreement factors for the satellite reflections. On reduction of the symmetry to the non-centrosymmetric monoclinic subgroups (Pn , $P2_1^{[100]}$, Pm , $P2_1^{[010]}$, Pn , $P2_1^{[001]}$), the agreement factors are in general further reduced, and four superspace group symmetries lead to a particularly good fit: $Pn.1'(0bg)ss$, $P2_1.1'(0bg)0s$, $Pa.1'(00g)0s$, and $P2_1.1'(a0g)0s$, with the last one being again slightly better than the other ones. The triclinic subgroups $P\bar{1}$ and $P1$ also lead to agreement factors similar to the other good fits; however, specifically subgroup $P1$ involves a significantly higher number of free magnetic parameters for no significant improvement in the agreement factor. The other symmetries with good fit involve the same number of refined parameters and thus the same parameter/data ratio for similar agreement factors. The agreement factors for superspace groups with fewer parameters and thus a better parameter/data ratio are generally significantly worse, and the reduction of free parameters is furthermore coupled to a restraining of the magnetic moments in one crystallographic direction or plane that would impose a crucial but rather unfounded restriction (see Table 8.2). Comparing the highlighted symmetries to Table 8.2 shows that one common feature is the lack of any restriction in the directional components of the magnetic moment, indicating consistently that the magnetic structure cannot be described with the spins oriented along one crystallographic axis.

Table 8.3: Final agreement factors of all tested magnetic models for CrAs based on the refinement of the neutron single-crystal data at $p_{\text{nom}} = 0.17\text{ GPa}$. The superscripts [100], [010] and [001] do not belong to the formal space group symbol, but indicate the direction in which the two-fold screw axis of the respective space group $P2_1$ is oriented in order to allow differentiation. A space group symbol in parentheses indicates an artificially lowered symmetry where the $Pnma$ symmetry is retained by suitable restrictions.

Nuclear space group	Magnetic superspace group	No. mag. parameters	all		satellites	
			R (obs/all)	wR (obs/all)	wR (obs/all)	wR (obs/all)
$Pnma$	$Pnma.1'(00g)000s$	2	9.95/13.12	22.55/22.66	80.45/89.37	92.51/92.62
	$Pnma.1'(00g)ss0s$	4	9.00/12.51	16.94/17.16	54.88/73.71	67.39/67.90
	$Pnma.1'(00g)0s0s$	4	8.37/11.55	10.08/10.31	37.96/48.99	34.37/34.65
	$Pnma.1'(00g)s00s$	2	9.66/12.93	15.01/15.23	72.69/84.56	58.53/58.96
$(P2_1ma)$	$P2_1ma.1'(00g)000s$	4	8.30/13.27	10.35/10.76	33.48/63.54	33.57/34.51
	$P2_1ma.1'(00g)0s0s$	8	8.16/13.15	10.03/10.47	29.18/60.51	31.90/32.97
$(Pn2_1a)$	$Pn2_1a.1'(00g)000s$	6	8.25/12.66	10.58/10.94	34.38/49.72	38.02/38.34
	$Pn2_1a.1'(00g)s00s$	6	8.12/12.60	9.48/9.85	31.22/48.38	31.66/31.86
$(Pnm2_1)$	$Pnm2_1.1'(00g)000s$	4	10.32/15.26	24.05/24.28	78.42/93.01	93.01/93.07
	$Pnm2_1.1'(00g)ss0s$	8	9.03/14.11	17.19/17.44	42.70/65.53	63.49/63.62
	$Pnm2_1.1'(00g)0sss$	4	9.08/14.29	11.92/12.44	44.02/70.16	39.11/40.35
	$Pnm2_1.1'(00g)s0ss$	8	8.79/14.27	10.77/11.21	35.96/69.60	33.24/33.98
$(P2_12_12_1)$	$P2_12_12_1.1'(00g)000s$	12	8.67/13.52	14.05/14.39	32.39/48.64	55.48/55.77
	$P2_12_12_1.1'(00g)00ss$	12	8.69/13.68	9.66/10.06	33.02/53.06	31.39/31.67
$(P2_1/n)$	$P2_1/n.1'(0bg)00s$	6	8.66/13.30	13.24/13.76	48.16/68.77	52.70/53.56
	$P2_1/n.1'(0bg)0ss$	6	7.83/12.25	9.01/9.66	21.64/38.26	28.43/29.69
$(P2_1/m)$	$P2_1/m.1'(a0g)00s$	4	8.75/14.75	9.57/10.14	30.64/55.88	28.66/29.64
	$P2_1/m.1'(a0g)0ss$	8	8.90/14.66	11.33/11.76	35.01/53.53	39.08/39.33
$(P2_1/a)$	$P2_1/a.1'(00g)00s$	6	9.06/13.63	16.33/16.65	50.45/70.36	66.25/67.07
	$P2_1/a.1'(00g)s0s$	6	8.30/12.56	8.61/8.94	31.02/44.43	25.51/26.02
(Pn)	$Pn.1'(0bg)$	12	8.76/14.96	10.22/11.00	32.50/68.85	30.70/32.35
	$Pn.1'(0bg)ss$	12	8.39/14.47	8.50/9.44	22.52/58.07	19.50/22.34
$(P2_1^{[100]})$	$P2_1.1'(0bg)0s$	12	8.02/13.73	8.12/8.93	18.84/48.77	19.85/21.69
(Pm)	$Pm.1'(a0g)0s$	8	8.49/14.99	9.03/9.83	26.24/65.29	22.33/24.34
	$Pm.1'(a0g)ss$	16	8.77/15.17	10.99/11.63	34.04/69.84	33.93/35.09
$(P2_1^{[010]})$	$P2_1.1'(a0g)0s$	12	8.70/15.50	8.02/8.86	17.09/45.50	14.44/16.77
(Pa)	$Pa.1'(00g)0s$	12	7.77/13.86	7.80/8.43	21.29/52.56	19.53/21.25
$(P2_1^{[001]})$	$P2_1.1'(00g)0s$	12	9.04/16.78	16.78/17.20	37.72/62.45	62.78/62.97
	$P2_1.1'(00g)ss$	12	8.67/15.27	8.95/9.83	27.66/64.57	22.17/24.66
$(P\bar{1})$	$P\bar{1}.1'(abg)0s$	12	8.46/15.25	8.14/9.15	21.12/51.12	17.28/20.21
$(P1)$	$P1.1'(abg)0s$	24	8.51/15.78	8.53/9.67	20.69/60.85	18.43/21.46
	<i>double helix</i> $\uparrow c$	2	10.05/17.02	14.16/15.20	64.61/89.86	51.08/53.45

In addition to the refined models which follow from symmetry considerations, the double-helical model from the literature was considered. For this, the nuclear structure was described in space group $P1$ and suitable constraints for the magnetic moments enforcing the double-helical model were introduced. However, our data show conclusively that this model can definitely be discarded as the agreement factors for the satellite reflections are very high.

The model that describes the magnetic structure of CrAs instead cannot be asserted solely on the basis of the presented agreement factors. For the emphasized models, they are too close to each other to allow an unambiguous decision, and further analysis is necessary to possibly narrow down the potentially valid magnetic models.

In the refinements so far, the only restraints for the magnetic model were the ones posed by the symmetry of the respective superspace group. For the emphasized ‘good’ models, further refinements with additional restraints were performed in order to get insights into possible magnetic models in which the degree of freedom is reduced to allow physical restrictions. The first tested restraint is that the Cr atoms that are symmetrically independent carry an equal – but not constant – magnetic moment (“ M equal”). The second tested restraint is that the magnetic moments of the symmetrically independent Cr atoms are respectively constant at an optimal value (“ M optimal”). The third tested restraint combines the two previous ones, with all Cr atoms carrying the same constant magnetic moment (“ M equal+optimal”). Neither restraint is forced by the known properties of Cr in the CrAs system, but they can be taken as valid assumptions based on the fact that all Cr atoms in the crystal structure of CrAs are equivalent and thus indistinguishable. Hence, while they do not allow a conclusive discarding of any non-restrained model solely based on the agreement factors, they give an idea of how well the freely-refined model adheres to certain physical restrictions.

The obtained agreement factors for these refinements are given in Table 8.4. The full details of the refinements in the restrained magnetic models are given in the Appendix (Tables C.18), including corresponding visualizations (Figures C.1–C.7).

Table 8.4: Final agreement factors of the magnetic models for CrAs tested with additional restraints based on the refinement of the neutron single-crystal data at $p_{\text{hom}} = 0.17 \text{ GPa}$.

Nuclear space group	Magnetic superspace group	Restraints	No. mag. parameters	all		satellites		$ M $		$< M _{\text{max}}(\text{Cr}^{3+})$
				R (obs/all)	wR (obs/all)	R (obs/all)	wR (obs/all)	min	max	
$(P2_1/n)$	$P2_1/n, 1'(\text{obg})0s$	—	6	8.12/12.50	9.34/9.97	21.86/38.40	28.64/29.88	2.5(3)	3.6(3)	yes
		M optimal	5	8.43/12.83	10.01/10.64	28.93/45.55	32.95/34.19	3.15(10)	3.15(10)	yes
(Pn)	$Pn, 1'(\text{obg})0ss$	—	12	8.61/14.68	8.79/9.71	22.58/58.47	19.44/22.32	2(7)	6(7)	yes within error
		M equal	10	8.72/14.90	9.10/10.01	25.58/63.52	21.74/24.49	1.8(3)	5.1(3)	no
		M optimal	10	8.72/14.63	9.85/10.55	25.98/57.79	26.88/28.12	2.76(11)	4.26(11)	no
		M eq. + opt.	9	8.85/14.65	10.29/10.97	29.66/58.45	29.58/30.72	3.67(8)	3.67(8)	yes
$(P2_1^{[100]})$	$P2_1, 1'(\text{obg})0s$	—	12	8.31/13.98	8.49/9.28	19.03/49.98	19.99/21.84	0.2(16)	5.9(16)	no
		M equal	10	8.35/14.05	8.69/9.46	20.60/50.97	21.62/23.27	1.7(2)	4.2(2)	no
		M optimal	10	8.42/14.13	9.21/9.97	23.68/54.07	25.41/26.95	1.16(11)	4.34(11)	no
		M eq. + opt.	9	8.49/13.98	9.82/10.49	26.74/49.90	29.38/30.41	2.77(6)	2.77(6)	yes
$(P2_1^{[010]})$	$P2_1, 1'(\text{aog})0s$	—	12	8.97/15.73	8.35/9.18	17.18/45.33	14.58/16.86	1.2(14)	4.4(14)	yes within error
		M equal	10	8.99/15.83	8.43/9.31	17.68/47.60	15.49/18.27	2.29(11)	3.91(11)	yes within error
		M optimal	10	9.12/15.83	8.74/9.50	21.23/47.62	18.66/20.21	2.43(11)	3.73(11)	yes
		M eq. + opt.	9	9.08/15.94	8.66/9.48	20.21/49.96	17.88/19.97	3.16(8)	3.16(8)	yes
(Pa)	$Pa, 1'(\text{obg})0s$	—	12	8.16/14.12	8.40/8.97	21.41/52.30	19.60/21.27	1(2)	6(2)	no
		M equal	10	8.21/14.13	8.52/9.06	22.72/52.72	20.57/21.96	1.4(3)	4.4(3)	no
		M optimal	10	8.20/14.14	8.53/9.10	22.53/52.93	20.63/22.28	1.71(10)	4.21(10)	no
		M eq. + opt.	9	8.34/14.27	8.89/9.41	27.22/56.59	23.28/24.47	3.12(8)	3.12(8)	yes
$(P1)$	$P1, 1'(\text{abg})0s$	—	12	8.75/15.51	8.49/9.47	21.26/51.13	17.43/20.33	1.3(7)	4.5(7)	yes within error
		M equal	10	8.96/15.73	8.95/9.85	27.31/56.50	21.72/23.72	2.44(12)	3.90(12)	yes within error
		M optimal	10	8.97/15.82	9.06/9.95	27.55/58.54	22.67/24.52	2.7(2)	3.5(2)	yes
		M eq. + opt.	9	9.00/15.88	9.11/10.01	27.99/59.85	23.07/24.98	3.2(2)	3.2(2)	yes
$(P1)$	$P1, 1'(\text{abg})0s$	—	24	8.77/16.03	8.81/9.94	20.68/61.04	18.27/21.38	1(6)	7(6)	yes within error
		M equal	18	8.72/16.10	8.94/10.22	19.34/62.82	19.36/23.59	2.3(3)	4.7(3)	no
		M optimal	20	8.89/16.03	9.35/10.35	24.61/61.36	22.54/24.50	2.26(14)	4.98(14)	no
		M eq. + opt.	17	8.87/16.19	9.35/10.49	23.72/64.84	22.51/25.54	3.64(9)	3.64(9)	yes
	$double\ helix\ \uparrow c$	helix	2	10.05/16.47	14.65/15.41	58.53/70.62	53.26/54.21	2.25(8)	2.25(8)	yes

The number of refined magnetic parameters⁹ is reduced by the imposition of the respective restraint, which, as expected, leads to the agreement factors getting worse. In general, the restraint of an optimal value for the magnetic moments has a larger effect than the equalization of the magnetic moments despite the same or even lower (in the case of *P1*) number of refined magnetic parameters. More significance than to the agreement factors, however, can be assigned to the values obtained for the occurring magnetic moments in the differently restrained models. For the Cr atoms within CrAs – which are in the Cr^{3+} state¹⁰ – the maximum possible magnetic moment¹¹ is $|M|_{\text{max}} = \sqrt{3} \cdot (3 + 2) \mu_{\text{B}} = 3.87 \mu_{\text{B}}$. It is evident that for a considerable number of tested magnetic models the maximum magnetic moment exceeds this theoretical limit even considering the corresponding standard deviation; as a consequence, those models are disregarded as incompatible with a valence state of 3+ for Cr. The remaining magnetic models are discussed below in more detail.

8.3.3 Validation of the Magnetic Models with Powder Data

In order to confirm that the magnetic models obtained on the basis of the single-crystal data are also in agreement with the powder diffraction data, the (unrestrained) magnetic models described above were refined on the basis of the neutron powder diffraction measurements. For the data set at 1.5 K – essentially the temperature of the single-crystal measurements, albeit measured at ambient pressure – all superspace groups pertaining to the nuclear *Pnma* symmetry and its subgroups were tested (see Table C.19 in the Appendix). The results confirm that the previously emphasized ‘best’ superspace groups from the single-crystal data analysis do in fact lead to the best agreement, although the difference in agreement factors to some other superspace groups is quite small. Based on these results, for the analysis of the powder data at higher temperatures, only those superspace groups with sufficiently good agreement in both data sets – single-crystal data at low pressure as well as powder at the lowest temperature – were considered in addition to the double-helical literature model.

Table 8.5 shows the relevant refinement values for those superspace groups at two representative temperature points, 1.5 K (base temperature) and 240 K (the highest temperature in the magnetic phase where the pattern is not dominated by the high-temperature paramagnetic phase¹². The full list of refinement details for all temperatures is given in the Appendix (Table C.20).

⁹The number of refined magnetic parameters listed in Table 8.4 was determined from theoretical considerations based on the applied restraints.

¹⁰The Cr^{3+} was confirmed for the high-temperature state [12] and no significant change in the bond-valence-state is seen in our synchrotron X-ray data on going to the low-temperature phase of CrAs. Hence, the Cr^{3+} is present also in the low-temperature state of CrAs.

¹¹The maximum magnetic moment is determined by the number of unpaired electrons n as $|M|_{\text{max}} = \sqrt{n \cdot (n + 2)} \mu_{\text{B}}$, with $n = 3$ for Cr^{3+} following its electron configuration $[\text{Ar}]3d^3$ [220].

¹²In the measurement at 260 K, the low-temperature phase is visible in accordance with the transition temperature of $T_{\text{N}} = 267$ K, but the high-temperature phase is dominant in the pattern, resulting in a generally worse fit of the magnetic low-temperature phase compared to the measurement at 240 K.

Table 8.5: Final agreement factors for selected magnetic models based on the refinement of neutron powder data at two representative temperature points.

T [K]	Nuclear space group	Magnetic superspace group	satellites		profile	
			R (obs/all)	wR (obs/all)	R_p	wR_p
1.5	$P2_1/n$	$P2_1/n.1'(0bg)0ss$	8.74/8.92	6.69/6.71	6.55	8.86
	Pn	$Pn.1'(0bg)ss$	8.46/8.93	6.48/6.52	6.51	8.81
	$P2_1^{[100]}$	$P2_1.1'(0bg)0s$	6.31/6.36	5.51/5.52	5.99	8.10
	$P2_1^{[010]}$	$P2_1.1'(a0g)0s$	6.37/6.46	5.45/5.46	5.90	7.96
	Pa	$Pa.1'(00g)0s$	6.54/6.63	5.54/5.55	5.99	8.10
	$P\bar{1}$	$P\bar{1}.1'(abg)0s$	6.67/6.92	5.78/5.81	6.17	8.24
	$P1$	$P1.1'(abg)0s$	6.64/6.80	5.63/5.64	5.99	8.02
		<i>double helix</i> $\uparrow c$	5.81/6.27	4.90/4.96	6.12	8.30
240	$P2_1/n$	$P2_1/n.1'(0bg)0ss$	7.48/8.26	7.94/7.96	7.18	9.64
	Pn	$Pn.1'(0bg)ss$	6.83/8.74	7.76/7.83	7.16	9.60
	$P2_1^{[100]}$	$P2_1.1'(0bg)0s$	5.79/7.45	7.35/7.41	7.04	9.45
	$P2_1^{[010]}$	$P2_1.1'(a0g)0s$	5.79/6.36	6.92/6.93	7.16	9.56
	Pa	$Pa.1'(00g)0s$	5.99/7.50	7.32/7.38	7.09	9.50
	$P\bar{1}$	$P\bar{1}.1'(abg)0s$	6.06/6.61	6.81/6.83	7.13	9.51
	$P1$	$P1.1'(abg)0s$	5.50/6.00	6.90/6.91	7.16	9.54
		<i>double helix</i> $\uparrow c$	5.34/6.44	7.59/7.63	7.51	10.00

As in the case of the single-crystal data, the quality of the refinements for the seven best models is very similar and generally too close to each other to allow a definite selection of any one particular superspace group as the correct one. Comparing the models within this group, however, shows that the models corresponding to the superspace groups $P2_1/n.1'(0bg)0ss$ and $Pn.1'(0bg)ss$ exhibit consistently slightly worse agreement for the satellite reflections. In contrast to the single-crystal data, the agreement of the double-helical model with the data is approximately as good as for the other superspace groups. In fact, at low temperatures the double-helical model leads to a slightly better agreement of the satellite reflections, although this comes at the cost of a slightly worse agreement of the powder profile. At high temperature this is not the case anymore, with the double-helical model performing slightly worse than the other models.

8.3.4 Discussion

The double-helical model has been used to describe the magnetic structure of CrAs since the first experimental investigation. Subsequent studies built upon and improved the model, but did not put the assumed starting double-helical model itself into question. Our powder and single-crystal data allow the investigation of both characteristics of this structure: the propagation vector of the magnetic modulation, and the precise magnetic structure.

The one key feature that is indubitably preserved by confirmation *via* our neu-

tron powder data is the propagation vector \mathbf{k} . However, as mentioned before, it is independent of the precise magnetic structure, and this independence can explain why the magnetic structure of CrAs was not put into question sooner. Operating on the assumption that the double-helical model is correct, \mathbf{k} is generally the most interesting parameter, and if \mathbf{k} is the primary interest of investigation, powder diffraction is a good method of choice, as it allows a simple and fast determination of its precise value. As our own results show, powder diffraction data do indeed support – or, rather, they do not contradict – the double-helical model, so that the validity of the model is not put into question using this method. A review of the literature shows that all determinations of the magnetic structure of CrAs were in fact done on the basis of powder diffraction data, with only one exception [11], where only the position of the measured single-crystal reflections was used to determine the value of \mathbf{k} , and the data were apparently not refined for a full magnetic structure determination. Powder diffraction, however, inevitably entails a loss of information compared to single-crystal diffraction due to the reduction of three-dimensionally resolved information to one dimension. Hence, a conclusive determination of the magnetic structure of CrAs has to be based on single-crystal diffraction instead.

The results presented here indicate that, while the double-helical model from the literature leads indeed to a satisfactory fit of the powder diffraction data, the same is not true for the single-crystal data. Based on this observation, we conclude that this model is in fact incorrect. Although our single-crystal data were measured (nominally) under pressure, there is no indication of an additional magnetic phase transition within the antiferromagnetic phase region of CrAs, so that we generalize our finding to the whole corresponding stability region of the antiferromagnetically ordered phase. While we are thus confident to disregard the double-helical model described in the literature, it is not so simple to clearly identify which magnetic structure CrAs exhibits instead.

The agreement factors for the different magnetic models alone do certainly not allow a conclusive positive decision for one in particular, with several models yielding comparably good agreement factors. The analysis of these selected models is expanded by the introduction of restraints for the modulated magnetic moments of the Cr atoms. Taking into account the compatibility of the refinements with physical limitations, this allows to narrow down the possible models to those where the maximum magnetic moment does not violate the theoretical limit of $3.87 \mu_B$ for Cr^{3+} . While all those models are in principle compatible, only those with the best agreement factors are again considered in the following (see Table 8.4): $P2_1^{[010]}|_{\text{eq.}+\text{opt.}}$, $Pa|_{\text{eq.}+\text{opt.}}$, $P\bar{1}|_{\text{eq.}+\text{opt.}}$, and $P1|_{\text{eq.}+\text{opt.}}$ ¹³. In the cases of $P2_1^{[010]}$ and $P\bar{1}$, the unrestrained models would also be allowed, but in order to limit the analysis the respective restrained models ("M equal + optimal") were preferred – the corresponding significantly lower number of refinement parameters leading to only a slight worsening of the agreement factors indicates that the applied restraints are in good agreement with the data. For these four models, a visualization of the respective magnetic structure is shown in Figure 8.19; the modulation is shown over 20 nuclear unit cells containing 7 period lengths of the modulation corresponding to the

¹³Since only one magnetic superspace group is considered for each nuclear space group (see Table 8.4), in the following the latter is used in combination with the applied restraint in the description of the model for the sake of brevity.

propagation vector of $k_c = 0.35 = 7/20$ in good approximation of the incommensurate k_c .

In the models $P2_1^{[010]}|_{\text{eq.}+\text{opt.}}$ and $P\bar{1}|_{\text{eq.}+\text{opt.}}$ the Cr sites¹⁴ Cr_A and Cr_D are symmetrically equivalent, as are Cr_B and Cr_C , while in model $Pa|_{\text{eq.}+\text{opt.}}$ this holds for the site pairs Cr_A/Cr_B and Cr_C/Cr_D . In model $P1|_{\text{eq.}+\text{opt.}}$, all four Cr sites are symmetrically independent. The respective relation can be seen quite easily in the projection of the magnetic structure along the c -axis in Figure 8.19. The projection also shows that with one exception, the magnetic moments on the Cr sites can be described by a spiral¹⁵, although in some cases the moments rather lie on an ellipse. The exception is the Cr_C site in the $P1|_{\text{eq.}+\text{opt.}}$ model, which in the projection along c fluctuates linearly approximately in the a, b -diagonal instead. Information about the precise modulations on the different Cr sites in the models can more easily be seen Figure 8.20, showing a breakdown of the directional components along the x -, y - and z -axis (M_x , M_y and M_z , respectively). The absolute values $|M|$ of the magnetic moment are also shown. The full details can be found in the Appendix (Table C.18).

The fact that the magnetic moment in all models considered here is constant and the same for all Cr sites is a consequence of the imposed restraints, and can thus in itself not be considered a common emergent feature of the models. Remarkably, however, the value of the magnetic moment is within the error the same at about $3.2(2) \mu_B$ for the models $P2_1^{[010]}|_{\text{eq.}+\text{opt.}}$, $Pa|_{\text{eq.}+\text{opt.}}$ and $P\bar{1}|_{\text{eq.}+\text{opt.}}$, and with $3.6(1) \mu_B$ just a bit higher in model $P1|_{\text{eq.}+\text{opt.}}$. This agreement in the approximate size of the magnetic moment between the different models could indicate that the actual value is close to this range.

Another common feature – or rather lack thereof – of the four models is any clear magnetic coupling of neighboring Cr sites, be it ferro- or antiferromagnetic. The magnetic moments on Cr site pairs associated with non-trivial interactions¹⁶ in the electronic model ($\text{Cr}^{\text{I}}\text{--}\text{Cr}^{\text{II}}$ and $\text{Cr}^{\text{I}}\text{--}\text{Cr}^{\text{IV}}$ in the crystallographic description, corresponding to $\text{Cr}_A\text{--}\text{Cr}_B$ and $\text{Cr}_A\text{--}\text{Cr}_D$ in the geometric description, respectively) show no indication of any systematic local magnetic order. The global antiferromagnetic order of CrAs is, however, preserved by the general modulation, where the oscillating directional components do not allow a net magnetic moment.

Aside from these observations about common features of the relevant models, our data are not suited to make a concrete decision about the actually correct model. Hence, a discussion of model-specific details is not productive at this point.

¹⁴For the description of the magnetic models the Cr sites are labeled Cr_i , $i = A, B, C, D$, to distinguish the general geometrical sites here from crystallographic sites (e.g. Cr^{I} , Chapter 8.2) and symmetry-related sites (e.g. $\text{Cr}1, 1$, Table C.18).

¹⁵For the description of the magnetic structure, a distinction is made here between *spiral* and *helix*. *Spiral* is used for any order with a rotating constant magnetic moment, while *helix* is used for the special case of a spiral where the moments are confined to the plane perpendicular to the propagation vector. This distinction is made here specifically with the intention to help the comparison of general spiral models and the helical model from the literature.

¹⁶Neighboring Cr^{I} atoms are coupled by symmetry which is preserved in the magnetic superspace group, so they exhibit strict ferromagnetic coupling by definition.

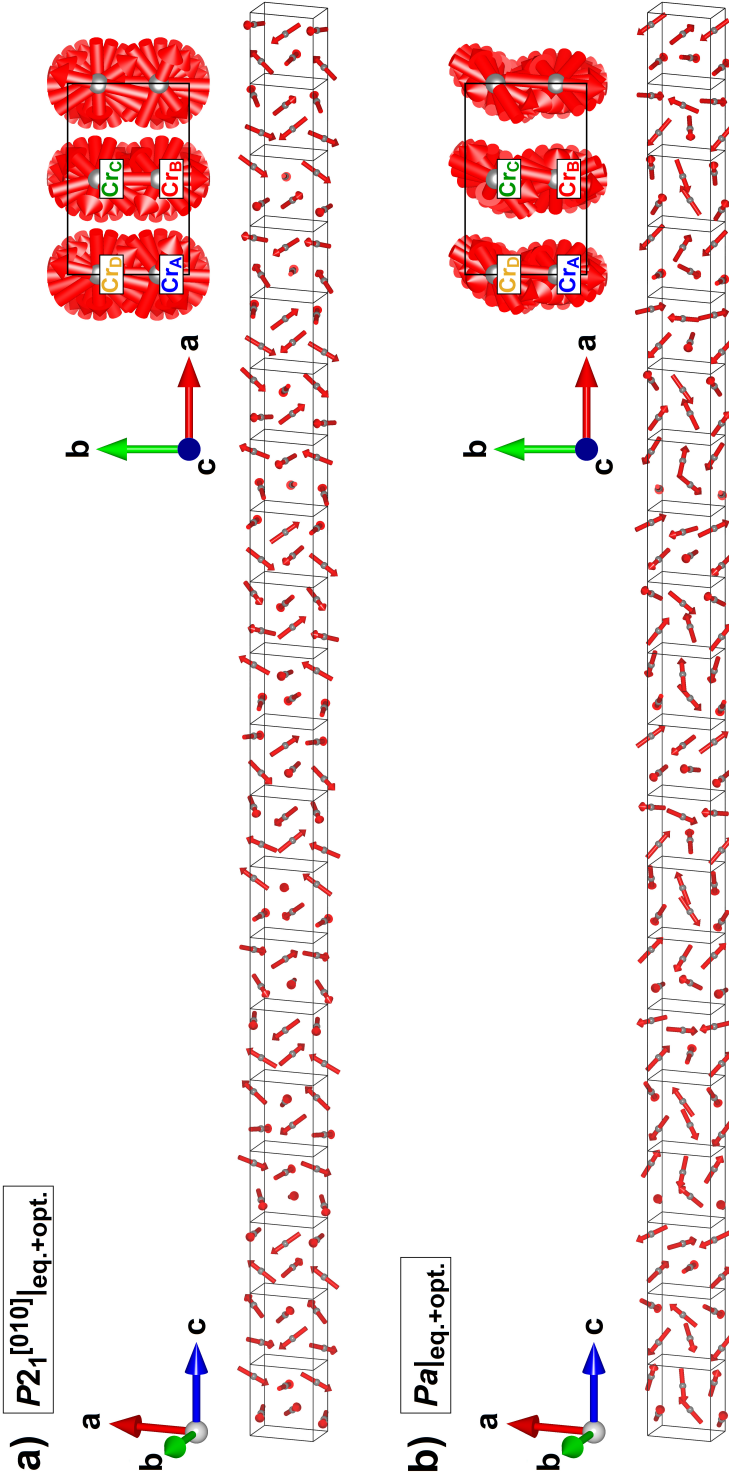


Figure 8.19: The magnetic structure of CrAs refined in the four magnetic models with the best agreement factors: a) $P2_1[010]_{|eq.+opt.}$, b) $Pa_{|eq.+opt.}$, c) $P1_{|eq.+opt.}$ and d) $P1_{|eq.+opt.}$ in tilted projection approximately along the b -axis, shown is the approximate structure with $c' = \frac{20}{7} \cdot c$ of the basic structure. For clarity, only the Cr atoms are shown.

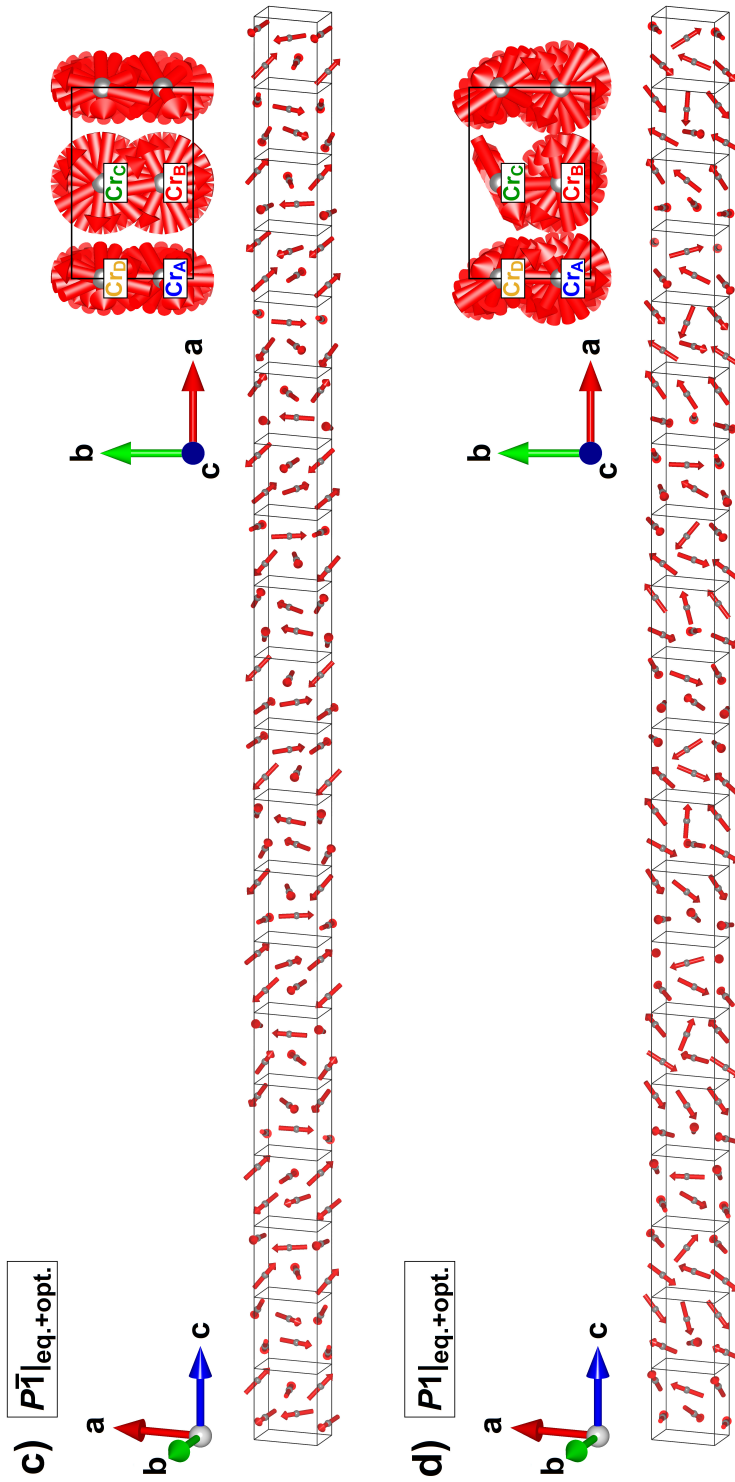


Figure 8.19 (continued): The magnetic structure of CrAs refined in the four magnetic models with the best agreement factors: a) $P2_1[010]|_{\text{eq.}+\text{opt.}}$, b) $P4|_{\text{eq.}+\text{opt.}}$, c) $P\bar{1}|_{\text{eq.}+\text{opt.}}$ and d) $P1|_{\text{eq.}+\text{opt.}}$; projection along the c -axis and in tilted projection approximately along the b -axis, shown is the approximate structure with $c' = 20/7 \cdot c$ of the basic structure. For clarity, only the Cr atoms are shown.

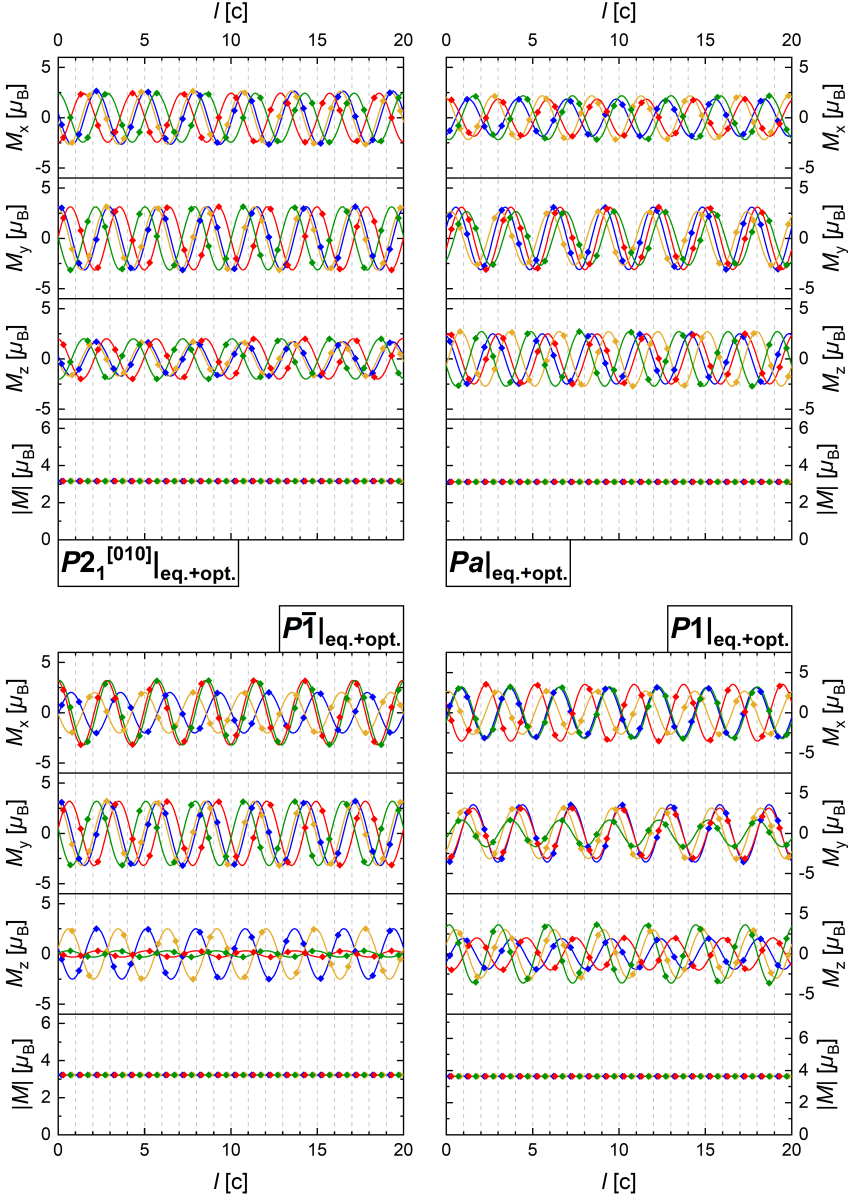


Figure 8.20: The directional components of the magnetic moment along the x -, y - and z -axis (M_x , M_y and M_z , respectively) and the absolute value $|M|$ of the magnetic moment in the approximate structure with $c' = 20/7 \cdot c$ of the basic structure for the four best magnetic models for CrAs. Points indicate values realized on Cr sites, full lines show the underlying modulation function. The colors correspond to the Cr sites as marked in Figure 8.19 and Table C.18. The dashed gray lines mark the unit cell borders of the basic crystal structure.

While the double-helical model reported in the literature does clearly not fit the data as evidenced by the poor agreement factors, it is still compared to the magnetic models described above in order to identify potential characteristics that are either consistently preserved or repudiated. For this, the double-helical model is shown in a similar way as the other models in the restrained model $P1|_{\text{helix}}$ in Figure 8.21.

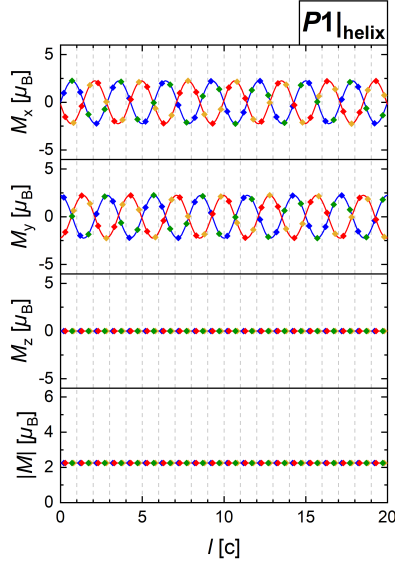


Figure 8.21: The directional components of the magnetic moment along the x -, y - and z -axis (M_x , M_y and M_z , respectively) and the absolute value $|M|$ of the magnetic moment in the approximate structure with $c' = 20/7 \cdot c$ of the basic structure for the double-helical magnetic model for CrAs reported in the literature described in model $P1|_{\text{helix}}$. Points indicate values realized on Cr sites, full lines show the underlying modulation function. The colors correspond to the Cr sites as marked in Figure 8.19 and Table C.18. The dashed gray lines mark the unit cell borders of the basic crystal structure.

Like the previously considered models, the double-helical model has the same constant magnetic moment on all Cr sites as a consequence of the applied restraints. While the other models are in rather good agreement regarding the value of that magnetic moment, the one of the double-helical model is with $2.25(8) \mu_B$ significantly lower, although still larger than the one reported in the literature ($\sim 1.7 \mu_B$). A significantly larger magnetic moment would have considerable ramifications for the whole description of the CrAs system: The generic electronic model for CrAs postulated by Boller and Kallel, 1971 [14], and Zavadskii and Sibarova, 1980 [16], was based on the value of $1.7 \mu_B$ determined from neutron powder diffraction measurements. To accommodate the larger magnetic moment, the description of the electronic configuration would have to be changed significantly. This in turn would potentially invalidate the conclusions that were drawn from it with regard to the effects on the crystal structure. However, as our own investigation of the crystal

structure shows, the model can be used to explain the observed behavior of the crystal structure at and below the phase transition quite well, and can thus not simply be seen as obsolete. To resolve this issue, further investigation to determine the magnetic structure of CrAs unambiguously have to be conducted, before the electronic model is adjusted accordingly.

Another notable difference between the four emphasized magnetic models on the one hand and the double-helical literature model on the other hand is the generally non-vanishing M_z component; the confinement of the magnetic moment of the Cr atoms to the a, b -plane postulated within the double-helical model is not reproduced. In addition, even if considering only the projection of the models along the c -axis, the double-helical model is not replicated by the other models. Although, as mentioned before, the models show a spiral-like behavior in the projection to varying degrees (see Figure 8.19), the detailed behavior of the involved directional components (M_x and M_y) is notably different. For the presence of two in-phase helices as described in the double-helical model, there are three conditions: to realize a circular helix, M_x and M_y must have the same amplitude and a phase difference of $\pm 90^\circ$, and to realize in-phase helices on different Cr sites, the relevant modulations naturally have to be in phase. Specifically regarding the latter condition, the double-helical model is fundamentally incompatible with all but the $P1|_{\text{eq.}+\text{opt.}}$ model, as the symmetry relation of the Cr site pairs Cr_A/Cr_C and Cr_B/Cr_D in the $P1|_{\text{helix}}$ model is not possible in $P2_1^{[010]}|_{\text{eq.}+\text{opt.}}$ and $P\bar{1}|_{\text{eq.}+\text{opt.}}$ (symmetrically related Cr_A/Cr_D and Cr_B/Cr_C) or $Pa|_{\text{eq.}+\text{opt.}}$ (symmetrically related Cr_A/Cr_B and Cr_C/Cr_D). In $P1|_{\text{eq.}+\text{opt.}}$ a site coupling of Cr_A/Cr_C and Cr_B/Cr_D would be allowed, but is not observed. The conditions of approximately the same amplitude in M_x and M_y as well as approximately a $\pm 90^\circ$ phase difference do occur, but not systematically so.

Ultimately, the present investigation of the magnetic structure of CrAs allows to definitely discard the double-helical model reported in the literature with certainty. However, an unambiguous identification of the correct magnetic model is not possible on the basis of our data. Hence, for a conclusive determination of the magnetic structure of CrAs, further dedicated investigations are necessary – however, our result that the previously unquestioned model of the magnetic structure is in fact not correct marks a crucial step for an unambiguous determination of the antiferromagnetic structure of CrAs.

Chapter 9

Summary and Outlook

CrAs was and is a subject of major research interest due to the observed antiferromagnetic phase, whose magnetic structure has been described as a double helix, and its pressure-induced superconductivity. In particular, CrAs is considered a model system for the coexistence of superconductivity and helimagnetism. In this work, the principal aim was the investigation of CrAs under extreme conditions in order to understand the influence of low temperature and high pressure on the crystal and magnetic structure and the interrelation of those two. To this effect, X-ray and neutron diffraction experiments on powder and single-crystal samples under various conditions were conducted. On the basis of these data, the previously reported behavior of the crystal and magnetic structure were revised and extended.

The crystal structure of CrAs was investigated at ambient pressure in the temperature range 35...400 K and at room temperature in the pressure range up to 9.46 GPa with synchrotron and laboratory X-ray single-crystal measurements.

The behavior of the lattice parameters as function of temperature has been investigated before, in particular in the context of the magnetostructural phase transition from the paramagnetic to antiferromagnetic phase at $T_N = 267$ K. Our results confirm the reported abrupt change in the lattice parameters on passing the transition temperature. The effect of the associated large change in the unit cell volume – the formation of microcracks – is directly seen in the condition of the employed samples and indirectly in supporting measurements of the macroscopic resistance of CrAs over several cooling/heating cycles. In addition to this known effect of the phase transition on the microstructure, our results show a second, previously not reported effect in that below the transition temperature, the microstructure exhibits severe twinning. The corresponding twinning element is a three-fold rotation axis along the a -axis. This symmetry element is not present in the orthorhombic $Pnma$ structure of CrAs, but emerges in form of a pseudo-threefold axis during the transition following the characteristic change in lattice parameters, where the ratio c/b goes from $c/b > \sqrt{3}$ to $c/b < \sqrt{3}$ upon cooling; a ratio of $c/b = \sqrt{3}$ corresponds to the orthohexagonal setting of the structure and is closely related to the hexagonal parent NiAs-type structure. As this transition-induced twinning is a direct consequence of the specific change in the lattice parameters, it is not a general feature of this type of structure. In contrast to the behavior observed in dependence on temperature, the application of pressure does not lead to any anomalous effect in the lattice parameters; they show a smooth decrease where the compressibility of the b -axis is

notably higher than that of the *a*- and *c*-axis. The unit cell volume as function of pressure can be fitted by a single equation of state, indicating that there is no phase transition in the investigated pressure range up to 9.46 GPa.

The behavior of the interatomic distances in the crystal structure of CrAs was not studied systematically up to now, with only few and isolated data points having been reported. The present study thus gives the first comprehensive overview of the underlying structural behavior of CrAs in dependence on temperature and on pressure. Of primary interest are the Cr–Cr distances, since the Cr atoms carry the magnetic moment responsible for the magnetic order and (presumably) for the superconductivity. On passing the transition temperature upon cooling, the Cr–Cr distances show abrupt changes (increase in Cr^I–Cr^I and Cr^I–Cr^{IV}, decrease in Cr^I–Cr^{II}); these are the cause for the previously mentioned changes in the lattice parameters. This behavior as well as the behavior at further cooling can be appropriately explained on the basis of an electronic model that has been proposed for CrAs. The observations above the transition temperature and at high pressures – in the paramagnetic phase region of CrAs –, however, are not accounted for by this model. Here, the two distances Cr^I–Cr^I and Cr^I–Cr^{IV} exhibit thermal expansion with increasing temperature and compression with increasing pressure as expected. The Cr^I–Cr^{II} distance – which is also the shortest Cr–Cr distance in the structure –, however, shows anomalous behavior in that neither the increasing temperature nor the increasing pressure have a significant effect within the experimental range, i.e. this distance remains in good approximation constant.

The behavior of the Cr–As distances can likewise be separated into two parts. During the phase transition, they also exhibit abrupt changes, which lower the variance in the distances (i.e. the longest Cr–As distance gets shorter and the shortest Cr–As distance gets longer); this, in concert with the related $\angle\text{As–Cr–As}$ angles, leads to a reduction of the distortions of the coordination polyhedra ([CrAs₆] octahedra and [AsCr₆] trigonal prisms) within the crystal structure. With increasing temperature above the transition temperature as well as with increasing pressure, the Cr–As distances exhibit the expected expansion/compression behavior. The As–As distances show some conspicuous features as function of temperature or of pressure, but since these distances are not coupled to any interactions within the electronic model of Cr, they are assumed to follow from the interplay of the changes in the Cr–Cr and Cr–As distances, and no further importance is attributed to them.

The observed pressure-dependent behavior of the crystal structure of CrAs is compared to other members of the group of transition-metal monopnictides (*TPn*) with the same MnP-type crystal structure. This shows that the trend seen for the Cr–Cr distances in CrAs is generally valid for the interatomic distances T – T , with one distance of low compressibility (T^{I} – T^{II}) and two considerably more compressive distances (T^{I} – T^{I} and T^{I} – T^{IV}). Hence, it can be inferred that the behavior of the T^{I} – T^{II} distance is a feature of the MnP-type structure as linking element. A comprehensive comparison, however, is not possible due to a lack of temperature-dependent data for other compounds.

Building on these results, the study of CrAs can be extended in various directions:

- First, as a direct continuation of the present work, X-ray single-crystal diffraction measurements at simultaneous low temperature and high pressure should be performed. The single-parameter measurements presented here provide a

foundation for the understanding of the two-parameter region, but to actually assess this region, dedicated experiments are inevitably needed. In particular the suppression of the phase transition with increasing pressure and its effect on the crystal structure behavior is of interest. Ultimately, the region of highest interest for CrAs is the superconducting phase region, and to connect features of the crystal structure directly to the emergence of superconductivity, corresponding measurements have to be performed under matching conditions. Due to the necessary extreme combination of low temperature and high pressure, this is not within routinely assessed experimental conditions, but without these, any postulated structure-property relation to elucidate the nature of the superconductivity will remain to some degree speculative.

- Second, to extend the investigation of CrAs in the range investigated in this work, further experimental methods should be employed. In particular with regard to the distinguished Cr^I–Cr^{II} distance, an investigation of the interatomic interactions would be of interest, e.g. by means of inelastic X-ray diffraction for phonon spectra. Such investigations would help to reveal why this specific distance is ‘protected’ in the crystal structure of CrAs and whether it plays a significant role in the observed physical properties of CrAs.
- Third, the effect of elemental substitution *via* doping could yield insights into the precise mechanisms of the pressure-induced properties of CrAs, most notably the superconductivity. The induced changes in the local electronic structure affect the interatomic interactions and thereby the crystal structure. A corresponding investigation could thus reveal potential differences in the behavior of the crystal structure as function of temperature and/or pressure, and allow to further elucidate the relevant interaction mechanics within the structure. While studies on doped CrAs – with substitution of either Cr or As – have been conducted in the past, the behavior of the crystal structure in the doped compounds was not investigated in detail.
- Fourth, on the basis of the available low-temperature and high-pressure data, density-functional theory calculations of the electronic structure should be performed. This would be again of particular interest with regard to the Cr^I–Cr^{II} distance and its role in the crystal structure of CrAs. In addition, these calculations would allow an assessment of the electronic model proposed and employed for CrAs, which seems to explain successfully the observed features at and below the phase transition. The calculated model on the basis of experimental data without further *a priori* assumptions can potentially further validate the inferences based on the established electronic model in this and other works, and furthermore allow an extension into the previously not further considered high-temperature region.
- Fifth, seeing CrAs as exemplary member of the group of transition-metal monpnictides with the same or related crystal structures, other members should be investigated with similar methods. This would provide the foundation for a systematic study of the role of the crystal structure in the various properties like magnetism and superconductivity. Although there have been investigations into some of the group’s compounds, the lack of comparable

data between compounds does not allow any conclusive assessment. Regarding CrAs, this is, however, necessary in order to separate general features of the crystal structure and specific features coupled to the particularities of the individual compound.

Within this work, the magnetic structure of CrAs was investigated by neutron powder diffraction at ambient pressure in the temperature range 1.5...300 K and by neutron single-crystal diffraction at 2 K at nominal pressures of 0.17 GPa and 1.2 GPa. To describe the incommensurately modulated magnetic structure of CrAs, two characteristics were determined independently: the propagation vector \mathbf{k} of the modulation, and the precise arrangement of the magnetic moments carried by the Cr atoms in one modulation period. Our neutron powder measurements confirm the previously reported \mathbf{k} -vector and its behavior as function of temperature. Beyond that, the powder measurements do not allow to differentiate between multiple specific magnetic structures which fit our data equally well. In the literature, the underlying magnetic structure is described as double helix – two in-phase pairs of magnetic moments on the four Cr atoms in one unit cell – with the helices propagating along the c -axis. On the basis of our neutron single-crystal measurements, however, it can be concluded that this is not a valid model for the magnetic structure of CrAs. Our data clearly show that the fit of the double-helical model from the literature does not yield satisfactory results and that it is significantly worse than various other models for the magnetic structure. Instead, we obtain several new models for the magnetic structure that fit the data equally well. These are described by the models $P2_1^{[010]}|_{\text{eq.}+\text{opt.}}$, $Pa|_{\text{eq.}+\text{opt.}}$, $P\bar{1}|_{\text{eq.}+\text{opt.}}$, and $P1|_{\text{eq.}+\text{opt.}}$, corresponding to descriptions in the magnetic superspace groups $P2_1.1'(\text{a}0\text{g})0\text{s}$, $Pa.1'(\text{0}0\text{g})0\text{s}$, $P\bar{1}.1'(\text{abg})0\text{s}$ and $P1.1'(\text{abg})0\text{s}$, in each case with the restriction of constant and equal magnetic moments for all Cr sites. Following this restriction, all models are spiral-like (rotating constant magnetic moment), with no spin-density wave character that would cause a non-constant magnetic moment. The common feature of a value of about $3.2(2) \mu_{\text{B}}$ for the magnetic moment of the Cr atoms indicates that also the previously assumed value $\sim 1.7 \mu_{\text{B}}$ is not correct. Since the electronic model used for CrAs is based on this value, our result has far-reaching consequences also for properties of CrAs not directly coupled to the magnetic moment itself.

To determine the actual magnetic structure unambiguously, polarized neutron single-crystal diffraction experiments could be of great help. Assuming that the magnetic structure of CrAs does not change within the antiferromagnetic phase region – for which there are no indications so far – these experiments do not have to be conducted at high pressure, which would be very challenging for polarized neutron radiation. Hence, purely temperature-dependent experiments below $T_{\text{N}} = 267 \text{ K}$ using polarized neutrons might be sufficient for an unambiguous identification of the correct model.

Apart from the attempts to determine the magnetic structure of CrAs unambiguously, additional measurements to investigate its behavior as function of temperature and pressure can be performed. In particular, experiments at simultaneously low temperatures and high pressures are of interest to elucidate the interplay of the magnetism and the superconductivity – while our results show that CrAs is, after all, not a model system for neighboring helimagnetic and superconducting phases, this does not change the fact that the nature of superconductivity in CrAs remains

unknown.

The prerequisite for such measurements at extreme conditions is the availability of suitable high-pressure devices for neutron diffraction. In the context of this work, several clamp cells have been developed, which allow measurements at low temperatures and high pressures, and in addition in combination with applied high magnetic fields. All cells were specifically designed to fit into the existing experimental setups of the instruments DNS, POLI and MIRA at the MLZ, but are intended for future use as generally available sample environment for any suitable instrument.

The cell types M1 and M1D are monobloc clamp cells, which are expected to reach maximum pressures of 1.1 GPa in the CuBe variant and 1.5 GPa in the NiCrAl variant based on simulations. Unlike the M1 type, the M1D type features an optical access path to the inner part of the cell, allowing the use of ruby luminescence to determine the applied pressure *in situ* during loading. Regarding their performance with pressure, the two monobloc cell types are identical. Based on the M1-CuBe, the pressure/load curve and the neutron transmission were determined experimentally by means of neutron radiation, and the suitability of the cell for the measurement of magnetic reflections was shown. In addition, for both cell types the thermal response in a cryostat was measured. Independent of neutron radiation, the M1D-type cells were used to obtain calibration curves for the pressure as function of the load force. The F1 type is a fretted cell, with theoretical limits of about 2.0 GPa in the NiCrAl/TiZr variant and 2.6 GPa in the NiCrAl/CuBe variant. Like the M1D cell type, it allows *in situ* pressure determination through an optical access path. For the F1 type, no practical tests were performed due to various delays caused by the SARS-CoV-2 pandemic.

In order to establish the cells for experimental use, further tests are needed, which could not be performed in the course of this thesis due to the unavailability of neutrons at the MLZ as a consequence of the pandemic and subsequent technical problems. For the M1/M1D cells, in addition to the already performed tests, a cross-calibration between the ruby pressure scale and the NaCl pressure scale is necessary to allow a targeted loading of the cell with regard to the actual pressure at the sample position. The more cross-calibration measurements as well as further neutron-independent load/pressure calibration measurements are performed, the more reliable is the resulting calibration. Aside from these preparative measurements, the cells have to be tested for use in full experiments for data collection. For the F1 cells, the same test and characterization measurements as for the M1/M1D cells have yet to be performed.

However, even while not all planned tests with the clamp cells could be performed within the context of this work, the various produced monobloc clamp cells already now present a new experimental option that is available for instruments at the MLZ and opens a wide field of new science under extreme conditions.

Bibliography

- [1] H. Nowotny and O. Årstad. Röntgenographische Untersuchung im System Cr–CrAs. *Z. Phys. Chem.*, 38B(1):461–465, 1938.
- [2] H. Boller and H. Nowotny. Kristallchemische Untersuchungen an Monophosphiden und -arseniden in den Systemen: Ti–{Cr,Mo,W}–{P,As}. *Monatsh. Chem.*, 96(3):852–862, 1965.
- [3] H. Haraldsen and E. Nygaard. Magnetische Untersuchungen am System Chrom-Arsen. *Z. Elektrochem.*, 45(9):686–688, 1939.
- [4] M. Yuzuri. On the Magnetic Properties of Cr₂As and Cu₂Sb. *J. Phys. Soc. Jpn.*, 15(11):2007–2012, 1960.
- [5] R. Sobczak, H. Boller, and H. Bittner. Magnetische Untersuchungen an Übergangsmetallarseniden. *Monatsh. Chem.*, 99(6):2227–2234, 1968.
- [6] H. Watanabe, N. Kazama, Y. Yamaguchi, and M. Ohashi. Magnetic Structure of CrAs and Mn-Substituted CrAs. *J. Appl. Phys.*, 40(3):1128–1129, 1969.
- [7] S. Rundqvist. Phosphides of the B31 (MnP) Structure Type. *Acta Chem. Scand.*, 16(2):287–292, 1962.
- [8] J. Cheng and J. Luo. Pressure-Induced Superconductivity in CrAs and MnP. *J. Phys.: Condens. Matter*, 29(38):383003, 2017.
- [9] K. Selte, A. Kjekshus, W.E. Jamison, A.F. Andresen, and J.E. Engebretsen. Magnetic Structure and Properties of CrAs. *Acta Chem. Scand.*, 25(5):1703–1714, 1971.
- [10] R.Y. Chen and N.L. Wang. Progress in Cr- and Mn-Based Superconductors: A Key Issues Review. *Rep. Prog. Phys.*, 82(1):012503, 2019.
- [11] M. Matsuda, F.K. Lin, R. Yu, J.-G. Cheng, W. Wu, J.P. Sun, J.H. Zhang, P.J. Sun, K. Matsubayashi, T. Miyake, T. Kato, J.-Q. Yan, M.B. Stone, Q. Si, J.L. Luo, and Y. Uwatoko. Evolution of Magnetic Double Helix and Quantum Criticality near a Dome of Superconductivity in CrAs. *Phys. Rev. X*, 8(3):031017, 2018.
- [12] B.Y. Pan, H.C. Xu, Y. Liu, R. Sutarto, F. He, Y. Shen, Y.Q. Hao, J. Zhao, L. Harriger, and D.L. Feng. Anomalous Helimagnetic Domain Shrinkage due to the Weakening of the Dzyaloshinskii-Moriya Interaction in CrAs. *Phys. Rev. B*, 102(10):104432, 2020.

- [13] L. Keller, J.S. White, M. Frontzek, P. Babkevich, M.A. Susner, Z.C. Sims, A.S. Sefat, H.M. Rønnow, and C. Rüegg. Pressure Dependence of the Magnetic Order in CrAs: A Neutron Diffraction Investigation. *Phys. Rev. B*, 91(2):020409(R), 2015.
- [14] H. Boller and A. Kallel. First Order Crystallographic and Magnetic Phase Transition in CrAs. *Solid State Commun.*, 9(19):1699–1706, 1971.
- [15] Y. Shen, Q. Wang, Y. Hao, B. Pan, Y. Feng, Q. Huang, L.W. Harriger, J.B. Leao, Y. Zhao, R.M. Chisnell, J.W. Lynn, H. Cao, J. Hu, and J. Zhao. Structural and Magnetic Phase Diagram of CrAs and its Relationship with Pressure-Induced Superconductivity. *Phys. Rev. B*, 93(6):060503(R), 2016.
- [16] É.A. Zavadskii and I.A. Sibarova. Some Features of Phase Transition in Chromium Arsenide at High Pressures. *Sov. Phys. JETP*, 51(3):542–527, 1980.
- [17] W. Wu, X.D. Zhang, Z.H. Yin, P. Zheng, N.L. Wang, and J.L. Luo. Low Temperature Properties of Pnictide CrAs Single Crystal. *Sci. China Phys. Mech. Astron.*, 53(7):1207–1211, 2010.
- [18] J.-Q. Yan, A. Kreyssig, S. Nandi, N. Ni, S.L. Bud’ko, A. Kracher, R.J. McQueeney, R.W. McCallum, T.A. Lograsso, A.I. Goldman, and P.C. Canfield. Structural Transition and Anisotropic Properties of Single-Crystalline SrFe_2As_2 . *Phys. Rev. B*, 78(2):024516, 2008.
- [19] X.F. Wang, T. Wu, G. Wu, H. Chen, Y.L. Xie, J.J. Ying, Y.J. Yan, R.H. Liu, and X.H. Chen. Anisotropy in the Electrical Resistivity and Susceptibility of Superconducting BaFe_2As_2 Single Crystals. *Phys. Rev. Lett.*, 102(11):117005, 2009.
- [20] K. Selte and A. Kjekshus. On Phase Transitions between the MnP and NiAs Type Structures. *Acta Chem. Scand.*, 27(9):3195–3206, 1973.
- [21] R. Blachnik, G. Kudermann, F. Grønvold, A. Alles, B. Falk, and E.F. Westrum, Jr. CrAs: Heat Capacity, Enthalpy Increments, Thermodynamic Properties from 5 to 1280 K, and Transitions. *J. Chem. Thermodyn.*, 10(6):507–522, 1978.
- [22] H. Kotegawa, K. Matsushima, S. Nakahara, H. Tou, J. Kaneyoshi, T. Nishiwaki, E. Matsuoka, H. Sugawara, and H. Harima. Superconductivity and Magnetic Fluctuations Developing in the Vicinity of Strong First-Order Magnetic Transition in CrAs. *J. Phys.: Condens. Matter*, 29(23):234002, 2017.
- [23] N. Kazama and H. Watanabe. Magnetic Properties of $\text{Cr}_{1-x}\text{Mn}_x\text{As}$ System. *J. Phys. Soc. Jpn.*, 30(5):1319–1329, 1971.
- [24] N. Kazama and H. Watanabe. Study of the Magnetic Transition of CrAs. *J. Phys. Soc. Jpn.*, 31(3):943, 1971.
- [25] K. Sen, Y. Yao, R. Heid, A. Omoumi, F. Hardy, K. Willa, M. Merz, A.A. Haghighirad, and M. Le Tacon. Raman Scattering Study of Lattice and Magnetic Excitations in CrAs. *Phys. Rev. B*, 100(10):104301, 2019.

-
- [26] H. Kotegawa, S. Nakahara, H. Tou, and H. Sugawara. Superconductivity of 2.2 K under Pressure in Helimagnet CrAs. *J. Phys. Soc. Jpn.*, 83(9):093702, 2014.
- [27] S.-I. Kim, S.-G. Jung, S. Shin, W.N. Kang, and T. Park. Anisotropic Upper Critical Field in Pressure-Induced CrAs Superconductor. *J. Appl. Phys.*, 122(24):243902, 2017.
- [28] W. Wu, J. Cheng, K. Matsubayashi, P. Kong, F. Lin, C. Jin, N. Wang, Y. Uwatoko, and J. Luo. Superconductivity in the Vicinity of Antiferromagnetic Order in CrAs. *Nat. Commun.*, 5:5508, 2014.
- [29] H. Kotegawa, S. Nakahara, R. Akamatsu, H. Tou, H. Sugawara, and H. Harima. Detection of an Unconventional Superconducting Phase in the Vicinity of the Strong First-Order Magnetic Transition in CrAs using ^{75}As -Nuclear Quadrupole Resonance. *Phys. Rev. Lett.*, 114(11):117002, 2015.
- [30] Z. Yu, W. Wu, Q. Hu, J. Zhao, C. Li, K. Yang, J. Cheng, J. Luo, L. Wang, and H.-K. Mao. Anomalous Anisotropic Compression Behavior of Superconducting CrAs under High Pressure. *Proc. Natl. Acad. Sci. U.S.A.*, 112(48):14766–14770, 2015.
- [31] B. Wang, Q. Lu, Y. Ge, K. Zhang, W. Xie, W.-M. Liu, and Y. Liu. Magnetic Diversity in Stable and Metastable Structures of CrAs. *Phys. Rev. B*, 96(13):134116, 2017.
- [32] J.B. Goodenough. Localized vs Collective Descriptions of Magnetic Electrons. *J. Appl. Phys.*, 39(2):403–411, 1968.
- [33] R. Khasanov, Z. Guguchia, I. Eremin, H. Luetkens, A. Amato, P.K. Biswas, C. Rüegg, M.A. Susner, A.S. Sefat, N.D. Zhigadlo, and E. Morenzoni. Pressure-Induced Electronic Phase Separation of Magnetism and Superconductivity in CrAs. *Sci. Rep.*, 5:13788, 2015.
- [34] N.D. Mathur, F.M. Grosche, S.R. Julian, I.R. Walker, D.M. Freye, R.K.W. Haselwimmer, and G.G. Lonzarich. Magnetically Mediated Superconductivity in Heavy Fermion Compounds. *Nature*, 394(6688):39–43, 1998.
- [35] K. Jin, N.P. Butch, K. Kirshenbaum, J. Paglione, and R.L. Greene. Link between Spin Fluctuations and Electron Pairing in Copper Oxide Superconductors. *Nature*, 476(7358):73–75, 2011.
- [36] J. Paglione and R.L. Greene. High-Temperature Superconductivity in Iron-Based Materials. *Nat. Phys.*, 6(9):645–658, 2010.
- [37] J. Bardeen, L.N. Cooper, and J.R. Schrieffer. Microscopic Theory of Superconductivity. *Phys. Rev.*, 106(1):162–164, 1957.
- [38] W. Buckel and R. Kleiner. *Superconductivity: Fundamentals and Applications*. Wiley-VCH, 2004. ISBN 3-527-40349-3.
- [39] L.C. Hebel and C.P. Slichter. Nuclear Spin Relaxation in Normal and Superconducting Aluminum. *Phys. Rev.*, 113(6):1504–1519, 1959.

- [40] M. Tinkham. *Introduction to Superconductivity*. Dover Publications, 1996. ISBN 978-0-486-46739-9.
- [41] A. Nigro, P. Marra, C. Autieri, W. Wu, J. Cheng, J. Luo, and C. Noce. Resistivity Measurements Unveil Microscopic Properties of CrAs. *EPL*, 125(5):57002, 2019.
- [42] C.Y. Guo, M. Smidmann, B. Shen, W. Wu, F.K. Lin, X.L. Han, Y. Chen, F. Wu, Y.F. Wang, W.B. Jiang, X. Lu, J.P. Hu, J.L. Luo, and H.Q. Yuan. Evidence for Triplet Superconductivity near an Antiferromagnetic Instability in CrAs. *Phys. Rev. B*, 98(2):024520, 2018.
- [43] S. Sachdev and B. Keimer. Quantum Criticality. *Phys. Today*, 62(2):29–35, 2011.
- [44] P. Coleman and A.J. Schofield. Quantum Criticality. *Nature*, 433(7023):226–229, 2005.
- [45] S. Park, S. Shin, S.-I. Kim, S. Kim, C.-K. Park, J.D. Thompson, and T. Park. Tunable Quantum Critical Point and Detached Superconductivity in Al-Doped CrAs. *npj Quantum Mater.*, 4:49, 2019.
- [46] K. Motizuki, H. Ido, T. Itoh, and M. Morifuji. *Electronic Structure and Magnetism of 3d-Transition Metal Pnictides*. Springer, Berlin, 2009.
- [47] R.D. Heyding and L.D. Calvert. Arsenides of Transition Metals: The Arsenides of Iron and Cobalt. *Can. J. Chem.*, 35(5):449–457, 1957.
- [48] R.H. Wilson and J.S. Kasper. The Crystal Structure of MnAs above 40 °C. *Acta Cryst.*, 17(2):95–101, 1964.
- [49] K. Selte, H. Hjersing, A. Kjekshus, A.F. Andresen, and P. Fischer. Magnetic Structures and Properties of CrP_{1-x}As_x. *Acta Chem. Scand. A*, 29(7):695–698, 1975.
- [50] T. Suzuki and H. Ido. Crystallographic and Magnetic Properties of CrAs_{1-x}Sb_x. *J. Magn. Magn. Mater.*, 54–57:935–936, 1986.
- [51] B.T.M. Willis and H.P. Rooksby. Magnetic Transitions and Structural Changes in Hexagonal Manganese Compounds. *Proc. Phys. Soc. B*, 67(412):290–296, 1954.
- [52] H. Fjellvåg and A. Kjekshus. Magnetic and Structural Properties of Transition Metal Substituted MnP. I. Mn_{1-t}Co_tP (0.00 ≤ t ≤ 0.30). *Acta Chem. Scand. A*, 38(7):563–573, 1984.
- [53] N.D. Zhigadlo, N. Barbero, and T. Shiroka. Growth of Bulk Single-Crystal MnP Helimagnet and its Structural and NMR Characterization. *J. Alloys Compd.*, 725:1027–1034, 2017.
- [54] B. Westerstrandh, L. Lundgren, U. Gäfvert, and B. Carlsson. Magnetic Susceptibility Resistivity and Thermal Expansion Measurements on FeP. *Physica Scripta*, 15(4):276–280, 1977.

-
- [55] I.O. Chernyavskii, S.E. Nikitin, Y.A. Onykienko, D.S. Inosov, Q. Stahl, J. Geck, X.C. Hong, C. Hess, S. Gass, A.U.B. Wolter, D. Wolf, A. Lubk, D.V. Efremov, F. Yokaichiya, S. Aswartham, B. Büchner, and I.V. Morozov. Incommensurate Magnet Iron Monophosphide FeP: Crystal Growth and Characterization. *Phys. Rev. Mater.*, 4(8):083403, 2020.
- [56] K. Selte, A. Kjekshus, and A.F. Andresen. Magnetic Structure and Properties of FeAs. *Acta Chem. Scand.*, 26(8):3101–3113, 1972.
- [57] K. Selte and A. Kjekshus. Redetermined Crystal Structure of FeAs. *Acta Chem. Scand.*, 27(4):1448–1449, 1973.
- [58] A.G. Christy. Isosymmetric Structural Phase Transitions: Phenomenology and Examples. *Acta Cryst. B*, 51(5):753–757, 1995.
- [59] Y. Shapira, C.C. Becerra, N.F. Oliveira, Jr., and T.S. Chang. Phase Diagram, Susceptibility, and Magnetostriction of MnP: Evidence for a Lifshitz Point. *Phys. Rev. B*, 24(5):2780–2806, 1981.
- [60] T. Okamoto, T. Kamigaichi, N. Iwata, and E. Tatsumoto. Anisotropic Linear Thermal Expansion of MnP Single Crystal. *J. Phys. Soc. Jpn.*, 25(6):1730, 1968.
- [61] K. Selte, A. Kjekshus, and A.F. Andresen. Structural and Magnetic Properties of CrP. *Acta Chem. Scand.*, 26(8):4188–4190, 1972.
- [62] S. Rundqvist and P.C. Nawapong. Crystal Structure Refinements of Some MnP-Type Phosphides. *Acta Chem. Scand.*, 19(4):1006–1008, 1965.
- [63] N. Schönberg. An X-Ray Investigation of Transition Metal Phosphides. *Acta Chem. Scand.*, 8(2):226–239, 1954.
- [64] Y. Wang, Y. Feng, J.-G. Cheng, W. Wu, and T.F. Rosenbaum. Spiral Magnetic Order and Pressure-Induced Superconductivity in Transition Metal Compounds. *Nat. Commun.*, 7:13037, 2016.
- [65] E.E. Huber, Jr. and D.H. Ridgley. Magnetic Properties of a Single Crystal of Manganese Phosphide. *Phys. Rev.*, 135(4A):A1033–A1040, 1964.
- [66] H. Fjellvåg and A. Kjekshus. Single Crystal Study of $\text{Mn}_{0.8}\text{Co}_{0.2}\text{P}$. *Acta Chem. Scand.*, A40(9):634–636, 1986.
- [67] F. Han, D. Wang, Y. Wang, N. Li, J.-K. Bao, B. Li, A.S. Botana, Y. Xiao, P. Chow, D.Y. Chung, J. Chen, X. Wan, M.G. Kanatzidis, W. Yang, and H.-K. Mao. Spin Quenching Assisted by a Strongly Anisotropic Compression Behavior in MnP. *New J. Phys.*, 20:023012, 2018.
- [68] J.-G. Cheng, K. Matsubayashi, W. Wu, J.P. Sun, F.K. Lin, J.L. Luo, and Y. Uwatoko. Pressure Induced Superconductivity on the Border of Magnetic Order in MnP. *Phys. Rev. Lett.*, 114(11):117001, 2015.
- [69] T. Komatsubara, T. Suzuki, and E. Hirahara. Magnetization Process and Spin-Structure Diagram in Manganese Phosphide Single Crystal. *J. Phys. Soc. Jpn.*, 28(2):317–320, 1970.

- [70] K. Selte, L. Birkeland, and A. Kjekshus. On the Structural and Magnetic Properties of $\text{Cr}_{1-t}\text{Fe}_t\text{P}$, $\text{Mn}_{1-t}\text{Co}_t\text{P}$ and $\text{Fe}_{1-t}\text{Co}_t\text{P}$. *Acta Chem. Scand. A*, 32(8):731–735, 1978.
- [71] S. Yano, D. Lançon, H.M. Rønnow, T.C. Hansen, E. Ressouche, N. Qureshi, B. Ouladdiaf, and J.S. Gardner. Suppression of Magnetic Order before the Superconducting Dome in MnP. *J. Phys. Soc. Jpn.*, 87(2):023703, 2018.
- [72] G.P. Felcher, F.A. Smith, D. Bellavance, and A. Wold. Magnetic Structure of Iron Monophosphide. *Phys. Rev. B*, 3(9):3046–3052, 1971.
- [73] K. Selte and A. Kjekshus. Structural and Magnetic Properties of FeP. *Acta Chem. Scand.*, 26(3):1276–1277, 1972.
- [74] T. Gu, X. Wu, S. Qin, and L. Dubrovinsky. *In Situ* High-Pressure Study of FeP: Implications for Planetary Cores. *Phys. Earth Planet. Inter.*, 184(3–4):154–159, 2011.
- [75] K. Selte, A. Kjekshus, and A.F. Andresen. Structural and Magnetic Properties of VP and VAs. *Acta Chem. Scand.*, 26(10):4057–4062, 1972.
- [76] K. Bachmayer and H. Nowotny. Untersuchungen im System V–As. *Monatsh. Chem.*, 86:741–744, 1955.
- [77] T. Suzuki and H. Ido. 3d Metal-Substitution Effects on Magnetic and Crystallographic Properties of CrAs. *J. Appl. Phys.*, 69(8):4624–4624, 1991.
- [78] K. Kanaya, S. Abe, H. Yoshida, K. Kamigaki, and T. Kaneko. Magnetic and Structural Properties of Pseudo-Binary Compounds $\text{CrAs}_{1-x}\text{P}_x$. *J. Alloys Compd.*, 383(1–2):189–194, 2004.
- [79] A. Zięba, Y. Shapira, and S. Foner. Magnetic Phase Diagram of MnAs: Effect of Magnetic Field on Structural and Magnetic Transitions. *Phys. Lett.*, 91A(5):243–245, 1982.
- [80] H. Nowotny, R. Funk, and J. Pesl. Kristallchemische Untersuchungen in den Systemen Mn–As, V–Sb, Ti–Sb. *Monatsh. Chem.*, 82(3):513–525, 1951.
- [81] M. Yuzuri and M. Yamada. On the Magnetic Properties of the Compound Mn_2As . *J. Phys. Soc. Jpn.*, 15(10):1845–1850, 1960.
- [82] T. Suzuki. The Crystal Structure of MnAs. *Tohoku Gakuin Daigaku Kogakubu Kenkyu Hokoku*, 13:57–61, 1978.
- [83] A. Zięba, K. Selte, A. Kjekshus, and A.F. Andresen. Phase Transitions in MnAs. *Acta Chem. Scand. A*, 32(2):173–177, 1978.
- [84] V.P. Glazkov, D.P. Kozlenko, K.M. Podurets, B.N. Savenko, and V.A. Somenkov. Neutron Diffraction Investigation of the Atomic and Magnetic Structures of MnAs at High Pressures. *Crystallogr. Rep.*, 48(1):54–57, 2003.
- [85] T. Suzuki and H. Ido. Relation between Structural and Magnetic Properties of Compound $\text{MnAs}_{1-x}\text{P}_x$ ($0 \leq x \leq 0.275$). *J. Phys. Soc. Jpn.*, 51(10):3149–3156, 1982.

-
- [86] K. Selte and A. Kjekshus. The Crystal Structure of FeAs. *Acta Chem. Scand.*, 23(6):2047–2054, 1969.
- [87] P.S. Lyman and C.T. Prewitt. Room- and High-Pressure Crystal Chemistry of CoAs and FeAs. *Acta Cryst. B*, 40:14–20, 1984.
- [88] K. Selte and A. Kjekshus. Structural and Magnetic Properties of CoAs. *Acta Chem. Scand.*, 25(9):3277–3284, 1971.
- [89] W. Tremel, R. Hoffmann, and J. Silvestre. Transitions between NiAs and MnP Type Phases: An Electronically Driven Distortion of Triangular (3^6) Nets. *J. Am. Chem. Soc.*, 108(17):5174–5187, 1986.
- [90] C. Hermann. Zur Systematischen Strukturtheorie – IV. Untergruppen. *Z. Kristallogr.*, 69:533–555, 1929.
- [91] P.J. Brown, A.G. Fox, E.N. Maslen, M.A. O’Keefe, and B.T.M. Willis. Intensity of Diffracted Intensities. In E. Prince, editor, *International Tables for Crystallography Volume C*, pages 554–595. Springer, 2006.
- [92] P.J. Brown. Magnetic Form Factors. In E. Prince, editor, *International Tables for Crystallography Volume C*, pages 454–461. Springer, 2006.
- [93] T. Janssen, A. Janner, A. Looijenga-Vos, and P.M. De Wolff. Incommensurate and Commensurate Modulated Structures. In E. Prince, editor, *International Tables for Crystallography Volume C*, pages 907–955. Springer, 2006.
- [94] P.M. De Wolff. The Pseudo-Symmetry of Modulated Crystal Structures. *Acta Cryst. A*, 30(6):777–785, 1974.
- [95] J.M. Perez-Mato, J.L. Ribeiro, V. Petříček, and M.I. Aroyo. Magnetic Superspace Groups and Symmetry Constraints in Incommensurate Magnetic Phases. *J. Phys.: Condens. Matter*, 24(16):163201, 2012.
- [96] E.F. Bertaut. Representation Analysis of Magnetic Structures. *Acta Cryst. A*, 24(1):217–231, 1968.
- [97] V. Petříček, J. Fuksa, and M. Dušek. Magnetic Space and Superspace Groups, Representation Analysis: Competing of Friendly Concepts? *Acta Cryst. A*, 66(6):649–655, 2010.
- [98] J. Binns, K.V. Kamenev, G.J. McIntyre, S.A. Moggach, and S. Parsons. Use of a Miniature Diamond-Anvil Cell in High-Pressure Single-Crystal Neutron Laue Diffraction. *IUCrJ*, 3(3):168–179, 2016.
- [99] R. Boehler, M. Guthrie, J.J. Molaison, A.M. dos Santos, S. Sinogeikin, S. Machida, N. Pradhan, and C.A. Tulk. Large-Volume Diamond Cells for Neutron Diffraction above 90 GPa. *High Press. Res.*, 33(3):546–554, 2013.
- [100] R. Boehler, J.J. Molaison, and B. Haberl. Novel Diamond Cells for Neutron Diffraction using Multi-Carat CVD Anvils. *Rev. Sci. Instrum.*, 88(8):083905, 2017.

- [101] I.N. Goncharenko. Neutron Diffraction Experiments in Diamond and Sapphire Anvil Cells. *High Press. Res.*, 24(1):193–204, 2004.
- [102] I.N. Goncharenko. New Techniques for High-Pressure Neutron and X-ray Studies. *High Press. Res.*, 27(1):183–188, 2007.
- [103] A. Grzechnik, M. Meven, and K. Friese. Single-Crystal Neutron Diffraction in Diamond Anvil Cells with Hot Neutrons. *J. Appl. Cryst.*, 51(2):351–356, 2018.
- [104] A. Grzechnik, M. Meven, C. Paulmann, and K. Friese. Combined X-ray and Neutron Single-Crystal Diffraction in Diamond Anvil Cells. *J. Appl. Cryst.*, 53(1):9–14, 2020.
- [105] B. Haberl, S. Dissanayake, F. Ye, L.L. Daemen, Y. Cheng, C.W. Li, A.-J. Ramirez-Cuesta, M. Matsuda, J.J. Molaison, and R. Boehler. Wide-Angle Diamond Cell for Neutron Scattering. *High Press. Res.*, 37(4):495–506, 2017.
- [106] B. Haberl, S. Dissanayake, Y. Wu, D.A.A. Myles, A.M. dos Santos, M. Loguillo, G.M. Rucker, D.P. Armitage, M. Cochran, K.M. Andrews, C. Hoffmann, H. Cao, M. Matsuda, F. Meilleur, F. Ye, J.J. Molaison, and R. Boehler. Next-Generation Diamond Cell and Applications to Single-Crystal Neutron Diffraction. *Rev. Sci. Instrum.*, 89(9):092902, 2018.
- [107] B. Haberl, J.J. Molaison, J.C. Neuerfeind, L.L. Daemen, and R. Boehler. Modified Bridgman Anvils for High Pressure Synthesis and Neutron Scattering. *High Press. Res.*, 39(3):426–437, 2019.
- [108] A. Jayaraman. Ultrahigh Pressures. *Rev. Sci. Instrum.*, 57(6):1013–1031, 1986.
- [109] C.H. Polsky and E. Van Valkenburg. The Diamond Anvil Cell. In *Handbook of Vibrational Spectroscopy*. John Wiley & Sons, Ltd., 2006.
- [110] R. LeToullec, J.P. Pinceaux, and P. Loubeyre. The Membrane Diamond Anvil Cell: A New Device for Generating Continuous Pressure and Temperature Variations. *High Press. Res.*, 1(1):77–90, 1988.
- [111] M.H. Grimsditch and A.K. Ramdas. Brillouin Scattering in Diamond. *Phys. Rev. B*, 11(8):3139–3148, 1975.
- [112] N. Savvides and T.J. Bell. Microhardness and Young’s Modulus of Diamond and Diamondlike Carbon Films. *J. Appl. Phys.*, 72(7):2791–2796, 1992.
- [113] K.E. Spear and J.P. Dismukes, editors. *Synthetic Diamond: Emerging CVD Science and Technology*. John Wiley & Sons Ltd., 1994. ISBN 978-0-471-53589-8.
- [114] D.J. Dunstan and I.L. Spain. The Technology of Diamond Anvil High-Pressure Cells: I. Principles, Design and Construction. *J. Phys. E: Sci. Instrum.*, 22(11):913–923, 1989.

-
- [115] M. Guthrie, C.G. Pruteanu, M.-E. Donnelly, J.J. Molaison, A.M. dos Santos, J.S. Loveday, R. Boehler, and C.A. Tulk. Radiation Attenuation by Single-Crystal Diamond Windows. *J. Appl. Cryst.*, 50(1):76–86, 2017.
- [116] H. Ahsbahs. New Pressure Cell for Single-Crystal X-ray Investigations on Diffractometers with Area Detectors. *Z. Kristallogr.*, 219(6):305–308, 2004.
- [117] R. Boehler. New Diamond Cell for Single-Crystal X-ray Diffraction. *Rev. Sci. Instrum.*, 77(11):115103, 2006.
- [118] Y. Cheng. A Diamond Anvil Cell for Combined X-Ray and Neutron Single-Crystal Studies. Master’s thesis, Institute of Crystallography, RWTH Aachen University, Aachen, Germany, June 2018.
- [119] S. Klotz. *Techniques in High Pressure Neutron Scattering*. CRC Press, Taylor & Francis, 2013. ISBN 978-1-4398-3563-0.
- [120] M.I. Eremets. *High Pressure Experimental Methods*. Oxford University Press, 1996. ISBN 978-0-1985-6269-6.
- [121] J.C. Cooley and M.C. Aronson. Origins of Paramagnetism in Beryllium–Copper Alloys. *J. Alloys Compds.*, 228(2):195–200, 1995.
- [122] I.R. Walker. Nonmagnetic Piston-Cylinder Pressure Cell for Use at 35 kbar and above. *Rev. Sci. Instrum.*, 70(8):3402–3412, 1999.
- [123] I.R. Walker. Considerations on the Selection of Alloys for Use in Pressure Cells at Low Temperatures. *Cryogenics*, 45(2):87–108, 2005.
- [124] Y. Cheng, J. Brenk, B. Friedrich, J. Perkon, N. Maraytta, J.S.K.-L. Gibson, S. Korte-Kerzel, G. Roth, Y. Su, F. Zhu, C. Paulmann, and A. Grzechnik. Ni–Cr–Al Alloy for Neutron Scattering at High Pressures. *Mater. Sci. Technol.*, 36(9):949–954, 2020.
- [125] DAC Tools LLC, Naperville, Illinois, USA. Diamond anvil cells. <https://www.dactools.com/diamond-cells>. Accessed February 07, 2022.
- [126] R. Sadykov, C. Pappas, L.J. Bannenberg, R.M. Dalglish, P. Falus, C. Goodway, and E. Lelièvre-Berna. 1.5 GPa Compact Double-Wall Clamp Cell for SANS and NSE Studies at Low Temperatures and High Magnetic Fields. *J. Neutron Res.*, 20(1–2):25–33, 2018.
- [127] H. Rauch and W. Waschkowski. Neutron Scattering Lengths. In A.-J. Dianoux and G. Lander, editors, *ILL Neutron Data Booklet (second edition)*. Old City Publishing, 2003. ISBN 978-0-9704143-7-4.
- [128] V.F. Sears. Scattering Lengths for Neutrons. In E. Prince, editor, *International Tables for Crystallography Volume C: Mathematical, Physical and Chemical Tables*. Kluwer Academic Publishers, 2006. ISBN 978-1-4020-1900-5.
- [129] P. Kienzle. Neutron activation and scattering calculator. <https://www.ncnr.nist.gov/resources/activation/>, November 2020. Accessed May 11, 2021.

- [130] M.G. Kibble, V. Laliena, C.M. Goodway, E. Lelièvre-Berna, K.V. Kamenev, S. Klotz, and O. Kirichuk. Low-Background Materials for High Pressure Cells used in Inelastic Neutron Scattering Experiments. *J. Neutron Res.*, 21(3–4): 105–116, 2019.
- [131] C.L. Bull, A.D. Fortes, C.J. Ridley, I.G. Wood, D.P. Dobson, N.P. Funnell, A.S. Gibbs, C. Goodway, R. Sadykov, and K.S. Knight. High-Resolution Neutron-Diffraction Measurements to 8 kbar. *High Press. Res.*, 37(4):486–494, 2017.
- [132] N. Fujiwara, T. Matsumoto, K. Koyama-Nakazawa, A. Hisada, and Y. Uwatoko. Fabrication and Efficiency Evaluation of a Hybrid NiCrAl Pressure Cell up to 4 GPa. *Rev. Sci. Instrum.*, 78(7):073905, 2007.
- [133] N. Fujiwara, Y. Uwatoko, and T. Matsumoto. A NiCrAl Pressure Cell up to 4.6 GPa and its Application to Cuprate and Pnictide Superconductors. *J. Phys.: Conf. Ser.*, 500:032008, 2014.
- [134] J. Kamarád, Z. Machátová, and Z. Arnold. High Pressure Cells for Magnetic Measurements – Destruction and Functional Tests. *Rev. Sci. Instrum.*, 75(11): 5022–5025, 2004.
- [135] K. Koyama, S. Hane, K. Kamishima, and T. Goto. Instrument for High Resolution Magnetization Measurements at High Pressures, High Magnetic Fields and Low Temperatures. *Rev. Sci. Instrum.*, 69(8):3009–3014, 1998.
- [136] R.A. Sadykov, N.S. Bezaeva, A.I. Kharkovsky, P. Rochette, J. Gattacceca, and V.I. Trukhin. Nonmagnetic High Pressure Cell for Magnetic Remanence Measurements up to 1.5 GPa in a Superconducting Quantum Interference Device Magnetometer. *Rev. Sci. Instrum.*, 79(11):115102, 2008.
- [137] R.A. Sadykov, T. Strassle, A. Podlesnyak, L. Keller, B. Fak, and J. Mesot. High-Pressure Cells for Study of Condensed Matter by Diffraction and Inelastic Neutron Scattering at Low Temperatures and in Strong Magnetic Fields. *J. Phys.: Conf. Ser.*, 941:012082, 2017.
- [138] B. Fåk, R.A. Sadykov, J. Flouquet, and G. Lapertot. Pressure Dependence of the Magnetic Structure of the Itinerant Electron Magnet MnSi. *J. Phys.: Condens. Matter*, 17(10):1635–1644, 2005.
- [139] J.D. Barnett, S. Block, and G.J. Piermarini. An Optical Fluorescence System for Quantitative Pressure Measurement in the Diamond-Anvil Cell. *Rev. Sci. Instrum.*, 44(1):1–9, 1973.
- [140] H.K. Mao, P.M. Bell, J.W. Shaner, and D.J. Steinberg. Specific Volume Measurements of Cu, Mo, Pd, and Ag and Calibration of the Ruby R_1 Fluorescence Pressure Gauge from 0.06 to 1 Mbar. *J. Appl. Phys.*, 49(6):3276–3283, 1978.
- [141] R.E. Newnham and Y.M. De Haan. Refinement of the α Al_2O_3 , Ti_2O_3 , V_2O_3 and Cr_2O_3 Structures. *Z. Kristallogr.*, 117(2–3):235–237, 1962.
- [142] L. Pauling and S.B. Hendricks. The Crystal Structures of Hematite and Corundum. *J. Am. Ceram. Soc.*, 47:781–790, 1925.

-
- [143] D.S. McClure. Optical Spectra of Transition-Metal Ions in Corundum. *J. Chem. Phys.*, 36(10):2757–2779, 1962.
- [144] S.C. Moss and R.E. Newnham. The Chromium Position in Ruby. *Z. Kristallogr.*, 120(4–5):359–363, 1964.
- [145] J.W. McCauley and G.V. Gibbs. Redetermination of the Chromium Position in Ruby. *Z. Kristallogr.*, 135(5–6):453–455, 1972.
- [146] T.H. Maiman. Stimulated Optical Radiation in Ruby. *Nature*, 187(4736):493–494, 1960.
- [147] K. S. *DatLab Manual*, 1998.
- [148] Q. Ma and D.R. Clarke. Piezospectroscopic Determination of Residual Stresses in Polycrystalline Alumina. *J. Am. Ceram. Soc.*, 77(2):298–302, 1994.
- [149] E.F. Skelton, A.W. Webb, S.B. Qadri, S.A. Wolf, R.C. Lacoe, J.L. Feldman, W.T. Elam, E.R. Carpenter, Jr., and C.Y. Huang. Energy-Dispersive X-ray Diffraction with Synchrotron Radiation at Cryogenic Temperatures. *Rev. Sci. Instrum.*, 55(6):849–855, 1984.
- [150] J.M. Brown. The NaCl Pressure Standard. *J. Appl. Phys.*, 86(10):5801–5808, 1999.
- [151] G. Shen, Y. Wang, A. Dewaele, C. Wu, D.E. Fratanduono, J. Eggert, S. Klotz, K.F. Dziubek, P. Loubeyre, O.V. Fat’yanov, P.D. Asimow, T. Mashimo, R.M.M. Wentzcovitch, and other members of the IPPS task group. Toward an International Practical Pressure Scale: A Proposal for an IPPS Ruby Gauge (IPPS-Ruby2020). *High Press. Res.*, 40(3):299–314, 2020.
- [152] F. Datchi, A. Dewaele, P. Loubeyre, R. Letoullec, Y. Le Godec, and B. Canny. Optical Pressure Sensors for High-Pressure–High-Temperature Studies in a Diamond Anvil Cell. *High Press. Res.*, 27(4):447–463, 2007.
- [153] S. Rekhi, L.S. Dubrovinsky, and S.K. Saxena. Temperature-Induced Ruby Fluorescence Shifts up to a Pressure of 15 GPa in an Externally Heated Diamond Anvil Cell. *High Temp. High Press.*, 31(3):299–305, 1999.
- [154] A. Podlesnyak, M. Loguillo, G.M. Rucker, B. Haberl, R. Boehler, G. Ehlers, L.L. Daemen, D. Armitage, M.D. Frontzek, and M. Lumsden. Clamp Cell with *In Situ* Pressure Monitoring for Low-Temperature Neutron Scattering Measurements. *High Press. Res.*, 38(4):482–492, 2018.
- [155] F. Datchi, R. LeToullec, and P. Loubeyre. Improved Calibration of the $\text{SrB}_4\text{O}_7\text{:Sm}^{2+}$ Optical Pressure Gauge: Advantages at Very High Pressures and High Temperatures. *J. Appl. Phys.*, 81(8):3333–3339, 1997.
- [156] A. Lacam and C. Cheteau. High-Pressure Measurements at Moderate Temperatures in a Diamond Anvil Cell with a New Optical Sensor: $\text{SrB}_4\text{O}_7\text{:Sm}^{2+}$. *J. Appl. Phys.*, 66(1):366–372, 1989.

- [157] S. Otto, J.P. Harris, K. Heinze, and C. Reber. Molecular Ruby under Pressure. *Angew. Chem. Int. Ed.*, 57(34):11069–11073, 2018.
- [158] S. Otto, M. Dorn, C. Förster, M. Bauer, M. Seitz, and K. Heinze. Understanding and Exploiting Long-Lived Near-Infrared Emission of a Molecular Ruby. *Coord. Chem. Rev.*, 359:102–111, 2018.
- [159] C. Wang, S. Otto, M. Dorn, E. Kreidt, J. Lebon, L. Sršan, P. Di Martino-Fumo, M. Gerhards, U. Resch-Genger, M. Seitz, and K. Heinze. Deuterated Molecular Ruby with Record Luminescence Quantum Yield. *Angew. Chem. Int. Ed.*, 57(4):1112–1116, 2018.
- [160] A.W. Hull. The Positions of Atoms in Metals. *Transactions of the American Institute of Electrical Engineers*, 38(2):1445–1466, 1919.
- [161] S. Klotz, J.-C. Chervin, P. Munsch, and G. Le Marchand. Hydrostatic Limits of 11 Pressure Transmitting Media. *J. Phys. D: Appl. Phys.*, 42(7):075413, 2009.
- [162] X. Yan, X. Ren, and D. He. Pressure Calibration in Solid Pressure Transmitting Medium in Large Volume Press. *Rev. Sci. Instrum.*, 87(12):125006, 2016.
- [163] R.J. Angel, M. Bujak, J. Zhao, G.D. Gatta, and S.D. Jacobsen. Effective Hydrostatic Limits of Pressure Media for High-Pressure Crystallographic Studies. *J. Appl. Cryst.*, 40(1):26–32, 2007.
- [164] M.S. Torikachvili, S.K. Kim, E. Colombier, S.L. Bud’ko, and P.C. Canfield. Solidification and Loss of Hydrostaticity in Liquid Media used for Pressure Measurements. *Rev. Sci. Instrum.*, 86(12):123094, 2015.
- [165] V.A. Sidorov and R.A. Sadykov. Hydrostatic Limits of Fluorinert Liquids used for Neutron and Transport Studies at High Pressure. *J. Phys.: Condens. Matter*, 17(40):S3005–S008, 2005.
- [166] Quantum Design, Inc. *PPMS Physical Measurement Property System – Product Description*, 2019.
- [167] Quantum Design, Inc. *PPMS DynaCool – Product Description*, 2019.
- [168] S. Foner. Versatile and Sensitive Vibrating-Sample Magnetometer. *Rev. Sci. Instrum.*, 30(7):548–557, 1959.
- [169] D.O. Smith. Development of a Vibrating-Coil Magnetometer. *Rev. Sci. Instrum.*, 27(5):261–268, 1956.
- [170] Quantum Design, Inc. *Vibrating Sample Magnetometer (VSM) Option User’s Manual*, 2011.
- [171] Quantum Design, Inc. *Resistivity Option (ETO) User’s Manual*, 1999.
- [172] M. Ladd and R. Palmer. *Structure Determination by X-Ray Crystallography*. Springer, New York, 2013.

-
- [173] Multiwire Laboratories, Ltd. *MWL120 Real-Time Back-Reflection Laue Camera System*, 2013.
- [174] HUBER Diffraktionstechnik GmbH & Co. KG. *Guinier Imaging Plate Camera G670*, 2006.
- [175] Agilent Technologies XRD Products, Ltd. *SuperNova – X-ray Diffractometer System*, 2014.
- [176] M. Tolkiehn, H. Schulze-Ritter, W. Drube, C. Paulmann, A. Berghäuser, and D. Ropers. Beamline P24 – Chemical Crystallography. Technical report, DESY, 06 2014.
- [177] A. Hofmann. *The Physics of Synchrotron Radiation*. Cambridge University Press, New York, 2004.
- [178] P. Fischer, G. Frey, M. Koch, M. Könnecke, V. Pomjakushin, J. Schefer, R. Thut, N. Schlumpf, R. Bürge, U. Greuter, S. Bondt, and E. Berruyer. High-Resolution Powder Diffractometer HRPT for Thermal Neutrons at SINQ. *Physica B*, 276–278:146–147, 2000.
- [179] P. Fischer, J. Schefer, L. Keller, O. Zaharko, V. Pomjakushin, D. Sheptyakov, N. Aliouane, and M. Frontzek. 50 Years of Swiss Neutron Diffraction Instrumentation. *Swiss Neutron News*, 42:4–15, 2013.
- [180] Institut Laue-Langevin. *Instrument layout (D9)*. <https://www.ill.eu/users/instruments/instruments-list/d9/description/instrument-layout>. Accessed September 27, 2021.
- [181] B. Ouladdiaf, J. Archer, G.J. McIntyre, A.W. Hewat, D. Brau, and S. York. OrientExpress: A New System for Laue Neutron Diffraction. *Physica B*, 385–386:1052–1054, 2006.
- [182] Y. Su, K. Nemkovskiy, and S. Demirdiř. DNS: Diffuse Scattering Neutron Time-of-Flight Spectrometer. *Journal of Large-Scale Research Facilities*, 1: A27, 2015.
- [183] M. Meven and A. Sazonov. HEiDi: Single Crystal Diffractometer at Hot Source. *Journal of Large-Scale Research Facilities*, 1:A7, 2015.
- [184] V. Hutanu. POLI: Polarised Hot Neutron Diffractometer. *Journal of Large-Scale Research Facilities*, 1:A16, 2015.
- [185] R. Georgii and K. Seemann. MIRA: Dual Wavelength Band Instrument. *Journal of Large-Scale Research Facilities*, 1:A3, 2015.
- [186] D.B. McWhan, D. Bloch, and G. Parisot. Apparatus for Neutron Diffraction at High Pressure. *Rev. Sci. Instrum.*, 45(5):643–646, 1974.
- [187] J.M. Besson, R.J. Nemes, G. Hamel, J.S. Loveday, G. Weill, and S. Hull. Neutron Powder Diffraction Above 10 GPa. *Physica B*, 180&181(2):907–910, 1992.

- [188] W.F. Sherman and A.A. Stadtmuller. *Experimental Techniques in High-Pressure Research*. John Wiley & Sons Ltd., 1987. ISBN 978-0-471-10313-6.
- [189] S. Timoshenko, S. and J.N. Goodier. *Theory of Elasticity*. McGraw-Hill International Editions, 1970. ISBN 978-0-07-085805-5.
- [190] D.L. Decker. Equation of State of NaCl and Its Use as a Pressure Gauge in High-Pressure Research. *J. Appl. Phys.*, 36(1):157–161, 1965.
- [191] G.J. Piermarini, S. Block, J.D. Barnett, and R.A. Forman. Calibration of the Pressure Dependence of the R_1 Ruby Fluorescence Line to 195 kbar. *J. Appl. Phys.*, 46(6):2774–2780, 1975.
- [192] H.K. Mao, J. Xu, and P.M. Bell. Calibration of the Ruby Pressure Gauge to 800 kbar under Quasi-Hydrostatic Conditions. *J. Geophys. Res. Solid Earth*, 91(B5):4673–4676, 1986.
- [193] L.H. Adams, R.W. Goranson, and R.E. Gibson. Construction and Properties of the Manganin Resistance Pressure Gauge. *Rev. Sci. Instrum.*, 8:230–235, 1937.
- [194] A. Eiling and J.S. Schilling. Pressure and Temperature Dependence of Electrical Resistivity of Pb and Sn from 1–300 K and 0–10 GPa – Use as Continuous Resistive Pressure Monitor Accurate over Wide Temperature Range; Superconductivity under Pressure in Pb, Sn, and In. *J. Phys. F: Metal Phys.*, 11(3):623–639, 1981.
- [195] R. Boehler and K. de Hantsetters. New Anvil Designs in Diamond-Cells. *High Press. Res.*, 24(3):391–396, 2004.
- [196] A. Eich, M. Hölzle, Y. Su, V. Hutanu, R. Georgii, L. Beddrich, and A. Grzechnik. Clamp Cells for High Pressure Neutron Scattering at Low Temperatures and High Magnetic Fields at Heinz Maier-Leibnitz Zentrum (MLZ). *High Press. Res.*, 41(1):88–96, 2021.
- [197] S. Mühlbauer, B. Binz, F. Jonietz, C. Pfleiderer, A. Rosch, A. Neubauer, R. Georgii, and P. Böni. Skyrmion Lattice in a Chiral Magnet. *Science*, 323(5916):915–919, 2009.
- [198] R. Georgii and T. Weber. The Helical Magnet MnSi: Skyrmions and Magnons. *Quantum Beam Sci.*, 3(1):4, 2019.
- [199] Y. Ishikawa, K. Tajima, D. Bloch, and M. Roth. Helical Spin Structure in Manganese Silicide MnSi. *Solid State Commun.*, 19(6):525–528, 1976.
- [200] K. Syassen. Ruby Under Pressure. *High Press. Res.*, 28(2):75–126, 2008.
- [201] D.D. Ragan, R. Gustavsen, and D. Schiferl. Calibration of the Ruby R_1 and R_2 Fluorescence Shifts as a Function of Temperature from 0 to 600 K. *J. Appl. Phys.*, 72(12):5539–5544, 1992.
- [202] K. Friese, A. Grzechnik, J.M. Posse, and V. Petříček. Refinement of High Pressure Single-Crystal Diffraction Data using Jana2006. *High Press. Res.*, 33(1):196–201, 2013.

-
- [203] C. Wilkinson, H.W. Khamis, R.F.D. Stansfield, and G.J. McIntyre. Integration of Single-Crystal Reflection using Area Multidetectors. *Acta Cryst.*, 21(5): 471–478, 1988.
- [204] Y. Su and W. Jin. Private Communication, 2019.
- [205] V. Petříček, M. Dušek, and L. Palatinus. Crystallographic Computing System JANA2006: General Features. *Z. Kristallogr.*, 229(5):345–352, 2014.
- [206] L. Palatinus and G. Chapuis. SUPERFLIP – A Computer Program for the Solution of Crystal Structures by Charge Flipping in Arbitrary Dimensions. *J. Appl. Cryst.*, 40(4):786–790, 2007.
- [207] A. Le Bail, H. Duroy, and J.L. Fouquet. Ab-Initio Structure Determination of LiSbWO_6 by X-ray Powder Diffraction. *Mat. Res. Bull.*, 23(3):447–452, 1988.
- [208] M. Dušek, V. Petříček, M. Wunschel, R.E. Dinnebier, and S. van Smaalen. Refinement of Modulated Structures against X-ray Powder Diffraction Data with *JANA2000*. *J. Appl. Cryst.*, 34(3):398–404, 2001.
- [209] P.W. Stephens. Phenomenological Model of Anisotropic Peak Broadening in Powder Diffraction. *J. Appl. Cryst.*, 32(2):281–289, 1999.
- [210] J.-F. Bérar and P. Lelann. E.S.D.’s and Estimated Probable Error Obtained in Rietveld Refinements with Local Correlations. *J. Appl. Cryst.*, 24(1):1–5, 1991.
- [211] H.M. Rietveld. A Profile Refinement Method for Nuclear and Magnetic Structures. *J. Appl. Cryst.*, 2(2):65–71, 1969.
- [212] A. Eich, A. Grzechnik, C. Paulmann, T. Müller, Y. Su, T. Wolf, and K. Frieze. Comparison of the Temperature- and Pressure-Dependent Behavior of the Crystal Structure of CrAs. *Acta Cryst. B*, 77(4):594–604, 2021.
- [213] H. Pfisterer and K. Schubert. Neue Phasen vom MnP (B 31)-Typ. *Z. Metallkd.*, 41(10):358–367, 1950.
- [214] J.R. Jeffries, N.P. Butch, H. Cynn, S.R. Saha, K. Kirshenbaum, S.T. Weir, Y.K. Vohra, and J. Paglione. The Interplay between Magnetism, Structure, and Strong Electron-Phonon Coupling in Binary FeAs under Pressure. *Phys. Rev. B*, 83(13):134520, 2011.
- [215] F. Birch. Finite Elastic Strain of Cubic Crystals. *Phys. Rev. B*, 71(11):809–824, 1947.
- [216] F.D. Murnaghan. The Compressibility of Media under Extreme Pressures. *Proc. Natl. Acad. Sci. U.S.A.*, 30:244–247, 1944.
- [217] J.B. Goodenough. Spin Correlations among Narrow-Band Electrons. *J. Appl. Phys.*, 35(3):1083–1084, 1964.
- [218] G.P. Felcher. Magnetic Structure of MnP. *J. Appl. Phys.*, 37(3):1056–1058, 1966.

- [219] J.B. Forsyth, S.J. Pickart, and P.J. Brown. The Structure of the Metamagnetic Phase of MnP. *Proc. Phys. Soc.*, 88(2):333–339, 1966.
- [220] C. Kittel. *Einführung in die Festkörperphysik*. Oldenbourg, München, 2006.
- [221] W.H. Baur. The Geometry of Polyhedral Distortions. Predictive Relationships for the Phosphate Group. *Acta Cryst. B*, 30:1195–1215, 1974.
- [222] K. Robinson, G.V. Gibbs, and P.H. Ribbe. Quadratic Elongation: A Quantitative Measure of Distortion in Coordination Polyhedra. *Science*, 172(3983): 567–570, 1971.
- [223] I.D. Brown and R.D. Shannon. Empirical Bond-Strength–Bond-Length Curves for Oxides. *Acta Cryst. A*, 29:266–282, 1973.
- [224] N.V. Tarakina, A.P. Tyutyunnik, V.G. Zubkov, T.V. D'yachkova, Y.G. Zainulin, H. Hannerz, and G. Svensson. High Temperature/High Pressure Synthesis and Crystal Structure of the New Corundum Related Compounds $\text{Zn}_4\text{Nb}_2\text{O}_9$. *Solid State Sci.*, 5(7):459–463, 2003.
- [225] X. Wang and F. Liebau. Influence of Polyhedron Distortions on Calculated Bond-Valence Sums for Cations with One Lone Electron Pair. *Acta Cryst. B*, 63(2):216–228, 2007.
- [226] P. Guionneau, M. Marchivie, G. Bravic, J.-F. Létard, and D. Chasseau. Co(II) Molecular Complexes as a Reference for the Spin Crossover in Fe(II) Analogues. *J. Mater. Chem.*, 12(8):2546–2551, 2002.

List of Figures

2.1	MnP-type crystal structure of CrAs	3
2.2	Helimagnetic structure of CrAs	5
2.3	Reported lattice parameters of CrAs as function of temperature	7
2.4	p - T phase diagram of CrAs	9
2.5	Orientation of d -orbitals in CrAs	10
2.6	Band scheme of CrAs in the low- and high-temperature phase	11
3.1	Relation of the NiAs and MnP structure types	18
3.2	Cr-Cr interactions in the a, b -plane in the $Cmcm$ and $Pmcn$ structures	19
3.3	Basic types of magnetic order	21
3.4	Qualitative comparison of X-ray and nuclear/magnetic neutron scattering form factors	22
4.1	Basic principle of the DAC	26
4.2	Types of DAC used within this work	27
4.3	Calculated neutron transmission as function of neutron wavelength for TiZr, CuBe and NiCrAl	31
4.4	Experimentally determined neutron transmission as function of neutron wavelength for TiZr, CuBe and NiCrAl	32
4.5	Calculated neutron activation as function of time for TiZr, CuBe and NiCrAl	33
4.6	Magnetic susceptibility of WC variants as function of temperature . .	34
4.7	Magnetic susceptibility of WC variants as function of applied magnetic field	35
4.8	Coercive fields of WC variants	35
4.9	Energy levels of Cr^{3+} in ruby	37
4.10	Pressure (NaCl) inside of clamp cell as function of temperature	41
5.1	As-grown CrAs single crystals from tin-flux method	44
5.2	Working principle of the VSM option	45
5.3	Layout of beamline P24, PETRA III, DESY	49
5.4	Layout of the HRPT instrument at SINQ, PSI	50
5.5	Layout of the D9 instrument at ILL, EPN	51
5.6	Layout of the POLI instrument at FRM II, MLZ	53
5.7	Layout of the MIRA instrument at FRM II, MLZ	55
6.1	Schematic design of a monobloc clamp cell	58
6.2	Theoretical stress distribution in a monobloc cylinder	60

6.3	Schematic design of a fretted clamp cell and theoretical stress distribution in a fretted cylinder	61
6.4	Overview of the monobloc clamp cell type M1	64
6.5	Dimensions of the monobloc clamp cell type M1	64
6.6	Capsules and pistons of the monobloc clamp cell type M1	65
6.7	Application of pressure onto the monobloc clamp cell type M1	65
6.8	Pressure determination in the monobloc clamp cell type M1	66
6.9	Produced variants of the monobloc clamp cell type M1	67
6.10	Overview of the monobloc clamp cell type M1D	67
6.11	Dimensions of the monobloc clamp cell type M1D	68
6.12	Pressure determination in the monobloc clamp cell type M1D	69
6.13	Produced variants of the monobloc clamp cell type M1D	69
6.14	Bottom pistons with mounted diamond	70
6.15	Overview of the fretted clamp cell type F1	70
6.16	Dimensions of the fretted clamp cell type F1	71
6.17	Capsules and pistons of the fretted clamp cell type F1	72
6.18	Assembled F1-TiZr before final manufacturing	72
6.19	Calculated neutron transmission as function of neutron wavelength for the F1-CuBe and F1-TiZr clamp cells	73
6.20	Simulation-based safety factor in the M1-CuBe at 1.1 GPa	74
6.21	Simulation-based minimal safety factor in the M1 clamp cell type as function of pressure	74
6.22	Simulation-based minimal safety factor in the F1 clamp cell type as function of pressure	76
6.23	Pressure (NaCl) inside of clamp cell as function of force load.	77
6.24	Experimental neutron transmission measurement of the M1-CuBe clamp cell	79
6.25	Comparison of theoretical and experimentally determined neutron transmission for the M1-Cube clamp cell	80
6.26	Magnetic satellite reflections in the M1-CuBe clamp cell	81
6.27	Thermal response of the M1-CuBe and M1-NiCrAl clamp cells	82
6.28	Base temperature in the thermal response of the M1-CuBe and M1-NiCrAl clamp cells	83
6.29	Regular and Al-layer PTFE plugs	84
6.30	Offline ruby system	85
6.31	Ruby placed on the culet of the diamond	86
6.32	Comparison of ruby luminescence in direct orientation and through the diamond	86
6.33	Ruby luminescence spectra in dependence of temperature	87
6.34	Ruby luminescence wavelength as function of temperature in the M1D-CuBe clamp cell	88
6.35	Ruby luminescence pressure as function of temperature in the M1D-CuBe clamp cell	89
6.36	Ruby luminescence pressure as function of force load for the calibration tests with the M1D-CuBe and M1D-NiCrAl clamp cells	90
6.37	Geometrical model for the absorption correction in a monobloc clamp cell	94
6.38	Neutron beam paths through the wall of a monobloc clamp cell	95

6.39	Transmission loss correction factor as function of angle for the monobloc clamp cell types M1/M1D	96
6.40	Neutron beam paths through the wall of a fretted clamp cell	97
6.41	Transmission loss correction factor as function of angle for the fretted clamp cells type F1	98
6.42	Neutron beam paths through the wall of a fretted clamp cell with conical contact surface	99
6.43	Influence of conical angle on transmission loss correction factor as function of scattering angle for the fretted clamp cell type F1-CuBe .	100
7.1	Raw and masked frame from synchrotron X-ray single-crystal measurement	102
7.2	Raw frame from high-pressure synchrotron X-ray single-crystal measurement	102
7.3	Raw frame and ω -scan from neutron single-crystal measurement . . .	103
7.4	Graph of maximal subgroups of space group $Pnma$	105
8.1	Magnetic susceptibility of CrAs as function of temperature for $H\parallel a$ and $H\perp a$	108
8.2	Magnetic susceptibility of CrAs as function of temperature in the range 2...1000 K for $H\parallel a$	109
8.3	Magnetization of CrAs as function of applied magnetic field for $H\parallel a$ and $H\perp a$	109
8.4	Resistance of CrAs as function of temperature for $I \parallel a$	111
8.5	Crystal structure of CrAs	112
8.6	Normalized lattice parameters of CrAs as function of temperature . .	113
8.7	c/b ratio of CrAs as function of temperature	114
8.8	Normalized lattice parameters of CrAs as function of pressure	115
8.9	Comparison of compounds with the MnP-type structure: normalized unit cell volume as function of pressure and bulk modulus as function of unit cell volume	116
8.10	Reciprocal space reconstructions for CrAs at 275 K and 270 K	117
8.11	Comparison of measured and reported atom coordinates of CrAs as function of temperature	119
8.12	Interatomic distances in CrAs as function of temperature and pressure	120
8.13	Comparison of the Cr–Cr distances in CrAs below and above the phase transition	121
8.14	Angle $\angle \text{Cr}^{\text{I}}\text{--Cr}^{\text{II}}\text{--Cr}^{\text{I}}$ in CrAs as function of temperature and of pressure.	122
8.15	Distance and angular distortion of the coordination polyhedra in CrAs as function of temperature and of pressure	123
8.16	$\angle \text{Cr}^{\text{I}}\text{--Cr}^{\text{II}}\text{--Cr}^{\text{I}}$ as function of temperature and of pressure.	125
8.17	Comparison of neutron powder diffraction patterns of CrAs at 300 K and 1.5 K	128
8.18	Propagation vector of the magnetic structure of CrAs as function of temperature	129
8.19	Visualization of the magnetic structure of CrAs refined in the four best magnetic models	139
8.20	Directional components of the four best magnetic models for CrAs . .	141

8.21	Directional components of the double-helical magnetic model of CrAs	142
A.1	Equipment for the loading of a clamp cell	177
A.2	Loading procedure for a clamp cell	179
B.1	Ruby luminescence pressure as function of force load for the calibration tests with the M1D-NiCrAl and AlMg5 Capsules	182
B.2	Ruby luminescence pressure as function of force load for the calibration tests with the M1D-CuBe and AlMg5 Capsules	183
B.3	Ruby luminescence pressure as function of force load for the calibration tests with the M1D-NiCrAl and PTFE Capsules	184
B.4	Ruby luminescence pressure as function of force load for the calibration tests with the M1D-CuBe and AlMg5 Capsules	185
C.1	Directional components of the magnetic models for CrAs related to superspace group $P2_1/n.1'(0bg)0ss$	214
C.2	Directional components of the magnetic models for CrAs related to superspace group $Pn.1'(0bg)0ss$	215
C.3	Directional components of the magnetic models for CrAs related to superspace group $P2_1.1'(0bg)0s$ ($P2_1^{[100]}$)	216
C.4	Directional components of the magnetic models for CrAs related to superspace group $P2_1.1'(a0g)0s$ ($P2_1^{[010]}$)	217
C.5	Directional components of the magnetic models for CrAs related to superspace group $Pa.1'(00g)0s$	218
C.6	Directional components of the magnetic models for CrAs related to superspace group $P\bar{1}.1'(abg)0s$	219
C.7	Directional components of the magnetic models for CrAs related to superspace group $P1.1'(abg)0s$	220
D.1	Magnetic susceptibility of PTFE as function of temperature	227
D.2	Comparison of measured and reported normalized lattice parameters of CrAs as function of temperature	228
D.3	Harmonic and anharmonic ADP from the synchrotron X-ray measurements of CrAs as function of temperature	229
D.4	Comparison of measured and reported Cr–Cr distances in CrAs as function of temperature and of pressure	230
D.5	Shift of neutron powder diffraction peaks with temperature	231

List of Tables

2.1	Overview of the structural transitions of transition-metal mononictides with MnP-type structure	15
8.1	Bulk modulus values of MnP-type compounds	116
8.2	Allowed magnetic moment components in the magnetic superspace groups derived from space group $Pnma$	130
8.3	Final agreement factors for all tested magnetic models for CrAs based on the refinement of the neutron single-crystal data at $p_{\text{nom}} = 0.17$ GPa	132
8.4	Final agreement factors of restrained magnetic models for CrAs based on the single-crystal data at $p_{\text{nom}} = 0.17$ GPa.	134
8.5	Final agreement factors for selected magnetic models for CrAs based on the refinement of neutron powder data	136
C.1	List of scans in the temperature-dependent synchrotron X-ray single-crystal experiments	188
C.2	List of scans in the pressure-dependent synchrotron X-ray single-crystal experiments in a YaoDAC-type DAC	188
C.3	List of scans in the pressure-dependent synchrotron X-ray single-crystal experiments in an Ahsbals-type DAC	189
C.4	List of scans in the pressure-dependent synchrotron X-ray single-crystal experiments in a Boehler–Almax-type DAC	189
C.5	Refinement details of the temperature-dependent synchrotron X-ray single-crystal measurements	190
C.6	Refinement details: pressure-dependent synchrotron X-ray single-crystal measurements	192
C.7	Refinement details: temperature-dependent laboratory X-ray single-crystal measurements	193
C.8	Refined atom coordinates and isotropic ADP from the temperature-dependent synchrotron X-ray single-crystal measurements	196
C.9	Refined atom coordinates and isotropic ADP from the pressure-dependent synchrotron X-ray single-crystal measurements	197
C.10	Refined atom coordinates and isotropic ADP from the temperature-dependent laboratory X-ray single-crystal measurements	198
C.11	Key to the denotation of the interatomic distances in CrAs	199
C.12	Interatomic Cr–Cr and Cr–As distances from the temperature-dependent synchrotron X-ray single-crystal measurements	200
C.13	Interatomic Cr–Cr and Cr–As distances from the pressure-dependent synchrotron X-ray single-crystal Measurements	201

C.14	Interatomic Cr–Cr and Cr–As distances from the temperature-dependent laboratory X-ray single-crystal measurements	202
C.15	Final agreement factors for the neutron single-crystal data at $p_{\text{nom}} = 0.17$ GPa	203
C.16	Final agreement factors for the neutron single-crystal data at $p_{\text{nom}} = 1.2$ GPa	205
C.17	Final agreement factors for the neutron single-crystal data of CrAs at $p_{\text{nom}} = 1.2$ GPa for all tested nuclear space groups	207
C.18	Modulation values for the neutron single-crystal data of CrAs at $p_{\text{nom}} = 0.17$ GPa	208
C.19	Final agreement factors for the neutron powder data of CrAs at $T = 1.5$ K	221
C.20	Final agreement factors for the neutron powder data of CrAs in the relevant magnetic superspace groups	223
E.1	Angular distortion of the $[\text{CrAs}_6]$ octrahedron in CrAs	235
E.2	Angular distortion of the $[\text{AsCr}_6]$ trigonal prism in CrAs	235

Acknowledgments

This thesis would not have been possible without the support and contributions of a lot of people, and I have to thank all of them for giving me this opportunity. In particular, this included the following people, but the list is certainly not exhaustive, with many people helping in many ways that I cannot fit here.

Apl. Prof. Dr. Karen Friese for all kinds of things: the creation of the PhD project in the first place, the decision to let me work on it and the agreement to supervise that work, the support with experiments and analyses as well as simply with the understanding of the subject matter, and the various other small details that make finishing a thesis possible.

Dr. Andrzej Grzechnik for thinking that my Master's Thesis was sufficiently not bad to keep me around for a high-pressure PhD project and his subsequent support with the development of the clamp cells as well as the help with all the other experimental and analytical work.

Prof. Dr. Georg Roth for agreeing to be the second reviewer of this thesis after he already had to read all my previous theses.

Prof. Dr. Thomas Brückel for giving me the opportunity to work at his institute.

Dr. Yixi Su for wanting a high-pressure option on his instrument DNS and needing someone to develop it as well as providing the complementary thesis subject of CrAs in order to have the foundations for the PhD project.

Dr. Martin Meven for supporting the development of the clamp cells even though they are not primarily intended for HEiDi, and his help in general as well as in particular at HEiDi-related matters.

Dr. Vladimir Hutanu, Dr. Robert Georgii and **Lukas Beddrich** for their interest in the clamp cells and in particular for applying them in their beamtimes, which proved to be unintentionally crucial for this thesis.

Muni Kishore Babu Poli for his help with the development of the clamp cells, their practical application, and performing the corresponding simulations.

Dr. Carsten Paulmann, Dr. Denis Sheptyakov and **Dr. Bachir Ouladdiaf** for their support during my beamtimes at P24 (DESY), HRPT (PSI) and D9 (ILL), respectively.

The JCNS workshop, in particular **Jens Schnitzler** and **Andreas Enns** for their support on the organizational level and **Frederik Geisen** for doing most of the actual work to bring my clamp cells from concept to reality, but also the members

of the workshop in general who were always willing to help even on shortest notice.

Dr. Thomas Müller for his help with the thermal tests at DNS and his participation in the night shift of my beamtime at P24.

Wolfgang Luberstetter for his help in the experiments at HEiDi and POLI.

Jörg Persön for his help with the laboratory work and the synthesis of CrAs single crystals.

Micha Hölzle for having a look at my technical drawings and my technical problems.

Berthold Schmitz for his help with various technical issues, often on very short notice.

Dr. Shibabrata Nandi and **PD Dr. Oleg Petravic** for helping with the work on the PPMS, DynaCool and MPMS instruments.

JProf. Dr. Luana Caron for her help with the design and the tests of the magnetization clamp cell, even though it ultimately did not make it into this thesis.

Thomas Jansen for the sputtering of the plugs and making the necessary parts without any complications due to work across institute borders.

Dr. Jörg Voigt and **Prof. Dr. Manuel Angst** for listening in the group meetings to stuff they were more often than not rather uninvolved in and still had more qualified insights than I.

My past and present colleagues at JCNS-2, especially **Dr. Markus Herrmann** for helping me getting started at the Forschungszentrum, **Dr. Nour Maraytta** for making sharing an office for so long a pleasant experience, **Branislav Viliam Hakala** for letting me not be the only high-pressure PhD student anymore, and **Hend Shahed** for taking a lot of photos and participating in my beamtime.

Finally, my family and friends, who now either know a lot more about clamp cells and CrAs than they ever wanted to or still have mostly no idea about what exactly I did for a good three and half years, but did provide the crucial non-scientific support without which I definitely would not have finished this thesis with my sanity at least halfway intact.

List of Publications

- **A. Eich**, M. Hölzle, Y. Su, R. Georgii, L. Beddrich, and A. Grzechnik. Clamp Cells for High Pressure Neutron Scattering at Low Temperatures and High Magnetic Fields at Heinz Maier-Leibnitz Zentrum (MLZ). *High Press. Res.* **41**(1):88–96, 2021.
- **A. Eich**, A. Grzechnik, C. Paulmann, T. Müller, Y. Su, T. Wolf, and K. Frieze. Comparison of the Temperature- and Pressure-Dependent Behavior of the Crystal Structure of CrAs. *Acta Cryst. B* **77**(4):594–604, 2021.
- **A. Eich**, A. Grzechnik, L. Caron, Y. Cheng, J. Wilden, H. Deng, V. Hutanu, M. Meven, M. Hanfland, K. Glazyrin, P. Hering, M.G. Herrmann, M. Ait Haddouch, and K. Frieze. Magnetocaloric Mn_5Si_3 and MnFe_4Si_3 at Variable Pressure and Temperature. *Mater. Res. Express* **6**:096118, 2019.
- M.G. Herrmann, R.P. Stoffel, M. Küpers, M. Ait Haddouch, **A. Eich**, K. Glazyrin, A. Grzechnik, R. Dronskowski, and K. Frieze. New Insights on the $\text{GeSe}_x\text{Te}_{1-x}$ Phase Diagram from Theory and Experiment. *Acta Cryst. B* **75**(2):246–256, 2019.

Appendix A

Manual for the Loading of a Clamp Cell

The basic equipment necessary for the loading of a clamp cell is shown in Figure A.1. Below, the procedure for loading the clamp cell with the ruby luminescence option is given, which is also illustrated in Figure A.2. The loading of a clamp cell without ruby luminescence option is in principle the same, and the steps related to the ruby can simply be skipped.

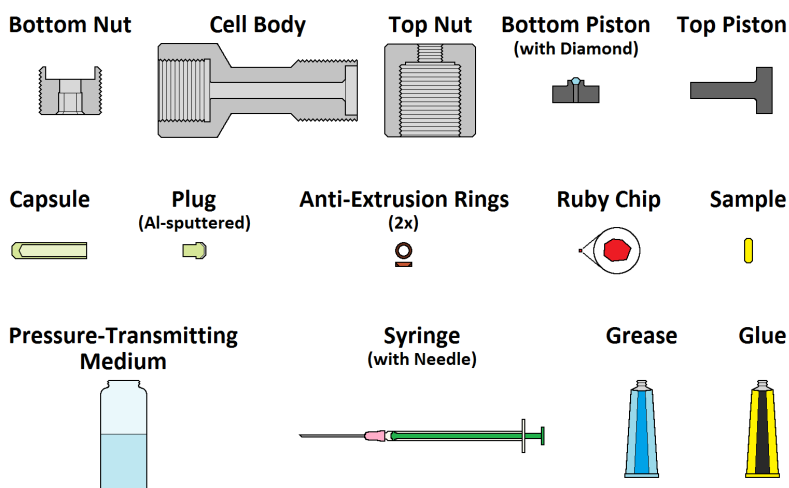


Figure A.1: Equipment for the loading of a clamp cell with ruby luminescence option.

1. The compatibility of the selected parts – cell body, capsule, plug, and anti-extrusion rings – is tested.
2. The ruby chip is mounted with grease on the diamond culet of the bottom piston.
3. The reference ruby luminescence spectrum at ambient conditions is measured.
4. The oriented sample is mounted on the plug with glue.
5. Grease is applied to the plug shaft for additional sealing.
6. The capsule is completely filled with pressure-transmitting medium.
7. The capsule is closed with the plug, with care being taken to avoid the inclusion of bubbles in the capsule.
8. The closed capsule is inserted into the cell with the plug facing the bottom end.
9. The anti-extrusion rings are inserted from both sides.
10. The bottom piston is inserted and the bottom nut is fixed.
11. The top piston is inserted and, if necessary, the capsule is pressed into contact with the bottom piston.
12. The top nut is closed without exerting force onto the top piston.
13. The ruby luminescence spectrum in the closed state is measured, and the cell is prepared.

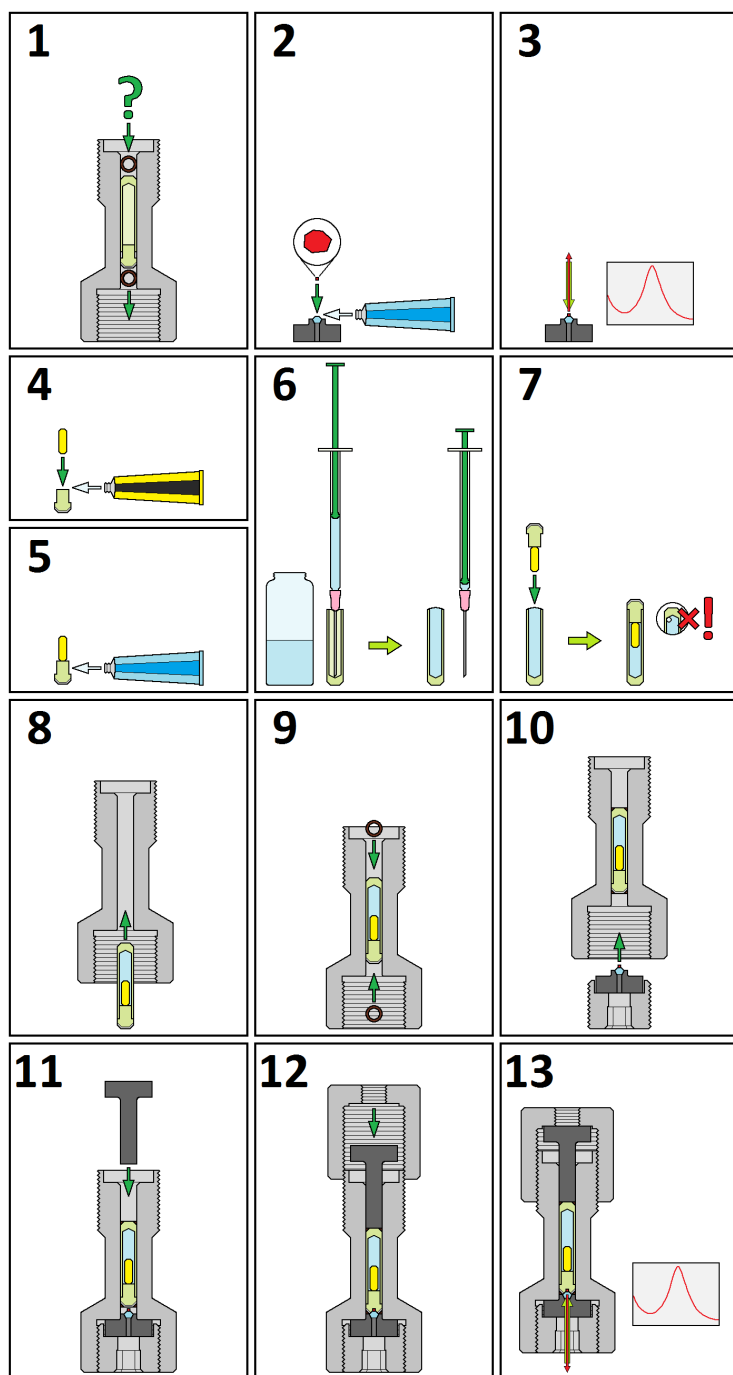


Figure A.2: Loading procedure for a clamp cell with ruby luminescence option.

Appendix B

Details of Ruby Luminescence Test Measurements

Lead Capsules

Three runs with lead capsules in the M1D-NiCrAl cell were performed. Due to the softness of the capsule material and the thus expected large deformation of the capsule, a long capsule (29 mm) was used in combination with the standard top piston.

In all three measurements, the maximum compression of the cell – a length change of about 12 mm – was reached before a force of 2 kN was reached on the press scale. The ruby luminescence measurements showed in all cases that no significant pressure was applied to the ruby.

Since these tests with the lead capsules in the M1D-NiCrAl were consistently showing that lead is not a suitable material (at least not with the present capsule design), tests with lead capsules in the M1D-CuBe were suspended.

AlMg5 Capsules in the M1D-NiCrAl Cell

Two runs with AlMg5 capsules in the M1D-NiCrAl cell were performed (Figure B.1), using standard length capsules (24 mm) with the standard top piston. In both runs, the force load was applied in steps of 2 kN, in run #1 only up to 16 kN instead of the then-used maximum of 18 kN.

The spread of pressure is quite large, especially above 12 kN, following from different behaviors seen in the two runs: run #1 has a kink at 12 kN and flattens at higher pressures, while run #2 increases more smoothly.

In both runs, the capsule was stuck in the cell after opening it.

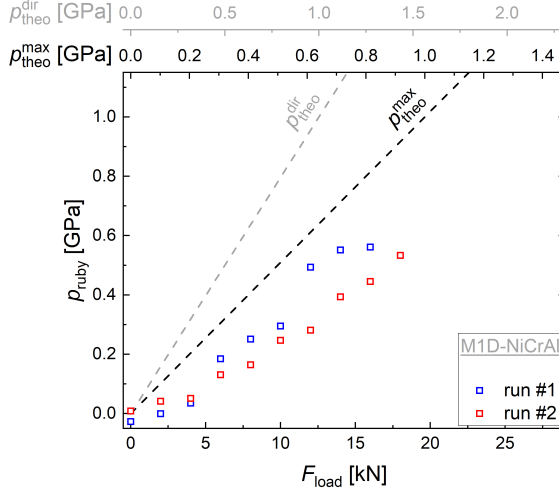


Figure B.1: The pressure calculated from the shift of the ruby luminescence as function of applied force load for the calibration tests with the M1D-NiCrAl and AlMg5 capsules. The black (gray) dashed lines mark the equivalence of p_{ruby} and $p_{\text{theo}}^{\text{max}}$ ($p_{\text{theo}}^{\text{dir}}$).

AlMg5 Capsules in the M1D-CuBe Cell

Three runs with AlMg5 capsules in the M1D-CuBe cell were performed (Figure B.2), using standard length capsules with the standard top piston. Run #1 was aborted early as no pressure was detected; in runs #2 and #3, the force load was applied in steps of 2 kN up to the then-used maximum of 12 kN.

The spread of the pressure is smaller than in the case of the M1D-NiCrAl and no obvious kink is observed, but even so the pressure spread is considerable (≈ 0.1 GPa).

As in the case of tests with AlMg5 capsules in the M1D-NiCrAl cell, the capsule was stuck in the cell after both runs.

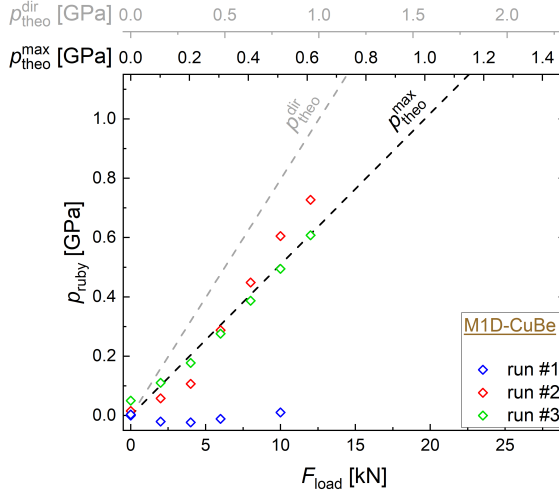


Figure B.2: The pressure calculated from the shift of the ruby luminescence as function of applied force load for the calibration tests with the M1D-CuBe and AlMg5 capsules. The black (gray) dashed lines mark the equivalence of p_{ruby} and $p_{\text{theo}}^{\text{max}}$ ($p_{\text{theo}}^{\text{dir}}$).

PTFE Capsules in the M1D-NiCrAl Cell

Seven runs with PTFE capsules in the M1D-NiCrAl cell were performed (Figure B.3), using long capsules to account for the expected large deformation due to the softness of PTFE with the standard top piston. Run #1, where the force load was applied in steps of 1 kN up to 8 kN and then in steps of 2 kN up to 12 kN, had to be aborted early due to time constraints. In runs #2 and #3, steps of 2 kN were applied up to the maximum of 18 kN. In run #4, the force load was applied in 2 kN steps up to 24 kN and then in 1 kN up to 27 kN, where the cell broke. In run #5–#7, force was generally applied in 2 kN steps, but the runs were finished when either the compression limit (runs #5 and #6) was reached or the cell broke (run #7).

Although there is again a spread in the pressure values (up to ≈ 0.13 GPa) of the curves, the observed behavior is very similar in all runs.

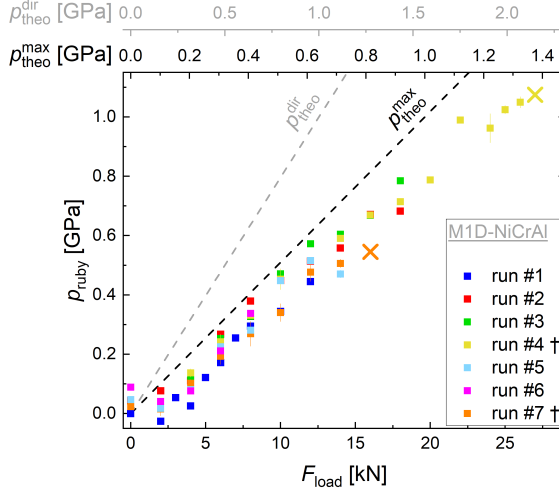


Figure B.3: The pressure calculated from the shift of the ruby luminescence as function of applied force load for the calibration tests with the M1D-NiCrAl and PTFE capsules. The crosses indicate that the used clamp cell broke. The black (gray) dashed lines mark the equivalence of p_{ruby} and $p_{\text{theo}}^{\text{max}}$ ($p_{\text{theo}}^{\text{dir}}$).

PTFE Capsules in the M1D-CuBe Cell

Five standard runs (#1–#3, #8, #9) with PTFE capsules in the M1D-CuBe were performed, using long capsules with the standard top piston. In the first runs (#1–#3), force load steps of 2 kN up to 6 kN and 1 kN steps up to 12 kN were used. In the runs up to the later maximum of 20 kN (#8, #9), force was applied in 2 kN steps up to 14 kN and in 1 kN steps above.

These standard-measurement curves are less similar than the ones from the measurements in the M1D-NiCrAl cells, and in all runs, some particularities can be seen. Overall, the spread in pressure between curves is ≈ 0.2 GPa.

In addition to the standard runs with PTFE capsules in the M1D-CuBe, four runs performed with varying load steps up to a maximum 12 kN: in run #4, the pressure was increased in steps of 3 kN, in runs #5 and #6 in steps of 6 kN and in run #7 in one step of 12 kN. This was done to see whether the step size – as most practical approximation of load rate – affects the pressure. While the runs with varied step size lead to a significantly increased spread in pressure (at 6 kN and 12 kN) which might be caused by the load step, there is no clear trend in the measured pressure with step size.

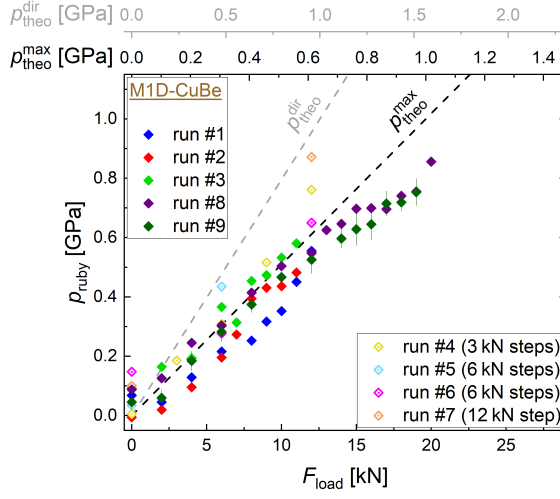


Figure B.4: The pressure calculated from the shift of the ruby luminescence as function of applied force load for the calibration tests with the M1D-CuBe and PTFE capsules. The black (gray) dashed lines mark the equivalence of p_{ruby} and $p_{\text{theo}}^{\text{max}}$ ($p_{\text{theo}}^{\text{dir}}$).

Appendix C

Measurement and Refinement Details

Table C.1: List of the experimental parameters used for the scans in the temperature-dependent synchrotron X-ray single-crystal measurements at P24, PETRA III, DESY.

No.	scan					2θ	χ	ω	κ
	angle	start	end	steps	t_{exp}				
#1	ϕ	0°	360°	360	2 s	0°	0°	90°	0°
#2	ϕ	0°	360°	360	5 s	45°	0°	90°	0°

No.	angle	start	end	steps	t_{exp}	2θ	χ	ϕ	κ
#3	ω	$-5.528\,78^\circ$	$54.471\,22^\circ$	60	5 s	45°	60°	$19.471\,22^\circ$	$70.528\,78^\circ$
#4	ω	$-5.528\,78^\circ$	$54.471\,22^\circ$	60	5 s	45°	60°	$79.471\,22^\circ$	$70.528\,78^\circ$
#5	ω	$-5.528\,78^\circ$	$54.471\,22^\circ$	60	5 s	45°	60°	$139.471\,22^\circ$	$70.528\,78^\circ$
#6	ω	$-5.528\,78^\circ$	$54.471\,22^\circ$	60	5 s	45°	60°	$199.471\,22^\circ$	$70.528\,78^\circ$
#7	ω	$-5.528\,78^\circ$	$54.471\,22^\circ$	60	5 s	45°	60°	$259.471\,22^\circ$	$70.528\,78^\circ$
#8	ω	$-5.528\,78^\circ$	$54.471\,22^\circ$	60	5 s	45°	60°	$319.471\,22^\circ$	$70.528\,78^\circ$

Table C.2: List of the experimental parameters used for the scans in the pressure-dependent synchrotron X-ray single-crystal measurements at P24, PETRA III, DESY, using the YaoDAC-type DAC.

No.	scan					2θ	χ	ω	κ
	angle	start	end	steps	t_{exp}				
#1	ϕ	37°	143°	112	1 s	0°	0°	90°	0°
#2	ϕ	217°	323°	106	1 s	0°	0°	90°	0°

No.	angle	start	end	steps	t_{exp}	2θ	χ	ϕ	κ
#3	ω	$-26.100\,57^\circ$	$8.899\,43^\circ$	35	1 s	0°	30°	$8.899\,43^\circ$	$34.778\,11^\circ$
#4	ω	$-26.100\,57^\circ$	$8.899\,43^\circ$	35	1 s	0°	30°	$188.899\,43^\circ$	$34.778\,11^\circ$
#5	ω	$-22.528\,78^\circ$	$19.471\,22^\circ$	42	1 s	45°	60°	$19.471\,22^\circ$	$70.528\,78^\circ$
#6	ω	$-22.528\,78^\circ$	$19.471\,22^\circ$	42	1 s	45°	60°	$199.471\,22^\circ$	$70.528\,78^\circ$
#7	ω	$-9.860\,68^\circ$	$35.264\,22^\circ$	45	1 s	45°	90°	$35.264\,22^\circ$	$109.471\,22^\circ$
#8	ω	$-9.860\,68^\circ$	$35.264\,22^\circ$	45	1 s	45°	90°	$215.264\,22^\circ$	$109.471\,22^\circ$

Table C.3: List of the experimental parameters used for the scans in the pressure-dependent synchrotron X-ray single-crystal measurements at P24, PETRA III, DESY, using the Ahsbahs-type DAC.

No.	scan					2θ	χ	ω	κ
	angle	start	end	steps	t_{exp}				
#1	ϕ	135°	225°	90	1 s	0°	0°	90°	0°
#2	ϕ	315°	405°	90	1 s	0°	0°	90°	0°

No.	angle	start	end	steps	t_{exp}	2θ	χ	ϕ	κ
#3	ω	$-26.100\,57^\circ$	$8.899\,43^\circ$	35	1 s	0°	30°	$98.899\,43^\circ$	$34.778\,11^\circ$
#4	ω	$-26.100\,57^\circ$	$8.899\,43^\circ$	35	1 s	0°	30°	$278.899\,43^\circ$	$34.778\,11^\circ$
#5	ω	$-22.528\,78^\circ$	$19.471\,22^\circ$	42	1 s	45°	60°	$109.471\,22^\circ$	$70.528\,78^\circ$
#6	ω	$-22.528\,78^\circ$	$19.471\,22^\circ$	42	1 s	45°	60°	$289.471\,22^\circ$	$70.528\,78^\circ$
#7	ω	$-9.860\,68^\circ$	$35.264\,22^\circ$	45	1 s	45°	90°	$125.264\,22^\circ$	$109.471\,22^\circ$
#8	ω	$-9.860\,68^\circ$	$35.264\,22^\circ$	45	1 s	45°	90°	$305.264\,22^\circ$	$109.471\,22^\circ$

Table C.4: List of the experimental parameters used for the scans in the pressure-dependent single-crystal measurements at P24, PETRA III, DESY, using the Boehler–Almax-type DAC.

No.	scan					2θ	χ	ω	κ
	angle	start	end	steps	t_{exp}				
#1	ϕ	45°	135°	90	1 s	0°	0°	90°	0°
#2	ϕ	225°	315°	90	1 s	0°	0°	90°	0°

No.	angle	start	end	steps	t_{exp}	2θ	χ	ϕ	κ
#3	ω	$-26.100\,57^\circ$	$8.899\,43^\circ$	35	1 s	0°	30°	$8.899\,43^\circ$	$34.778\,11^\circ$
#4	ω	$-26.100\,57^\circ$	$8.899\,43^\circ$	35	1 s	0°	30°	$188.899\,43^\circ$	$34.778\,11^\circ$
#5	ω	$-22.528\,78^\circ$	$19.471\,22^\circ$	42	1 s	45°	60°	$19.471\,22^\circ$	$70.528\,78^\circ$
#6	ω	$-22.528\,78^\circ$	$19.471\,22^\circ$	42	1 s	45°	60°	$199.471\,22^\circ$	$70.528\,78^\circ$
#7	ω	$-9.860\,68^\circ$	$35.264\,22^\circ$	45	1 s	45°	90°	$35.264\,22^\circ$	$109.471\,22^\circ$
#8	ω	$-9.860\,68^\circ$	$35.264\,22^\circ$	45	1 s	45°	90°	$215.264\,22^\circ$	$109.471\,22^\circ$

Table C.5: Refinement details of the temperature-dependent synchrotron X-ray single-crystal measurements on CrAs at ambient pressure. Refinements where not all parameters could be refined are marked: * the extinction coefficient G_{iso} could not be refined; † only one twin component could be refined; ‡ no twin component could be refined.

T [K]	No. meas. Ref. (obs/all)	$h_{\text{min}} \rightarrow h_{\text{max}}$ $k_{\text{min}} \rightarrow k_{\text{max}}$ $l_{\text{min}} \rightarrow l_{\text{max}}$	No. sym. ind. Refl. (obs/all)	$R(\text{int})$ (obs/all)	R (obs/all)	wR (obs/all)	No. param.	Space group	a [Å]	b [Å]	c [Å]	V [Å ³]
275	13472/15537	-14 → 16 -10 → 10 -17 → 18	1571/1718	7.88/7.88	3.13/3.23	3.80/3.81	14	$Pnma$	5.64298(5)	3.45198(8)	6.20197(8)	120.811(3)
270	14015/15983	-14 → 16 -10 → 10 -17 → 17	1646/1793	6.81/6.82	3.69/3.75	4.75/4.76	15*	$Pnma$	5.62063(9)	3.57308(6)	6.15072(10)	123.525(4)
260	13936/16041	-16 → 14 -10 → 10 -17 → 17	1613/1758	7.21/7.22	3.49/3.58	4.39/4.40	15*	$Pnma$	5.61887(10)	3.57531(6)	6.14917(11)	123.532(4)
250	13938/15994	-14 → 16 -10 → 10 -17 → 17	1619/1758	7.73/7.74	2.81/2.93	3.84/3.85	16	$Pnma$	5.61729(9)	3.57721(6)	6.14676(11)	123.514(3)
240	13929/15981	-14 → 16 -10 → 10 -17 → 17	1622/1757	7.13/7.14	2.41/2.53	3.29/3.31	16	$Pnma$	5.61599(10)	3.57836(6)	6.14550(11)	123.500(4)
220	14049/15996	-14 → 16 -10 → 10 -17 → 17	1623/1757	6.57/6.58	2.34/2.46	3.17/3.20	16	$Pnma$	5.61290(11)	3.58055(7)	6.14272(12)	123.452(4)
200	13924/15919	-14 → 16 -10 → 10 -17 → 17	1623/1755	7.76/7.76	2.56/2.69	3.36/3.37	16	$Pnma$	5.61059(12)	3.58148(8)	6.14112(13)	123.401(5)
185	13865/15795	-14 → 16 -10 → 10 -17 → 17	1629/1756	6.84/6.84	2.23/2.38	2.96/3.02	15†	$Pnma$	5.60945(12)	3.58259(7)	6.13862(13)	123.364(4)
170	14009/15871	-14 → 16 -10 → 10 -17 → 17	1631/1755	6.68/6.68	2.26/2.37	2.94/2.96	15†	$Pnma$	5.60797(12)	3.58313(8)	6.13709(13)	123.319(5)

Table C.5 (continued): Refinement details of the temperature-dependent synchrotron X-ray single-crystal measurements on CrAs at ambient pressure. Refinements where not all parameters could be refined are marked: * the extinction coefficient G_{iso} could not be refined; † only one twin component could be refined; ‡ no twin component could be refined.

T [K]	No. meas. Ref. (obs/all)	$h_{\text{min}} \rightarrow h_{\text{max}}$ $k_{\text{min}} \rightarrow k_{\text{max}}$ $l_{\text{min}} \rightarrow l_{\text{max}}$	No. sym. ind. Refl. (obs/all)	$R(\text{int})$ (obs/all)	R (obs/all)	wR (obs/all)	No. param.	Space group	a [Å]	b [Å]	c [Å]	V [Å ³]
155	13877/15765	-14 → 16 -10 → 10 -17 → 17	1637/1756	7.31/7.32	2.31/2.41	3.12/3.14	15 [†]	$Pnma$	5.60599(13)	3.58348(8)	6.13566(14)	123.259(5)
140	13751/15666	-16 → 14 -10 → 10 -17 → 17	1625/1756	7.65/7.66	2.58/2.70	3.43/3.44	15 [†]	$Pnma$	5.60404(14)	3.58394(8)	6.13451(15)	123.209(5)
125	13839/15652	-16 → 14 -10 → 10 -17 → 17	1633/1756	7.12/7.13	2.38/2.50	3.21/3.23	15 [†]	$Pnma$	5.60354(14)	3.58370(8)	6.13403(15)	123.180(5)
110	14014/15773	-14 → 16 -10 → 10 -17 → 17	1641/1755	6.86/6.87	2.20/2.30	3.11/3.12	15 [†]	$Pnma$	5.60289(13)	3.58401(8)	6.13266(15)	123.149(5)
95	14029/15734	-14 → 16 -10 → 10 -17 → 17	1646/1755	6.87/6.87	2.08/2.19	2.90/2.92	15 [†]	$Pnma$	5.60187(14)	3.58416(8)	6.13183(15)	123.115(5)
80	13424/15253	-14 → 16 -10 → 10 -17 → 17	1628/1753	8.45/8.46	2.90/3.01	3.98/3.99	15 [†]	$Pnma$	5.60069(11)	3.58377(7)	6.13051(12)	123.049(4)
65	14064/15701	-14 → 16 -10 → 10 -17 → 17	1647/1754	6.31/6.32	1.90/2.00	2.52/2.54	15 [†]	$Pnma$	5.59944(10)	3.58433(6)	6.12896(11)	123.010(4)
50	14038/15655	-14 → 16 -10 → 10 -17 → 17	1650/1753	6.61/6.61	1.98/2.08	2.62/2.64	15 [†]	$Pnma$	5.59880(10)	3.58443(6)	6.12843(11)	122.988(4)
35	13035/15114	-14 → 16 -10 → 10 -17 → 17	1614/1751	10.38/10.39	4.13/4.28	5.91/5.93	15 [†]	$Pnma$	5.59704(12)	3.58436(8)	6.13032(14)	122.985(5)

Table C.6: Refinement details of the pressure-dependent synchrotron X-ray single-crystal measurements on CrAs at room temperature. Refinements where not all parameters could be refined are marked: * the extinction coefficient G_{iso} could not be refined; † only one twin component could be refined; ‡ no twin component could be refined.

p [GPa]	No. meas. Ref. (obs/all)	$h_{\text{min}} \rightarrow h_{\text{max}}$ $k_{\text{min}} \rightarrow k_{\text{max}}$ $l_{\text{min}} \rightarrow l_{\text{max}}$	No. sym. ind. Refl. (obs/all)	$R(\text{int})$ (obs/all)	R (obs/all)	wR (obs/all)	No. param.	Space group	a [Å]	b [Å]	c [Å]	V [Å ³]
1.03	1437/2173	-9 → 9 -4 → 4 -10 → 10	195/268	5.99/6.19	3.12/4.36	3.55/3.65	15 [†]	$Pnma$	5.6271(5)	3.3902(10)	6.1909(7)	118.10(12)
2.53	1367/2192	-9 → 9 -4 → 4 -10 → 10	185/265	8.72/9.03	3.54/5.47	3.70/3.87	14 [‡]	$Pnma$	5.6147(5)	3.3418(11)	6.1760(9)	115.88(4)
3.13	1322/2079	-9 → 9 -5 → 5 -10 → 10	222/300	8.90/9.09	4.25/5.47	4.59/4.67	14 [‡]	$Pnma$	5.610(2)	3.3255(11)	6.162(2)	114.96(7)
4.45	1421/1991	-7 → 6 -5 → 5 -10 → 10	202/242	14.65/14.79	7.56/8.39	8.19/8.29	14 [‡]	$Pnma$	5.593(5)	3.3003(8)	6.1478(13)	113.47(10)
6.05	683/1029	-7 → 7 -5 → 5 -10 → 10	169/207	6.64/6.76	7.15/7.62	8.42/8.43	14 [‡]	$Pnma$	5.581(3)	3.2734(6)	6.1287(10)	111.97(7)
7.32	1722/1984	-9 → 9 -5 → 5 -8 → 8	226/247	8.34/8.35	4.20/4.33	4.90/4.91	15 [†]	$Pnma$	5.5765(9)	3.2539(4)	6.118(2)	111.01(5)
8.09	1050/1742	-9 → 9 -5 → 5 -10 → 9	212/283	7.75/8.03	4.73/7.55	4.91/5.17	14 [‡]	$Pnma$	5.5721(12)	3.2432(7)	6.1128(14)	110.47(4)
9.46	1678/1967	-9 → 9 -5 → 5 -8 → 8	210/241	7.50/7.52	4.77/4.99	5.41/5.42	14 [‡]	$Pnma$	5.5628(7)	3.2258(3)	6.0966(15)	109.40(3)

Table C.7: Refinement details of the temperature-dependent laboratory X-ray single-crystal measurements on CrAs at ambient pressure. Refinements where not all parameters could be refined are marked: * the extinction coefficient G_{iso} could not be refined; † only one twin component could be refined; ‡ no twin component could be refined.

T [K]	No. meas. Ref. (obs/all)	$h_{\text{min}} \rightarrow h_{\text{max}}$ $k_{\text{min}} \rightarrow k_{\text{max}}$ $l_{\text{min}} \rightarrow l_{\text{max}}$	No. sym. ind. Refl. (obs/all)	$R(\text{int})$ (obs/all)	R (obs/all)	wR (obs/all)	No. param.	Space group	a [Å]	b [Å]	c [Å]	V [Å ³]
300	2183/2509	$-7 \rightarrow 7$ $-4 \rightarrow 4$ $-8 \rightarrow 8$	169/188	6.47/6.51	1.95/2.27	2.19/2.24	14 [‡]	$Pnma$	5.6442(10)	3.4671(6)	6.2019(10)	121.37(4)
310	2291/2657	$-7 \rightarrow 7$ $-4 \rightarrow 4$ $-8 \rightarrow 8$	173/192	6.05/6.10	1.78/2.07	1.91/1.95	14 [‡]	$Pnma$	5.6448(11)	3.4706(7)	6.1991(11)	121.45(4)
320	2045/2338	$-7 \rightarrow 7$ $-4 \rightarrow 4$ $-8 \rightarrow 8$	173/187	6.36/6.38	2.22/2.42	2.46/2.50	14 [‡]	$Pnma$	5.6475(11)	3.4714(6)	6.2010(11)	121.57(4)
330	2248/2563	$-7 \rightarrow 7$ $-4 \rightarrow 4$ $-8 \rightarrow 8$	173/188	6.98/7.00	2.26/2.61	2.58/2.66	14 [‡]	$Pnma$	5.6475(11)	3.4757(6)	6.2025(11)	121.75(4)
340	2167/2515	$-7 \rightarrow 7$ $-4 \rightarrow 4$ $-8 \rightarrow 8$	171/190	6.08/6.11	1.85/2.23	2.08/2.17	14 [‡]	$Pnma$	5.6487(10)	3.4767(6)	6.2033(11)	121.83(4)
350	2190/2518	$-7 \rightarrow 7$ $-4 \rightarrow 4$ $-8 \rightarrow 8$	175/190	7.07/7.10	2.25/2.49	2.42/2.52	14 [‡]	$Pnma$	5.6501(8)	3.4794(5)	6.2054(8)	121.99(3)
360	2126/2491	$-7 \rightarrow 7$ $-4 \rightarrow 4$ $-8 \rightarrow 8$	171/189	6.67/6.70	2.15/2.47	2.32/2.45	14 [‡]	$Pnma$	5.6527(9)	3.4819(5)	6.2024(9)	122.07(3)
370	2256/2578	$-7 \rightarrow 7$ $-4 \rightarrow 4$ $-8 \rightarrow 8$	172/189	5.92/5.96	1.98/2.24	2.25/2.33	14 [‡]	$Pnma$	5.6529(10)	3.4851(6)	6.2015(11)	122.18(4)
380	2197/2530	$-7 \rightarrow 7$ $-4 \rightarrow 4$ $-8 \rightarrow 8$	176/190	6.30/6.33	2.18/2.41	2.38/2.48	14 [‡]	$Pnma$	5.6543(9)	3.4860(5)	6.2046(10)	122.30(3)

Table C.7 (continued): Refinement details of the temperature-dependent laboratory X-ray single-crystal measurements on CrAs at ambient pressure. Refinements where not all parameters could be refined are marked: * the extinction coefficient G_{150} could not be refined; † only one twin component could be refined; ‡ no twin component could be refined.

T [K]	No. meas. Ref. (obs/all)	$h_{\min} \rightarrow h_{\max}$ $k_{\min} \rightarrow k_{\max}$ $l_{\min} \rightarrow l_{\max}$	No. sym. ind. Refl. (obs/all)	$R(\text{int})$ (obs/all)	R (obs/all)	wR (obs/all)	No. param.	Space group	a [Å]	b [Å]	c [Å]	V [Å ³]
390	2348/2663	$-7 \rightarrow 7$ $-4 \rightarrow 4$ $-8 \rightarrow 8$	178/192	5.78/5.82	1.94/2.11	2.14/2.17	14 [‡]	$Pnma$	5.6532(9)	3.4869(5)	6.2083(9)	122.38(3)
400	2439/2783	$-7 \rightarrow 7$ $-4 \rightarrow 4$ $-8 \rightarrow 8$	176/191	6.56/6.60	1.84/2.13	1.98/2.11	14 [‡]	$Pnma$	5.6548(9)	3.4901(6)	6.2080(9)	122.52(3)
290	2132/2465	$-7 \rightarrow 7$ $-4 \rightarrow 4$ $-8 \rightarrow 8$	172/188	6.43/6.47	2.21/2.49	2.35/2.41	14 [‡]	$Pnma$	5.6434(10)	3.4630(6)	6.2027(11)	121.22(4)
280	2320/2656	$-7 \rightarrow 7$ $-4 \rightarrow 4$ $-8 \rightarrow 8$	172/188	6.62/6.66	2.24/2.51	2.51/2.57	14 [‡]	$Pnma$	5.6445(9)	3.4597(6)	6.1997(10)	121.07(3)
300	2240/2561	$-7 \rightarrow 7$ $-4 \rightarrow 4$ $-8 \rightarrow 8$	175/189	6.50/6.53	2.04/2.21	2.20/2.23	14 [‡]	$Pnma$	5.6473(10)	3.4666(6)	6.2002(10)	121.38(4)
310	2384/2781	$-7 \rightarrow 7$ $-4 \rightarrow 4$ $-8 \rightarrow 8$	173/190	5.23/5.27	1.40/1.92	1.58/1.72	14 [‡]	$Pnma$	5.6477(9)	3.4693(6)	6.1995(10)	121.47(3)
320	2382/2782	$-7 \rightarrow 7$ $-4 \rightarrow 4$ $-8 \rightarrow 8$	174/191	5.55/5.59	1.81/2.02	1.95/1.99	14 [‡]	$Pnma$	5.6485(9)	3.4717(6)	6.1998(10)	121.58(3)
275	2202/2487	$-7 \rightarrow 7$ $-4 \rightarrow 4$ $-8 \rightarrow 8$	173/186	5.70/5.73	2.20/2.40	2.33/2.40	14 [‡]	$Pnma$	5.6412(10)	3.4540(6)	6.1995(11)	120.79(4)
240	2566/2961	$-7 \rightarrow 7$ $-4 \rightarrow 4$ $-8 \rightarrow 8$	182/195	4.42/4.44	1.91/2.25	2.46/2.49	14 [‡]	$Pnma$	5.6172(8)	3.5776(5)	6.1449(13)	123.49(3)

Table C.7 (continued): Refinement details of the temperature-dependent laboratory X-ray single-crystal measurements on CrAs at ambient pressure. Refinements where not all parameters could be refined are marked: * the extinction coefficient G_{iso} could not be refined; † only one twin component could be refined; ‡ no twin component could be refined.

T [K]	No. meas. Ref. (obs/all)	$h_{\min} \rightarrow h_{\max}$ $k_{\min} \rightarrow k_{\max}$ $l_{\min} \rightarrow l_{\max}$	No. sym. ind. Refl. (obs/all)	$R(\text{int})$ (obs/all)	R (obs/all)	wR (obs/all)	No. param.	Space group	a [Å]	b [Å]	c [Å]	V [Å ³]
250	2599/2964	$-7 \rightarrow 7$ $-4 \rightarrow 4$ $-8 \rightarrow 8$	184/195	4.71/4.73	2.05/2.17	2.89/2.90	14 [‡]	$Pnma$	5.6183(8)	3.5757(5)	6.1488(9)	123.52(3)
270	2582/2919	$-7 \rightarrow 7$ $-4 \rightarrow 4$ $-8 \rightarrow 8$	181/192	4.36/4.39	1.49/1.74	1.76/1.82	14 [‡]	$Pnma$	5.6445(12)	3.4579(8)	6.2078(13)	121.17(4)
280	2517/2927	$-7 \rightarrow 7$ $-4 \rightarrow 4$ $-8 \rightarrow 8$	177/192	4.75/4.78	1.53/1.74	1.78/1.84	14 [‡]	$Pnma$	5.6450(10)	3.4590(6)	6.2001(11)	121.06(4)

Table C.8: Refined atom coordinates (x , z) and isotropic ADP (U_{iso}) for Cr and As from the synchrotron X-ray single-crystal diffraction measurements as function of temperature at ambient pressure.

T [K]	Cr (x_{Cr} , $1/4$, z_{Cr})			As (x_{As} , $1/4$, z_{As})			U_{iso} [\AA^2]	
	x_{Cr}	z_{Cr}		x_{As}		z_{As}	U_{iso} [Cr]	U_{iso} [As]
275	0.00642(3)	0.20040(3)		0.20133(20)		0.57619(18)	0.00973(3)	0.00924(20)
270	0.00686(4)	0.20533(4)		0.20581(3)		0.58268(3)	0.00935(3)	0.00910(3)
260	0.00688(4)	0.20551(4)		0.20582(3)		0.58283(3)	0.00900(3)	0.00878(3)
250	0.00695(3)	0.20554(3)		0.20581(3)		0.58293(19)	0.00531(3)	0.00510(20)
240	0.00700(3)	0.20554(3)		0.20580(18)		0.58302(16)	0.00511(3)	0.00491(17)
220	0.00708(3)	0.20547(3)		0.20574(17)		0.58317(15)	0.00487(20)	0.00468(16)
200	0.00714(3)	0.20539(3)		0.20562(18)		0.58329(16)	0.00459(3)	0.00440(17)
185	0.00718(3)	0.20535(3)		0.20556(16)		0.58334(15)	0.00432(18)	0.00414(15)
170	0.00724(3)	0.20530(3)		0.20549(15)		0.58337(14)	0.00409(18)	0.00390(15)
155	0.00728(3)	0.20522(3)		0.20540(16)		0.58340(15)	0.00399(19)	0.00380(16)
140	0.00732(3)	0.20514(3)		0.20532(18)		0.58342(17)	0.00386(3)	0.00366(17)
125	0.00736(3)	0.20508(3)		0.20526(17)		0.58343(15)	0.00364(19)	0.00342(16)
110	0.00739(3)	0.20504(3)		0.20518(16)		0.58347(15)	0.00349(18)	0.00328(15)
95	0.00740(20)	0.20493(20)		0.20510(15)		0.58348(14)	0.00329(17)	0.00307(14)
80	0.00745(3)	0.20491(3)		0.20499(20)		0.58347(19)	0.00322(3)	0.00300(20)
65	0.00751(18)	0.20480(17)		0.20492(13)		0.58348(11)	0.00284(15)	0.00259(12)
50	0.00752(18)	0.20474(17)		0.20486(13)		0.58348(12)	0.00271(15)	0.00244(13)
35	0.00753(5)	0.20473(5)		0.20486(4)		0.58347(3)	0.00324(4)	0.00298(3)

Table C.9: Refined atom coordinates (x , z) and isotropic ADP (U_{iso}) for Cr and As from the synchrotron X-ray single-crystal diffraction measurements as function of pressure at room temperature.

p [GPa]	Cr (x_{Cr} , $1/4$, z_{Cr})			As (x_{As} , $1/4$, z_{As})			U_{iso} [Å ²]	
	x_{Cr}	z_{Cr}		x_{As}		z_{As}	$U_{\text{iso}}[\text{Cr}]$	$U_{\text{iso}}[\text{As}]$
1.03	0.00629(17)	0.19832(18)		0.19901(11)		0.57407(11)	0.0163(5)	0.0152(3)
2.53	0.00676(19)	0.19605(19)		0.19680(13)		0.57242(12)	0.0158(5)	0.0154(3)
3.13	0.0067(3)	0.1956(3)		0.19610(15)		0.57182(13)	0.0156(4)	0.0155(3)
4.45	0.0070(7)	0.1944(3)		0.1948(4)		0.57133(17)	0.0170(9)	0.0158(6)
6.05	0.0084(8)	0.1936(4)		0.1941(5)		0.57039(19)	0.016(11)	0.0157(8)
7.32	0.00742(18)	0.1930(3)		0.19293(12)		0.56996(14)	0.0137(4)	0.0132(3)
8.09	0.0078(3)	0.1926(3)		0.19252(14)		0.56959(15)	0.0156(4)	0.0156(3)
9.46	0.0075(3)	0.1920(3)		0.19160(13)		0.56928(16)	0.0135(5)	0.0134(4)

Table C.10: Refined atom coordinates (x , z) and isotropic ADP (U_{iso}) for Cr and As from the laboratory X-ray single-crystal diffraction measurements as function of temperature at ambient pressure.

T [K]	Cr (x_{Cr} , $1/4$, z_{Cr})			As (x_{As} , $1/4$, z_{As})			U_{iso} [Å ²]	
	x_{Cr}	z_{Cr}		x_{As}	z_{As}		$U_{\text{iso}}[\text{Cr}]$	$U_{\text{iso}}[\text{As}]$
300	0.00592(13)	0.20325(12)		0.20404(9)	0.57776(7)		0.0049(3)	0.0044(2)
310	0.00602(13)	0.20307(12)		0.20383(10)	0.57772(7)		0.0048(3)	0.0043(2)
320	0.00596(16)	0.20303(15)		0.20366(11)	0.57768(8)		0.0052(3)	0.0047(3)
330	0.00603(15)	0.20290(14)		0.20369(11)	0.57764(8)		0.0057(2)	0.0053(3)
340	0.00625(16)	0.20264(15)		0.20357(12)	0.57751(9)		0.0056(3)	0.0051(2)
350	0.00613(16)	0.20258(15)		0.20346(12)	0.57743(9)		0.0056(3)	0.0051(3)
360	0.00610(14)	0.20226(13)		0.20328(11)	0.57737(8)		0.0059(3)	0.0055(3)
370	0.00620(17)	0.20222(15)		0.20311(12)	0.57718(9)		0.0062(3)	0.0058(3)
380	0.00611(16)	0.20208(15)		0.20305(12)	0.57712(9)		0.0064(3)	0.0059(3)
390	0.00616(13)	0.20149(11)		0.20243(9)	0.57703(7)		0.0066(3)	0.0062(2)
400	0.00627(15)	0.20152(13)		0.20264(11)	0.57684(8)		0.0067(3)	0.0062(2)
290	0.00626(16)	0.20128(14)		0.20241(11)	0.57674(9)		0.0046(3)	0.0044(3)
280	0.00625(16)	0.20116(15)		0.20218(12)	0.57651(9)		0.0049(3)	0.0044(3)
300	0.00630(14)	0.20152(13)		0.20236(10)	0.57690(8)		0.0046(3)	0.0042(2)
310	0.00622(11)	0.20150(10)		0.20245(8)	0.57697(6)		0.0046(2)	0.0042(2)
320	0.00627(13)	0.20175(12)		0.20274(9)	0.57717(7)		0.0048(3)	0.0045(2)
275	0.00622(15)	0.20110(14)		0.20182(11)	0.57640(8)		0.0040(3)	0.0038(3)
240	0.00686(15)	0.20602(14)		0.20618(10)	0.58287(8)		0.0046(3)	0.0040(3)
250	0.00690(16)	0.20624(16)		0.20636(11)	0.58284(9)		0.0048(3)	0.0044(3)
270	0.00652(11)	0.20057(10)		0.20156(7)	0.57631(6)		0.0050(2)	0.0045(2)
280	0.00625(12)	0.20081(11)		0.20183(8)	0.57650(6)		0.0049(3)	0.0045(2)

Table C.11: Key to the denotation of the interatomic distances in CrAs. Symmetry code: (I) x, y, z ; (II) $x+1/2, -y+1/2, -z+1/2$; (III) $-x+1/2, -y, z+1/2$; (IV) $-x, y+1/2, -z$; (V) $-x, -y, -z$; (VI) $x+1/2, y, -z+1/2$; (VII) $x, -y+1/2, z$; (VIII) $-x+1/2, y+1/2, z+1/2$. In the MnP-type structure with both Cr and As occupying Wyckoff $4c$ positions at $(x, 1/4, z)$, the sites (I)/(VII), (II)/(VI), (III)/(VIII) and (IV)/(V) are pairwise degenerated. Symmetrically equivalent positions outside of the unit cell are marked by the according translation vector, e.g. “I (0,1,0)” for the position $(x, y+1, z)$. The color markings correspond to the ones shown in Figure 8.12.

Distance shorthand	Cr-Cr			Cr-As			
	<div><div></div>Cr^I-Cr^I</div>	<div><div></div>Cr^I-Cr^{II}</div>	<div><div></div>Cr^I-Cr^{IV}</div>	<div><div></div>Cr^I-As^I</div>	<div><div></div>Cr^I-As^{II}</div>	<div><div></div>Cr^I-As^{III}</div>	<div><div></div>Cr^I-As^{IV}</div>
Distances from Cr ^I	Cr ^I -Cr ^I (0,1,0)	Cr ^I -Cr ^{II}	Cr ^I -Cr ^{IV}	Cr ^I -As ^I	Cr ^I -As ^{II} (-1,0,0)	Cr ^I -As ^{III} (0,0,-1)	Cr ^I -As ^{IV} (0,0,1)
	Cr ^I -Cr ^I (0,-1,0)	Cr ^I -Cr ^{II} (-1,0,0)	Cr ^I -Cr ^{IV} (0,1,0)			Cr ^I -As ^{III} (0,1,-1)	Cr ^I -As ^{IV} (0,1,1)
Equivalent distances	Cr ^{II} -Cr ^{II} (0,1,0)	Cr ^{III} -Cr ^{IV} (0,0,1)	Cr ^{II} -Cr ^{III}	Cr ^{II} -As ^{II}	Cr ^{II} -As ^I	Cr ^{II} -As ^{IV} (1,0,1)	Cr ^{II} -As ^{III} (0,0,-1)
	Cr ^{II} -Cr ^{II} (0,-1,0)	Cr ^{III} -Cr ^{IV} (1,0,1)	Cr ^{II} -Cr ^{III} (0,1,0)	Cr ^{III} -As ^{III}	Cr ^{III} -As ^{IV} (1,0,1)	Cr ^{II} -As ^{IV} (1,1,1)	Cr ^{II} -As ^{III} (0,1,-1)
	Cr ^{III} -Cr ^{III} (0,1,0)			Cr ^{IV} -As ^{IV}	Cr ^{IV} -As ^{III} (0,0,-1)	Cr ^{III} -As ^I	Cr ^{III} -As ^{II} (0,0,1)
	Cr ^{III} -Cr ^{III} (0,-1,0)					Cr ^{III} -As ^I (0,-1,0)	Cr ^{III} -As ^{II} (0,-1,1)
	Cr ^{IV} -Cr ^{IV} (0,1,0)					Cr ^{IV} -As ^{II} (-1,0,0)	Cr ^{IV} -As ^I (0,0,-1)
	Cr ^{IV} -Cr ^{IV} (0,-1,0)					Cr ^{IV} -As ^{II} (-1,-1,0)	Cr ^{IV} -As ^I (0,-1,-1)

Table C.12: Interatomic Cr–Cr and Cr–As distances in CrAs calculated from the synchrotron X-ray single-crystal diffraction measurements as function of temperature at ambient pressure. The denotation of the distances follows Table C.11.

T [K]	Cr–Cr			Cr–As			
	■ Cr ^I –Cr ^I [Å]	■ Cr ^I –Cr ^{II} [Å]	■ Cr ^I –Cr ^{IV} [Å]	■ Cr ^I –As ^I [Å]	■ Cr ^I –As ^{II} [Å]	■ Cr ^I –As ^{III} [Å]	■ Cr ^I –As ^{IV} [Å]
275	3.4520(2)	2.8878(2)	3.0271(2)	2.5772(2)	2.4303(2)	2.50846(16)	2.50465(16)
270	3.5731(2)	2.8630(3)	3.0968(3)	2.5752(3)	2.4506(3)	2.52406(19)	2.5135(2)
260	3.5753(2)	2.8622(3)	3.0967(3)	2.5754(3)	2.4506(3)	2.52406(18)	2.51359(19)
250	3.5772(2)	2.8614(2)	3.0967(2)	2.5747(2)	2.4507(2)	2.52398(16)	2.51357(16)
240	3.5784(2)	2.8607(2)	3.0967(2)	2.57448(19)	2.45072(19)	2.52380(14)	2.51357(15)
220	3.5805(2)	2.8593(2)	3.09564(19)	2.57413(18)	2.45039(18)	2.52342(14)	2.51349(14)
200	3.5815(2)	2.8583(2)	3.0946(2)	2.57410(19)	2.45042(19)	2.52313(14)	2.51315(15)
185	3.5826(4)	2.8578(3)	3.0937(2)	2.5734(2)	2.4501(2)	2.52315(19)	2.51306(19)
170	3.5831(2)	2.8572(3)	3.0929(2)	2.5729(2)	2.44994(19)	2.52288(15)	2.51296(14)
155	3.5835(2)	2.8564(3)	3.0917(2)	2.5725(2)	2.4495(2)	2.52257(15)	2.51282(14)
140	3.5839(2)	2.8555(3)	3.0907(2)	2.5722(2)	2.4490(2)	2.52227(16)	2.51269(16)
125	3.5837(2)	2.8554(3)	3.0899(2)	2.5721(2)	2.4490(2)	2.52206(15)	2.51259(15)
110	3.5840(2)	2.8552(3)	3.0891(2)	2.5718(2)	2.4490(2)	2.52206(15)	2.51235(14)
95	3.5842(2)	2.8550(3)	3.0878(2)	2.5719(2)	2.44851(19)	2.52192(14)	2.51236(14)
80	3.5838(2)	2.8544(3)	3.0871(2)	2.5710(2)	2.4485(2)	2.52173(17)	2.51187(17)
65	3.5843(2)	2.85401(17)	3.08560(19)	2.57077(19)	2.44795(16)	2.52139(12)	2.51208(12)
50	3.5844(2)	2.85383(17)	3.08491(19)	2.57059(19)	2.44775(16)	2.52137(12)	2.51204(12)
35	3.5844(2)	2.8530(4)	3.0854(3)	2.5711(3)	2.4477(3)	2.5211(2)	2.5122(2)

Table C.13: Interatomic Cr–Cr and Cr–As distances in CrAs calculated from the synchrotron X-ray single-crystal diffraction measurements as function of pressure at room temperature. The denotation of the distances follows Table C.11.

p [GPa]	Cr–Cr		Cr–As			
	■ Cr ^I –Cr ^I [Å]	■ Cr ^I –Cr ^{II} [Å]	■ Cr ^I –Cr ^{IV} [Å]	■ Cr ^I –As ^I [Å]	■ Cr ^I –As ^{II} [Å]	■ Cr ^I –As ^{III} [Å]
1.03	3.390(2)	2.8854(17)	2.9846(15)	2.5666(14)	2.4153(13)	2.4930(12)
2.53	3.342(2)	2.8854(18)	2.9431(16)	2.5577(15)	2.4037(14)	2.4790(13)
3.13	3.326(2)	2.884(3)	2.929(2)	2.550(2)	2.3981(19)	2.4750(16)
4.45	3.3003(16)	2.879(7)	2.906(2)	2.544(3)	2.391(4)	2.465(4)
6.05	3.2734(14)	2.875(7)	2.884(2)	2.531(3)	2.386(4)	2.451(4)
7.32	3.2539(12)	2.874(2)	2.868(4)	2.528(4)	2.380(2)	2.4506(13)
8.09	3.2432(10)	2.873(2)	2.860(2)	2.524(2)	2.3779(18)	2.4463(14)
9.46	3.2258(6)	2.8698(18)	2.845(2)	2.518(2)	2.3721(17)	2.4418(12)
						2.4385(13)

Table C.14: Interatomic Cr–Cr and Cr–As distances in CrAs calculated from the laboratory X-ray single-crystal diffraction measurements as function of temperature at ambient pressure. The denotation of the distances follows Table C.11.








T [K]	Cr–Cr			Cr–As			
	 Cr ^I –Cr ^I [Å]	 Cr ^I –Cr ^{II} [Å]	 Cr ^I –Cr ^{IV} [Å]	 Cr ^I –As ^I [Å]	 Cr ^I –As ^{II} [Å]	 Cr ^I –As ^{III} [Å]	 Cr ^I –As ^{IV} [Å]
300	3.4671(12)	2.8854(15)	3.0428(12)	2.5781(11)	2.4326(11)	2.5105(9)	2.5070(9)
310	3.4706(14)	2.8858(15)	3.0424(11)	2.5782(11)	2.4332(10)	2.5125(9)	2.5066(8)
320	3.4714(12)	2.8856(16)	3.0493(13)	2.5779(13)	2.4345(12)	2.5122(10)	2.5065(9)
330	3.4757(12)	2.8853(17)	3.0525(13)	2.5779(13)	2.4358(13)	2.5133(10)	2.5079(10)
340	3.4767(12)	2.8858(15)	3.0535(12)	2.5797(12)	2.4362(11)	2.5134(9)	2.5079(9)
350	3.4794(10)	2.8857(15)	3.0582(12)	2.5795(12)	2.4379(12)	2.5144(9)	2.5085(9)
360	3.4819(10)	2.8868(15)	3.0586(13)	2.5788(12)	2.4386(12)	2.5147(9)	2.5094(9)
370	3.4851(12)	2.8862(15)	3.0618(13)	2.5786(12)	2.4388(12)	2.5164(9)	2.5088(9)
380	3.4860(10)	2.8866(15)	3.0643(12)	2.5796(12)	2.4399(12)	2.5173(10)	2.5091(9)
390	3.4869(10)	2.8860(14)	3.0663(11)	2.5808(11)	2.4408(10)	2.5171(8)	2.5098(8)
400	3.4901(12)	2.8864(13)	3.0689(11)	2.5808(12)	2.4408(11)	2.5184(9)	2.5106(9)
290	3.4630(12)	2.8857(16)	3.0394(13)	2.5786(13)	2.4319(12)	2.5095(10)	2.5061(9)
280	3.4597(12)	2.8865(15)	3.0363(13)	2.5765(12)	2.4309(12)	2.5096(12)	2.5053(9)
300	3.4666(12)	2.8869(15)	3.0420(12)	2.5774(11)	2.4344(11)	2.5116(11)	2.5061(9)
310	3.4693(12)	2.8872(12)	3.0424(10)	2.5781(10)	2.4339(9)	2.5124(09)	2.5068(8)
320	3.4717(12)	2.8869(13)	3.0457(11)	2.5786(11)	2.4351(10)	2.5122(10)	2.5071(8)
275	3.4540(12)	2.8850(15)	3.0339(12)	2.5751(12)	2.4307(11)	2.5086(9)	2.5025(9)
240	3.5776(10)	2.8601(14)	3.1010(13)	2.5722(13)	2.4503(12)	2.5240(8)	2.5129(8)
250	3.5757(10)	2.8602(15)	3.1041(13)	2.5725(13)	2.4516(12)	2.5234(9)	2.5128(9)
270	3.4579(16)	2.8882(14)	3.0324(12)	2.5793(11)	2.4325(10)	2.5098(9)	2.5074(8)
280	3.4590(12)	2.8877(13)	3.0326(11)	2.5777(11)	2.4309(10)	2.5101(8)	2.5054(7)

Table C.15: Final agreement factors for the neutron single-crystal data of CrAs at $p_{\text{hom}} = 0.17$ GPa for all tested magnetic superspace groups. The superscripts [100], [010] and [001] do not belong to the formal space group symbol, but indicate the direction in which the two-fold screw axis of the respective space group $P2_1$ is oriented in order to allow differentiation. A space group symbol in parentheses indicates an artificially lowered symmetry where the $Pnma$ symmetry is retained by suitable restrictions.

No. meas. Refl. (obs/all)	$h_{\text{min}} \rightarrow h_{\text{max}}$ $k_{\text{min}} \rightarrow k_{\text{max}}$ $l_{\text{min}} \rightarrow l_{\text{max}}$	Nuclear space group	Magnetic superspace group	all			main			satellites	
				R (obs/all)	wR (obs/all)	R (obs/all)	R (obs/all)	wR (obs/all)	R (obs/all)	R (obs/all)	wR (obs/all)
424/682	$-1 \rightarrow 3$ $-7 \rightarrow 6$ $-12 \rightarrow 12$	$Pnma$	$Pnma.1'(00g)000s$	9.95/13.12	22.55/22.66	7.23/10.04	6.21/6.50	6.21/6.50	80.45/89.37	92.51/92.62	
			$Pnma.1'(00g)ss0s$	9.00/12.51	16.94/17.16	7.23/10.04	6.21/6.50	6.21/6.50	54.88/73.71	67.39/67.90	
			$Pnma.1'(00g)0s0s$	8.37/11.55	10.08/10.31	7.23/10.04	6.21/6.50	6.21/6.50	37.96/48.99	34.37/34.65	
			$Pnma.1'(00g)s00s$	9.66/12.93	15.01/15.23	7.23/10.04	6.21/6.50	6.21/6.50	72.69/84.56	58.53/58.96	
		$(P2_1ma)$	$P2_1ma.1'(00g)000s$	8.30/13.27	10.35/10.76	7.41/11.26	6.53/6.90	6.53/6.90	33.48/63.54	33.57/34.51	
			$P2_1ma.1'(00g)0s0s$	8.16/13.15	10.03/10.47	7.41/11.26	6.53/6.90	6.53/6.90	29.18/60.51	31.90/32.97	
			$Pn2_1a.1'(00g)000s$	8.25/12.66	10.58/10.94	7.15/11.01	6.47/6.97	6.47/6.97	34.38/49.72	38.02/38.34	
			$Pn2_1a.1'(00g)s00s$	8.12/12.60	9.48/9.85	7.14/11.01	6.47/6.97	6.47/6.97	31.22/48.38	31.66/31.86	
		$(Pnm2_1)$	$Pnm2_1.1'(00g)000s$	10.32/15.26	24.05/24.28	7.77/11.95	7.18/7.60	7.18/7.60	78.42/93.01	93.01/93.07	
			$Pnm2_1.1'(00g)ss0s$	9.03/14.11	17.19/17.44	7.77/11.95	7.18/7.60	7.18/7.60	42.70/65.53	63.49/63.62	
			$Pnm2_1.1'(00g)0ss$	9.08/14.29	11.92/12.44	7.77/11.95	7.18/7.60	7.18/7.60	44.02/70.16	39.11/40.35	
			$Pnm2_1.1'(00g)s0ss$	8.79/14.27	10.77/11.21	7.77/11.95	7.18/7.60	7.18/7.60	35.96/69.60	33.24/33.98	
		$(P2_12_12_1)$	$P2_12_12_1.1'(00g)000s$	8.67/13.52	14.05/14.39	7.86/12.22	6.82/7.31	6.82/7.31	32.39/48.64	55.48/55.77	
			$P2_12_12_1.1'(00g)00ss$	8.69/13.68	9.66/10.06	7.86/12.22	6.82/7.31	6.82/7.31	33.02/53.06	31.39/31.67	
			$P2_1n.1'(0bg)00s$	8.66/13.30	13.24/13.76	7.38/11.32	6.68/7.31	6.68/7.31	48.16/68.77	52.70/53.56	
			$P2_1n.1'(0bg)0ss$	7.83/12.25	9.01/9.66	7.38/11.32	6.68/7.31	6.68/7.31	21.64/38.26	28.43/29.69	
		$(P2_1/m)$	$P2_1/m.1'(a0g)00s$	8.75/14.75	9.57/10.14	7.93/13.02	7.16/7.71	7.16/7.71	30.64/55.88	28.66/29.64	
			$P2_1/m.1'(a0g)0ss$	8.90/14.66	11.33/11.76	7.93/13.02	7.16/7.71	7.16/7.71	35.01/53.53	39.08/39.33	
			$P2_1/a.1'(00g)00s$	9.06/13.63	16.33/16.65	7.37/11.19	6.55/6.88	6.55/6.88	50.45/70.36	66.25/67.07	
			$P2_1/a.1'(00g)s0s$	8.30/12.56	8.61/8.94	7.37/11.19	6.55/6.88	6.55/6.88	31.02/44.43	25.51/26.02	

Table C.15 (continued): Final agreement factors for the neutron single-crystal data of CrAs at $p_{\text{hom}} = 0.17 \text{ GPa}$ for all tested magnetic superspace groups. The superscripts [100], [010] and [001] do not belong to the formal space group symbol, but indicate the direction in which the two-fold screw axis of the respective space group $P2_1$ is oriented in order to allow differentiation. A space group symbol in parentheses indicates an artificially lowered symmetry where the $Pnma$ symmetry is retained by suitable restrictions.

No. meas. Refl. (obs/all)	$h_{\min} \rightarrow h_{\max}$ $k_{\min} \rightarrow k_{\max}$ $l_{\min} \rightarrow l_{\max}$	Nuclear space group	Magnetic superspace group	all		main		satellites	
				R (obs/all)	wR (obs/all)	R (obs/all)	wR (obs/all)	R (obs/all)	wR (obs/all)
424/682	$-1 \rightarrow 3$ $-7 \rightarrow 6$ $-12 \rightarrow 12$	(Pn)	$Pn.1'(\text{0bg})0s$	8.76/14.96	10.22/11.00	7.84/12.43	7.32/7.98	32.50/68.85	30.70/32.35
			$Pn.1'(\text{0bg})ss$	8.39/14.47	8.50/9.44	7.84/12.43	7.32/7.98	22.52/58.07	19.50/22.34
		$(P2_1[100])$	$P2_1.1'(\text{0bg})0s$	8.02/13.73	8.12/8.93	7.70/12.54	6.92/7.62	18.84/48.77	19.85/21.69
			$Pm.1'(\text{a0g})0s$	8.49/14.99	9.03/9.83	7.84/12.88	7.41/8.03	26.24/65.29	22.33/24.34
		(Pm)	$Pm.1'(\text{a0g})ss$	8.77/15.17	10.99/11.63	7.84/12.88	7.41/8.03	34.04/69.84	33.93/35.09
			$P2_1.1'(\text{a0g})0s$	8.70/15.50	8.02/8.86	8.38/14.12	7.55/8.24	17.09/45.50	14.44/16.77
		(Pa)	$Pa.1'(\text{00g})0s$	7.77/13.86	7.80/8.43	7.28/12.27	6.52/7.00	21.29/52.56	19.53/21.25
			$P2_1.1'(\text{00g})0s$	9.04/16.78	16.78/17.20	7.95/13.00	7.39/8.02	37.72/62.45	62.78/62.97
		$(P\bar{1})$	$P2_1.1'(\text{00g})ss$	8.67/15.27	8.95/9.83	7.95/13.00	7.39/8.02	27.66/64.57	22.17/24.66
			$P\bar{1}.1'(\text{abg})0s$	8.46/15.25	8.14/9.15	8.01/13.71	7.39/8.18	21.12/51.12	17.28/20.21
		(P1)	$P1.1'(\text{abg})0s$	8.51/15.78	8.53/9.67	8.07/13.77	7.54/8.44	20.69/60.85	18.43/21.46
			double hex $\uparrow c$	10.05/17.02	14.16/15.20	8.07/13.77	7.54/8.44	64.61/89.86	51.08/53.45

Table C.16: Final agreement factors for the neutron single-crystal data of CrAs at $p_{\text{nom}} = 1.2$ GPa for all tested magnetic superspace groups. The superscripts [100], [010] and [001] do not belong to the formal space group symbol, but indicate the direction in which the two-fold screw axis of the respective space group $P2_1$ is oriented in order to allow differentiation. A space group symbol in parentheses indicates an artificially lowered symmetry where the $Pnma$ symmetry is retained by suitable restrictions.

No. meas. Refl. (obs/all)	$h_{\text{min}} \rightarrow h_{\text{max}}$ $k_{\text{min}} \rightarrow k_{\text{max}}$ $l_{\text{min}} \rightarrow l_{\text{max}}$	Nuclear space group	Magnetic superspace group	all		main		satellites	
				R (obs/all)	wR (obs/all)	R (obs/all)	wR (obs/all)	R (obs/all)	wR (obs/all)
424/682	$-1 \rightarrow 3$ $-7 \rightarrow 6$ $-12 \rightarrow 12$	$Pnma$	$Pnma.1'(\text{00g})000s$	20.43/21.81	27.19/27.31	18.02/19.13	15.68/15.75	88.85/89.58	96.63/96.55
			$Pnma.1'(\text{00g})ss0s$	19.22/20.68	20.93/21.10	18.02/19.13	15.68/15.75	53.30/59.70	61.55/61.97
			$Pnma.1'(\text{00g})0s0s$	19.29/20.71	18.89/19.06	18.02/19.13	15.68/15.75	55.35/60.51	47.81/48.40
			$Pnma.1'(\text{00g})s00s$	19.62/21.17	19.73/19.96	18.02/19.13	15.68/15.75	65.04/72.56	53.73/54.67
		$(P2_1ma)$	$P2_1ma.1'(\text{00g})000s$	18.35/21.41	17.44/17.83	17.47/20.17	15.17/15.52	42.69/53.01	40.15/40.82
			$P2_1ma.1'(\text{00g})0s0s$	17.69/20.61	15.59/15.98	17.47/20.17	15.17/15.52	23.98/31.82	21.71/22.50
		$(Pn2_1a)$	$Pn2_1a.1'(\text{00g})000s$	19.27/20.86	16.75/17.03	18.94/20.13	16.26/16.38	27.48/35.55	24.13/26.05
			$Pn2_1a.1'(\text{00g})s00s$	19.18/20.64	16.68/16.87	18.94/20.13	16.26/16.38	25.13/31.15	23.12/24.10
		$(Pnm2_1)$	$Pnm2_1.1'(\text{00g})000s$	20.74/22.92	26.93/27.12	17.46/19.28	15.43/15.59	87.02/86.22	96.07/95.69
			$Pnm2_1.1'(\text{00g})ss0s$	18.41/20.56	19.60/19.76	17.46/19.28	15.43/15.59	37.49/42.73	54.15/53.95
			$Pnm2_1.1'(\text{00g})0sss$	18.91/21.21	17.98/18.30	17.46/19.28	15.43/15.59	48.43/54.85	42.54/43.67
			$Pnm2_1.1'(\text{00g})s0ss$	17.76/20.09	15.84/16.14	17.46/19.28	15.43/15.59	23.86/34.11	21.77/23.69
		$(P2_12_12_1)$	$P2_12_12_1.1'(\text{00g})000s$	18.55/21.21	19.34/19.64	17.88/20.46	15.56/15.88	37.57/40.12	54.05/53.97
			$P2_12_12_1.1'(\text{00g})00ss$	18.13/20.96	15.90/16.37	17.88/20.46	15.56/15.88	25.20/33.61	21.32/23.79
		$(P2_1/n)$	$P2_1/n.1'(\text{0bg})00s$	19.71/21.67	18.86/19.11	18.48/20.24	16.18/16.37	52.16/55.23	46.78/47.22
			$P2_1/n.1'(\text{0bg})0ss$	19.14/21.15	16.18/16.37	18.48/20.24	16.18/16.37	36.41/42.58	32.72/34.07
		$(P2_1/m)$	$P2_1/m.1'(\text{a0g})00s$	17.78/20.96	16.83/17.31	16.88/19.93	14.85/15.25	41.72/43.91	38.38/39.32
			$P2_1/m.1'(\text{a0g})0ss$	17.09/20.31	15.23/15.73	16.88/19.93	14.85/15.25	22.70/28.86	21.22/22.88
		$(P2_1/a)$	$P2_1/a.1'(\text{00g})00s$	19.56/22.01	20.52/20.81	18.36/20.52	15.65/15.93	50.45/55.63	60.76/60.74
			$P2_1/a.1'(\text{00g})s0s$	18.68/21.24	16.19/16.63	18.36/20.52	15.65/15.93	27.45/37.96	24.14/26.39

Table C.16 (continued): Final agreement factors for the neutron single-crystal data of CrAs at $p_{\text{hom}} = 1.2$ GPa for all tested magnetic superspace groups. The superscripts [100], [010] and [001] do not belong to the formal space group symbol, but indicate the direction in which the two-fold screw axis of the respective space group $P2_1$ is oriented in order to allow differentiation. A space group symbol in parentheses indicates an artificially lowered symmetry where the $Pnma$ symmetry is retained by suitable restrictions.

No. meas. Refl. (obs/all)	$h_{\min} \rightarrow h_{\max}$ $k_{\min} \rightarrow k_{\max}$ $l_{\min} \rightarrow l_{\max}$	Nuclear space group	Magnetic superspace group	all		main		satellites	
				R (obs/all)	wR (obs/all)	R (obs/all)	wR (obs/all)	R (obs/all)	wR (obs/all)
424/682	$-1 \rightarrow 3$ $-7 \rightarrow 6$ $-12 \rightarrow 12$	(Pn)	$Pn,1'(\text{0bg})0s$	18.74/21.24	16.39/16.74	18.36/20.11	16.03/16.21	26.30/36.90	22.16/24.24
			$Pn,1'(\text{0bg})ss$	18.88/21.20	16.64/16.93	18.36/20.11	16.03/16.21	29.22/36.34	25.64/26.60
		$(P2_1[100])$	$P2_1,1'(\text{0bg})0s$	17.75/21.37	16.04/16.58	17.58/21.03	15.78/16.26	22.18/29.62	20.50/21.74
			$Pm,1'(\text{a0g})0s$	17.91/21.39	16.57/17.02	17.02/20.05	14.92/15.32	36.17/45.80	34.84/35.48
		(Pm)	$Pm,1'(\text{a0g})ss$	17.14/20.61	15.19/15.67	17.02/20.05	14.92/15.32	19.72/30.73	19.57/20.92
			$P2_1,1'(\text{a0g})0s$	17.67/21.49	15.94/16.54	17.27/20.91	15.48/15.99	27.68/31.93	23.40/24.71
		(Pa)	$Pa,1'(\text{00g})0s$	17.92/21.47	16.00/16.50	17.85/21.07	15.84/16.28	19.65/30.18	18.79/20.10
			$P2_1,1'(\text{00g})0s$	18.56/21.50	19.30/19.55	17.60/20.11	15.25/15.51	38.56/42.11	55.02/53.86
		$(P2_1[001])$	$P2_1,1'(\text{00g})ss$	18.00/21.12	15.64/16.09	17.60/20.11	15.25/15.51	26.25/36.42	21.79/24.16
			$P\bar{1},1'(\text{abg})0s$	17.74/21.51	15.89/16.44	17.40/20.99	15.54/16.05	26.40/31.24	21.94/22.68
		$(P\bar{1})$	$P1,1'(\text{abg})0s$	17.71/21.68	15.84/16.39	17.40/20.99	15.54/16.05	24.00/32.29	20.89/21.58
			<i>double hex</i> $\uparrow c$	19.13/24.04	18.21/19.46	17.40/20.99	15.54/16.05	54.53/71.07	45.59/50.76

Table C.17: Final agreement factors for the neutron single-crystal data of CrAs at $p_{\text{nom}} = 1.2$ GPa for all tested nuclear space groups. The superscripts [100], [010] and [001] do not belong to the formal space group symbol, but indicate the direction in which the two-fold screw axis of the respective space group $P2_1$ is oriented in order to allow differentiation.

Nuclear space group	all	
	R (obs/all)	wR (obs/all)
$Pnma$	19.77/21.12	17.27/17.36
$P2_1ma$	16.37/19.09	15.40/15.60
$Pn2_1a$	20.22/21.67	17.73/17.86
$Pnm2_1$	16.40/19.70	15.59/15.83
$P2_12_12_1$	18.80/21.73	17.25/17.53
$P2_1/n$	20.00/22.00	17.91/18.08
$P2_1/m$	17.88/20.98	16.54/16.87
$P2_1/a$	19.35/21.69	16.47/16.72
Pn	13.93/17.30	12.33/12.72
$P2_1^{[100]}$	13.76/19.76	12.63/13.36
Pm	15.53/18.71	15.05/15.28
$P2_1^{[010]}$	18.35/22.33	17.23/17.70
Pa	14.08/16.68	12.75/13.01
$P2_1^{[001]}$	14.19/18.11	12.46/12.84
$P\bar{1}$	15.58/19.52	13.96/14.55
$P1$	12.67/16.75	11.27/11.79

Table C.18: Modulation amplitudes and phase shifts (relative to the origin) for the refinements in all tested restrained magnetic superspace groups of the neutron single-crystal data of CrAs at $p_{\text{nom}} = 0.17$ GPa. The superscripts [100], [010] and [001] do not belong to the formal space group symbol, but indicate the direction in which the two-fold screw axis of the respective space group $P2_1$ is oriented in order to allow differentiation. A space group symbol in parentheses indicates an artificially lowered symmetry where the $Pnma$ symmetry is retained by suitable restrictions.

Nuclear space group	Magnetic superspace group	Restraints	M_x		M_y		M_z		$ M $	
			A_x [μ_B]	φ [°]	A_y [μ_B]	σ [°]	A_z [μ_B]	τ [°]	min	max
$(P2_1/n)$	$P2_1/n.1'(0bg)0ss$	—	Cr1,1 3.2	-16	$\varphi_{1,1}$	2.3	240	$\sigma_{1,1}$	2.1	2.5(3)
			Cr1,2 3.2	16	$-\varphi_{1,1}$	2.3	-60	$180 - \sigma_{1,1}$	2.1	2.5(3)
			Cr1,3 3.2	164	$180 + \varphi_{1,1}$	2.3	240	$\sigma_{1,1}$	2.1	2.5(3)
			Cr1,4 3.2	196	$180 - \varphi_{1,1}$	2.3	-60	$180 - \sigma_{1,1}$	2.1	2.5(3)
	M equal	M equal	Cr1,1 2.97	-11	$\varphi_{1,1}$	2.67	246	$\sigma_{1,1}$	1.97	3.15(10)
			Cr1,2 2.97	11	$-\varphi_{1,1}$	2.67	-66	$180 - \sigma_{1,1}$	1.97	3.15(10)
			Cr1,3 2.97	169	$180 + \varphi_{1,1}$	2.67	246	$\sigma_{1,1}$	1.97	3.15(10)
			Cr1,4 2.97	191	$180 - \varphi_{1,1}$	2.67	-66	$180 - \sigma_{1,1}$	1.97	3.15(10)
	(Pn)	—	Cr1,1 3	-51	$\varphi_{1,1}$	2	24	$\sigma_{1,1}$	1	2(7)
			Cr3,1 3	-20	$-\varphi_{3,1}$	5	-51	$\sigma_{3,1}$	1	45
			Cr1,2 3	129	$180 + \varphi_{1,1}$	2	24	$\sigma_{1,1}$	1	17
			Cr3,2 3	160	$180 + \varphi_{3,1}$	5	-51	$180 - \sigma_{3,1}$	1	45
	M equal	M equal	Cr1,1 4.5	-23	$\varphi_{1,1}$	1.7	9	$\sigma_{1,1}$	2.5	1.8(3)
			Cr3,1 1.8	12	$\varphi_{3,1}$	5.1	-65	$\sigma_{3,1}$	0.1	-44
			Cr1,2 4.5	157	$180 + \varphi_{1,1}$	1.7	9	$\sigma_{1,1}$	2.5	23
			Cr3,2 1.8	192	$180 + \varphi_{3,1}$	5.1	-65	$\sigma_{3,1}$	0.1	-44
	M optimal	M optimal	Cr1,1 2.37	-1	$\varphi_{1,1}$	1.41	2	$\sigma_{1,1}$	2.76	-90
			Cr3,1 3.91	26	$\varphi_{3,1}$	4.24	-61	$\sigma_{3,1}$	1.75	42
			Cr1,2 2.37	179	$180 + \varphi_{1,1}$	1.41	2	$\sigma_{1,1}$	2.76	-90
			Cr3,2 3.91	206	$180 + \varphi_{3,1}$	4.24	-61	$\sigma_{3,1}$	1.75	42
	M equal + optimal	M equal + optimal	Cr1,1 2.92	-24	$\varphi_{1,1}$	2.23	-23	$\sigma_{1,1}$	3.68	66
			Cr3,1 3.24	11	$\varphi_{3,1}$	3.62	-74	$\sigma_{3,1}$	1.84	213
			Cr1,2 2.92	156	$180 + \varphi_{1,1}$	2.23	-23	$\sigma_{1,1}$	3.68	66
			Cr3,2 3.24	191	$180 + \varphi_{3,1}$	3.62	-74	$\sigma_{3,1}$	1.84	213

Table C.18 (continued): Modulation amplitudes and phase shifts (relative to the origin) for the refinements in all tested restrained magnetic superspace groups of the neutron single-crystal data of CrAs at $p_{\text{nom}} = 0.17$ GPa. The superscripts [100], [010] and [001] do not belong to the formal space group symbol, but indicate the direction in which the two-fold screw axis of the respective space group $P2_1$ is oriented in order to allow differentiation. A space group symbol in parentheses indicates an artificially lowered symmetry where the $Pnma$ symmetry is retained by suitable restrictions.

















Nuclear space group ($P2_1^{[100]}$)	Magnetic superspace group $P2_1.1'/(0\text{bg})0s$	Restraints	M_x				M_y		M_z		$ M $		
			A_x [μB]	φ [°]	A_y [μB]	σ [°]	A_z [μB]	τ [°]	min	max			
	—	 Cr1,1	3.9	-61	$\varphi_{1,1}$	4.6	-38	$\sigma_{1,1}$	0.2	-16	$\tau_{1,1}$	1.2(16)	5.9(16)
		 Cr1,2	3.9	241	$180 - \varphi_{1,1}$	4.6	38	$-\sigma_{1,1}$	0.2	16	$-\tau_{1,1}$	1.2(16)	5.9(16)
		 Cr2,1	1.6	2	$\varphi_{2,1}$	0.3	149	$\sigma_{2,1}$	0.1	46	$\tau_{2,1}$	0.2(16)	1.6(16)
		 Cr2,2	1.6	178	$180 - \varphi_{2,1}$	0.3	211	$-\sigma_{2,1}$	0.1	-46	$-\tau_{2,1}$	0.2(16)	1.6(16)
	M equal	 Cr1,1	4.0	-77	$\varphi_{1,1}$	0.2	-47	$\sigma_{1,1}$	2.0	41	$\tau_{1,1}$	1.7(2)	4.2(2)
		 Cr1,2	4.0	257	$180 - \varphi_{1,1}$	0.2	47	$-\sigma_{1,1}$	2.0	-41	$-\tau_{1,1}$	1.7(2)	4.2(2)
		 Cr2,1	2.0	9	$\varphi_{2,1}$	4.0	-52	$\sigma_{2,1}$	0.5	201	$\tau_{2,1}$	1.7(2)	4.2(2)
		 Cr2,2	2.0	171	$180 - \varphi_{2,1}$	4.0	52	$-\sigma_{2,1}$	0.5	159	$-\tau_{2,1}$	1.7(2)	4.2(2)
	M optimal	 Cr1,1	2.70	266	$\varphi_{1,1}$	4.32	-13	$\sigma_{1,1}$	3.45	72	$\tau_{1,1}$	4.34(11)	4.34(11)
		 Cr1,2	2.70	-86	$180 - \varphi_{1,1}$	4.32	13	$-\sigma_{1,1}$	3.45	-72	$-\tau_{1,1}$	4.34(11)	4.34(11)
		 Cr2,1	1.12	2	$\varphi_{2,1}$	0.32	6	$\sigma_{2,1}$	1.16	93	$\tau_{2,1}$	1.16(11)	1.16(11)
		 Cr2,2	1.12	178	$180 - \varphi_{2,1}$	0.32	-6	$-\sigma_{2,1}$	1.16	267	$-\tau_{2,1}$	1.16(11)	1.16(11)
	M equal + optimal	 Cr1,1	2.34	263	$\varphi_{1,1}$	2.50	-24	$\sigma_{1,1}$	1.90	35	$\tau_{1,1}$	2.77(6)	2.77(6)
		 Cr1,2	2.34	-83	$180 - \varphi_{1,1}$	2.50	24	$-\sigma_{1,1}$	1.90	-35	$-\tau_{1,1}$	2.77(6)	2.77(6)
		 Cr2,1	1.33	18	$\varphi_{2,1}$	2.45	3	$\sigma_{2,1}$	1.75	97	$\tau_{2,1}$	2.77(6)	2.77(6)
		 Cr2,2	1.33	162	$180 - \varphi_{2,1}$	2.45	-3	$-\sigma_{2,1}$	1.75	263	$-\tau_{2,1}$	2.77(6)	2.77(6)

Table C.18 (continued): Modulation amplitudes and phase shifts (relative to the origin) for the refinements in all tested restrained magnetic superspace groups of the neutron single-crystal data of CrAs at $p_{\text{nom}} = 0.17$ GPa. The superscripts [100], [010] and [001] do not belong to the formal space group symbol, but indicate the direction in which the two-fold screw axis of the respective space group $P2_1$ is oriented in order to allow differentiation. A space group symbol in parentheses indicates an artificially lowered symmetry where the $Pnma$ symmetry is retained by suitable restrictions.

















Nuclear space group ($P2_1^{(010)}$)	Magnetic superspace group $P2_1,1'(\text{a0g}0\text{s})$	Restraints	M_x				M_y		M_z		$ M $		
			A_x [μB]	φ [°]	A_y [μB]	σ [°]	A_z [μB]	τ [°]	min	max			
	—	 Cr1,1  Cr2,1  Cr2,2  Cr1,2	1.5	161	$\varphi_{1,1}$	2.9	-78	$\sigma_{1,1}$	1.1	102	$\tau_{1,1}$	1.2(14)	3.3(14)
			3.5	112	$\varphi_{2,1}$	3.6	-4	$\sigma_{2,1}$	1.4	181	$\tau_{2,1}$	2.8(14)	4.4(14)
			3.5	248	$-\varphi_{2,1}$	3.6	184	$180 - \sigma_{2,1}$	1.4	179	$-\tau_{2,1}$	2.8(14)	4.4(14)
			1.5	199	$-\varphi_{1,1}$	2.9	258	$180 - \sigma_{1,1}$	1.1	258	$-\tau_{1,1}$	1.2(14)	3.3(14)
	M equal	 Cr1,1  Cr2,1  Cr2,2  Cr1,2	2.38	187	$\varphi_{1,1}$	3.51	-70	$\sigma_{1,1}$	1.60	117	$\tau_{1,1}$	2.29(11)	3.91(11)
			2.13	101	$\varphi_{2,1}$	3.82	0	$\sigma_{2,1}$	1.16	233	$\tau_{2,1}$	2.29(11)	3.91(11)
			2.13	259	$-\varphi_{2,1}$	3.82	180	$180 - \sigma_{2,1}$	1.16	127	$-\tau_{2,1}$	2.29(11)	3.91(11)
			2.38	173	$-\varphi_{1,1}$	3.51	250	$180 - \sigma_{1,1}$	1.60	243	$-\tau_{1,1}$	2.29(11)	3.91(11)
	M optimal	 Cr1,1  Cr2,1  Cr2,2  Cr1,2	2.13	186	$\varphi_{1,1}$	2.42	-82	$\sigma_{1,1}$	1.19	196	$\tau_{1,1}$	2.43(11)	2.43(11)
			2.32	108	$\varphi_{2,1}$	3.63	1	$\sigma_{2,1}$	3.05	261	$\tau_{2,1}$	3.73(11)	3.73(11)
			2.32	252	$-\varphi_{2,1}$	3.63	179	$180 - \sigma_{2,1}$	3.05	99	$-\tau_{2,1}$	3.73(11)	3.73(11)
			2.13	174	$-\varphi_{1,1}$	2.42	262	$180 - \sigma_{1,1}$	1.19	164	$-\tau_{1,1}$	2.43(11)	2.43(11)
	M equal + optimal	 Cr1,1  Cr2,1  Cr2,2  Cr1,2	2.65	190	$\varphi_{1,1}$	3.16	-80	$\sigma_{1,1}$	1.71	189	$\tau_{1,1}$	3.16(8)	3.16(8)
			2.45	91	$\varphi_{2,1}$	3.15	-2	$\sigma_{2,1}$	2.01	-98	$\tau_{2,1}$	3.16(8)	3.16(8)
			2.45	269	$-\varphi_{2,1}$	3.15	182	$180 - \sigma_{2,1}$	2.01	98	$-\tau_{2,1}$	3.16(8)	3.16(8)
			2.65	170	$-\varphi_{1,1}$	3.16	260	$180 - \sigma_{1,1}$	1.71	171	$-\tau_{1,1}$	3.16(8)	3.16(8)

Table C.18 (continued): Modulation amplitudes and phase shifts (relative to the origin) for the refinements in all tested restrained magnetic superspace groups of the neutron single-crystal data of CrAs at $p_{\text{nom}} = 0.17$ GPa. The superscripts [100], [010] and [001] do not belong to the formal space group symbol, but indicate the direction in which the two-fold screw axis of the respective space group $P2_1$ is oriented in order to allow differentiation. A space group symbol in parentheses indicates an artificially lowered symmetry where the $Pnma$ symmetry is retained by suitable restrictions.

















Nuclear space group (Pa)	Magnetic superspace group $Pa.1'(00g)0s$	Restraints	M_x		M_y		M_z		$ M $	
			A_x [μ_B]	φ [°]	A_y [μ_B]	σ [°]	A_z [μ_B]	τ [°]	min	max
		—	Cr1,1 	69	5	-11	3	195	$\tau_{1,1}$	2(2)
			Cr1,2 	-69	5	11	3	-15	$180 - \tau_{1,1}$	2(2)
			Cr2,1 	85	1	107	1	240	$\tau_{2,1}$	2(2)
			Cr2,2 	-85	1	253	1	-60	$180 - \tau_{2,1}$	2(2)
		M equal	Cr1,1 	88	4.3	-11	0.3	164	$\tau_{1,1}$	1.4(3)
			Cr1,2 	-88	4.3	11	0.3	16	$180 - \tau_{1,1}$	1.4(3)
			Cr2,1 	70	0.8	80	3.4	216	$\tau_{2,1}$	1.4(3)
			Cr2,2 	-70	0.8	-80	3.4	-36	$180 - \tau_{2,1}$	1.4(3)
		M optimal	Cr1,1 	68	4.21	-23	2.73	244	$\tau_{1,1}$	4.21(10)
			Cr1,2 	-68	4.21	23	2.73	-64	$180 - \tau_{1,1}$	4.21(10)
			Cr2,1 	75	1.15	74	1.71	165	$\tau_{2,1}$	1.71(10)
			Cr2,2 	-75	1.15	-74	1.71	15	$180 - \tau_{2,1}$	1.71(10)
		M equal + optimal	Cr1,1 	70	3.12	-20	2.50	250	$\tau_{1,1}$	3.12(8)
			Cr1,2 	-70	3.12	20	2.50	-70	$180 - \tau_{1,1}$	3.12(8)
			Cr2,1 	110	2.68	57	2.73	166	$\tau_{2,1}$	3.12(8)
			Cr2,2 	250	2.68	-57	2.73	14	$180 - \tau_{2,1}$	3.12(8)

Table C.18 (continued): Modulation amplitudes and phase shifts (relative to the origin) for the refinements in all tested restrained magnetic superspace groups of the neutron single-crystal data of CrAs at $p_{\text{nom}} = 0.17$ GPa. The superscripts [100], [010] and [001] do not belong to the formal space group symbol, but indicate the direction in which the two-fold screw axis of the respective space group $P2_1$ is oriented in order to allow differentiation. A space group symbol in parentheses indicates an artificially lowered symmetry where the $Pnma$ symmetry is retained by suitable restrictions.

Nuclear space group ($P\bar{1}$)	Magnetic superspace group $P\bar{1}_1'(\text{abg})_0$ s	Restraints	M_x		M_y		M_z		$ M $	
			A_x [μ_B]	φ [°]	A_y [μ_B]	σ [°]	A_z [μ_B]	τ [°]	min	max
	—		2.2	-28	3.0	-64	0.9	255	1.3(7)	3.6(7)
			2.1	244	4.4	-4	0.5	-35	1.9(7)	4.5(7)
			2.1	-64	4.4	184	0.5	215	1.9(7)	4.5(7)
			2.2	208	3.0	244	0.9	-75	1.3(7)	3.6(7)
	M equal		1.25	-18	3.17	-59	3.10	188	2.44(12)	3.90(12)
			2.44	260	3.76	-13	1.05	-8	2.44(12)	3.90(12)
			2.44	-80	3.76	193	1.05	188	2.44(12)	3.90(12)
			1.25	198	3.17	239	3.10	-8	2.44(12)	3.90(12)
	M optimal		1.8	10	2.7	-78	2.0	194	2.7(2)	2.7(2)
			3.4	255	3.5	-15	0.6	242	3.5(2)	3.5(2)
			3.4	-75	3.5	195	0.6	-62	3.5(2)	3.5(2)
			1.8	170	2.7	258	2.0	-14	2.7(2)	2.7(2)
	M equal + optimal		2.0	4	3.2	-80	2.5	193	3.2(2)	3.2(2)
			3.2	262	3.2	-9	0.3	196	3.2(2)	3.2(2)
			3.2	-82	3.2	189	0.3	-16	3.2(2)	3.2(2)
			2.0	176	3.2	260	2.5	-13	3.2(2)	3.2(2)

Table C.18 (continued): Modulation amplitudes and phase shifts (relative to the origin) for the refinements in all tested restrained magnetic superspace groups of the neutron single-crystal data of CrAs at $p_{\text{nom}} = 0.17$ GPa. The superscripts [100], [010] and [001] do not belong to the formal space group symbol, but indicate the direction in which the two-fold screw axis of the respective space group $P2_1$ is oriented in order to allow differentiation. A space group symbol in parentheses indicates an artificially lowered symmetry where the $Pnma$ symmetry is retained by suitable restrictions.

Nuclear space group ($P1$)	Magnetic superspace group $P1.1'(\text{abg})_0$ s	Restraints	M_x		M_y		M_z		$ M $	
			A_x [μB]	φ [°]	A_y [μB]	σ [°]	A_z [μB]	τ [°]	min	max
	$P1.1'(\text{abg})_0$ s	—	2	-90	3	113	σ_1	1	τ_1	1(6)
			3	251	2	-3	σ_2	3	τ_2	3(6)
			2	50	2	-16	σ_3	0	τ_3	2(6)
			1	65	7	13	σ_4	1	τ_4	1(6)
		M equal	2.3	29	4.7	107	σ_1	0.3	τ_1	2.3(3)
			2.2	217	4.7	117	σ_2	0.7	τ_2	2.3(3)
			3.7	10	2.5	-50	σ_3	2.7	τ_3	2.3(3)
			2.8	-80	4.4	41	σ_4	0.8	τ_4	2.3(3)
		M optimal	2.83	249	0.76	127	σ_1	2.79	τ_1	2.86(14)
			1.21	63	3.41	-10	σ_2	3.23	τ_2	3.43(14)
			1.92	110	2.25	23	σ_3	1.21	τ_3	2.26(14)
			4.70	89	4.79	-6	σ_4	2.13	τ_4	4.98(14)
	M equal + optimal		3.15	10	3.59	106	σ_1	1.92	τ_1	3.64(9)
			3.54	201	3.15	103	σ_2	2.00	τ_2	3.64(9)
			3.23	21	1.66	21	σ_3	3.64	τ_3	3.64(9)
			2.69	-76	3.16	45	σ_4	3.03	τ_4	3.64(9)
	$double\ helix\ \uparrow c$	helix	2.25	0	2.25	-90	$\varphi_1 - 90$	0	*	2.25(8)
			2.25	174	2.25	84	$\varphi_2 - 90$	0	*	2.25(8)
			2.25	0	2.25	-90	$\varphi_1 - 90$	0	*	2.25(8)
			2.25	174	2.25	84	$\varphi_2 - 90$	0	*	2.25(8)

* fixed value

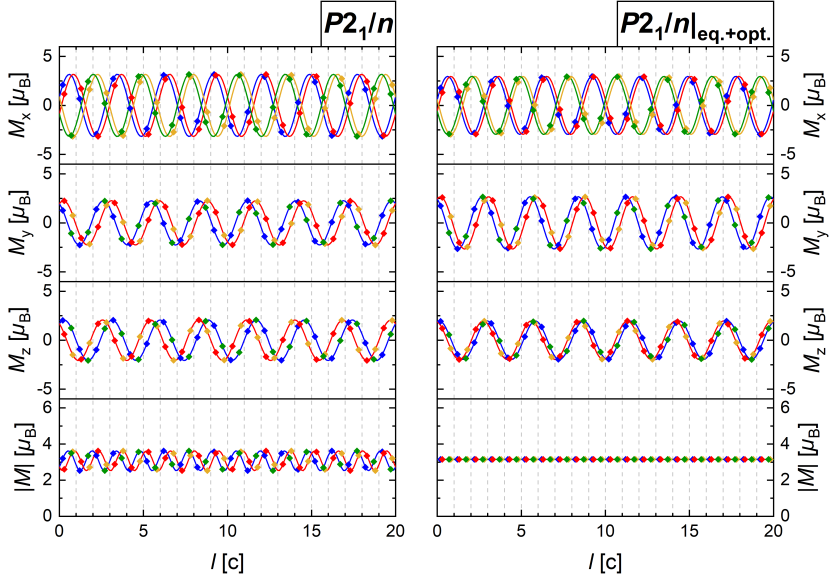


Figure C.1: The directional components of the magnetic moment along the x -, y - and z -axis (M_x , M_y and M_z , respectively) and the absolute value $|M|$ of the magnetic moment in the approximate structure with $c' = 20/7 \cdot c$ of the basic structure for the magnetic models related to the magnetic superspace group $P2_1/n.1'(0bg)0ss$. Points indicate values realized on Cr sites, full lines show the underlying modulation function. The colors correspond to the Cr sites as marked in Figure 8.19 and Table C.18. The dashed gray lines mark the unit cell borders of the basic crystal structure.

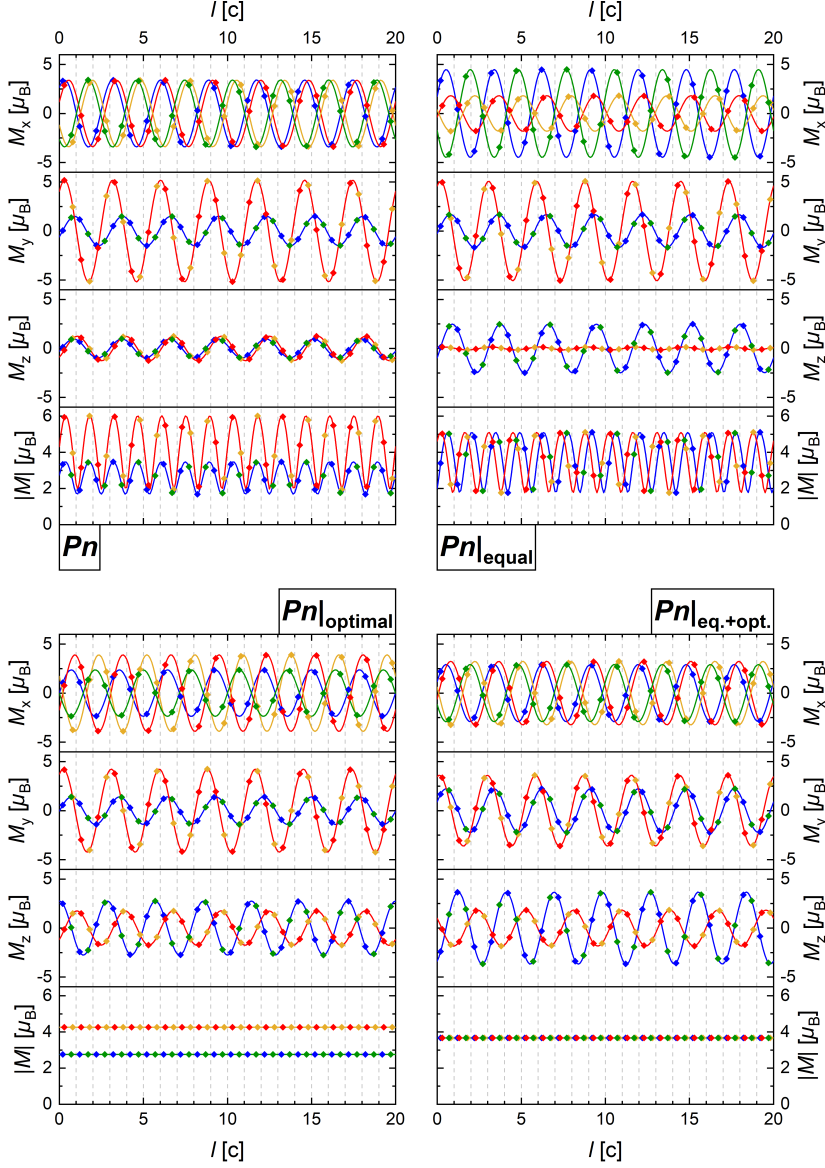


Figure C.2: The directional components of the magnetic moment along the x -, y - and z -axis (M_x , M_y and M_z , respectively) and the absolute value $|M|$ of the magnetic moment in the approximate structure with $c' = 20/7 \cdot c$ of the basic structure for the magnetic models related to the magnetic superspace group $Pn.1'(0bg)0ss$. Points indicate values realized on Cr sites, full lines show the underlying modulation function. The colors correspond to the Cr sites as marked in Figure 8.19 and Table C.18. The dashed gray lines mark the unit cell borders of the basic crystal structure.

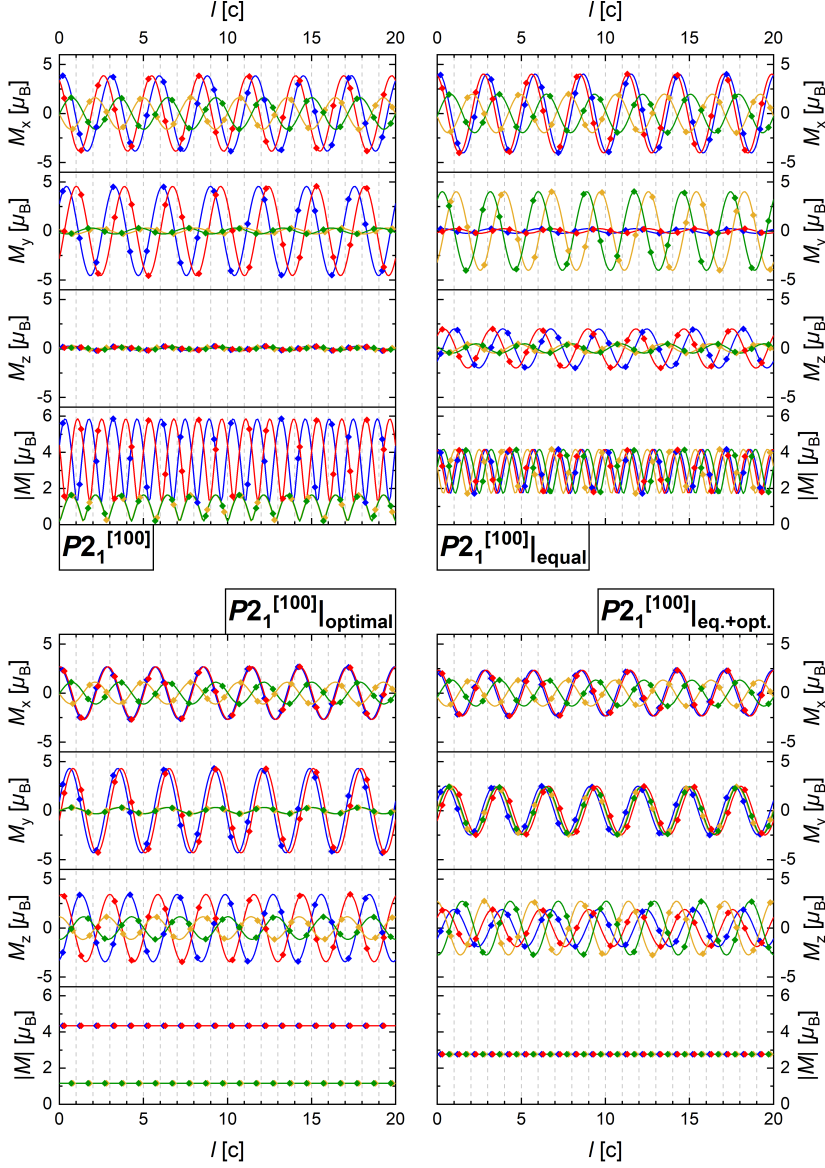


Figure C.3: The directional components of the magnetic moment along the x -, y - and z -axis (M_x , M_y and M_z , respectively) and the absolute value $|M|$ of the magnetic moment in the approximate structure with $c' = 20/7 \cdot c$ of the basic structure for the magnetic models related to the magnetic superspace group $P2_1.1'(0\text{bg})0s$ (space group $P2_1^{[100]}$). Points indicate values realized on Cr sites, full lines show the underlying modulation function. The colors correspond to the Cr sites as marked in Figure 8.19 and Table C.18. The dashed gray lines mark the unit cell borders of the basic crystal structure.

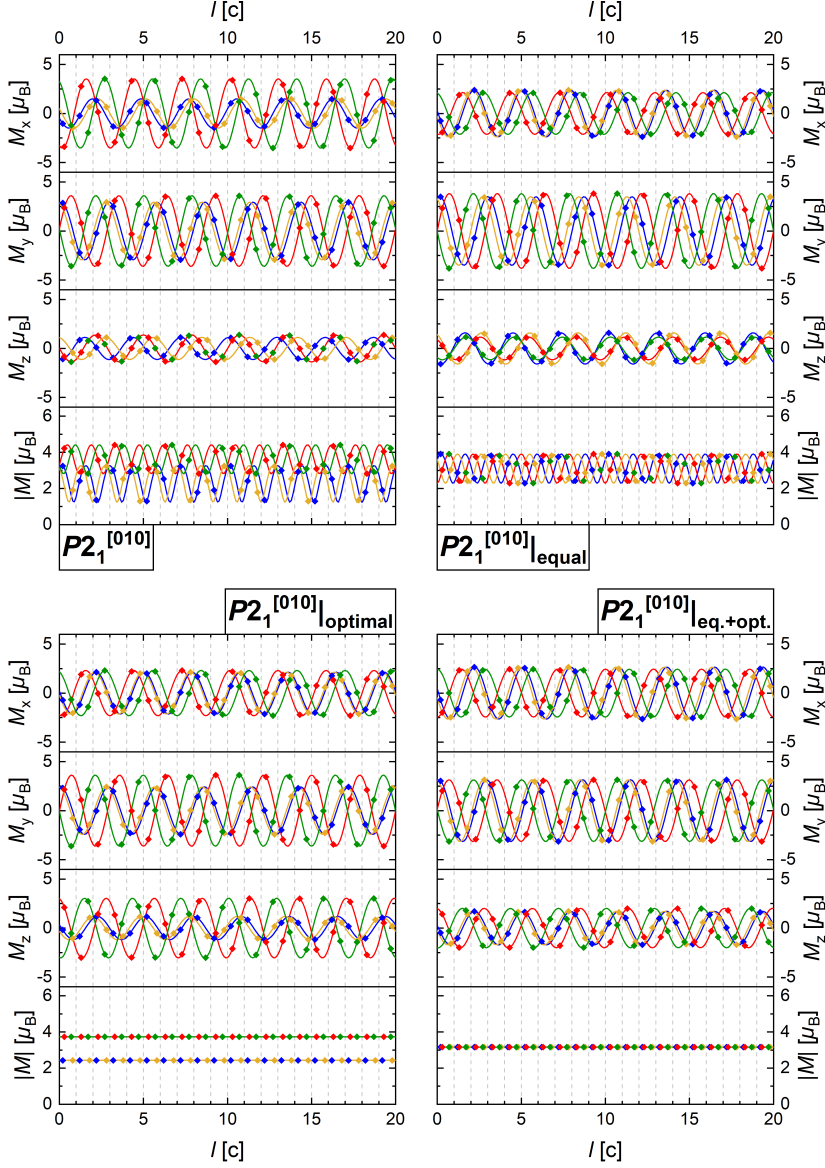


Figure C.4: The directional components of the magnetic moment along the x -, y - and z -axis (M_x , M_y and M_z , respectively) and the absolute value $|M|$ of the magnetic moment in the approximate structure with $c' = 20/7 \cdot c$ of the basic structure for the magnetic models related to the magnetic superspace group $P2_1.1'(a0g)0s$ (space group $P2_1^{[010]}$). Points indicate values realized on Cr sites, full lines show the underlying modulation function. The colors correspond to the Cr sites as marked in Figure 8.19 and Table C.18. The dashed gray lines mark the unit cell borders of the basic crystal structure.

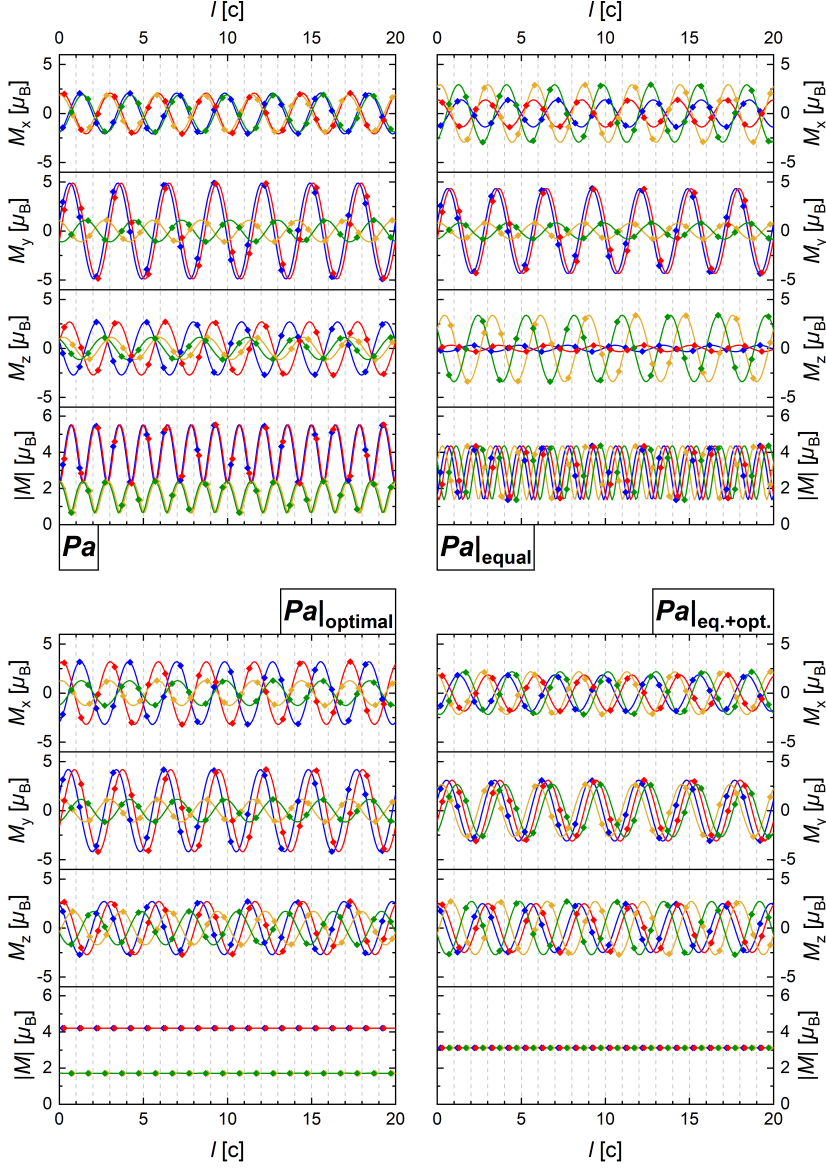


Figure C.5: The directional components of the magnetic moment along the x -, y - and z -axis (M_x , M_y and M_z , respectively) and the absolute value $|M|$ of the magnetic moment in the approximate structure with $c' = {}^{20}/_7 \cdot c$ of the basic structure for the magnetic models related to the magnetic superspace group $Pa.1'(00g)0s$. Points indicate values realized on Cr sites, full lines show the underlying modulation function. The colors correspond to the Cr sites as marked in Figure 8.19 and Table C.18. The dashed gray lines mark the unit cell borders of the basic crystal structure.

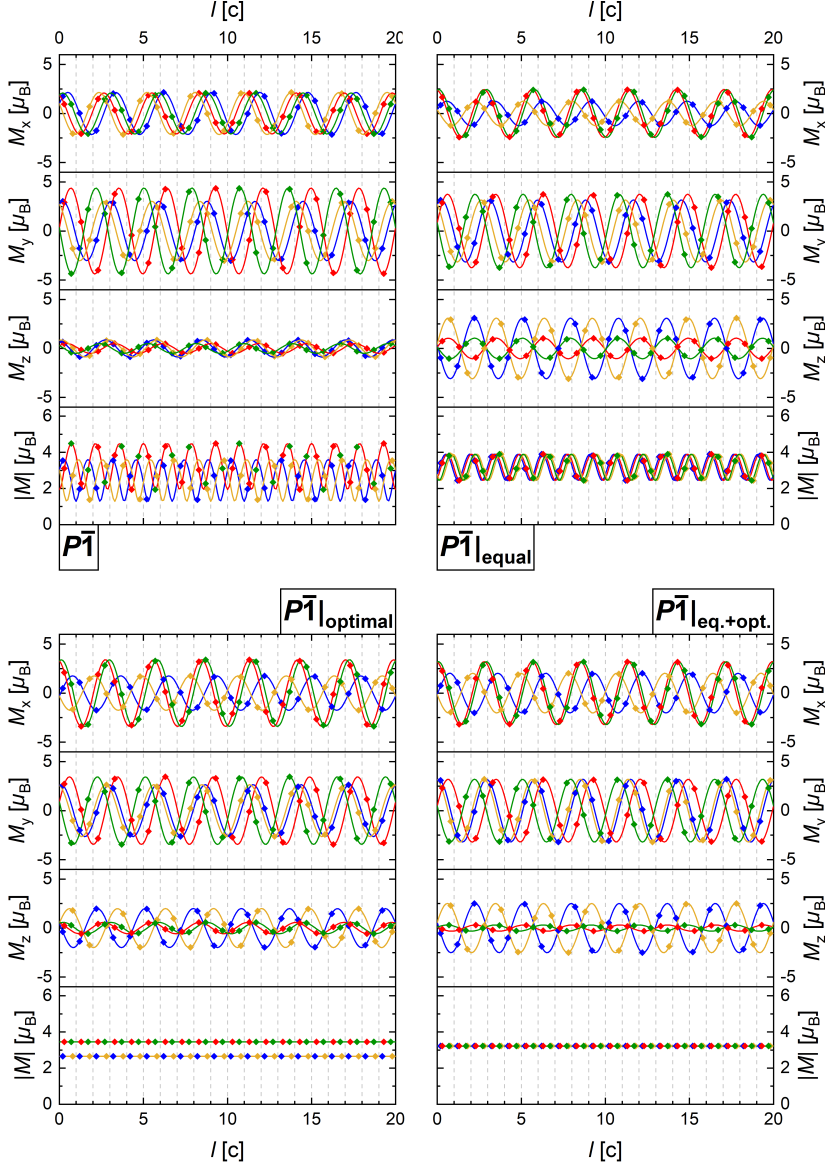


Figure C.6: The directional components of the magnetic moment along the x -, y - and z -axis (M_x , M_y and M_z , respectively) and the absolute value $|M|$ of the magnetic moment in the approximate structure with $c' = 20/7 \cdot c$ of the basic structure for the magnetic models related to the magnetic superspace group $P\bar{1}.1'(\text{abg})0s$. Points indicate values realized on Cr sites, full lines show the underlying modulation function. The colors correspond to the Cr sites as marked in Figure 8.19 and Table C.18. The dashed gray lines mark the unit cell borders of the basic crystal structure.

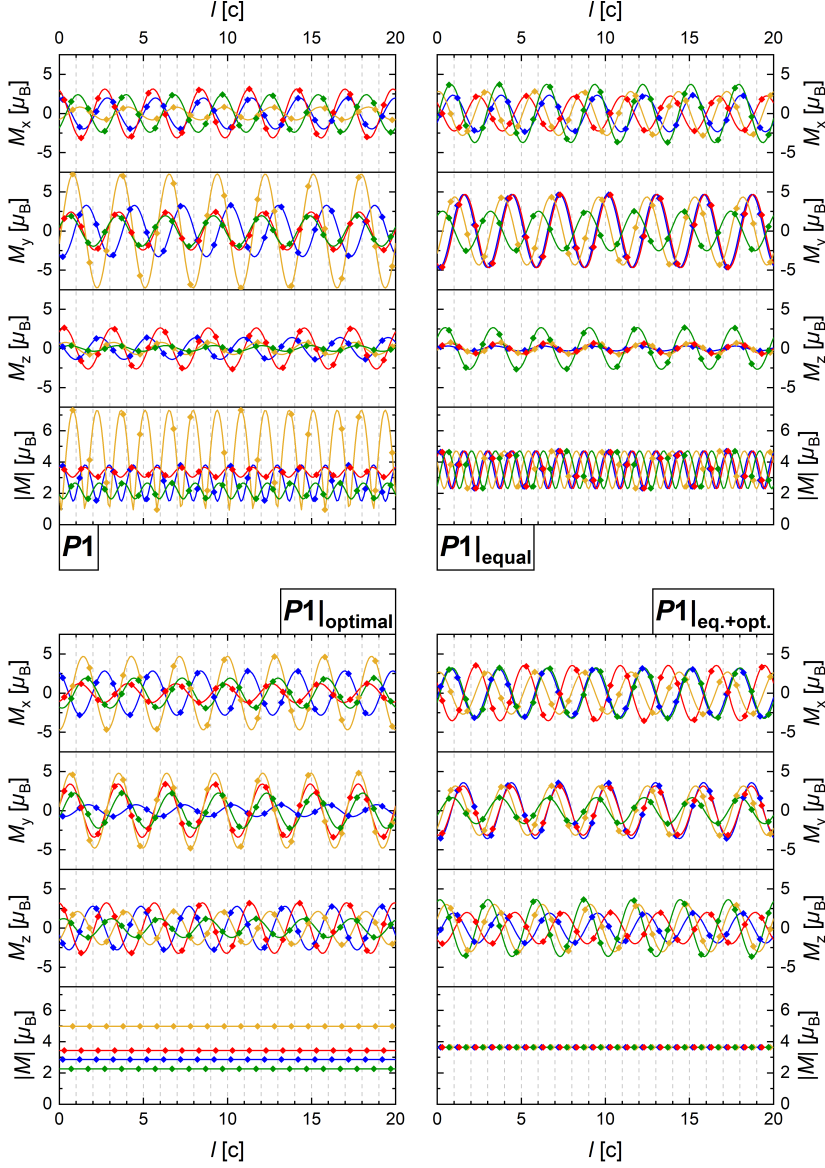


Figure C.7: The directional components of the magnetic moment along the x -, y - and z -axis (M_x , M_y and M_z , respectively) and the absolute value $|M|$ of the magnetic moment in the approximate structure with $c' = 20/7 \cdot c$ of the basic structure for the magnetic models related to the magnetic superspace group $P1.1'(\text{abg})0s$. Points indicate values realized on Cr sites, full lines show the underlying modulation function. The colors correspond to the Cr sites as marked in Figure 8.19 and Table C.18. The dashed gray lines mark the unit cell borders of the basic crystal structure.

Table C.19: Final agreement factors for the neutron powder data of CrAs at $T = 1.5$ K for all tested magnetic superspace groups. The superscripts [100], [010] and [001] do not belong to the formal space group symbol, but indicate the direction in which the two-fold screw axis of the respective space group $P2_1$ is oriented in order to allow differentiation.

Nuclear space group	Magnetic superspace group	all			main			satellites			profile	
		R (obs/all)	wR (obs/all)		R (obs/all)	wR (obs/all)		R (obs/all)	wR (obs/all)		Rp	wRp
$Pnma$	$Pnma.1'(00g)000s$	4.83/6.59	5.42/5.57		3.25/3.72	4.34/4.39		42.20/66.74	6.42/6.65		12.99	22.09
	$Pnma.1'(00g)s0s$	4.63/4.89	7.10/7.12		2.91/2.98	3.64/3.66		11.94/12.94	8.50/8.53		11.02	20.04
	$Pnma.1'(00g)0s0s$	4.29/4.31	6.31/6.33		2.82/2.82	3.64/3.64		8.09/8.13	7.37/7.39		6.75	9.38
	$Pnma.1'(00g)s00s$	4.41/4.57	5.85/5.89		2.84/2.90	3.73/3.73		10.02/10.56	6.96/7.01		6.87	9.39
$P2_1ma$	$P2_1ma.1'(00g)000s$	6.01/6.60	7.58/7.62		3.00/3.31	4.92/4.97		20.58/22.21	9.11/9.15		8.04	11.90
	$P2_1ma.1'(00g)0s0s$	4.28/4.34	6.14/6.15		2.60/2.60	4.01/4.01		8.72/8.90	7.11/7.12		6.56	8.81
$Pn2_1a$	$Pn2_1a.1'(00g)000s$	4.35/4.37	6.29/6.30		2.80/2.83	3.83/3.85		8.37/8.38	7.30/7.30		6.76	9.40
	$Pn2_1a.1'(00g)s00s$	4.18/4.22	5.91/5.92		2.76/2.76	3.58/3.58		8.79/8.94	6.87/6.88		6.54	8.87
$Pnm2_1$	$Pnm2_1.1'(00g)000s$	4.61/6.86	5.17/5.36		3.03/3.41	4.20/4.23		42.68/70.07	6.09/6.42		12.64	21.77
	$Pnm2_1.1'(00g)s00s$	4.80/6.39	7.44/7.59		2.91/3.18	3.89/4.02		11.00/16.68	8.77/8.94		11.36	20.69
	$Pnm2_1.1'(00g)0ss$	4.09/4.31	5.48/5.53		2.56/2.70	3.54/3.56		8.99/9.47	6.41/6.48		6.67	9.15
	$Pnm2_1.1'(00g)s0ss$	4.36/4.38	6.55/6.55		2.58/2.58	3.78/3.78		8.18/8.23	7.55/7.56		6.61	9.09
$P2_12_12_1$	$P2_12_12_1.1'(00g)000s$	5.43/6.98	7.10/7.29		3.08/3.14	4.57/4.61		12.32/18.19	8.27/8.51		12.76	30.86
	$P2_12_12_1.1'(00g)00ss$	3.82/3.85	5.37/5.38		2.74/2.78	3.97/3.99		6.61/6.62	6.03/6.03		6.27	8.36
$P2_1/n$	$P2_1/n.1'(00g)000s$	4.51/4.56	6.50/6.51		2.87/2.87	3.88/3.88		8.38/8.53	7.49/7.51		6.88	9.55
	$P2_1/n.1'(00g)00ss$	4.32/4.42	6.15/6.16		2.86/2.95	3.84/3.87		8.81/8.93	7.05/7.06		6.64	8.93
$P2_1/m$	$P2_1/m.1'(a0g)000s$	5.99/7.02	8.23/8.27		3.12/3.37	5.01/5.02		19.46/23.14	9.83/9.88		8.21	11.98
	$P2_1/m.1'(a0g)00ss$	4.38/4.44	5.66/5.67		2.83/2.83	3.96/3.96		8.33/8.51	6.39/6.41		6.62	8.86
$P2_1/a$	$P2_1/a.1'(00g)000s$	5.35/6.79	7.05/7.26		3.14/3.19	4.68/4.71		12.23/17.92	8.22/8.50		12.86	30.98
	$P2_1/a.1'(00g)s0s$	3.85/3.94	5.41/5.43		2.80/2.84	3.93/3.95		6.81/7.00	6.13/6.15		6.22	8.33

Table C.19 (continued): Final agreement factors for the neutron powder data of CrAs at $T = 1.5$ K for all tested magnetic superspace groups. The superscripts [100], [010] and [001] do not belong to the formal space group symbol, but indicate the direction in which the two-fold screw axis of the respective space group $P2_1$ is oriented in order to allow differentiation..

Nuclear space group	Magnetic superspace group	all		main		satellites		profile	
		R (obs/all)	wR (obs/all)	R (obs/all)	wR (obs/all)	R (obs/all)	wR (obs/all)	Rp	wRp
Pn	$Pn.1'(0bg)0s$	4.92/5.20	6.82/6.91	2.82/2.91	3.90/3.97	9.21/9.88	7.86/7.96	6.96	9.72
	$Pn.1'(0bg)ss$	4.32/4.39	6.04/6.04	2.83/2.92	3.89/3.91	8.66/8.67	6.87/6.87	6.60	8.89
$P2_1[100]$	$P2_1.1'(0bg)0s$	3.64/3.68	4.93/4.94	2.60/2.64	3.70/3.71	6.31/6.36	5.51/5.52	5.99	8.10
Pm	$Pm.1'(a0g)0s$	4.14/4.29	5.94/5.97	2.67/2.75	4.01/4.02	9.24/9.63	6.89/6.91	6.78	9.11
	$Pm.1'(a0g)ss$	4.21/4.41	5.78/5.82	2.74/2.81	4.10/4.14	7.79/8.29	6.51/6.54	6.52	8.70
$P2_1[010]$	$P2_1.1'(a0g)0s$	3.56/3.59	4.89/4.89	2.48/2.48	3.64/3.64	6.37/6.46	5.45/5.46	5.90	7.96
Pa	$Pa.1'(00g)0s$	3.63/3.68	4.91/4.92	2.60/2.64	3.65/3.66	6.54/6.63	5.54/5.55	5.99	8.10
	$P2_1.1'(00g)0s$	5.76/8.03	7.66/7.84	3.17/3.24	4.85/4.88	12.48/20.32	8.90/9.13	13.28	30.96
$P\bar{1}$	$P2_1.1'(00g)ss$	3.75/3.79	5.02/5.03	2.56/2.60	3.66/3.68	6.59/6.63	5.63/5.63	5.98	8.08
	$P\bar{1}.1'(abg)0s$	3.97/4.05	5.47/5.48	2.63/2.65	3.89/3.89	7.32/7.53	6.16/6.19	6.31	8.39
$P1$	$P1.1'(abg)0s$	3.71/3.78	5.04/5.05	2.54/2.58	3.72/3.74	6.64/6.80	5.63/5.64	5.99	8.02
	<i>double helix</i> $\uparrow c$	3.25/3.39	4.48/4.52	2.51/2.56	3.70/3.71	5.81/6.27	4.90/4.96	6.12	8.30

Table C.20: Final agreement factors for the neutron powder data in the relevant magnetic superspace groups. The superscripts [100], [010] and [001] do not belong to the formal space group symbol, but indicate the direction in which the two-fold screw axis of the respective space group $P2_1$ is oriented in order to allow differentiation.

T [K]	Nuclear space group	Magnetic superspace group	all		main		satellites		profile	
			R (obs/all)	wR (obs/all)	R (obs/all)	wR (obs/all)	R (obs/all)	wR (obs/all)	R_p	wR_p
10	$P2_1$ [100]	$P2_1.1'(\text{0bg})0s$	3.89/3.96	4.45/4.46	2.77/2.80	3.50/3.51	6.75/6.92	4.94/4.95	6.31	8.48
	$P2_1$ [010]	$P2_1.1'(\text{a0g})0s$	3.68/3.79	4.32/4.33	2.65/2.68	3.45/3.46	6.40/6.65	4.75/4.77	6.32	8.36
	Pa	$Pa.1'(\text{00g})0s$	3.72/3.82	4.40/4.42	2.74/2.77	3.46/3.46	6.51/6.80	4.93/4.95	6.32	8.48
	$P2_1$ [001]	$Pnma.1'(\text{00g})ss$	3.93/4.00	4.50/4.51	2.68/2.73	3.41/3.42	6.90/7.02	5.04/5.05	6.31	8.46
	$P1$	$P1.1'(\text{abg})0s$	3.73/3.79	4.32/4.33	2.67/2.70	3.43/3.43	6.34/6.45	4.76/4.77	6.27	8.38
		$double\ helix\ \uparrow c$	3.48/3.58	4.11/4.14	2.63/2.67	3.44/3.44	6.34/6.66	4.49/4.54	6.46	8.70
35	$P2_1$ [100]	$P2_1.1'(\text{0bg})0s$	3.76/3.88	4.40/4.42	2.68/2.72	3.46/3.47	6.58/6.85	4.89/4.91	6.27	8.44
	$P2_1$ [010]	$P2_1.1'(\text{a0g})0s$	3.66/3.79	4.23/4.25	2.58/2.63	3.40/3.42	6.46/6.78	4.65/4.67	6.23	8.35
	Pa	$Pa.1'(\text{00g})0s$	3.68/3.77	4.37/4.38	2.63/2.67	3.39/3.40	6.69/6.90	4.90/4.92	6.27	8.44
	$P2_1$ [001]	$Pnma.1'(\text{00g})ss$	3.86/3.97	4.47/4.49	2.58/2.65	3.37/3.39	6.89/7.09	5.02/5.04	6.27	8.42
	$P1$	$P1.1'(\text{abg})0s$	3.69/3.83	4.29/4.31	2.58/2.63	3.41/3.42	6.46/6.78	4.72/4.74	6.23	8.34
		$double\ helix\ \uparrow c$	3.46/3.63	4.00/4.05	2.57/2.63	3.41/3.42	6.57/7.05	4.35/4.41	6.44	8.68
50	$P2_1$ [100]	$P2_1.1'(\text{0bg})0s$	4.21/4.37	5.06/5.08	2.84/2.92	3.75/3.78	7.51/7.86	5.72/5.74	6.58	8.77
	$P2_1$ [010]	$P2_1.1'(\text{a0g})0s$	3.68/3.86	4.45/4.47	2.66/2.74	3.57/3.59	6.29/6.74	4.90/4.93	6.34	8.52
	Pa	$Pa.1'(\text{00g})0s$	3.70/3.86	4.58/4.60	2.76/2.82	3.63/3.64	6.38/6.79	5.12/5.14	6.41	8.63
	$P2_1$ [001]	$Pnma.1'(\text{00g})ss$	3.94/4.12	4.66/4.68	2.71/2.81	3.56/3.59	6.80/7.16	5.21/5.24	6.40	8.59
	$P1$	$P1.1'(\text{abg})0s$	3.74/3.94	4.47/4.50	2.68/2.76	3.58/3.60	6.41/6.87	4.93/4.96	6.34	8.50
		$double\ helix\ \uparrow c$	3.45/3.63	4.22/4.24	2.65/2.75	3.61/3.62	6.21/6.63	4.58/4.62	6.54	8.81

Table C.20 (continued): Final agreement factors for the neutron powder data in the relevant magnetic superspace groups. The superscripts [100], [010] and [001] do not belong to the formal space group symbol, but indicate the direction in which the two-fold screw axis of the respective space group $P2_1$ is oriented in order to allow differentiation.

T [K]	Nuclear space group	Magnetic superspace group	all		main		satellites		profile	
			R (obs/all)	wR (obs/all)	R (obs/all)	wR (obs/all)	R (obs/all)	wR (obs/all)	R_p	wR_p
65	$P2_1$ [100]	$P2_1.1'(0bg)0s$	3.50/3.72	4.32/4.36	2.56/2.64	3.35/3.36	5.91/6.51	4.83/4.87	6.32	8.45
	$P2_1$ [010]	$P2_1.1'(a0g)0s$	3.42/3.81	4.20/4.26	2.45/2.54	3.32/3.25	5.98/7.11	4.70/4.77	6.24	8.41
	Pa	$Pa.1'(00g)0s$	3.51/3.76	4.34/4.39	2.59/2.66	3.39/3.41	6.16/6.88	4.87/4.93	6.33	8.45
	$P2_1$ [001]	$Pnma.1'(00g)ss$	3.62/3.85	4.39/4.43	2.54/2.63	3.29/3.31	6.21/6.76	4.94/4.98	6.32	8.42
	$P1$	$P1.1'(abg)0s$	3.46/3.81	4.29/4.34	2.46/2.55	3.25/3.26	5.97/6.94	4.81/4.87	6.26	8.39
		<i>double helix</i> $\uparrow c$	3.22/3.41	3.93/3.97	2.48/2.57	3.26/3.27	5.78/6.27	4.32/4.39	6.43	8.70
80	$P2_1$ [100]	$P2_1.1'(0bg)0s$	4.10/4.33	4.86/4.89	2.53/2.61	3.35/3.38	8.00/8.56	5.61/5.65	6.48	8.74
	$P2_1$ [010]	$P2_1.1'(a0g)0s$	3.50/3.87	4.16/4.22	2.39/2.47	3.18/3.20	6.47/7.54	4.67/4.75	6.25	8.50
	Pa	$Pa.1'(00g)0s$	3.58/3.83	4.28/4.32	2.44/2.51	3.20/3.22	6.90/7.61	4.88/4.93	6.29	8.56
	$P2_1$ [001]	$Pnma.1'(00g)ss$	3.74/3.98	4.38/4.41	2.41/2.50	3.17/3.19	6.96/7.53	4.98/5.02	6.28	8.54
	$P1$	$P1.1'(abg)0s$	3.51/3.85	4.21/4.26	2.38/2.46	3.18/3.20	6.40/7.37	4.73/4.80	6.26	8.48
		<i>double helix</i> $\uparrow c$	3.22/3.43	3.86/3.90	2.40/2.49	3.19/3.20	6.12/6.69	4.26/4.32	6.42	8.80
95	$P2_1$ [100]	$P2_1.1'(0bg)0s$	3.64/3.89	4.40/4.43	2.34/2.44	3.13/3.16	6.90/7.47	5.04/5.08	6.52	8.75
	$P2_1$ [010]	$P2_1.1'(a0g)0s$	3.56/3.90	4.21/4.26	2.28/2.38	3.06/3.09	6.81/7.69	4.78/4.85	6.50	8.72
	Pa	$Pa.1'(00g)0s$	3.53/3.76	4.30/4.34	2.32/2.41	3.10/3.12	6.88/7.46	4.95/4.99	6.52	8.75
	$P2_1$ [001]	$Pnma.1'(00g)ss$	3.39/3.66	3.90/3.95	2.23/2.34	2.99/3.02	6.19/6.81	4.37/4.42	6.33	8.58
	$P1$	$P1.1'(abg)0s$	3.24/3.55	3.76/3.81	2.19/2.29	2.98/3.00	5.93/6.75	4.17/4.23	6.30	8.53
		<i>double helix</i> $\uparrow c$	2.88/3.06	3.40/3.44	2.21/2.32	2.98/2.99	5.21/5.68	3.67/3.72	6.49	8.85

Table C.20 (continued): Final agreement factors for the neutron powder data in the relevant magnetic superspace groups. The superscripts [100], [010] and [001] do not belong to the formal space group symbol, but indicate the direction in which the two-fold screw axis of the respective space group $P2_1$ is oriented in order to allow differentiation.

T [K]	Nuclear space group	Magnetic superspace group	all			main			satellites		profile	
			R (obs/all)	wR (obs/all)		R (obs/all)	wR (obs/all)		R (obs/all)	wR (obs/all)	R_p	wR_p
110	$P2_1$ [100]	$P2_1.1'(\text{0bg})0s$	3.44/3.66	4.07/4.10		2.18/2.24	2.90/2.91		6.77/7.34	4.68/4.71	6.29	8.53
	$P2_1$ [010]	$P2_1.1'(\text{a0g})0s$	3.36/3.64	3.93/3.97		2.20/2.27	2.91/2.92		6.49/7.27	4.45/4.50	6.30	8.50
	Pa	$Pa.1'(\text{00g})0s$	3.38/3.57	4.07/4.09		2.22/2.29	2.92/2.93		6.78/7.27	4.70/4.73	6.29	8.52
	$P2_1$ [001]	$Pnma.1'(\text{00g})ss$	3.50/3.71	4.10/4.12		2.15/2.24	2.83/2.85		6.84/7.32	4.71/4.75	6.30	8.49
	$P1$	$P1.1'(\text{abg})0s$	3.29/3.50	3.84/3.87		2.07/2.15	2.78/2.80		6.43/6.94	4.37/4.40	6.28	8.48
		$double\ helix\ \uparrow c$	2.97/3.12	3.46/3.49		2.11/2.19	2.83/2.84		6.02/6.39	3.85/3.88	6.47	8.81
155	$P2_1$ [100]	$P2_1.1'(\text{0bg})0s$	3.00/3.17	3.53/3.55		2.02/2.08	2.65/2.66		5.78/6.22	4.01/4.03	6.38	8.80
	$P2_1$ [010]	$P2_1.1'(\text{a0g})0s$	2.83/2.94	3.35/3.37		1.89/1.94	2.52/2.53		5.23/5.48	3.73/3.76	6.46	8.90
	Pa	$Pa.1'(\text{00g})0s$	3.20/3.31	4.04/4.06		2.09/2.14	2.61/2.62		6.50/6.74	4.81/4.82	6.60	9.03
	$P2_1$ [001]	$Pnma.1'(\text{00g})ss$	2.85/2.99	3.42/3.44		1.88/1.95	2.48/2.49		5.43/5.70	3.91/3.93	6.37	8.82
	$P1$	$P1.1'(\text{abg})0s$	2.83/2.94	3.38/3.40		1.86/1.91	2.47/2.49		5.20/5.46	3.78/3.80	6.44	8.88
		$double\ helix\ \uparrow c$	2.42/2.52	3.07/3.10		1.87/1.91	2.55/2.55		4.44/4.72	3.35/3.39	6.67	9.39
200	$P2_1$ [100]	$P2_1.1'(\text{0bg})0s$	3.11/3.52	3.65/3.69		2.13/2.22	2.91/2.92		6.25/7.57	4.09/4.14	7.11	9.97
	$P2_1$ [010]	$P2_1.1'(\text{a0g})0s$	3.17/3.37	3.87/3.91		2.13/2.20	2.87/2.88		5.90/6.42	4.31/4.36	7.47	10.31
	Pa	$Pa.1'(\text{00g})0s$	2.96/3.30	3.80/3.83		2.21/2.28	3.04/3.05		5.60/6.77	4.27/4.31	7.17	10.00
	$P2_1$ [001]	$Pnma.1'(\text{00g})ss$	2.92/3.60	3.56/3.72		2.06/2.15	2.79/2.80		5.48/7.79	3.99/4.22	7.13	9.97
	$P1$	$P1.1'(\text{abg})0s$	3.00/3.20	3.63/3.67		2.09/2.16	2.98/2.99		5.37/5.88	3.93/3.98	7.38	10.20
		$double\ helix\ \uparrow c$	2.90/3.06	3.58/3.62		2.13/2.23	2.89/2.90		6.00/6.37	3.95/4.00	7.63	10.74

Table C.20 (continued): Final agreement factors for the neutron powder data in the relevant magnetic superspace groups. The superscripts [100], [010] and [001] do not belong to the formal space group symbol, but indicate the direction in which the two-fold screw axis of the respective space group $P2_1$ is oriented in order to allow differentiation.

T [K]	Nuclear space group	Magnetic superspace group	all			main			satellites		profile	
			R (obs/all)	wR (obs/all)		R (obs/all)	wR (obs/all)		R (obs/all)	wR (obs/all)	R_p	wRp
240	$P2_1$ [100]	$P2_1.1'(0bg)0s$	3.03/3.51	6.13/6.17		2.21/2.29	3.76/3.76		5.79/7.45	7.35/7.41	7.04	9.45
	$P2_1$ [010]	$P2_1.1'(a0g)0s$	3.09/3.32	6.00/6.01		2.15/2.23	3.70/3.71		5.79/6.36	6.92/6.93	7.16	9.56
	Pa	$Pa.1'(00g)0s$	2.95/3.37	6.01/6.06		2.11/2.19	3.58/3.59		5.99/7.50	7.32/7.38	7.09	9.50
	$P2_1$ [001]	$Pnma.1'(00g)ss$	3.11/3.59	6.05/6.09		2.22/2.32	3.65/3.66		5.82/7.25	7.24/7.29	7.10	9.50
	$P1$	$P1.1'(abg)0s$	3.09/3.30	5.99/6.00		2.19/2.26	3.69/3.70		5.50/6.00	6.90/6.91	7.16	9.54
		$double\ helix\uparrow c$	2.90/3.20	6.33/6.37		2.32/2.41	3.64/3.65		5.34/6.44	7.59/7.63	7.51	10.00
260	$P2_1$ [100]	$P2_1.1'(0bg)0s$	5.56/6.80	9.18/9.26		4.79/5.09	7.19/7.21		8.54/12.67	10.42/10.54	9.35	13.69
	$P2_1$ [010]	$P2_1.1'(a0g)0s$	5.53/6.81	9.28/9.38		4.74/5.04	7.18/7.19		8.65/12.92	10.60/10.73	9.35	13.69
	Pa	$Pa.1'(00g)0s$	5.43/6.29	9.20/9.26		4.77/5.06	7.12/7.13		8.45/11.51	10.61/10.70	9.33	13.68
	$P2_1$ [001]	$Pnma.1'(00g)ss$	5.44/6.66	9.25/9.32		4.83/5.33	7.27/7.28		7.99/11.62	10.49/10.58	9.36	13.69
	$P1$	$P1.1'(abg)0s$	5.60/6.57	9.42/9.50		4.79/5.11	7.23/7.25		8.97/12.16	10.80/10.91	9.34	13.67
		$double\ helix\uparrow c$	5.32/6.34	9.49/9.53		4.89/5.19	7.45/7.46		8.00/12.75	11.11/11.18	9.41	13.79

Appendix D

Supporting Figures to Chapter “Results and Discussion”

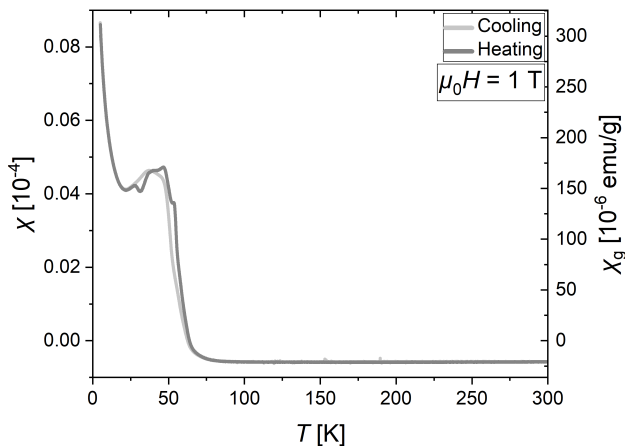


Figure D.1: The magnetic susceptibility of PTFE as function of temperature with an applied magnetic field of $\mu_0 H = 1$ T. χ is the unitless magnetic susceptibility, χ_g is the often-used, non-SI mass susceptibility.

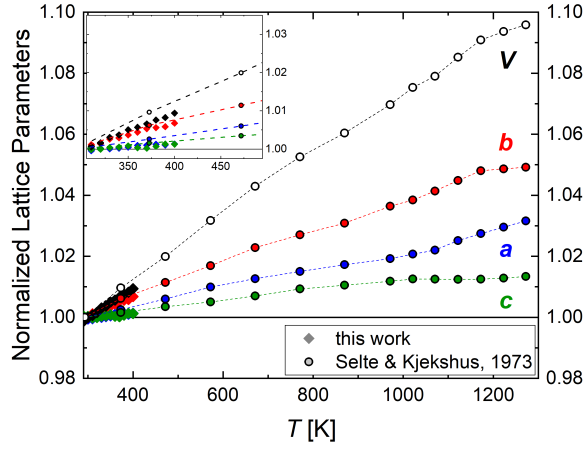


Figure D.2: Comparison of the lattice parameters and unit cell volume of CrAs normalized to their respective values at room temperature as a function of temperature between the present work and the literature (Selte and Kjekshus, 1971 [20]).

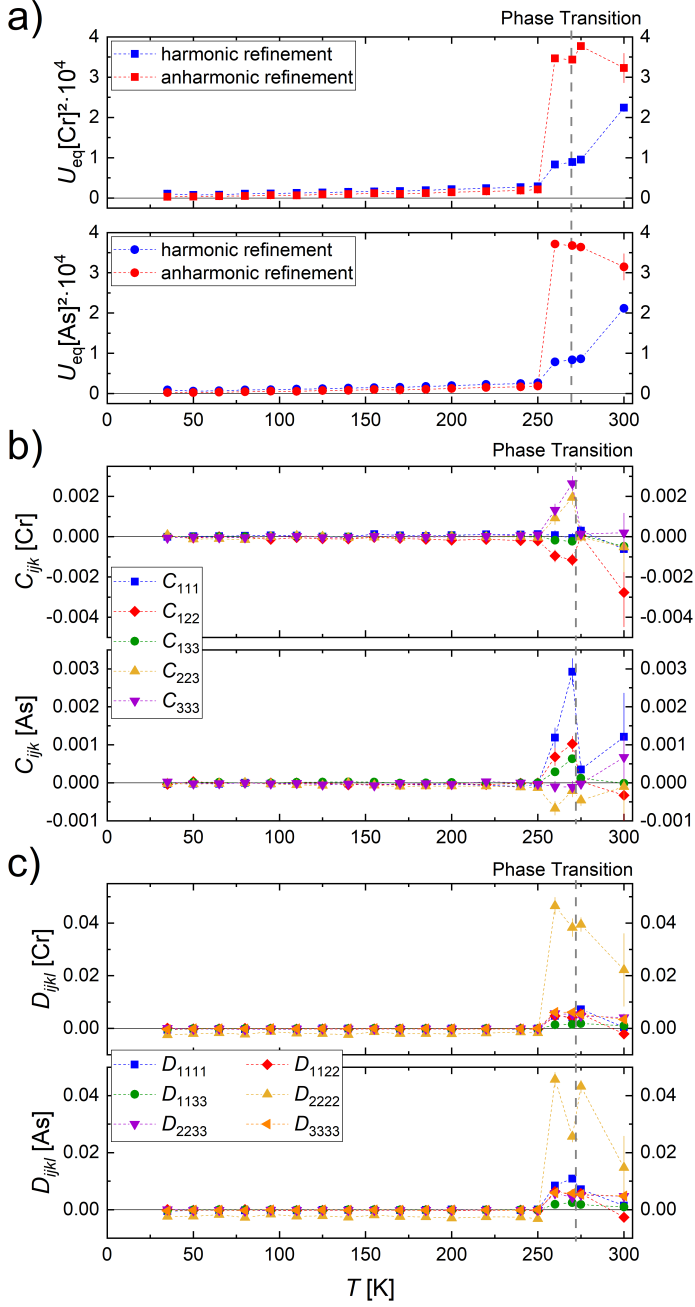


Figure D.3: The harmonic ADP U_{eq}^2 (a) and the anharmonic ADP of third order C_{ijk} (b) and fourth order D_{ijkl} (c) from the synchrotron X-ray measurements on CrAs as function of temperature. Only the significant parameters are shown as function of temperature at ambient pressure. The dashed lines are guides for the eye.

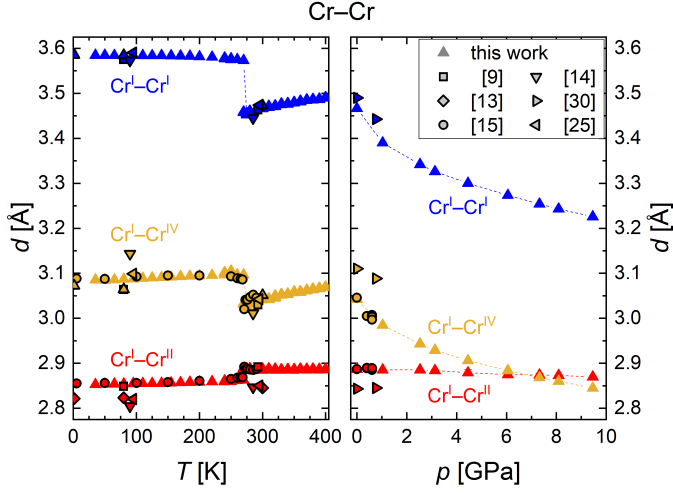


Figure D.4: Comparison of the measured Cr–Cr distances as function of temperature (*left*) and of pressure (*right*) for CrAs within this work and reported in the literature (Selte and Kjekshus, 1971 [9]; Boller and Kallel, 1971 [14]; Keller *et al.*, 2015 [13]; Yu *et al.*, 2015 [30]; Shen *et al.*, 2016 [15]; Sen *et al.*, 2019 [25]). The dashed lines are guides for the eye.

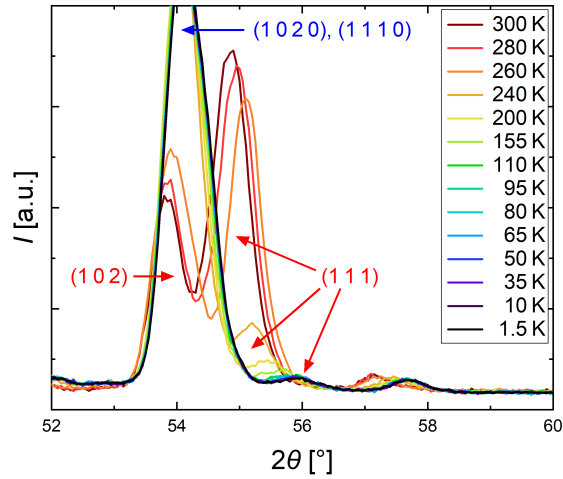


Figure D.5: Detail of the neutron powder diffraction pattern at different temperatures. Peaks of the high-temperature phase of CrAs are indicated in red with three indices, peaks of the low-temperature phase of CrAs are indicated in blue with four indices. The (111) peak decreases in intensity below the phase transition, but is still clearly visible down to 1.5 K, with a continuous shift towards higher 2θ values. The (102) peak is not visible beneath the (1020)/(1110) double peak.

Appendix E

Calculation of Distance Distortion and Angular Distortion

Within this work and as part of the overall study of the CrAs structure, the structural distortion of two coordination polyhedra – the $[\text{CrAs}_6]$ octahedron and the $[\text{AsCr}_6]$ trigonal prism – was quantified to measure the effect of temperature and pressure. While a number of different distortion parameters exists for the octahedron – and, in general, for the “ideal” polyhedra – [221–226], those are not easily suitable to be applied to the non-“ideal” trigonal prism. In order to keep the calculated distortion for the octahedron and the trigonal prism analogous, distortion parameters that can be seen as generalized adaptations of previously reported distortion parameters are used.

In the mentioned definitions of the various distortion parameters, the distortion is – directly or indirectly – calculated as deviation from the ideal values of the considered polyhedra. Those values are fixed for the “ideal” polyhedra, but this principle cannot simply be generalized. Hence, to take into account non-“ideal” polyhedra, instead of using any fixed values the underlying idea is to consider the symmetry restrictions of a given polyhedral shape.

The general polyhedron is described by the center C – either a central atom or a void – and the vertices V – in most cases occupied by the coordination atoms. Based on this, the two geometrical measurements considered for the distortion parameters are the distances $d(V) = C-V$ and the angles $\varphi(VV') = \angle V-C-V'$.

In a completely unrestricted polyhedron, the distances d are all independent and the angles φ only restricted by the (potential) overdetermination of the system¹. For a polyhedron with a higher symmetry, restrictions are posed on the distances and angles that lead to some degeneration, e.g. $d(V) = d(V')$. Following these restrictions, groups of distances and angles that are degenerated in the considered symmetry can be identified.

The basic idea to calculate the distortion of some real polyhedron from the reference polyhedron with the ideal symmetry is then to take the deviation of the individual distances/angles from the respective group average, to add this up for all groups and normalize it to the number of entities. This way, the distortion can be

¹In general, for n vertices and $n \geq 3$, the number of independent angles is at most $3(n-2)$ (to add an additional vertex, three angles to other vertices are sufficient to define its angular position), with $\sum_{i=1}^n (i-1) = \frac{(n-1)n}{2}$ angles (vertex pairs VV') in total (the i th vertex that is added yields $i-1$ angles with the other vertices).

calculated for any symmetry and without the need to specify any absolute value.

The distance distortion δ_D is thus in general defined as

$$\delta_D = \frac{1}{n} \cdot \sqrt{\sum_{i=1}^p \sum_{j=1}^{q_i} \left(\frac{d_{i,j} - \bar{d}_i}{\bar{d}_i} \right)^2},$$

with the number of vertices n and the center-vertex distances d that are divided into p groups of distances that are degenerated in the reference structure, each group (index i) comprising q_i distances with average \bar{d}_i . For the cases of octahedron and trigonal prism – the ones relevant in the context of this work – this gets simplified as in both ideal structures all distances are equal and thus only one group of degenerated distances exists, comprising all n distances:

$$\delta_D = \frac{1}{n} \cdot \sqrt{\sum_{j=1}^n \left(\frac{d_j - \bar{d}}{\bar{d}} \right)^2},$$

This special case is very similar to the distance distortion introduced by Baur [221] for the octahedron.

The angular distortion δ_A is defined in the same way as

$$\delta_A = \frac{1}{m} \cdot \sqrt{\sum_{i=1}^s \sum_{j=1}^{t_i} \left(\frac{\varphi_{i,j} - \bar{\varphi}_i}{\bar{\varphi}_i} \right)^2},$$

with the number of vertex pairs m and the vertex-center-vertex angles φ that are divided into s groups of angles that are degenerated in the reference structure, each group (index i) comprising t_i angles with average $\bar{\varphi}_i$.

The details for the two considered coordination polyhedra regarding the degeneration groups are shown in Table E.1 and Table E.2.

For both the distance and the angular distortion the absolute value is rather secondary, but higher values indicate a larger distortion. If the real polyhedron meets the restrictions of the ideal one, the distortion is 0. A comparison between different distortions should only be done between polyhedra with the same reference structure.

Table E.1: Details for the calculation of the angular distortion δ_A of the distorted $[\text{CrAs}_6]$ octahedron in the crystal structure of CrAs.

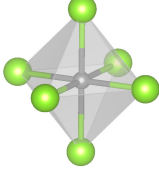
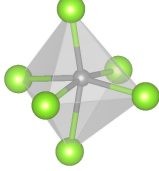
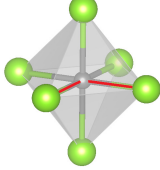
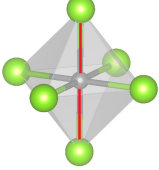
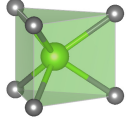
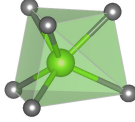
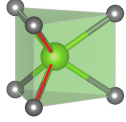
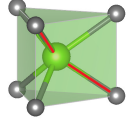
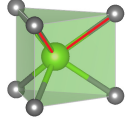
$[\text{CrAs}_6]$	Ideal Structure (Octahedron)		Real Structure
			
Angle Group i	$i = 1$	$i = 2$	
Visualization			
Degeneracy t_i	$t_1 = 12$	$t_2 = 3$	

 Table E.2: Details for the calculation of the angular distortion δ_A of the distorted $[\text{AsCr}_6]$ trigonal prism in the crystal structure of CrAs.

$[\text{AsCr}_6]$	Ideal Structure (Trigonal Prism)		Real Structure
			
Angle Group i	$i = 1$	$i = 2$	$i = 3$
Visualization			
Degeneracy t_i	$t_1 = 3$	$t_2 = 6$	$t_3 = 6$

Band / Volume 247

Stoichiometric control and magnetoelectric coupling in artificial multiferroic heterostructures

P. Schöffmann (2021), vii, 176 pp

ISBN: 978-3-95806-575-8

Band / Volume 248

A Unified Framework for Functional Renormalisation Group Calculations and its Application to Three Dimensional Hubbard Models

J. Ehrlich (2021), xvi, 213 pp

ISBN: 978-3-95806-582-6

Band / Volume 249

Photoemission electron microscopy of magneto-ionic effects in $\text{La}_{0.7}\text{Sr}_{0.3}\text{MnO}_3$

M. Wilhelm (2021), 134 pp

ISBN: 978-3-95806-592-5

Band / Volume 250

Development of a Multiplexer System and Measurement of the Neutron Yield for a Low-Energy Accelerator-Driven Neutron Source

M. Rimpler (2021), v, 200 pp

ISBN: 978-3-95806-600-7

Band / Volume 251

Resolving interface effects in voltage controlled magnetic heterostructures using advanced neutron scattering and electron microscopy methods

T. Bhatnagar-Schöffmann (2021), ix, 171 pp

ISBN: 978-3-95806-604-5

Band / Volume 252

Strain development of *Gluconobacter oxydans* and *Pseudomonas putida* for production of the sweetener 5-ketofructose

K. Wohlers (2022), VI, 118 pp

ISBN: 978-3-95806-612-0

Band / Volume 253

Topological magnonic properties of two-dimensional magnetic materials

L. Zhang (2022), xx, 154 pp

ISBN: 978-3-95806-621-2

Band / Volume 254

Role of secondary metabolites in antiphage defense in *Streptomyces*

Aël Hardy (2022), IV, 193 pp

ISBN: 978-3-95806-633-5

Band / Volume 255

Neutron Scattering

Lectures of the JCNS Laboratory Course held at Forschungszentrum Jülich
and at the Heinz-Maier-Leibnitz Zentrum Garching

edited by T. Brückel, S. Förster, M. Kruteva, M. Zobel, and R. Zorn (2022),
ca. 300 pp

ISBN: 978-3-95806-634-2

Band / Volume 256

**Magnetoelectric Interactions in Multiferroic Thin-film Heterosystems
and Nanostructures**

H. Gökdemir (2022), x, 140 pp

ISBN: 978-3-95806-635-9

Band / Volume 257

**High-Performance Computing Approach to Hybrid Functionals
in the All-Electron DFT Code FLEUR**

M. Redies (2022), xi, 109 pp

ISBN: 978-3-95806-639-7

Band / Volume 258

**Establishing regulatable expression systems in the acetic acid bacterium
Gluconobacter oxydans 621H**

P. M. Fricke (2022), VIII, 187 pp

ISBN: 978-3-95806-642-7

Band / Volume 259

**Density-Functional Perturbation Theory within the All-Electron Full-
Potential Linearized Augmented Plane-Wave Method: Application to
Phonons**

C.-R. Gerhorst (2022), xvi, 317 pp

ISBN: 978-3-95806-649-6

Band / Volume 260

Crystal and Magnetic Structure of CrAs under Extreme Conditions

A. Eich (2022), viii, 235 pp

ISBN: 978-3-95806-655-7

Weitere **Schriften des Verlags im Forschungszentrum Jülich** unter
<http://www.zbw1.fz-juelich.de/verlagextern1/index.asp>

Schlüsseltechnologien / Key Technologies
Band / Volume 260
ISBN 978-3-95806-655-7